UNIVERSITÄT
SIEGEN

Rannam Chaaban

Frequency-Domain Fatigue Analysis of Wind Trubine Structures and Fatigue Damage Detection: Performance Evaluation of Spectral-Based Methods Against The Rainflow Counting Algorithm

Schriftenreihe der Arbeitsgruppe
für Technische Mechanik
im Institut für Mechanik und Regelungstechnik - Mechatronik

Herausgeber: Claus-Peter Fritzen

Band 18

Impressum

Prof. Dr.-Ing. Claus-Peter Fritzen
Arbeitsgruppe für Technische Mechanik
Institut für Mechanik und Regelungstechnik - Mechatronik
Universität Siegen
57068 Siegen
ISSN 2191-5601
URN urn:nbn:de:hbz:467-19485
DOI 10.25819/ubsi/9962
Zugl.: Siegen, Univ., Diss., 2021

Frequency-Domain Fatigue Analysis of Wind Turbine Structures and Fatigue Damage Detection: Performance Evaluation of Spectral-Based Methods Against The Rainflow Counting Algorithm

genehmigte
DISSERTATION
zur Erlangung des Grades eines Doktors
der Ingenieurwissenschaften

vorgelegt von
M.Sc. Rannam Chaaban

eingereicht bei der
Naturwissenschaftlich-Technischen Fakultät
der Universität Siegen
Siegen 2021

Betreuer und erster Gutachter
Prof. Dr.-Ing. Claus-Peter Fritzen
Universität Siegen

Zweiter Gutachter
Univ.-Prof. Dr.-Ing. Dirk Söffker
Universität Duisburg-Essen

Tag der mündlichen Prüfung
26. Februar 2021

Acknowledgement

Pursuing my doctoral research had been a fantastic experience accompanied by many ingenious people. Without their support this thesis would not exist in its current form.

First and foremost, I would like to thank my advisor Prof. Dr.-Ing. Claus-Peter Fritzen for his guidance, patience and all the trust put into me. Always supportive and never constraining my academic freedoms, Prof. Fritzen presented a great encouragement during all phases of my research work. My gratitude and appreciation goes beyond professional matters. It was an honour to work for you, Professor Fritzen, Ihnen gebührt mein aufrichtiger Dank!

A special thanks for Prof. Dr.-Ing. Rüdiger Höffer at the Ruhr-Universität Bochum for providing the utility-scale turbine measurements. Without his support, I wouldn't have been able to do the work that is in this thesis.

Also, I would like to express my sincere gratitude and appreciation to Prof. Dr.-Ing. Otmar Loffeld not only for giving me the opportunity to join the research school of Multi-Modal Sensor Systems for Environmental Exploration (MOSES) at the Centre for Sensor Systems (ZESS) but also for his continuous and valuable suggestions focused on the improvement of the scientific quality of my work.

My gratitude extends to Dipl.-Ing. Wolfgang Richter, Mr. Gerhard Dietrich and Mrs. Gisela Thomas for their support during the majority of the experiments discussed in this thesis; and for helping me out with the many bureaucratic processes of the university.

The work group of "Technische Mechanik" is a terrific place full of amazing and interesting people, many of whom became friends. To you I want to say: It was a fantastic time indeed! I savoured to the fullest spending time with you inside and outside the lab and wish you all the best for your lives.

I want to express my deepest gratitude to my parents and my brothers, who encouraged and supported me in every phase of my life. Everyone of them, in their very own way, were crucial to become the person I am.

Finally, I want to thank my wife Souhair and my amazing sons Marcel and Daniel for their love and care. Souhair supported me unconditionally in good times as well as in bad times. Words can not describe how much you mean to me. Souhair, you are wonderful!

Siegen, October 2020 Rannam Chaaban

Abstract

Fatigue failure of metallic structures such as wind turbine towers is a problem that affects their remaining service life. Fatigue cracks are most likely to initiate in the structural hot spots such as holes or welded joints. The time-domain approach in dealing with the fatigue analysis problem is the industry standard of fatigue load certification and fatigue damage assessment on wind turbines systems. The time-domain approach is based on time domain cycle counting and a linear fatigue accumulation rule to estimate a cumulative fatigue damage index. By comparing this index to a reference value, fatigue failure prediction and fatigue life estimation are possible.

The development of an equivalent formulation to the time-domain fatigue analysis problem has been an active topic of research in the past few years. This equivalent formulation is based on the random vibration fatigue theory where fatigue analysis is done in the frequency domain. The frequency-domain fatigue analysis has found it's way into many applications subject to random loading. However, the frequency-domain fatigue analysis is developed under certain assumptions that are hard to meet in the case of wind turbine loading. This includes for example the stationarity of the loading, the assumption of zero-mean and the Gaussian amplitude distribution of the stochastic loading.

This thesis sets three objectives. The first objective is to address systematically the assumptions required by the spectral fatigue analysis methods in order to be able to accept the obtained results. To achieve this objective, the theoretical basis of the spectral fatigue analysis is reviewed and the limitations of the frequency-domain methods are addressed. Furthermore, a new strategy that enables using the spectral methods for wind turbine fatigue analysis is developed.

The second objective is the performance assessment of the equivalent formulations of fatigue analysis problem, the frequency-domain against the industry standard time-domain. This is achieved using two different data-sets: simulation and operational. The simulation-based data-set is generated using hi-fidelity wind turbine simulation tool and aims to replicate the integrated design process at early stages; while the operational data-set is obtained from tower loading measurements of an operating small and utility-scale wind turbines and used to evaluate the performance of different spectral fatigue analysis methods against the well-established rainflow cycle counting method in time domain.

The third objective is to explore the potentials of using comparative sensor data approach in the early detection in structural failure. This approach is based on monitoring the linear

correlation of the measured strain or estimated fatigue damage at pre-defined sensor locations. An experimental validation of this method is presented in this thesis, and the obtained results demonstrate the possibility of using this technique for structural failure detection.

The proposed objectives aim to meet the challenges of optimizing wind turbine structures in terms of cost, fatigue damage and service life time by developing new approaches capable of saving time, computational effort, resources in addition to reducing cost of energy.

Contents

Nomenclature

Abbreviations

$\alpha_{0.75}$	Empirical $\alpha_{0.75}$ method
cG	Corrected Gaussian fatigue damage
G	Gaussian fatigue damage
tG	Transformed Gaussian model approach
BLCS	Baseline control system,
BM	Bands method
CDF	Cumulative distribution function
CM	Condition monitoring
CPSD	Cross power spectral density
DK	Dirlik method
DLC	Design load case
DOF	Degree of freedom
ESE	East-south-east
EW	East-west
FAST	Fatigue, aerodynamics, structures and turbulence
FRF	Frequency response function
GSPI	Gain-scheduled proportional integral
MATE	Moving average trend estimator
NB	Narrow-band method
NREL	National renewable energy laboratory
NS	North-south
OC	Ortiz-Chen method
OWT	Offshore wind turbine
PbP	Projection-by-projection
PDF	Probability density function
PSD	Power spectral density
PZ	Petrucci-Zuccarello method
RFC	Rainflow counting algorithm
RMS	Root mean square
RWT	Reference wind turbine

SHM	Structural health monitoring
SM	Single-moment method
TB1	1^{st} Tovo-Benasciutti method
TB2	2^{nd} Tovo-Benasciutti method
TLP	Tension leg platform
WL	Wirsching-Light method
WSW	West-south-west
ZBi	Zaho-Baker improved method
ZBs	Zhao-Baker simplified method

Mathematical Symbols

α_i	Bandwidth parameter
$\bar{s}$	Stress mean value
β_i	i-th generalized spectral band-width parameter
χ	Correction factor
δ_v	Anmarcke's parameter
$\dot{\mathcal{D}}\left(T\right)$	Fatigue damage rate over the time period T
$\operatorname{erf}\left(\,\cdot\,\right)$	Error function
η_i^k	Normalised fatigue damage index of the spectral method $k \in \{NB, OC, SM, \dots\}$ calculated using the $i \in \{G, cG, tG\}$ appraoch
$\Gamma(\,\cdot\,)$	Euler gamma function
γ_{IF}	Irregularity factor
γ_{Ku}	Kurtosis
γ_{Sk}	Skewness
$\Gamma_x\left(\,\cdot\,\right)$	Auto-covariance function of the signal $x(t)$
$\hat{\underline{z}}$	Estimation of the vector $\underline{z}$
λ_i	i-th moment of a random variable
Λ_m	m-th moment of the probability distribution $p_a\left(s\right)$
$\mathbb{R}^+$	Set of positive real numbers
$\mathcal{D}\left(T\right)$	Fatigue damage over the period T
$\mathcal{D}_{cr}$	Critical fatigue damage
$\underline{\underline{\Sigma}}_s$	Shape matrix
$\underline{\underline{A}}$	Matrix notation
$\underline{\underline{A}}$	State transition matrix
$\underline{\underline{A}}_c$	Closed loop state transition matrix
$\underline{\underline{B}}$	Input gain matrix

$\underline{\underline{C}}$	Observation matrix
$\underline{\underline{C}}_c$	Closed-loop measurement matrix
$\underline{\underline{C}}_d$	Damping matrix
$\underline{\underline{D}}$	Direct feed-through matrix
$\underline{\underline{F}}_u$	Deterministic excitation gain matrix
$\underline{\underline{F}}_w$	Random excitation gain matrix
$\underline{\underline{G}}$	Disturbance gain matrix
$\underline{\underline{H}}(s)$	Transfer function matrix
$\underline{\underline{K}}$	Stiffness matrix
$\underline{\underline{K}}_g$	Controller gain matrix
$\underline{\underline{L}}$	Observer gain matrix
$\underline{\underline{M}}$	Mass matrix
μ_x	Mean value of single $x(t)$
ν	Poison's ratio
ν_0	Expected zero up-crossing rate
ν_c	Expected cycle rate
ν_p	Expected peak rate
Ω_g	Generator speed
ω_n	Natural circular frequency
σ_x	Standard deviation of the variable x
$\tilde{\eta}_i^k$	Normalized accumulative fatigue damage index of the spectral method $k \in \{NB, OC, SM, \dots\}$ calculated using the $i \in \{G, cG, tG\}$ appraoch
$\tilde{\mathcal{D}}$	Accumulative fatigue damage
ε	Spectral width parameter
$\varepsilon_x, \varepsilon_y, \varepsilon_z$	Strain on $x-, y-, z-$axes
$\underline{q}, \underline{\dot{q}}, \underline{\ddot{q}}$	Distplacement, velocity, acceleration vectors
$\underline{s}(t)$	Stress vector
$\underline{u}$	Deterministic loading
$\underline{w}$	Stochastic loading
$\underline{X}(s)$	Laplace transformation of the vector $\underline{x}(t)$
$\underline{x}(t)$	State vector
$\underline{z}$	Vector notation
ζ	Damping ratio
E	Young's modulus
f_{dt}	Drive-train natural frequency
f_{PFp}	Platform pitch natural frequency

f_{PFr}	Platform roll natural frequency
f_{PFy}	Platform yaw natural frequency
f_{T1fa}	Tower fore-aft first natural frequency
f_{T1ss}	Tower side-side first natural frequency
f_{T2fa}	Tower fore-aft second natural frequency
f_{T2ss}	Tower side-side second natural frequency
$G\left(\,\cdot\,\right)$	Transformation from non-Gaussian to Gaussian
$G_x\left(\,\cdot\,\right)$	One-sided power spectral density of the signal $x(t)$
K	Fatigue constant
K_i	Stress correction factor $i \in \{$Goodman, Soderberg, Gerber$\}$
M	Window length of the moving average trend estimator
m	Fatigue exponent
$N(T)$	Number of cycles to failure during the period T
$N\left(s, \bar{s}\right)$	Number of cycles to failure at ampltidue s and mean value $\bar{s}$
$n\left(s, \bar{s}\right)$	Number of cycles with ampltidue s and mean value $\bar{s}$
n_q	Number of degrees of freedom
n_u	Number of controlled inputs
n_w	Number of disturbance inputs
n_y	Number of measured outputs
N_i	Number of cycles to failure at the stress amplitude s_i
$P\left(\,\cdot\,\right)$	Probability distribution
$p\left(\,\cdot\,\right)$	Probability density function
P_g	Generator power
$p_{a,m}(s, \bar{s})$	Stress ampltidue-mean joint probability density function
$p_a(s)$	Marginal stress probability density function
$R_x\left(\,\cdot\,\right)$	Auto-correlation function of the signal $x(t)$
s	Stress amplitude
s_e	Equivalent stress range
s_p	Stress peak value
s_r	Stress range
s_v	Stress valey value
s_x, s_y, s_z	Stress on $x-, y-, z-$directions
S_∞	Endurance limit
S_u	Ultimate tensile strength
$S_x\left(\,\cdot\,\right)$	Two-sided power spectral density of the signal $x(t)$
T_g	Generator torque

$T_{Failure}$	Time till fatigue failure
T_{life}	Fatigue life time
$X(t)$	Stochastic process

Mathematical Operators

$\mathbb{E}(\,\cdot\,)$	Expected value
$(\,\cdot\,)^{-1}$	Inverse
$\mathrm{Prob}(\,\cdot\,)$	Probability
$\mathrm{tr}(\,\cdot\,)$	Trace operator
$\mathrm{Var}(\,\cdot\,)$	Variance
$\underline{\underline{H}}^*$	Conjugate transpose (Hermitian) of $\underline{\underline{H}}$

Subscripts

$(\,\cdot\,)_{\alpha_{0.75}}$	Index for empirical $\alpha_{0.75}$ method
$(\,\cdot\,)_{BM}$	Index for bands method
$(\,\cdot\,)_{cG}$	Index of corrected Gaussian
$(\,\cdot\,)_{DK}$	Index for Dirlik method
$(\,\cdot\,)_{d}$	Index of deterministic
$(\,\cdot\,)_{G}$	Index of Gaussian
$(\,\cdot\,)_{m}$	Index of measured
$(\,\cdot\,)_{NB}$	Index for narrow-band method
$(\,\cdot\,)_{nG}$	Index of non-Gaussian
$(\,\cdot\,)_{OC}$	Index for Ortiz-Chen method
$(\,\cdot\,)_{PbP}$	Index of projection-by-projection
$(\,\cdot\,)_{PZ}$	Index for Petrucci-Zuccarello method
$(\,\cdot\,)_{RFC}$	Index for rainflow counting method
$(\,\cdot\,)_{SM}$	Index for single-moment method
$(\,\cdot\,)_{s}$	Index of stochastic
$(\,\cdot\,)_{TB1}$	Index for 1st Tovo-Benasciutti method
$(\,\cdot\,)_{TB2}$	Index for 2nd Tovo-Benasciutti method
$(\,\cdot\,)_{tG}$	Index of transformed Gaussian model
$(\,\cdot\,)_{WL}$	Index for Wirsching-Light method
$(\,\cdot\,)_{ZBi}$	Index for improved Zhao-Baker method
$(\,\cdot\,)_{ZBs}$	Index for simplified Zhao-Baker method

Chapter 1

Introduction

Thats the whole problem with science. You've got a bunch of empiricists trying to describe things of unimaginable wonder.

— Bill Watterson

Contents

Wind power stations have to fulfil the "L^3 conditions": low cost, long-lasting and low service requirement [van Kuik et al., 2016]. Therefore, they should be seen from an integrated approach, as the design and optimisation for only one of these three objectives is not efficient. The main objective of the design and optimisation of wind power stations is to maximise the generated power while, at the same time, to maintain the lowest possible fatigue and extreme loading in the rotor, drive-train, tower and support structure, in addition to achieve the highest possible reliability of operation.

The state-of-the-art of the reliability assessment of modern onshore wind turbines is currently at an acceptable level [van Kuik et al., 2016]. This could be confirmed by less than one week of yearly downtime due to service and repair. Or in other words, assuming 100 % site accessibility and implementing a well organised efficient maintenance strategy, more onshore turbines show availability levels of above 98 %. Many reasons contribute to this, such as the gained knowledge of the operating conditions of onshore wind turbines, the increased use of condition monitoring (CM) systems, structural health monitoring (SHM) systems, in addition to the easy access to the turbines.

With the emerge of offshore wind turbine industry, different institutions such as the Federal

Maritime and Hydrographic Authority in 2007 and the German Lloyd Renewables in 2010, pushed in their standards toward the extension of the wind turbine condition monitoring system to include not only the drive-train but also the blades, tower, support structure in addition to the foundation [Schäfer, 2016]. The motivation to extend the CM systems to other turbine parts is based on the fact that modern offshore wind turbines operate in harsh and unexplored environment. This is mainly related to the increased height of the turbines which is too high for all other users of the sea i.e., fishery, shipping routes and defence and too low for aviation and weather forecast experts. In addition to the random wind loading, offshore wind turbines are also excited by the stochastic loading of the waves and currents on the support/floating structure. This means that offshore and floating turbines have new dynamics when compared to land-based ones. Another factor that motivates this shift is that many turbine warranties are expiring and the maintenance costs start to explode. To combat this, wind farm owners and operators are deploying CM systems to detect faults as early as possible before they cause secondary damage, therefore, reducing repair costs.

1.1 Problem Formulation / Motivation

The key challenge in the design of the offshore wind turbines (OWTs) is the cost reduction of the substructures and installation which typically contribute $25\,\% - 30\,\%$ of the cost of a wind farm development. The proper design of the substructures can reduce the cost substantially, thereby, making the OWTs more competitive by reducing their cost of energy.

OWTs operate in a harsh environment, therefore, the support structure should be designed carefully. Support structure of OWTs such as monopile or jackets, have natural frequencies close to the excitation frequency of the wind and waves. Floating platforms add extra degrees of freedom to the turbine which result into larger dynamic loading being transferred to the tower and substructure. This results into a dynamic amplification of the environmental loading close the these frequencies due to resonance. In order to avoid that, an integrated design approach of OWTs should be adopted to avoid resonance and loading close to natural frequencies should be, actively or passively, mitigated. This integrated design process should optimise the tower, substructure and foundation in terms of cost, fatigue damage and service lifetime. However, the key element in this new design approach is the rapid way in estimating the fatigue damage.

Fatigue loading and fatigue damage of wind turbines have been seen from different aspects by the research community. The first one is from the integrated design approach of wind turbine control systems where controller objectives are extended to reduce fatigue loading. The second aspect is as part of the SHM and CM systems, where expected service life and early fatigue damage detection plays the key role in reducing the cost of energy.

The integrated approach in wind turbine design has evolved in the past few years and the reduction of fatigue loading plays now the main role in new controller design. The first attempts in this direction employed the classical control theory with different single-input-single-output control loops [Bossanyi, 2009] with the aim to reduce blade, drive-train and tower loading by appropriate control of rotor speed, generator torque and blades collective and individual pitch angles according to the operating region. Later, the modern control theory is used for controller design to achieve the same objectives. This includes for example: the robust control [Lescher et al., 2006] theory, linear-parameter-varying (LPV) control [Kumar, 2011], disturbance accommodation control [Namik, 2012], in addition to optimal control techniques such as the linear-quadratic-Gaussian (LQG) control [Camblong et al., 2011; Nourdine et al., 2010] and the model predictive control [Chaaban et al., 2013; Chaaban et al., 2014a; Körber, 2014]. A detailed review of the state-of-the-art wind turbine control systems that go under the integrated wind turbine design approach is provided by [Njiri et al., 2016].

The reduction in fatigue loading is achieved through feeding back the measured structure loading signals such as: tower base bending load, blade root loading and tower top acceleration. The controller is tuned to reduce this loading at a given frequency that corresponds to the natural frequency of the monitored component. An exception to this approach is the work presented by [Hammerum et al., 2007] where a formula for fatigue damage rate derived using the frequency domain fatigue analysis theory is used in the controller design.

The traditional method of controller performance assessment is using time domain rainflow-counting. The obtained field results indicate load reduction that varies according to the component and to the wind speed [Bossanyi et al., 2012]. Most of the modern controllers are tuned using hi-fidelity simulation environments (such as FAST [Jonkman et al., 2005]) and the obtained results revealed the potentials of the new integrated controller design approach; and at the same time, these results motivate the efforts to look for different fatigue analysis approach that can reduce the long simulation time and the high computational effort and gives at the same time comparable results.

Lifetime monitoring is an essential part of any SHM and CM systems for wind turbines as these systems are very capable in tracking fatigue loading and in predicting the corresponding service life [Màrquez et al., 2012; Tchakoua et al., 2014; Thöns, 2012]. The standard practice of wind turbine fatigue analysis is the time domain cycle counting such as ASTM's rainflow cycle counting algorithm [IEC, 2005] in addition to the linear fatigue damage accumulation theory [Miner, 1645]. An extensive review of this approach is available in [Sutherland, 1999]. Fatigue analysis is either based on the measured loading such as the measured stress in the tower, drive-train, hub or the blades [Lachmann, 2014], or using the standard monitoring signals of the turbine such as the wind and rotor speed [Cosack, 2010]. Another approach is based on using observer techniques that employ system model and responses to estimate the loading at critical locations which are hard to measure, then using these estimations for fatigue analysis [Maes et al., 2016; Papadimitriou et al., 2011].

This analysis requires very large time records with high sampling rates in order to capture correctly the signal dynamics (peaks and valleys), not to forget the needed computational power and the huge required transmission band-width and storage space for such measured signals or to generate numerical time series using wind turbine modelling software. Another concern is the capabilities of the data acquisition system which should be able to collect the sensor measurements at the required rates [Wedman, 2010]. On the other side, condition monitoring and assessment of remaining service life rely on the clever algorithms that process the collected data.

Due to the stochastic nature of the turbine loading (wind and waves), another approach for fatigue analysis is possible. In this approach, the random turbine loading is modelled as a stationary random process and the frequency-domain fatigue analysis methods are used to estimate the statistical distribution of the rainflow cycle counts. Over the past few years, many spectral fatigue analysis methods have been developed [Benasciutti, 2012; Braccesi et al., 2015b; Dirlik, 1985; Jiao et al., 1990; Larsen et al., 1991; Nieslony, 2010; Petrucci et al., 2004; Tovo, 2002]. Fatigue analysis using these methods in some applications gives comparable results to that obtained from the time-domain cycle counting.

Spectral methods for fatigue analysis of wind turbines have been explored in a very few publications such as [Arany et al., 2014; Ragan et al., 2007]. Using utility scale wind turbine tower and blade loading measurements, both papers compared the fatigue analysis results obtained from different spectral methods to the results obtained using time-domain analysis. The conclusion obtained from these studies highlighted the potentials of the spectral methods and both recommended additional studies either based on simulation or field data to address the limitations of the spectral methods related to the assumed nature of the loading (stationary, Gaussian, zero-mean) which are hardly to meet in wind turbines.

The main advantage of using spectral fatigue analysis is the reduced computational effort needed when compared to the time-domain analysis, therefore, they are more suitable for parametric studies. For example, in the early design stages, when only a finite element model of the structure is available, the knowledge of the power spectral distribution of the wind and wave could be used along with the frequency response function which could be simply obtained from the finite element model to estimate the rainflow cycle counts at the structural critical locations (hot spots). To obtain the same result using the time-domain method, loading (wind and/or wave) time series should be generated from the power spectral distribution. This step is followed by comprehensive simulation of the generated loading applied to the finite element model. Finally, the simulation results are processed with the rainflow counting to obtain the cycle distribution. The time-domain simulation process are repeated many times to improve the statistical certainty of the results. The reduction of the computational effort is very important when the turbine control system is extended from power optimization to include the reduction of fatigue loading. The traditional way in controller design and tuning requires too many simulations. Spectral methods present a very efficient and attractive alternative solution at this design step because they allow to by-pass the computational complexity faced when using the traditional time-domain method.

However, spectral methods are not as flexible as the time-domain ones. This is basically due to the assumptions used in developing the related theory. The first assumption is the stationarity of the stochastic loading which is hard to achieve in the case of wind and wave loading. While the second assumption is related to the nature of the loading amplitude distribution, which is assumed to be Gaussian. In addition to these two assumptions, spectral methods assumes zero loading mean value. Wind and wave random loading on wind turbines is non-stationary and due to the nature of wind and wave loading, not to forget the non-linearity of the aerodynamic of the turbine rotor, the loading amplitude distribution is far from being Gaussian. Furthermore, the changing mean wind speed and its direction over time and consequently the change of loading mean value according to the operating condition violates the required zero mean loading assumption.

There are other approaches for fatigue analysis, such as the probability evolution methods where fatigue is modelled as stochastic process using for example Markov chain where the state transitions are described with a stochastic matrix [Eiken, 2017]; and the hysteresis operator which enables online fatigue estimation [Berglind et al., 2014; Barradas Berglind et al., 2015]. However both approaches are difficult to implement due to the unknown parameters, the abstract formulation, the computational demands for high dimensional problems and not to forget the required approximations.

1.2 Research Objective and Scope

The main research objective is to explore the potentials of using spectral methods in wind turbine fatigue analysis and to quantify the performance of these methods against the standard time-domain cycle counting method. The results and the conclusions of this work are intended to be used either by designers and developers of wind power plants using the integrated design approach; or in fast processing of the collected turbine loading data over the years to get better understanding of their fatigue life in a more effective way. Finally the results and the conclusions are also intended for the developers of new structural health monitoring systems based on modern approaches.

The research undertaken explores the theoretical basics of the spectral fatigue damage analysis and reviews the major methods available in the literature and the constraints arising from the assumptions required by the theory such as: stationariness of the loading, nature of the amplitude distribution (Gaussian of non-Gaussian), in addition to the mean value of the loading time history. As these assumptions are not valid in the case of wind turbine loading, a new strategy has been proposed to handle them in a systematic way.

The results presented are divided into three categories, simulation, operational and experimental. The simulation results are based entirely on hi-fidelity simulation and, therefore, the results are bounded by the limitations of the used simulation tools and their associate assumptions. However, the results are presented in a relative sense (normalised values) and the absolute values obtained from simulations are not used. The used relative sense helps to draw the right conclusions based on the physical interpretations of the wind turbine system and its supporting structure. The fatigue analysis under normal operating conditions and using different methods is based on the Design Load Case (DLC) 1.2 in the IEC 61400-3 standard for offshore wind turbines. Simulations are carried out using FAST (Fatigue, Aerodynamics, Structures and Turbulence) [Jonkman et al., 2005], as a well established wind turbine design and simulation tool. In addition to that, MATLAB®/Simulink®are used for simulation and fatigue analysis.

The operational fatigue analysis uses two different data-sets. The first one is collected in 2018 over a two months period from a small wind turbine with rated power of $2.5kW$ available at the University of Siegen. The second operational data-set represents a one day measurements from the research wind turbine Enercon $E40 - 500kW$ located in Dortmund. This data-set is collected in 2010 by Dr. Lachmann as part of his research project [Lachmann, 2014] at the Institute of “Windingenieurwesen und Strömungsmechanik” (Prof. Dr.-Ing. Rüdiger Höffer) at the Ruhr-Universität Bochum. Prof. Höffer has kindly shared this data with the “Institut für Mechanik und Regelungstechnik - Mechatronik” - “Arbeitsgruppe Technische Mechanik” (Prof. Dr.-Ing. Claus-Peter Fritzen) at the University of Siegen as part of a cooperation project between the two institutes. Fatigue analysis of both data-sets is achieved using MATLAB®.

The third data-set is collected from an experimental setup that used two sets of specimen with different materials, aluminium, and construction steel. The choice of these two different materials is due to the ductile and brittle fracture characteristics of aluminium and construction steel, respectively. Data has been collected using dSpace control board in addition to MATLAB®which is used also for fatigue analysis.

Finally, the research undertaken in this thesis address the following research objectives (in no particular order of importance).

1. It is clear that fatigue analysis of wind turbines using spectral methods has promising potentials, however, the assumptions used in developing the related theory are hardly to meet in wind power plants. These assumptions should be addressed systematically in order to be able to accept the results on the spectral fatigue analysis. Therefore, this research aims firstly to review the theoretical basis of the spectral fatigue analysis; secondly, to address the limitations of the frequency-domain methods and to develop a new strategy that enables using spectral methods for wind turbine fatigue analysis.
2. To evaluate the performance of the frequency-domain methods against the standard time-domain cycle counting. This comparison is done using the above mentioned data-sets: simulation and operational. The simulation data-set aims to replicate the integrated design process at early stages. While the operational data-set from small and utility scale wind turbine aims to evaluate the performance of the spectral-based methods against the industry standard rainflow cycle counting algorithm using operational stress measurement.
3. To explore the potentials of using the online estimated fatigue damage for early detection of fatigue failure. This point is very important for implementing an online fatigue detection as part of a structural health monitoring system.

In addition to the above listed objectives and research topics, it is important to define what is out of the scope of this research. Following are several items that are not part of the research undertaken in this thesis.

Both fatigue analysis methods, either the time-domain or the frequency domain, have been historically developed to handle uni-axial loading. Multi-axial fatigue analysis has been a wealthy research topic for the past few decades and the estimation of fatigue life under multi-axial random loading is still an extremely complex task. Variety of multi-axial fatigue analysis methods in time and frequency domains are available in literature [Carpinteri et al., 2017]. This thesis aims to explore new approaches in fatigue analysis of wind turbine, therefore, it is limited to the uni-axial loading case while making use of a multi-axial fatigue analysis concept called projection-by-projection. Consequently, the multi-axial fatigue analysis of wind turbines is considered out of the scope of this work.

Moreover, the scope of this work is limited to developing new methods and strategies that help in the early detection of fatigue damage using measured loading; hence, the fatigue mechanism is not discussed. In addition to that, a simplified material $S-N$ curve is considered with only one slope. The simplified curve also does not consider any endurance limit. This could be justified as the measured signals are low-pass filtered and the effect of high frequency cycles with small amplitude is considered marginal.

As most of the spectral methods are designed for materials with $S - N$ curve with slope less than 8, this limits the use of spectral fatigue analysis to the tower (welded construction steel) and possibly to the drive-train (cast nodular iron) components. On the other hand, the blades are mostly made of composite materials with $S - N$ curve slope of about 10, therefore, the spectral fatigue analysis of the blades is considered out of the scope of this work.

1.3 Thesis Outline

Chapter 2 reviews the basics of random vibration, stress calculation in addition to the general fatigue nomenclature. This chapter also review the linear fatigue damage accumulation hypothesis and the time-domain cycle counting used in time-domain fatigue analysis. Various spectral fatigue damage estimation methods under the Gaussian assumption for narrow and wide-band loading have been surveyed. Two methods that address the non-Gaussian loading have been also inspected. Moreover, a new strategy have been proposed to address the non-stationary loading. Finally, this chapter ends with summarizing the proposed procedure for fatigue analysis in the frequency domain.

Chapter 3 goes through the modelling, simulation, and analysis tools used in this research. At first a brief review of the used turbine modelling tool, the used turbine model, the considered different turbine configurations (land-based and different floating platforms), the reference control system in addition to the wind and wave loading. This chapter also review briefly the fatigue analysis recommended by the international standard IEC 61400-3 and the reference locations and the operating conditions at these locations used in simulation. The chapter ends with defining the different performance metrics used in fatigue analysis and in comparing the time and frequency domain estimations.

Chapter 4 includes the fatigue analysis results divided into four different sections. The first section goes through the fatigue analysis results obtained from simulation data-set for different onshore and floating (Barge, Spar-Buoy and TLP) wind turbine configurations and it ends with a detailed comparison between the different frequency domain methods (under Gaussian and non-Gaussian assumptions) and the time-domain cycle counting at different mean wind speed levels in addition to the overall weighted fatigue damage estimation. In order to compare the performance of the different methods, the spectral fatigue damage estimation results are normalised by that obtained using the rainflow cycle counting. The performance trends across the operating regions for the different turbine configurations are also analysed.

The second section in this chapter goes through the operational fatigue analysis of small wind turbine tower loading. Turbine location, main specifications and the data acquisition system are briefly described. The measured wind and tower loading characteristics have been analysed and performance of the proposed fatigue analysis strategy is validated. Finally, a new scheme for fatigue damage detection based on the estimated fatigue damage rate is proposed. In the third section the same work steps are repeated, however using operational utility scale wind turbine tower loading data.

This chapter ends with an experimental fatigue damage detection of two different sets of specimen made of aluminium and construction steel and subject to “random” loading. The experimental setup, specimen properties and the used data acquisition system are described in details. Moreover, the proposed fatigue damage detection scheme is validated for both specimen.

Finally, conclusions and recommendations for future work are presented in Chapter 5.

Chapter 2

Random Response Fatigue Analysis

The ability to simplify means to eliminate the unnessary so that the necessary may speak.

— Hans Hofmann

Contents

Wind turbine systems are subject to random wind and wave loading. Dealing with random vibration problems require very good knowledge in statistics and in stochastic theory in order to be able to characterise the random vibrations. This chapter starts with a brief introduction to the main concepts of random vibrations. Failure analysis in time and frequency domains are presented and a new strategy is proposed for fatigue damage analysis in frequency domain of wind turbines. It is assumed that the system structure is deterministic and therefore, not subject to random change on its characteristics.

2.1 Preliminary Concepts and Definitions

The theory of stochastic processes is the main tool used to describe random signals. Therefore, some of the basic concepts of statistics and stochastic process theory are briefly recapitulated.

2.1.1 Stationarity and Ergodicity

Let $X(t)$ be a random process and let $x(t) \in X(t)$ be a realization of it. If all statistical properties of the stochastic process are time independent, the random process is defined as strongly or strictly stationary. This means for example that the expected value $\mathbb{E}[\,\cdot\,]$ (defined later in this chapter) is time independent, or in other words

$$\mathbb{E}[X(t_1)] = \mathbb{E}[X(t_2)] \tag{2.1}$$

for any arbitrary times t_1 and t_2.

The strictly stationary condition could be weakened to obtain a weak stationary time-series in which only the mean and the covariance of the time-series are time independent. In many statistical procedures, stationarity is the main underlying assumption used in time-series analysis. The most common violation of stationarity is to have a deterministic trend or mean value of the data. Such non-stationary data are often transformed to become stationary.

A random process is considered ergodic if it is stationary and its ensemble properties and time properties are equal [Brandt, 2011]. This means that the mean value calculated from a single realization using

$$\mathbb{E}\left[x\left(t\right)\right] = \mu_x = \lim_{T\to\infty} \frac{1}{2T} \int\limits_{-T}^{T} x\left(t\right) dt \tag{2.2}$$

is equal to the mean calculated for any other realization of the random process $X\left(t\right)$, or in other words, the mean value of the stationary ergodic process $X\left(t\right)$ is the same for all it's realizations $x\left(t\right) \in X\left(t\right)$.

2.1.2 Probability Distribution and Probability Density Function

Let $P\left(x\right) = \mathrm{Prob}\left[X \leq x\right]$ be the probability distribution of $x\left(t\right) \in X\left(t\right)$. The probability density function (PDF) is then given by

$$p\left(x\right) = \frac{\mathrm{d}P\left(x\right)}{\mathrm{d}x}, \tag{2.3}$$

from this last equation, it follows that

$$P\left(x\right) = \int\limits_{-\infty}^{x} p\left(u\right) \mathrm{d}u. \tag{2.4}$$

The probability density function $p\left(x\right)$ gives the relative occurrence of amplitudes in $x\left(t\right)$ and thus contains the complete information about the probability characteristics of $x\left(t\right)$.

For a function $g\left(x\right)$ of a random signal $x\left(t\right)$ with probability density $p\left(x\right)$, the expected value, $\mathbb{E}\left[g\left(x\right)\right]$, is defined by

$$\mathbb{E}\left[g\left(x\right)\right] = \int\limits_{-\infty}^{+\infty} g\left(x\right) p\left(x\right) \mathrm{d}x. \tag{2.5}$$

This gives directly the expected value of $x\left(t\right)$, or the mean value, as

$$\mu_x = \mathbb{E}\left[x\right] = \int\limits_{-\infty}^{+\infty} x p\left(x\right) \mathrm{d}x. \tag{2.6}$$

The moments of a random variable give useful information in terms of numerical parameters,

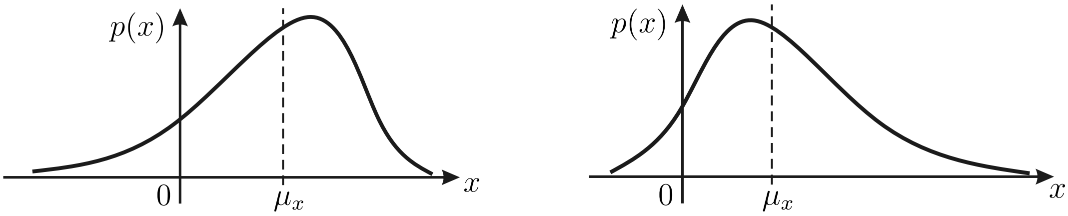

(a) Negative skewness **(b)** Positive skewness

Figure 2.1 Skewed probability density functions

these moments are calculated using

$$\lambda_i = \mathbb{E}\left[(x-\mu_x)^i\right], \tag{2.7}$$

where $i \in \mathbb{R}^+$ is a positive real number. These moments are called the central moments of the signal $x(t)$. Eq. 2.7 results that $\lambda_1 = 0$ and $\lambda_2 = \sigma_x^2$ where σ_x is the standard deviation and consequently λ_2 is the variance of the random signal $x(t)$.

The third moment λ_3 enables calculating the skewness of the dynamic signal $x(t)$ such as

$$\gamma_{Sk} = \frac{\lambda_3}{\sigma_x^3}. \tag{2.8}$$

The skewness γ_{Sk} is a dimensionless parameter that measures to which degree the signal is non-symmetric around its mean. For symmetric signals, the skewness is zero; which is the case of many random vibration signals that enjoy a symmetric probability distribution around the mean (i.e. Gaussian distribution). This makes the skewness a good parameter for analysing the non-Gaussian processes. Fig. 2.1 illustrates the skewness effect on the Gaussian distribution process.

Another commonly used dimensionless parameter is the Kurtosis γ_{Ku} which is related to the fourth moment λ_4 such as

$$\gamma_{Ku} = \frac{\lambda_4}{\sigma_x^4}. \tag{2.9}$$

The kurtosis measures the degree of flattening of a probability density function where it compares the tails of the probability density function with that of the normal distribution. For normally distributed variables (Gaussian distribution) the kurtosis is exactly 3. If the distribution has a kurtosis larger than 3 the distribution is called *leptokurtic* (more peaky than Gaussian), and if the kurtosis is less than 3 the distribution is called *platykurtic* (more flattened than Gaussian). This is illustrated in fig. 2.2.

The skewness and kurtosis can be used to detect non-Gaussian processes. They can also be used to detect the non-linearity since non-linear systems exhibit non-Gaussian responses.

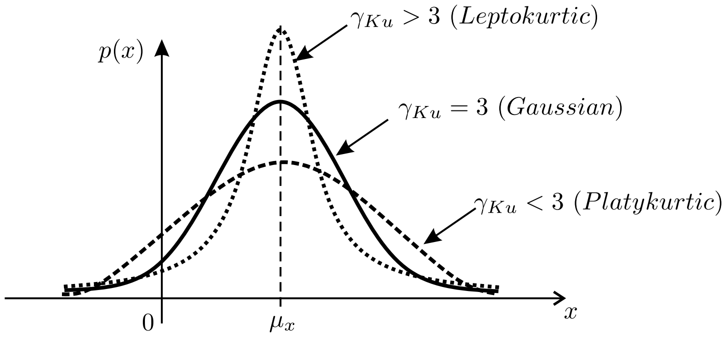

Figure 2.2 Probability density functions with different values of kurtosis

2.1.3 Histogram

The probability distribution and density functions are theoretical functions that cannot be estimated from real-life signals. Therefore, the amplitude histogram is estimated from the discrete signal $x(n)$ that represents the time dependent signal $x(t)$. The amplitude histogram illustrates the distribution of samples over uniformly spaced amplitude intervals (each of width w) called the bins. Fig. 2.3 presents the amplitude histogram of a given discrete signal $x(n)$.

Let v_i be the bin value, c_i the number of samples in the bin, w the bin width, N_b the number of bins in the histogram and N_s the number of samples in the discrete data $x(n)$. According to the calculated bin value v_i, the histogram estimates the probability distribution for $v_i = \frac{c_i}{N_s}$, the probability density function for $v_i = \frac{c_i}{N_S w}$ and the cumulative density function for $v_i = \frac{1}{N_s} \sum_{j=1}^{i} c_j$.

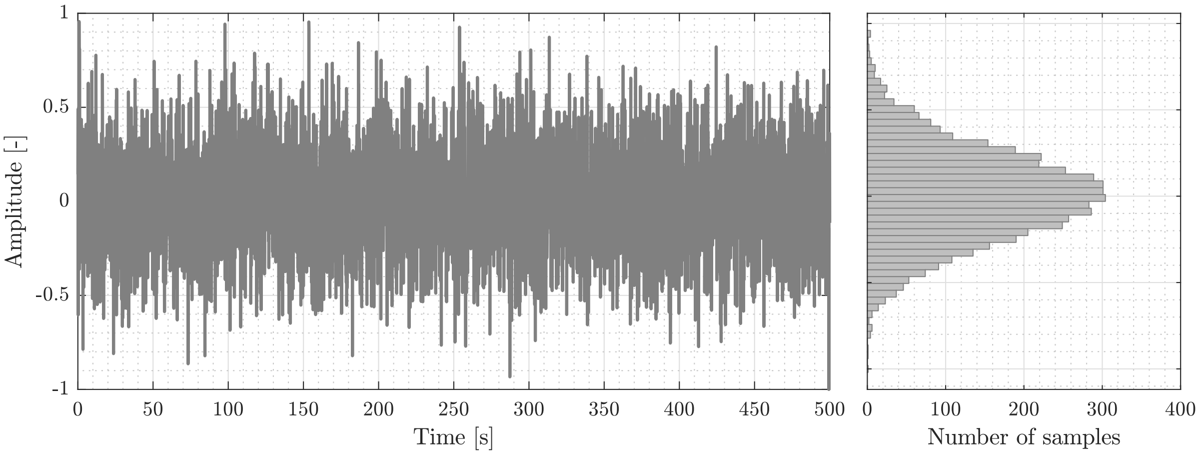

Figure 2.3 Amplitude Histogram of a given signal $x(n)$.

The choice of the bin width w of the bins is very important as it controls the smoothness of the calculated histogram. The recommended bin width according to [Brandt, 2011] should be less than the fifth of the standard deviation σ_x of the time signal $x(n)$. In addition to that, [Brandt, 2011] recommends a minimum number of points of $N_s = 10^4$ per each discrete time-series $x(n)$.

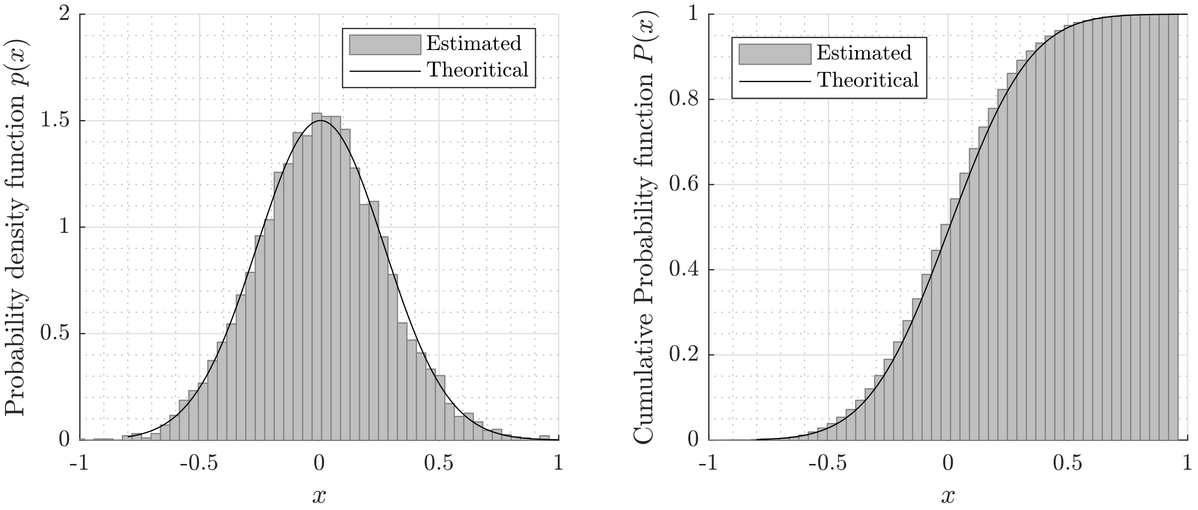

Figure 2.4 Theoretical and estimated probability density and cumulative probability functions of a random signal $x(t)$ with mean value $\mu_x = 0$ and standard deviation $\sigma_x = 1$.

Following the choice of the bin width w, it is possible to calculate the total number of classes used to build the histogram using

$$N_b = \frac{x_{max} - x_{min}}{w}, \tag{2.10}$$

with $x_{min} = \min(x(n))$ and $x_{max} = \max(x(n))$ as the minimum and maximum values of the time-series, respectively. Finally, the number of classes/bins N_b is rounded to the nearest integer value.

2.1.4 Gaussian Probability Distribution

The most common probability distribution is the Gaussian distribution, which is also known as the normal distribution. The random signal $x(t)$ is said to have a Gaussian distribution when its amplitude probability density function satisfies

$$p(x) = \frac{1}{\sigma_x\sqrt{2\pi}} e^{-\frac{1}{2}\left(\frac{x-\mu_x}{\sigma_x}\right)^2}, \tag{2.11}$$

where μ_x and σ_x are the mean and the standard deviation of the random signal $x(t)$, respectively. The normal probability density and the cumulative probability functions estimated for the signal presented in fig. 2.3 using its mean and its standard deviation values are presented in fig. 2.4. It gets clear from this example, that the considered time signal $x(t)$ has a Gaussian distribution with an acceptable error.

By integrating the probability density function $p(x)$ given in eq. 2.11 between $-\infty$ and the amplitude x it is possible to calculate the cumulative probability of amplitudes that lies in the range $-\infty < u \leq x$. This cumulative probability is given by

$$P(u \leq x) = \frac{1}{2}\left[1 + \operatorname{erf}\left(\frac{x - \mu_x}{\sqrt{2}\sigma_x}\right)\right], \tag{2.12}$$

where $\mathrm{erf}(x)$ is the error function defined by

$$\mathrm{erf}\left(x\right) = \frac{2}{\sqrt{\pi}} \int\limits_{0}^{x} e^{-t^2} \mathrm{d}t. \tag{2.13}$$

From eq. 2.12, it is also possible to obtain the probability of amplitudes that lies within the range $b \leq x \leq a$ using

$$P\left(b \leq x \leq a\right) = P\left(x \leq a\right) - P\left(x \leq b\right)$$

and the probability of amplitudes that lies within $\pm\sigma_x$, $\pm 2\sigma_x$, and $\pm 3\sigma_x$ around the mean μ_x are given by 68.3 %, 95.5 % and 99.7 %, respectively.

2.2 Fundamental Properties of Stationary Ergodic Stochastic Process

2.2.1 Correlation Function and Power Spectral Density

The most important statistical information about a random process is contained in the auto-correlation function $R_x\left(\tau\right)$ defined by

$$R_x\left(\tau\right) = \mathbb{E}\left[x\left(t\right) x\left(t+\tau\right)\right], \tag{2.14}$$

which can be interpreted as a measure of the similarity a signal has with a time shifted version of itself (shifted by τ). If the time shift has zero value, namely $\tau = 0$, the auto-correlation function is equal to the mean square value

$$R_x\left(\tau\right) = \mathbb{E}\left[x^2\left(t\right)\right]. \tag{2.15}$$

The auto-covariance function is obtained in a similar way to the auto-correlation function when the process is considered with respect to its mean value μ_x such as

$$\Gamma_x\left(\tau\right) = \mathbb{E}\left[\left(x\left(t\right) - \mu_x\right)\left(x\left(t+\tau\right) - \mu_x\right)\right].$$

If the process has zero mean $\mu_x = 0$, the auto-correlation and auto-covariance functions are identical. Furthermore, for $\tau = 0$, $\Gamma_x\left(0\right) = \sigma_x^2$, or in other words, is equal to the variance of the process which (together with the mean μ_x) are the most important statistical information about the magnitude of the process. However, the variance and the mean does not give any information about the frequency content. This information is contained in the auto-correlation function $R_x\left(\tau\right)$ and can be extracted in the form of the two-sided power spectral density $S_x\left(\omega\right)$ defined on the positive and negative frequencies such as

$$S_x\left(\omega\right) = \int\limits_{-\infty}^{+\infty} R_x\left(\tau\right) e^{-i\omega\tau} \mathrm{d}\tau,$$

where $\omega = 2\pi f$ is the circular frequency in $\frac{rad}{s}$ and f is the frequency in Hz. The one-sided spectral density

$$G_x(\omega) = \begin{cases} 2S_x(\omega) & \omega > 0 \\ S_x(\omega) & \omega = 0 \\ 0 & \omega < 0 \end{cases} \tag{2.16}$$

is defined only on the positive frequencies.

2.2.2 Random Response of Linear Systems

In the time domain, the input-output relationship of a linear system is given by

$$\underline{y}(t) = \int_{-\infty}^{\infty} \underline{\underline{H}}(t-\tau)\,\underline{x}(\tau)\,\mathrm{d}\tau, \tag{2.17}$$

with $\underline{\underline{H}}(t)$ is the impulse response matrix. The element $h_{ij}(t)$ is the time response of the output i to a unit impulse applied to the input j. In frequency domain, this relationship is given by

$$\underline{y}(\omega) = \underline{\underline{H}}(\omega)\,\underline{x}(\omega), \tag{2.18}$$

where $\underline{x}(\omega)$ and $\underline{y}(\omega)$ are the Fourier transformation of $\underline{x}(t)$ and $\underline{y}(t)$, respectively; while $\underline{\underline{H}}(\omega)$ is the frequency response function (FRF) matrix. $h_{ij}(\omega)$ is the Fourier transform of $h_{ij}(t)$ and it gives the complex amplitude of the harmonic response of the output i to a harmonic excitation of unit amplitude at j input.

If the system is subject to independent inputs each is characterised by its power spectral density (PSD) $S_{x,i}(\omega)$, the input-output relationship between stationary excitation and stationary response is given by

$$\underline{\underline{S}}_y(\omega) = \underline{\underline{H}}(\omega)\,\underline{\underline{S}}_x(\omega)\,\underline{\underline{H}}^*(\omega), \tag{2.19}$$

where

$$\underline{\underline{S}}_x(\omega) = \mathrm{diag}\left(\left[S_{x,1}(\omega), S_{x,2}(\omega), \ldots, S_{x,n_i}(\omega)\right]\right) \tag{2.20}$$

is a diagonal matrix with the PSD $S_{x,i}(\omega)$ of each input i, while n_i is the number of system inputs and $\underline{\underline{H}}^*(\omega)$ is the conjugate transpose (Hermitian) of $\underline{\underline{H}}(\omega)$. The only restriction to this relation is that the system must be linear. For the case of single-input-single-output (SISO) systems eq. 2.19 could be simplified to

$$S_y(\omega) = |H(\omega)|^2\,S_x(\omega). \tag{2.21}$$

A very interesting result could be obtained from this last equation. For the SISO linear systems, it is possible to calculate the output PSD by knowing the input PSD and the system FRF $H(\omega)$.

The FRF $H(\omega)$ could be estimated using different methods, such as the finite-element model of the system.

2.2.3 Spectral Moments, Rice Formula, and Band-Width Parameters

The statistical properties of the stationary random process $x(t) \in X(t)$ and its n-th time derivatives $\frac{\mathrm{d}^n}{\mathrm{d}t^n}(x(t))$ are described by the moments of the power spectral density

$$\lambda_i = \int\limits_{-\infty}^{\infty} |\omega|^i \, S_x(\omega) \, \mathrm{d}\omega = \int\limits_{0}^{\infty} \omega^i G_x(\omega) \, \mathrm{d}\omega, \quad i \in \mathbb{R}^+, \tag{2.22}$$

where λ_i is the i-th spectral moment of the random process $x(t)$ and $i \in \mathbb{R}^+$ might be any real number greater than zero. The statistical properties of the random process $x(t)$ and its time derivatives are contained in the spectral moments such as

$$\lambda_0 = \sigma_x^2, \tag{2.23}$$

$$\lambda_2 = \sigma_{\dot{x}}^2, \tag{2.24}$$

$$\lambda_4 = \sigma_{\ddot{x}}^2, \tag{2.25}$$

where σ_x^2, $\sigma_{\dot{x}}^2$, and $\sigma_{\ddot{x}}^2$ are the variance of the random process $x(t)$, its first time derivative $\dot{x}(t)$ and its second time derivative $\ddot{x}(t)$, respectively; while λ_0, λ_2, and λ_4 are the 0-th, the 2-nd and the 4-th spectral moments of the random process $x(t)$, respectively. Furthermore, the standard deviation of $x(t)$ is $\sigma_x = \sqrt{\lambda_0}$. For fatigue analysis, the moments up to λ_4 are normally used.

For a zero-mean stationary Gaussian process $x(t)$, [Rice, 1944] has demonstrated that the average number per unit of time of zero up-crossings ν_o is given by

$$\nu_0 = \frac{1}{2\pi}\frac{\sigma_{\dot{x}}}{\sigma_x} = \frac{1}{2\pi}\sqrt{\frac{\lambda_2}{\lambda_0}}. \tag{2.26}$$

Similarly, the expected zero up-crossing rate of the time derivative $\dot{x}(t)$, which also represents the expected peak rate ν_p, is defined as

$$\nu_p = \frac{1}{2\pi}\frac{\sigma_{\ddot{x}}}{\sigma_{\dot{x}}} = \frac{1}{2\pi}\sqrt{\frac{\lambda_4}{\lambda_2}}. \tag{2.27}$$

Generally, the expected up-crossing rate ν_0 is different from ν_p (i.e. $\nu_0 = \alpha_2 \nu_p$), and the more the process is narrow-banded the more the rate of up-crossing ν_0 approaches the expected rate of peaks ν_p. The analytical derivation of eq. 2.26 and eq. 2.27 are described by [Rice, 1944] and [Newland, 1993].

Based on this, it is possible to define the irregularity factor γ_{IF} that measures the number of peaks counted in between two consecutive mean up-crossings such as

$$\gamma_{IF} = \frac{\nu_0}{\nu_p} = \frac{\lambda_2}{\sqrt{\lambda_0\lambda_4}}, \quad 0 \le \gamma_{IF} \le 1, \tag{2.28}$$

Table 2.1 Irregularity factors and the band-width parameters

	α_i	δ_v	ε
Ideal narrow-band process	1.0	0.0	0.0
Ideal wide-band process	0.0	1.0	1.0

where γ_{IF} ranges from zero for the broad-band process to unity for the narrow-band process.

Another non-dimensional bandwidth parameters α_i could be also used to characterise the distribution of the extremes (peaks and valleys) of the random process, these parameters are defined by

$$\alpha_i = \frac{\lambda_i}{\sqrt{\lambda_0 \lambda_{2i}}}, \quad 0 \leq \alpha_i \leq 1, \tag{2.29}$$

where the index i in this formula might take also non-integer values, therefore, $i \in \mathbb{R}^+$. In this family of the bandwidth parameters, three different parameters are mostly used in literature which are α_1, α_2, and $\alpha_{0.75}$, being $\alpha_{0.75} \geq \alpha_1 \geq \alpha_2$ [Benasciutti, 2012]. For a narrow-band process, α_i values approach unity, and the higher the value of α_i the narrower is the process in the frequency domain and vice-versa. Furthermore, for *Gaussian* process $\gamma_{IF} = \alpha_2$, however, for *non-Gaussian* process, γ_{IF} and α_2 are not identical, but they will generally be quite similar [Benasciutti, 2012].

Another frequently used parameters are the Vanmarcke's parameter δ_v defined by

$$\delta_v = \sqrt{1 - \alpha_1^2}, \quad 0 \leq \delta_v \leq 1, \tag{2.30}$$

and the spectral width parameter ε [Wirsching et al., 1980] given as

$$\varepsilon = \sqrt{1 - \alpha_2^2}, \quad 0 \leq \varepsilon \leq 1, \tag{2.31}$$

where both are dimensionless measure of the dispersion of the PSD about a central frequency. Therefore, for a narrow-band process δ_v tends to zero, however, it approaches unity as the band-width increases. Tab 2.1 summaries the irregularity factors and their interpretation with regard the band-width.

2.3 Stress Estimation

2.3.1 Stress Estimation from State Vector

Consider the dynamic response of a time-invariant linear structural system with n_q degrees of freedom subject to n_u deterministic excitations (i.e. actuators excitation) in addition to n_w external random excitations (i.e. wind or wave). The equation of motion of such dynamic system is then given by

$$\underline{\underline{M}}\,\underline{\ddot{q}}\left(t\right) + \underline{\underline{C}}_d\,\underline{\dot{q}}\left(t\right) + \underline{\underline{K}}\,\underline{q}\left(t\right) = \underline{\underline{F}}_u\,\underline{u}\left(t\right) + \underline{\underline{F}}_w\,\underline{w}\left(t\right), \tag{2.32}$$

where $\underline{q}\left(t\right) \in \mathbb{R}^{n_q}$ is the displacement vector, $\underline{\dot{q}}\left(t\right)$ and $\underline{\ddot{q}}\left(t\right)$ are the velocity and acceleration vectors, $\underline{\underline{M}}$, $\underline{\underline{C}}_d$ and $\underline{\underline{K}} \in \mathbb{R}^{n_q \times n_q}$ are the mass, damping and stiffness matrices, $\underline{\underline{F}}_u \in \mathbb{R}^{n_q \times n_u}$ and $\underline{\underline{F}}_w \in \mathbb{R}^{n_q \times n_w}$ are the deterministic and random excitation gain matrices, respectively, finally $\underline{u} \in \mathbb{R}^{n_u}$ and $\underline{w} \in \mathbb{R}^{n_w}$ are the applied deterministic and stochastic loading on the system, respectively. Furthermore, let $\underline{y}\left(t\right) \in \mathbb{R}^{n_y}$ be the measurement vector that collects the measurements from different sensors installed on the structure such as accelerometers, strain gauges, etc.

Let the state vector be

$$\underline{x}\left(t\right) = \begin{bmatrix} \underline{q}\left(t\right) \\ \underline{\dot{q}}\left(t\right) \end{bmatrix} \in \mathbb{R}^{2n_q}, \tag{2.33}$$

then the system dynamics could be expressed in terms of the following state-space form

$$\underline{\dot{x}}\left(t\right) = \underline{\underline{A}}\,\underline{x}\left(t\right) + \underline{\underline{B}}\,\underline{u}\left(t\right) + \underline{\underline{G}}\,\underline{w}\left(t\right), \tag{2.34}$$

$$\underline{y}\left(t\right) = \underline{\underline{C}}\,\underline{x}\left(t\right) + \underline{\underline{D}}\,\underline{u}\left(t\right), \tag{2.35}$$

where the state transition matrix $\underline{\underline{A}} \in \mathbb{R}^{2n_q \times 2n_q}$, the deterministic input gain matrix $\underline{\underline{B}} \in \mathbb{R}^{2n_q \times n_u}$ and the disturbance gain matrix $\underline{\underline{G}} \in \mathbb{R}^{2n_q \times n_w}$ are given by

$$\underline{\underline{A}} = \begin{bmatrix} \underline{\underline{0}} & \underline{\underline{I}} \\ -\underline{\underline{M}}^{-1}\underline{\underline{K}} & -\underline{\underline{M}}^{-1}\underline{\underline{C}}_d \end{bmatrix}, \tag{2.36}$$

$$\underline{\underline{B}} = \begin{bmatrix} \underline{\underline{0}} \\ \underline{\underline{M}}^{-1}\underline{\underline{F}}_u \end{bmatrix}, \tag{2.37}$$

$$\underline{\underline{G}} = \begin{bmatrix} \underline{\underline{0}} \\ \underline{\underline{M}}^{-1}\underline{\underline{F}}_w \end{bmatrix}, \tag{2.38}$$

respectively. Furthermore $\underline{\underline{C}} \in \mathbb{R}^{n_y \times 2n_q}$ is the observation matrix and $\underline{\underline{D}} \in \mathbb{R}^{n_y \times n_u}$ is the direct feed-through matrix. These two matrices depend on the location and type of the used sensors. The deterministic input is normally the actuator input and it follows a specific control low. Assuming for example the full state feedback control low given by

$$\underline{u} = -\underline{\underline{K}}_g\,\underline{x}, \tag{2.39}$$

with $\underline{\underline{K}}_g$ is the controller gain matrix. The closed loop state space system is given by

$$\underline{\dot{x}}\left(t\right) = \underline{\underline{A}}_c\,\underline{x}\left(t\right) + \underline{\underline{G}}\,\underline{w}\left(t\right), \tag{2.40}$$

$$\underline{y}\left(t\right) = \underline{\underline{C}}_c\,\underline{x}, \tag{2.41}$$

with $\underline{\underline{A}}_c = \underline{\underline{A}} - \underline{\underline{B}}\,\underline{\underline{K}}_g$ is the closed loop transition matrix, and $\underline{\underline{C}}_c = \underline{\underline{C}} - \underline{\underline{D}}\,\underline{\underline{K}}_g$ is the closed loop measurement matrix. If the open loop system is observable, then it is possible to estimate the full state vector. Let $\underline{\hat{x}}(t)$ be an estimation of the state vector, then the corresponding estimate of the stress vector $\hat{s}(t)$ is given by

$$\hat{s}(t) = \underline{\underline{\Sigma}}_s \hat{x}(t), \tag{2.42}$$

where $\underline{\underline{\Sigma}}_s$ is the shape matrix that depends on the finite element type in addition to the Young's modulus E and Poison's ratio ν. In fact, the estimated stress vector depends only on the estimated nodal displacement vector $\underline{\hat{q}}(t)$ which is part of the estimated state vector $\hat{x}(t)$. With the help of a finite element mesh with known element type and node coordinates, it is possible to estimate the stress vector $\hat{s}(t)$ as per eq. 2.42.

Using the definition of the cross power spectral density (CPSD), the CPSD $\underline{\underline{S}}_{\underline{\hat{s}}}(\omega)$ of the stress response $\underline{\hat{s}}(t)$ can be obtained with respect to the CPSD $\underline{\underline{S}}_{\underline{\hat{x}}}(\omega)$ of the estimated state vector $\underline{\hat{x}}(t)$ in the form

$$\underline{\underline{S}}_{\underline{\hat{s}}}(\omega) = \underline{\underline{\Sigma}}_s \underline{\underline{S}}_{\underline{\hat{x}}}(\omega) \underline{\underline{\Sigma}}_s^*. \tag{2.43}$$

An estimation of the state vector could be obtained using for example a Luenberger observer of the closed loop system given in eqs. 2.40, 2.41. Such observer takes the following form

$$\underline{\dot{\hat{x}}}(t) = \underline{\underline{A}}_c \underline{\hat{x}}(t) + \underline{\underline{L}}\left(\underline{y}(t) - \underline{\hat{y}}(t)\right), \tag{2.44}$$

$$\underline{\hat{y}}(t) = \underline{\underline{C}}_c \underline{\hat{x}}(t), \tag{2.45}$$

with the matrix $\underline{\underline{L}}$ is the observer gain matrix. By taking Laplace transformation, and manipulating the observer equations, it is possible to obtain

$$\underline{\hat{X}}(s) = \left(s\underline{\underline{I}} - \underline{\underline{A}} + \underline{\underline{L}}\underline{\underline{C}}_c\right)^{-1} \underline{\underline{L}}\underline{Y}(s), \tag{2.46}$$

where $\underline{\hat{X}}(s)$ and $\underline{Y}(s)$ are the Laplace transformation of $\underline{\hat{x}}(t)$ and $\underline{y}(t)$, respectively, and s is the complex Laplace variable. This last equation gives the relation between the cross power spectral density of the estimated state vector and the CPSD of the measured output vector such as

$$\underline{\underline{S}}_{\underline{\hat{x}}}(\omega) = \left(\left(s\underline{\underline{I}} - \underline{\underline{A}} + \underline{\underline{L}}\underline{\underline{C}}_c\right)^{-1} \underline{\underline{L}}\right) \underline{\underline{S}}_{\underline{y}}(\omega) \left(\left(s\underline{\underline{I}} - \underline{\underline{A}} + \underline{\underline{L}}\underline{\underline{C}}_c\right)^{-1} \underline{\underline{L}}\right)^*. \tag{2.47}$$

Similarly, the relation between the disturbance input and the measured output of the closed loop system is given by

$$\underline{Y}(s) = \underline{\underline{H}}(s)\underline{W}(s), \tag{2.48}$$

with $\underline{W}(s)$ is the Laplace transformation of $\underline{w}(t)$ and $\underline{\underline{H}}(s)$ is the transfer function matrix between the disturbance input and the measured output given by

$$\underline{\underline{H}}(s) = \underline{\underline{C}}_c\left(s\underline{\underline{I}} - \underline{\underline{A}}_c\right)\underline{\underline{G}}, \tag{2.49}$$

and the relation between the CPSD of disturbance and the CPSD of the measured output is

$$\underline{\underline{S}}_{y}(\omega) = \underline{\underline{H}}(s)\,\underline{\underline{S}}_{w}(\omega)\,\underline{\underline{H}}^{*}(s)\,. \tag{2.50}$$

The main conclusion obtained from this derivation is that, in linear systems, it is possible to estimate the power spectral density of the stress at any location in the structure using either the spectral density of the measured output vector, or the spectral density of the input. This is possible under the following conditions: the first one is the linearity of the system, which is an essential condition. The second condition is the observability of the system, otherwise, it would not be possible to estimate the state vector, and consequently the nodal locations. The third condition, is the knowledge of the finite element mesh, element types, nodes coordinates, in addition to the material properties such as Young's modulus and Poison's ratio.

If the system is weakly non-linear, a linearised model could give a good approximation to the system, therefore, it could be used in the previous derivation. Furthermore, it is possible to replace the strict observability condition with the slightly weaker detectability condition.

The advantage obtained from this derivation is that by knowing the power spectral density of the disturbance input, such as the wind and wave loading on the turbine, or by knowing the PSD of the measurements it is possible to derive the PSD of the stress at any given location on the structure. This has a major advantage in the early design steps of the wind turbine, as it allows reducing the simulation time and the corresponding effort when only the installation site is known (wind and wave loading spectrum is known) and rough design details are available at this stage. Using spectral methods in fatigue damage estimation, it is possible to check the design against fatigue damage using the estimated stress spectral density at the critical locations on the structure.

2.3.2 Stress Calculation from Strain Measurement

In most cases the stress value is not measured directly, but estimated using strain measurement at given locations. This applies for the case of tower base fore-aft and side-side loading. In both cases, strain sensors are employed to measure the deformation at given location of the cross section and the stress value is calculated from the measured strain field using

$$\begin{bmatrix} \varepsilon_x \\ \varepsilon_y \\ \varepsilon_z \end{bmatrix} = \frac{1}{E} \begin{bmatrix} 1 & -\nu & -\nu \\ -\nu & 1 & -\nu \\ -\nu & -\nu & 1 \end{bmatrix} \begin{bmatrix} s_x \\ s_y \\ s_z \end{bmatrix}, \tag{2.51}$$

where ε_x, ε_y, and ε_z are the strains in the $x-$, $y-$, and $z-$ directions, and s_x, s_y, and s_z are the corresponding stresses in the same directions, respectively. Assuming that the tower cross section is located in the $x-y$ plane, and the $z-$axis is defined along the tower axis; and considering that the thickness of the tower wall is small compared to the other geometrical dimensions, therefore, the axial stress could be neglected $s_z = 0$. By substituting this into eq. 2.51, it is possible to obtain

$$\begin{bmatrix} \varepsilon_x \\ \varepsilon_y \\ \varepsilon_z \end{bmatrix} = \frac{1}{E} \begin{bmatrix} 1 & -\nu \\ -\nu & 1 \\ -\nu & -\nu \end{bmatrix} \begin{bmatrix} s_x \\ s_y \end{bmatrix}. \tag{2.52}$$

The stress components s_x and s_y are given by

$$\begin{bmatrix} s_x \\ s_y \end{bmatrix} = \frac{E}{1-\nu^2} \begin{bmatrix} 1 & -\nu \\ -\nu & 1 \end{bmatrix} \begin{bmatrix} \varepsilon_x \\ \varepsilon_y \end{bmatrix}. \tag{2.53}$$

Using this last formula, it is possible to estimate the stresses in the $x-$ and $y-$directions using the tower material properties.

2.4 General Fatigue Nomenclature

The fatigue cycle is a closed stress-strain hysteresis loop in the stress time-series of a solid material [Sutherland, 1999]. Each fatigue cycle in a random loading can be characterised by its peak value s_p and valley value s_v (being always $s_p \geq s_v$) as illustrated in fig 2.5. Furthermore, the local mean stress $\bar{s}$ per each loading cycle is defined as

$$\bar{s} = \frac{1}{2}\left(s_p + s_v\right), \tag{2.54}$$

and the stress range r is

$$s_r = s_p - s_v, \tag{2.55}$$

while the amplitude of the stress cycle is half the range such as

$$s = \frac{1}{2} s_r = \frac{1}{2}\left(s_p - s_v\right). \tag{2.56}$$

Furthermore, the stress peak and valley values could be also expressed in terms of stress mean and amplitude using

$$s_p = \bar{s} + s, \tag{2.57}$$

$$s_v = \bar{s} - s. \tag{2.58}$$

In the case of stochastic loading time history $s(t)$, the counted random cycles could be characterised in a probabilistic sense using the joint probability density function (PDF) $h(s_p, s_v)$, depending on the peak s_p and valley s_v events and defined only for $s_p \geq s_v$. The corresponding cumulative distribution function (CDF)

$$H\left(s_p, s_v\right) = \int\limits_{-\infty}^{s_p} \int\limits_{-\infty}^{s_v} h\left(x, y\right) \mathrm{d}x \mathrm{d}y, \tag{2.59}$$

gives the probability to count a cycle with peak lower or equal to level s_p and valley lower or equal to level s_v. From the peak-valley joint probability density function and using a simple change of variable, it is possible to express the cycle distribution in terms of stress amplitude and stress mean values

$$p_{a,m}\left(s, \bar{s}\right) = 2h\left(\bar{s} + s, \bar{s} - s\right), \tag{2.60}$$

Furthermore, the following marginal probability density function

$$p_a\left(s\right) = \int\limits_{-\infty}^{\infty} p_{a,m}\left(s, \bar{s}\right) \mathrm{d}\bar{s} \tag{2.61}$$

gives the distribution of counted cycles as a function of amplitudes.

In a complete counting method, a cycle is attached to each maximum in the history, therefore, the expected intensity of counted cycles ν_c is equal to the expected intensity of peaks ν_p, i.e. $\nu_c = \nu_p$. Based on this, the marginal distribution of cycles can be also related to the distribution of peaks and valleys [Tovo, 2002] using

$$p_p\left(s_p\right) = \int\limits_{-\infty}^{s_p} h\left(s_p, v\right) \mathrm{d}v, \tag{2.62}$$

$$p_v\left(s_v\right) = \int\limits_{s_v}^{+\infty} h\left(p, s_v\right) \mathrm{d}p, \tag{2.63}$$

where both equations are valid for the Gaussian, and non-Gaussian processes. Furthermore, it is possible to define the cumulative cycle spectrum, also known as the loading cycle spectrum, using

$$F\left(s\right) = \int\limits_{s}^{+\infty} p_a\left(x\right) \mathrm{d}x, \tag{2.64}$$

which defines the percentile of cycles having amplitudes higher than or equal to s.

2.4.1 Material Properties (The $S-N$ Curve)

The fatigue strength of a material depends primarily on the stress amplitude s of the loading cycles. For a constant amplitude, the fatigue life of some materials can be infinite if the amplitude is below the endurance limit S_∞ (the existence of such limit is still under debate [Sonsino, 2007]). Contrary to that the fatigue life of the material could end immediately if the stress amplitude is larger than the ultimate tensile strength S_u. The material fatigue strength could

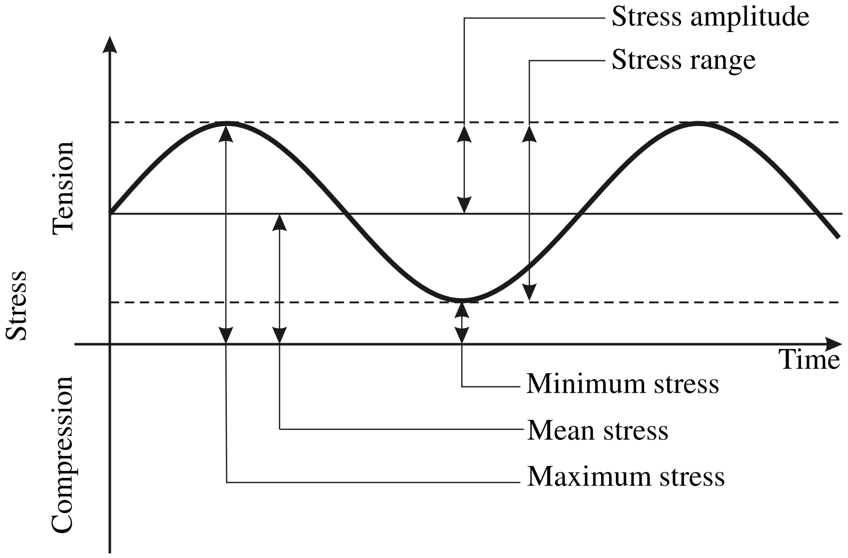

Figure 2.5 Fatigue nomenclature

be illustrated with the help of Wöhler curve (known also as the $S-N$ curve) defined by

$$N(s,\bar{s}) = \begin{cases} 0 & S_u \leq s \\ K(\bar{s})\, s^{-m} & S_\infty < s < S_u \\ \infty & s \leq S_\infty \end{cases} \tag{2.65}$$

with $N(s,\bar{s})$ is the number of cycles to failure at the constant stress amplitude s and mean stress $\bar{s}$, m is a material property (referred to later as the fatigue exponent) that determines the slop of the $S-N$ line on a *log-log* scale and $K(\bar{s})$ is another material parameter (referred to later as fatigue constant) that is proportional to the number of cycles a material can withstand before failure. The above definition of the $S-N$ curve accounts for the static strength and the fatigue limit and by considering only the region between these two limits the Wöhler curve could simply be expressed using the following formula

$$N(s,\bar{s})\, s^m = K(\bar{s}), \tag{2.66}$$

which would be used throughout this thesis.

The Wöhler curve defines the failure zone for any $S-N$ pair that falls above the line. Typically, the $S-N$ curve is derived from experimental tests on samples of the material to be characterised. In fatigue analysis the $S-N$ curve selected for design is associated with a given survival probability which is often 95 %, and level of confidence (often 95 %) in determining the curve from materials data. Thus, the desired minimum level of reliability may be expected when the damage sums to unity.

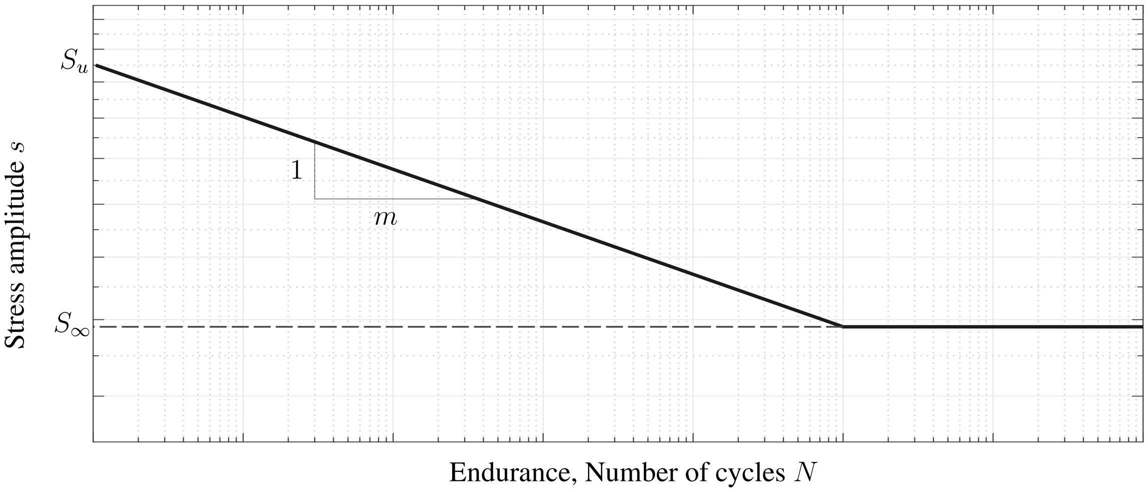

Figure 2.6 Normalised S-N curve

2.4.2 Effect of Mean Stress

The general definition of the mean stress value $\bar{s}$ considered in the process of fatigue life assessment is defined as the static component of the stress history $s(t)$ given by

$$\bar{s} = \lim_{T \to \infty} \frac{1}{T} \int_0^T s(t)\, dt, \tag{2.67}$$

with $s(t)$ is the amplitude of the stress time history of time duration T. The mean stress could also be obtained from the two-sided power spectral density S_s associated with the time history $s(t)$ as the peak at the $0Hz$ using

$$\bar{s} = \sqrt{\int_{0^-}^{0^+} S_s(w)\, \mathrm{d}w}. \tag{2.68}$$

A set of $S-N$ curves are normally given for each material according to the mean stress value $\bar{s}$ used in the carried fatigue test with constant loading amplitude s. In order to simplify fatigue calculation and to be able to use only one $S-N$ curve with zero-mean stress, an equivalent stress amplitude value s_e with zero-mean is derived from the actual stress amplitude s with $\bar{s}$ mean stress value, such as

$$s_e = K_i(\bar{s})\, s, \tag{2.69}$$

with $K_i(\bar{s})$ is a correction factor that could be defined according to one (but not limited to) of the following models available in literature:

- The **Goodman** model

$$K_D(\bar{s}) = \begin{cases} \frac{1}{1-\frac{\bar{s}}{S_u}} & \text{for } 0 < \bar{s} < S_u \\ 1 & \text{for } -S_u < \bar{s} \leq 0 \end{cases} \tag{2.70}$$

- The **Soderberg** model

$$K_S\left(\bar{s}\right)=\begin{cases}\frac{1}{1-\frac{\bar{s}}{S_y}} & \text{for } 0<\bar{s}<S_y\\ 1 & \text{for } -S_y<\bar{s}\leq 0\end{cases} \tag{2.71}$$

- The **Gerber** model

$$K_R\left(\bar{s}\right)=\frac{1}{1-\left(\frac{\bar{s}}{S_u}\right)^2} \text{ for } -S_u<\bar{s}<S_u \tag{2.72}$$

with S_u is the ultimate tensile strength, and S_y is the yield strength of the considered material. While the Gerber model is not sensitive to the mean stress sign, Goodman and Soderberg models consider only the case of positive mean stress (tensile stress). This is based on the observation that negative mean stress (compression) has negligible effect on crack propagation, and consequently on material failure. In practice, the use of the correction factor model depends on the mean stress value sensitivity of the considered material, and in general, Goodman correction is considered to provide a lower bound on the available experimental data.

A distinction should be made at this point between the local mean stress calculated per each loading cycle as defined in eq. 2.54 and the global mean stress calculate for the stress time history $s\left(t\right)$ as defined in eq. 2.67. While the local mean is changing with each loading cycle, the global mean stress is constant for the case of stationary loading. Both mean stress values use the same symbol, however, it is always possible to distinguish them through the context.

The effect of mean stress value could be easily considered with the rainflow algorithm by cycle counting using the equivalent stress amplitude. However, when spectral method is used for fatigue estimation, it is hard to take into account the effect of the mean stress due to the use of the power spectral density function of the stress course and the information related to the occurring globally and locally mean value are contained in the PSD in a way that is difficult to use in practice. Several suggestions are available in literature to handle this issue, such as [Kihl et al., 1999] and [Nieslony et al., 2012]. The proposed method of [Nieslony et al., 2012] is based on transforming the PSD function of the non zero-mean stress course $G_s\left(\omega\right)$ into an equivalent PSD function of zero-mean stress course $G_{s,e}\left(\omega\right)$, this transformation is done using

$$G_{s,e}\left(\omega\right)=K_i^2\left(\bar{s}\right)G_s\left(\omega\right), \tag{2.73}$$

where the mean stress value $\bar{s}$ could be estimated using eq. 2.68. The main advantage of this method is that the transformed PSD $G_{s,e}\left(\omega\right)$ represents a zero-mean stress course, which enables the use of the various spectral methods developed with the assumption of zero-mean stress time history for the narrow-band and broad-band stochastic loading characteristics.

2.5 Linear Accumulation Hypothesis (Miner's Rule)

Miner's Rule assumes a linear accumulation of the partial damage introduced by $n(s,\bar{s})$ cycles each with mean stress value $\bar{s}$ and stress amplitude s [Miner, 1645]. If $N(s,\bar{s})$ is the number of cycles to failure at the same stress mean and stress level, then the accumulated fatigue damage $\mathcal{D}(T)$ through the loading time history $s(t)$, $0 \leq t \leq T$ under the linear damage accumulation rule in its integral form is given by

$$\mathcal{D}(T) = \int\limits_{0}^{\infty}\int\limits_{-\infty}^{\infty} \frac{n(s,\bar{s})}{N(s,\bar{s})} \mathrm{d}\bar{s}\mathrm{d}s, \tag{2.74}$$

where $\mathcal{D}(T)$ is the accumulated fatigue damage during the time duration T.

According to this rule, it is assumed that the structural failure will occur when the accumulated fatigue damage $\mathcal{D}(T_{life})$ over the lifetime of the structure T_{life} reaches a critical level $\mathcal{D}_{cr}$. This critical level is often taken to be unity, namely $\mathcal{D}_{cr} = 1$. However, the computed critical fatigue damage $\mathcal{D}_{cr}$ at failure over a wide range of references varies for the case of wind turbines between $\mathcal{D}_{cr,min} = 0.79$ and $\mathcal{D}_{cr,max} = 1.53$ [Sutherland, 1999].

Damage intensity $\dot{\mathcal{D}}(T)$ (called also damage rate) as defined in eq. 2.75 is also used to express how fast the damage is accumulated through time.

$$\dot{\mathcal{D}}(T) = \frac{\mathcal{D}(T)}{T}. \tag{2.75}$$

If the calculated damage intensity $\dot{\mathcal{D}}(T)$ during the loading time T is representative to the average damage rate accumulated by a component over its service lifetime T_{life}, namely, $\dot{\mathcal{D}}(T) = \dot{\mathcal{D}}(T_{life})$, then the service lifetime of the structure T_{life} is given according to eq. 2.75 by

$$T_{life} = \frac{\mathcal{D}_{cr}}{\dot{\mathcal{D}}(T)}. \tag{2.76}$$

The classical, linear and memory-less summation rule presented in eq. 2.74 is usually written in two different forms. The first one is used for fatigue damage calculation in the time domain. In this form, the zero-mean equivalent stress range s_e is obtained using Goodman correction (eq. 2.70) and a counting algorithm is employed to obtain the number of all counted cycles $N(T)$. Thus, the total damage is given by

$$\mathcal{D}(T) = \sum_{i=1}^{N(T)} \frac{1}{N_i}, \tag{2.77}$$

with N_i is the number of cycles to failure at the equivalent stress amplitude s_i. By using eq. 2.66, this last equation takes also the following form

$$\mathcal{D}(T) = \frac{1}{K}\sum_{i=1}^{N(T)} s_i^m. \tag{2.78}$$

The second form of the Miner's rule is used for fatigue damage estimation in the frequency domain and is applied for a system subject to a random loading $s\left(t\right)$. Due to the random nature of the stress loading, the total damage $\mathcal{D}\left(T\right)$ is replaced by the expected value of the fatigue damage and eq. 2.78 is re-written in the following form

$$\mathcal{D}\left(T\right) = E\left[\frac{1}{K}\sum_{i=1}^{N(T)} s_i^m\right]. \tag{2.79}$$

Under the assumption of large number of counted cycles $N\left(T\right)$, and that the amplitudes have the same distribution with weak dependency between them, then the expected fatigue damage could be calculated using

$$\mathcal{D}\left(T\right) = \frac{1}{K}E\left[N\left(T\right)\right]E\left[s^m\right], \tag{2.80}$$

with $E\left[N\left(T\right)\right]$ is the expected number of cycles counted in the time interval T. By considering a stationary process, $E\left[N\left(T\right)\right]$ could be estimated with the help of the expected intensity of counted cycles ν_c in the case of rainflow counting, this means

$$E\left[N\left(T\right)\right] = \nu_c T. \tag{2.81}$$

Furthermore, in a stationary process, $E\left[s^m\right]$ could also be estimated with the help of the m-th moment of the probability density function $p_a\left(s\right)$ of amplitude s defined by the the counting method adopted (e.g. rainflow count). With the assumption of zero mean value of the stress s, the expected fatigue damage is then given by

$$\mathcal{D}\left(T\right) = T\nu_c K^{-1}\int\limits_0^{+\infty} s^m p_a\left(s\right)\mathrm{d}s, \tag{2.82}$$

and the expected fatigue damage intensity is defined as

$$\dot{\mathcal{D}}\left(T\right) = \nu_c K^{-1}\int\limits_0^{+\infty} s^m p_a\left(s\right)\mathrm{d}s. \tag{2.83}$$

This last formula clearly states that for a random stationary process having a zero-mean stress, the expected fatigue damage intensity depends uniquely on the counting method used to build the distribution $p_a\left(s\right)$. As the rainflow method is the industry standard counting algorithm, it is mainly used in this work. Furthermore, eqs. 2.82 and 2.83 are valid only for the case of stationary random process with zero mean.

Formula 2.83 could be generalised for the case of stress loading $s\left(t\right)$ having mean stress $\bar{s}$ using the equivalent stress to the following form

$$\dot{\mathcal{D}}\left(T\right) = \nu_c K^{-1}\int\limits_0^{+\infty}\int\limits_{-\infty}^{+\infty} p_a\left(s_e, \bar{s}\right) s_e^m \mathrm{d}\bar{s}\mathrm{d}s, \tag{2.84}$$

where s_e is the equivalent stress amplitude as given per eq. 2.69.

It is worth to notice at this point, that normalizing the fatigue damage calculated using eq. 2.82

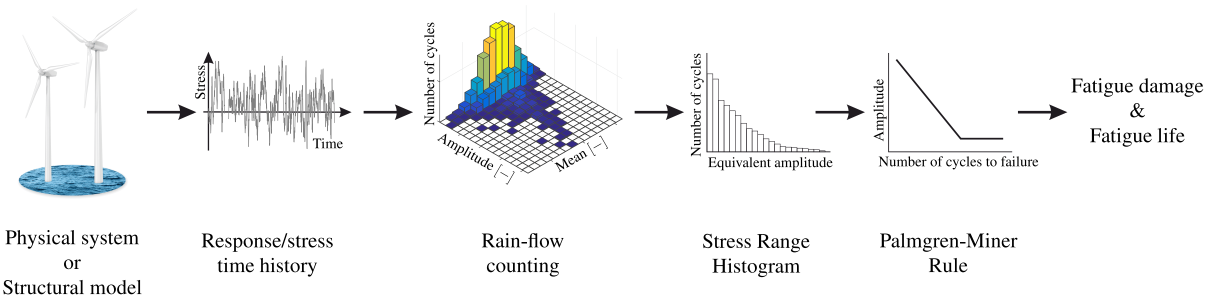

Figure 2.7 Procedure of fatigue damage estimation in time domain using rainflow counting algorithm.

by the fatigue damage calculated using the rainflow counting method in time domain will result to

$$\eta = \frac{\mathcal{D}\left(T\right)}{\mathcal{D}_{RFC}\left(T\right)} = \frac{\nu_c T \int_0^{+\infty} s^m p_a\left(s\right) \mathrm{d}s}{\sum_{i=1}^{N(T)} s_i^m}. \tag{2.85}$$

The normalised fatigue damage index η depends only on the material parameter m in addition to the nature of the random loading. The normalised fatigue damage index is very useful when comparing fatigue damage estimation using different spectral methods with respect to the industry standard rainflow counting method. The optimal value of the normalised fatigue index is close to unity, namely $\eta \approx 1$. This means that the estimated fatigue damage in frequency domain gives similar result to that estimated in the time domain. A value larger than unity of the normalised fatigue index indicates that the spectral method gives more conservative fatigue damage estimation than the time domain. Conversely, if $\eta < 1$ then the spectral method fails to predict the material failure.

2.6 Time-Domain Approach

Cycle counting is the industry standard and the general best practice in fatigue damage calculation for wind turbines in time-domain analysis. The widely used cycle counting algorithm is the rainflow cycle counting which is first introduced by Matsuishi and Endo to the scientific community in 1968 [Murakami, 1992]. Later in 1982, Downing and Socie [Downing et al., 1982] has developed one of the most widely referenced and used rainflow cycle-counting algorithm. This algorithm is the one outlined in the Annex G of the IEC61400 − 1 edition 3 [IEC, 2005]. In this method, the cycle count distribution is presented as the stress amplitude-mean histogram $n\left(s, \bar{s}\right)$ where the cycles are classified according to their stress level and mean values (fig. 2.7) as a first step, then Goodman correction might be used to compensate for the mean stress value (local or global) before employing the Miner's rule (eq. 2.78) to assess the fatigue life/damage of the structure or component. The work steps in this approach are illustrated in

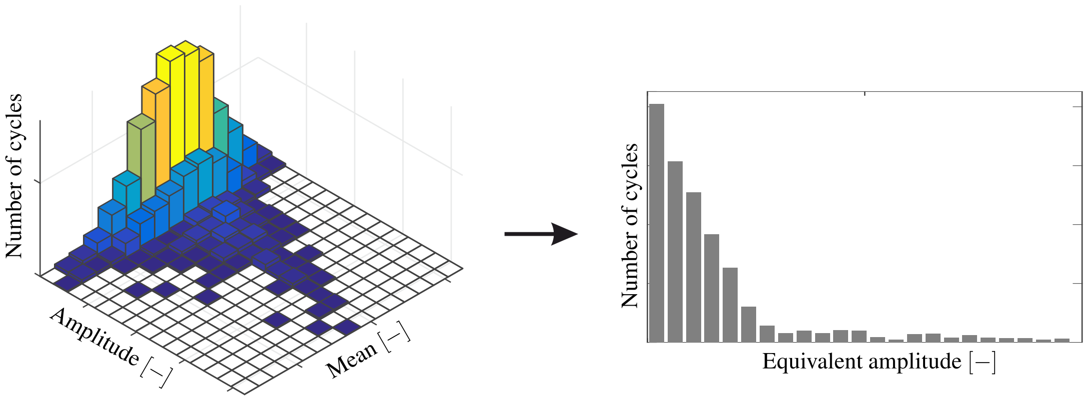

Amplitude-mean histogram
$n(s, \bar{s})$

Equivalent amplitude histogram
$n(s_e)$

Figure 2.8 Amplitude-mean histogram and equivalent amplitude histogram.

fig. 2.7.

The amplitude-mean histogram $n\left(s, \bar{s}\right)$ depends on two variables, the mean stress value $\bar{s}$ and the stress amplitude s. Using one of the previously presented models in sec. 2.4.2 for mean stress compensation, the amplitude-mean histogram could be transformed into an equivalent histogram $n\left(s_e\right)$ that depends only on the equivalent stress level s_e. An example of such transformation is illustrated in fig. 2.8.

The rainflow counting algorithm is a non-linear numerical algorithm. It has a complex sequential structure that requires significant loading history window in order to decompose arbitrary sequences of loads into cycles. To calculate fatigue damage from a stress loading history, the RFC algorithm counts the loading cycles and the maxima, then the Palmgren-Miner rule is applied to compute the expected fatigue damage and the fatigue life. Due to the requirements and the complexity of the RFC algorithm, it can only be used as a post-processing algorithm, or in other words, it is always performed offline.

Traditionally, fatigue damage has been estimated using the rainflow counting technique with satisfactory results obtained from the periodic loading time signals, such as from the stress or strain measurements. However, the main critics of this approach is the need for very large time records with high sampling rates in order to capture correctly signal dynamics (peaks and valleys) in addition to the needed computational power and the huge required storage space for such measured signals or to generate numerical time-series using wind turbine modelling software. These points limit the designer's ability to do fatigue calculation using the time-domain approach.

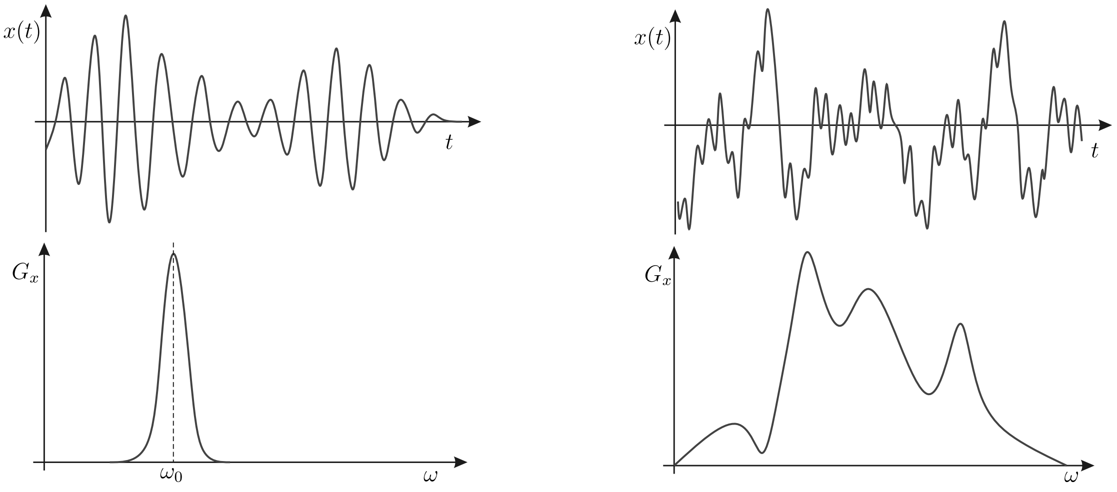

(a) Narrow-band process **(b)** Wide-band process

Figure 2.9 Narrow-band and Wide-band processes

2.7 Frequency-Domain Approach

While fatigue damage estimation in time-domain follows a direct approach in building the amplitude-mean histogram $n\left(s, \bar{s}\right)$ by direct cycle counting and classification of the loading time-series amplitude, the frequency-domain approach handles the problem of cycle counting by estimating the probability density function (PDF) of stress mean and amplitude $p_{a,m}\left(s, \bar{s}\right)$ by using the extracted statistical properties of a stationary stochastic process from the corresponding power spectral density (PSD). The joint amplitude-mean distribution $p_{a,m}\left(s, \bar{s}\right)$ is then used in the linear damage accumulation as presented in sec. 2.5 to calculate the fatigue damage ratio and the fatigue life time of the structure.

Most of the early developed spectral methods neglect the effect of the mean stress or the process is assumed to have a zero-mean stress value in order to be able to estimate the marginal PDF $p_a\left(s\right)$. This could be justified as the mean stress is related to the static loading which should be calculated separately and it does not affect the fatigue damage calculations if the appropriate $S-N$ curve that corresponds to the mean stress is used. However, the recently developed spectral methods enable considering the mean stress value by estimating the joint probability density function $p_{a,m}\left(s, \bar{s}\right)$ instead of only approximating the marginal PDF $p_a\left(s\right)$. Recently, [Niesłony et al., 2015] proposed a method that enables handling the mean stress in spectral fatigue estimation by means of transforming the PSD obtained from non-zero mean stress using one of the previously defined mean-stress compensation models (sec. 2.4.2). This approach when combined with the first set of methods that estimate directly $p_a\left(s\right)$ would enable taking the mean stress value into account.

By neglecting the mean stress effect, or by using the equivalent stress amplitude with zero mean value, the problem of fatigue estimation using spectral methods is simplified from finding a general and more realistic expression of the joint probability density function $p_{a,m}(s, \bar{s})$ into approximating the probability density function of amplitudes $p_a(s)$ which is the main challenge for all spectral methods. For this purpose, different assumptions on the loading signals are assumed and a number of approximations have been proposed in the literature. The main simplifying hypothesis is the *Gaussian* loading assumption which is reasonable if the stochastic loading has Gaussian distribution characteristics and the excited structure has linear behaviour. The main benefit of the Gaussian assumption is that it simplifies finding an explicit formula for both cycle distribution and fatigue damage [Rice, 1944].

Under the Gaussian assumption, the spectral methods could be classified according to the energy distribution over frequency in the PSD and consequently the used approximation of the probability density function. Therefore, it is possible to distinguish between the narrow- and wide-band methods. In the narrow-band processes, the PSD has most of its significant values on a very limited frequency range and the peaks and valleys are almost symmetrically placed with respect to the mean level. Furthermore, the consecutive peaks and valleys cannot occur without a mean level crossing (see fig. 2.9). This means that in frequency-domain the loading cycles distribution could be determined using analytical solutions such as the one proposed by [Miles, 1954] and [Bendat, 1964]. On the contrary, the wide-band process does not share those properties of the narrow-band which makes the definition of loading cycles not an obvious task and empirical estimation of the cycle distribution should be considered.

At this point, it is possible to identify four main categories in fatigue damage estimation for the wide-band processes. In the first category the proposed methods try to extend the narrow-band results to the wide-band process by employing correction factors based on the spectral moments such as the methods proposed by [Benasciutti, 2012; Fu et al., 2000; Gao et al., 2007; Larsen et al., 1991; Tovo, 2002; Wirsching et al., 1977] and [Gao et al., 2008]. The main drawback of such methods is that no exact estimation of the rainflow amplitude distribution of the wide-band process is estimated; and the relating information are lost because only the fatigue damage is calculate at the end. The methods of the second category attempt to approximate the real cycle amplitude distribution $p_a(s)$ as a weighted combination of different basic distributions such as Rayleigh, Weibull, Exponential, etc. The weighting factors depend on the spectral moments and are empirically estimated either using numerical simulations or experimental results. The proposed methods: Dirlik [Dirlik, 1985], Jiao-Moan [Zhao et al., 1992], Petrucci-Zuccarello [Petrucci et al., 2004], Bands-method [Braccesi et al., 2005], and Tovo-Benasciutti [Benasciutti et al., 2005b] go under this category. In the third category (or the special methods category) the fatigue damage intensity of the wide-band process is esti-

Table 2.2 Classification of spectral methods of fatigue damage estimation

Spectral method	Reference	short-name	Narrow-band	Wide-band - Category		
				First	Second	Third
Narrow-band	[Rychlik, 1993]	NB	•			
Wirsching-Light	[Wirsching et al., 1980]	WL		•		
Ortiz-Chen	[Ortiz et al., 1987]	OC		•		
Single-Moment	[Benasciutti et al., 2013; Larsen et al., 1991]	SM		•		
Empirical $\alpha_{0.75}$	[Benasciutti et al., 2004]	$\alpha_{0.75}$		•		
1st Tovo-Benasciutti	[Benasciutti, 2012; Tovo, 2002]	TB1			•	
2nd Tovo-Benasciutti	[Benasciutti, 2012; Tovo, 2002]	TB2			•	
Dirlik	[Dirlik, 1985]	DK			•	
Simplified Zhao-Baker	[Zhao et al., 1992]	ZBs			•	
Improved Zhao-Baker	[Zhao et al., 1992]	ZBi			•	
Petrucci-Zuccarello	[Petrucci et al., 2004]	PZ				•
Bands Method	[Braccesi et al., 2015a]	BM				•

mated directly without the need to estimate the corresponding amplitude distribution. Under this category goes for example the method proposed by [Petrucci et al., 2004] where the problem of damage estimation is reformulated into estimating an integral that represents the m-th moment of the amplitude PDF in terms of various spectral parameters. The Bands method proposed recently by [Braccesi et al., 2015a] goes also under this category. This method reformulates the fatigue damage estimation of the wide-band process as a non-linear summation of fatigue damage estimated for n narrow bands using the narrow-band method. Finally, the fourth category tries to translate the procedure of hysteresis loop identification in time domain into the frequency domain [Olagnon, 1994; Rychlik, 1987], however, these methods require large computational effort and are, therefore, difficult to implement. Tab. 2.2 summaries the spectral methods considered in this thesis and their corresponding category.

The general work steps for fatigue damage estimation of a Gaussian loading using spectral methods are illustrated in fig. 2.10. These steps start by building the power spectral density of the stationary stochastic process (structural response or measured stress), followed by extracting the statistical properties necessary for fatigue damage calculation using the appropriate estimation category/method. A detailed review of the different spectral methods is presented by [Sherratt et al., 2005] and recently by [Mršnik et al., 2013].

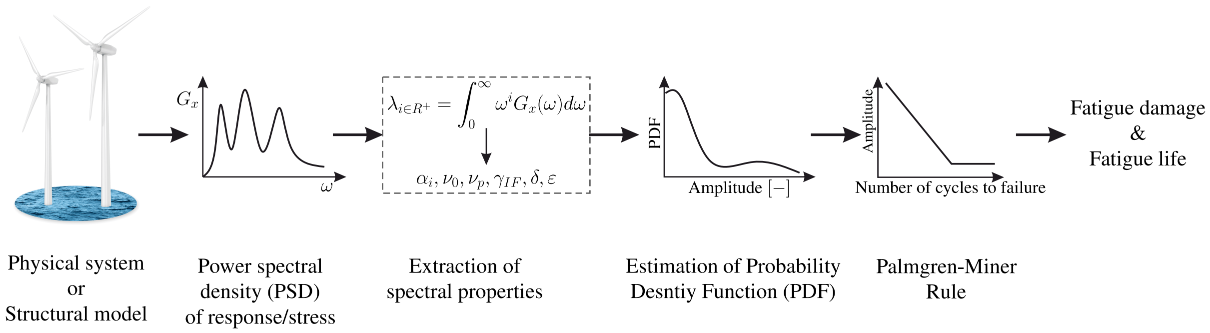

Figure 2.10 General procedure of fatigue damage estimation in frequency domain.

The structural response of the wind turbine has a non-Gaussian characteristics due to two main reasons. The first one is the non-Gaussian characteristics of the wind and wave loading on the wind turbine. The second reason is the structural non-linearity (aerodynamics and hydrodynamic loading) of the wind turbines. As the Gaussian assumption is critical for the frequency domain fatigue analysis, the non-Gaussianity of the structural response should be taken into account. Two different approaches are proposed in literature to handle this problem, both of them make use of the developed methods under the Gaussian assumption. These approaches are explored in details later in this section.

2.7.1 Spectral Fatigue Damage Estimation of Gaussian Loading

Spectral fatigue damage assessment under the Gaussian assumption has been widely studied and many methods have been developed to address this topic. This section goes through the methods previously identified in the first three categories as they could be used for fatigue damage estimation of wind turbines. A short formulation of each method is presented. Furthermore, Table 2.3 summaries the considered methods and the needed parameters in addition to the resulted outputs.

2.7.1.1 Narrow-Band Approximation

The Narrow-Band (NB) approximation assumes that the cycle amplitude distribution $p_a(s)$ coincides with the peak distribution $p_p(s)$ which converges to a *Rayleigh* probability distribution given by

$$p_a(s) = \frac{s}{\lambda_0} e^{-\frac{s^2}{2\lambda_0}}. \tag{2.86}$$

Furthermore, the intensity of counted cycles ν_c can be taken to be equal to the mean up-crossing intensity ν_0. The estimated fatigue damage of the NB method $\mathcal{D}_{NB}$ during the time duration

Table 2.3 Comparison between the various spectral methods under the Gaussian assumption in terms of the required spectral moments and the resulted outputs.

Spectral Method	Required spectral moment λ_i								Probability distribution	$\mathcal{D}$
	λ_0	λ_1	λ_2	λ_4	$\lambda_{\frac{2}{m}}$	$\lambda_{\frac{2}{m}+2}$	$\lambda_{0.75}$	$\lambda_{1.5}$	$p_a\left(s\right)$	
Narrow-band (NB)	•		•						•	•
Wirsching-Light (WL)	•		•						•	•
Ortiz-Chen (OC)	•		•	•	•	•			•	•
Single-Moment (SM)					•				•	•
1st Tovo-Benasciutti (TB1)	•	•	•	•					•	•
2nd Tovo-Benasciutti (TB2)	•	•	•	•					•	•
Empirical $\alpha_{0.75}(\alpha_{0.75})$	•		•				•	•	•	•
Dirlik (DK)	•	•	•	•					•	•
Zhao-Baker simplified (ZBs)	•		•	•					•	•
Zhao-Baker improved (ZBi)	•		•	•			•	•	•	•
Petrucci-Zuccarello (PZ)	•	•	•	•						•
Band Method (BM)	•		•							•

T in its closed form is then given by

$$\mathcal{D}_{NB} = T\frac{\nu_0}{K}\left(\sqrt{2\lambda_0}\right)^m \Gamma\left(1+\frac{m}{2}\right), \tag{2.87}$$

with $\Gamma\left(\;\cdot\;\right)$ as the Euler gamma function defined by

$$\Gamma\left(z\right) = \int\limits_0^{+\infty} t^{z-1}e^{-t}\mathrm{d}t, \tag{2.88}$$

where ν_0, K and λ_0 are as given in eq. 2.26, eq. 2.66, and eq. 2.22, respectively. A very important notice is that the narrow-band damage intensity depends only on the 0-th and 2-nd moments, namely on λ_0 and λ_2, in addition to the material properties K and m.

If the narrow band-band fatigue damage approximation is used with a wide-band process, it is widely accepted that this approximation tends to overestimate the rainflow fatigue damage [Rychlik, 1993].

2.7.1.2 Single-Moment Method

This method is developed by [Larsen et al., 1991] where the authors have proposed an empirical relation for the fatigue damage. This method is often referred to, in the literature, as the Single-Moment (SM) method [Larsen et al., 2015]. The mathematical interpretation of this method has been recently provided by [Benasciutti et al., 2013] using the multi-axial fatigue damage estimation approach known as “Projection-by-Projection” (see sec. 2.8.2). This approach proves that the Single-Moment method implies a non-linear summation of damage contributions of narrow frequency bands given by a spectral decomposition of the PSD of $s\left(t\right)$. In the SM method, the empirical fatigue damage during the time duration T is given by

$$\mathcal{D}_{SM} = T\frac{2^{\frac{m}{2}}}{2\pi K}\left(\lambda_{\frac{2}{m}}\right)^{\frac{m}{2}}\Gamma\left(1+\frac{m}{2}\right). \tag{2.89}$$

It is clear that this method depends only on the spectral moment $\lambda_{\frac{2}{m}}$ and the material properties m and K.

2.7.1.3 Wirsching-Light Method

The fatigue damage of the wide-band process estimated using [Wirsching et al., 1980] method is simply an extension to the narrow-band estimation by an empirical correction (reduction) factor such as

$$\mathcal{D}_{WL} = \chi_{WL}\mathcal{D}_{NB}. \tag{2.90}$$

The empirical correction factor χ_{WL} is assumed to be dependent on the fatigue curve parameter, namely m, and on the spectral width parameter ε (eq. 2.31) such as

$$\chi_{WL} = a\left(m\right) + \left[1 - a\left(m\right)\right]\left(1-\varepsilon\right)^{b\left(m\right)},$$

with the best fitting parameters $a\left(m\right)$ and $b\left(m\right)$ are given by

$$a\left(m\right) = 0.926 - 0.033m, \tag{2.91}$$

$$b\left(m\right) = 1.587m - 2.323. \tag{2.92}$$

For narrow-band process $\varepsilon = 0$, Wirsching-Light method gives the same result as the narrow-band ($\chi_{WL} = 1$). However, unlike the narrow-band method, this method assumes that the rainflow cycle counting is dependent on three spectral moments λ_0, λ_2 and λ_4 through ε, and consequently through α_2 parameter. Finally, Wirsching-Light method has been developed for $S-N$ slope value of $m = 3, 4, 5$, and 6. For slope values $m > 6$, the method has not been tested and the obtained results are questionable.

2.7.1.4 Ortiz-Chen Method

The Ortiz-Chen (OC) method is another method that tries to correct the estimated fatigue damage using the narrow-band assumption. This method has been developed by [Ortiz et al., 1987], and the estimate fatigue damage is given by

$$\mathcal{D}_{OC} = \chi_{OC}\mathcal{D}_{NB},$$

where the correction factor χ_{OC} is defined as

$$\chi_{OC} = \frac{\beta_i^m}{\alpha_2},$$

with β_i being the generalized spectral band width

$$\beta_i = \sqrt{\frac{\lambda_2\lambda_i}{\lambda_0\lambda_{i+2}}}. \tag{2.93}$$

The authors have proposed the following value for $i = \frac{2}{m}$. Therefore, this method depends on λ_0, λ_2, λ_4, $\lambda_{\frac{2}{m}}$ and $\lambda_{\frac{2}{m}+2}$ spectral moments, in addition to its dependency on the material parameters m and K.

2.7.1.5 Tovo-Benasciutti Methods

This method has been proposed by [Tovo, 2002] and [Benasciutti, 2012]. It is based on the fact that the rainflow amplitude probability density function $p_a(s)$ can be estimated using

$$p_a(s) = b p_a^{LCC}(s) + (1-b)\, p_a^{RC}(s), \tag{2.94}$$

where $p_a^{LCC}(s)$ is the amplitude PDF of level-crossing counting (LCC) method, i.e. narrow-band approximation, and $p_a^{RC}(s)$ is the amplitude PDF of range counting (RC) method (see [Benasciutti, 2012] for more details), while b is a constant determined using the spectral properties of the process. The amplitude PDF for level crossing and range counting methods are given by

$$p_a^{LCC}(s) = \alpha_2 \frac{s}{\lambda_0} e^{-\frac{s^2}{2\lambda_0}}, \tag{2.95}$$

$$p_a^{RC}(s) = \frac{s}{\lambda_0 \alpha_2^2} e^{-\frac{s^2}{2\alpha_2^2\lambda_0}}, \tag{2.96}$$

and there corresponding cumulative density functions are

$$P_a^{LCC}(s) = \alpha_2 \left(1 - e^{-\frac{s^2}{2\lambda_0}}\right), \tag{2.97}$$

$$P_a^{RC}(s) = 1 - e^{-\frac{s^2}{2\alpha_2^2\lambda_0}}. \tag{2.98}$$

Eq. 2.94 leads to the following estimation of the fatigue damage

$$\mathcal{D}_{TB} = \chi_{TB} \mathcal{D}_{NB}, \tag{2.99}$$

where the correction factor is given by

$$\chi_{TB} = b + (1-b)\, \alpha_2^{m-1}. \tag{2.100}$$

The parameter b is numerically approximated by one of the following suggested two functions

$$b_{TB1} = \min\left\{\frac{\alpha_1 - \alpha_2}{1 - \alpha_1}, 1\right\}, \tag{2.101}$$

$$b_{TB2} = \frac{\alpha_1 - \alpha_2}{(\alpha_2 - 1)^2}\left[1.112 \times (1 + \alpha_1\alpha_2 - (\alpha_1 + \alpha_2))\, e^{2.11\alpha_2} + (\alpha_1 - \alpha_2)\right]. \tag{2.102}$$

This approach is supported by the analytical derivation of the lower and upper fatigue intensity limits, whereas the linear combination parameter b in both forms depends implicitly on four spectral moments λ_0, λ_1, λ_2, and λ_4 through α_1 and α_2 band width parameters in addition to the material constants m and K. The estimated fatigue damage using Tovo-Benasciutti methods are referred to as $\mathcal{D}_{TB1}$ and $\mathcal{D}_{TB2}$ according to the used constants b_{TB1} and b_{TB2} in the correction factor χ_{TB}, respectively.

2.7.1.6 The $\alpha_{0.75}$ Method

Similar to the previous method presented in Sec. 2.7.1.5, the $\alpha_{0.75}$ method, as proposed by [Benasciutti et al., 2004], estimates the fatigue damage in eq. 2.99 using a correction factor $\chi_{\alpha_{0.75}}$ chosen on pure empirical bases and given by

$$\chi_{\alpha_{0.75}} = \alpha_{0.75}^2,$$

where $\alpha_{0.75}$ could be calculated using eq. 2.29. And the estimated fatigue damage using this method is identified as $\mathcal{D}_{\alpha_{0.75}}$. It is clear from this formulation that the correction factor is independent of the fatigue exponent m, however, the method still depends on λ_0, λ_2, $\lambda_{0.75}$ and $\lambda_{1.5}$ in addition to the material constants m and K.

2.7.1.7 Dirlik Method

The rainflow amplitude distribution $p_a(s)$ is approximated in Dirlik method (DK) using a combination of an exponential and two Rayleigh probability densities [Dirlik, 1985]. The approximated closed-form expression of the probability density function of rainflow amplitude s is given by

$$p_a(s) = \frac{1}{\sqrt{\lambda_0}}\left[\frac{G_1}{Q}e^{-\frac{z}{Q}} + \frac{G_2 z}{R^2}e^{-\frac{z^2}{2R^2}} + G_3 z e^{-\frac{z^2}{2}}\right], \tag{2.103}$$

with z as the normalised stress amplitude given by

$$z = \frac{s}{\sqrt{\lambda_0}}. \tag{2.104}$$

In addition to that, the following parameters are defined

$$x_m = \frac{\lambda_1}{\lambda_0}\sqrt{\frac{\lambda_2}{\lambda_4}}, \tag{2.105}$$

$$G_1 = \frac{2\left(x_m - \alpha_2^2\right)}{1+\alpha_2^2}, \tag{2.106}$$

$$G_2 = \frac{1-\alpha_2 - G_1 + G_1^2}{1-R}, \tag{2.107}$$

$$G_3 = 1 - G_1 - G_2, \tag{2.108}$$

$$R = \frac{\alpha_2 - x_m - G_1^2}{1 - \alpha_2 - G_1 + G_1^2}, \tag{2.109}$$

$$Q = \frac{1.25\left(\alpha_2 - G_3 - G_2 R\right)}{G_1}. \tag{2.110}$$

The closed form expression for the fatigue damage using the linear fatigue accumulation rule could be calculated by substituting eq. 2.103 into eq. 2.83 to obtain

$$\mathcal{D}_{DK} = \nu_p T K^{-1} \lambda_0^{\frac{m}{2}} \left[G_1 Q^m \Gamma\left(1+m\right) + 2^{\frac{m}{2}} \Gamma\left(1+\frac{m}{2}\right)\left(G_2\left|R\right|^m + G_3\right)\right] \tag{2.111}$$

Dirlik method presents a very good approximation of the rainflow amplitude distribution. However, this method does not account for the mean value dependency, and with the absence of the theoretical background, as it is developed as a completely approximate approach, it is hard to extend it to handle non-Gaussian processes.

2.7.1.8 Zhao-Baker Method

It is possible to distinguish two forms of Zhao-Baker method which are recognised as the simplified and improved forms [Zhao et al., 1992]. Both forms of Zhao-Baker method follow the same concept of Dirlik by approximating the rainflow amplitude distribution $p_a\left(s\right)$ using a weighted linear sum of Weibull and Rayleigh distributions such as

$$p_a\left(z\right) = w \underbrace{abz^{b-1}e^{-az^b}}_{\text{Weibull}} + \left(1-w\right)\underbrace{ze^{-\frac{z^2}{2}}}_{\text{Rayleigh}}, \tag{2.112}$$

with w as the weighting factor $0 \leq w \leq 1$ given by

$$w = \frac{1-\alpha_2}{1-\sqrt{\frac{2}{\pi}}\Gamma\left(1+\frac{1}{b}\right)a^{-\frac{1}{b}}}, \tag{2.113}$$

while z is the normalised stress amplitude as given in eq 2.104. Furthermore, the Weibull distribution parameters $a > 0$ and $b > 0$ are calculated with the help of the spectral properties. The calculation of these parameters in the simplified form of [Zhao et al., 1992] is done using

$$a = 8 - 7\alpha_2, \tag{2.114}$$

$$b = \begin{cases} 1.1 & \alpha_2 < 0.9 \\ 1.1 + 9\left(\alpha_2 - 0.9\right) & \alpha_2 \geq 0.9 \end{cases}, \tag{2.115}$$

and in this approximation, if $\alpha_2 \leq 0.13$ it happens that $w > 1$, which is not correct.

The improved form of [Zhao et al., 1992] method suggests an improved version of the a parameter for the case of small values of m (e.g. $m = 3$) where the rainflow damage is more closely related to $\alpha_{0.75}$ than α_2. The a parameter in this improved version is calculated using $a = d^{-b}$, where d is the solution of

$$\Gamma\left(1+\frac{3}{b}\right)\left(1-\alpha_2\right)d^3 + 3\Gamma\left(1+\frac{1}{b}\right)\left(\chi_{ZB}\alpha_2 - 1\right)d + 3\sqrt{\frac{\pi}{2}}\alpha_2\left(1-\chi_{ZB}\right) = 0, \tag{2.116}$$

with χ_{ZB} is given according to [Zhao et al., 1992] as

$$\chi_{ZB}\rvert_{m=3} = \begin{cases} -0.4154 + 1.392\alpha_{0.75} & \text{if } \alpha_{0.75} \geq 0.5 \\ 0.28 & \text{if } \alpha_{0.75} < 0.5 \end{cases}. \tag{2.117}$$

Once again, this improved formulation has some weak points, such as having negative values of w when considering particular values of $\alpha_{0.75}$ and α_2. Furthermore, both the simplified and improved forms of the [Zhao et al., 1992] method gives the amplitude density function as

$$p_a(s) = w\frac{ab}{\sqrt{\lambda_0}}\left(\frac{s}{\sqrt{\lambda_0}}\right)^{b-1} e^{-\alpha\left(\frac{s}{\sqrt{\lambda_0}}\right)^{b}} + (1-w)\frac{s}{\lambda_0}e^{-\frac{1}{2}\left(\frac{s}{\sqrt{\lambda_0}}\right)^{2}}, \tag{2.118}$$

and the closed form of fatigue damage according to Palmgren-Miner rule is calculated using

$$\mathcal{D}_{ZB} = \nu_p T K^{-1}\lambda_0^{\frac{m}{2}}\left[wa^{-\frac{m}{b}}\Gamma\left(1+\frac{m}{b}\right) + (1-w)\,2^{\frac{m}{2}}\Gamma\left(1+\frac{m}{2}\right)\right]. \tag{2.119}$$

Finally, the estimated fatigue damage using [Zhao et al., 1992] method in its simplified form depends on λ_0, λ_2 and λ_4 while the improved form depends in addition to that on $\lambda_{0.75}$ and $\lambda_{0.5}$. Both forms require also to the material constants m and K.

2.7.1.9 Petrucci-Zuccarello Method

Unlike the previous methods in fatigue damage estimation where the probability distribution function of the amplitudes $p_a(s)$ is firstly approximated, then the damage intensity is calculate using eq. 2.83; [Petrucci et al., 2004] has proposed another approach in handling the problem of fatigue damage estimation. The proposed method starts from eq. 2.83 and taking the number of expected cycle rate to be equal to the number of peak rate (i.e. $\nu_c = \nu_p$), then re-writing the equation to the following from

$$\mathcal{D}_{PZ} = \nu_p T K^{-1}\int\limits_0^{+\infty} s_e^m p(s_e)\,\mathrm{d}s_e = \nu_p K^{-1}\Lambda_m, \tag{2.120}$$

where Λ_m represents the m-th moment of the probability distribution $p_a(s)$ of the rainflow equivalent amplitude which depends on unknown set of spectral parameters

$$\Lambda_m = \int\limits_0^{+\infty} s_e^m p(s_e)\,\mathrm{d}s_e. \tag{2.121}$$

Based on this re-formulation, the problem of fatigue damage estimation becomes a problem of the correct estimation of the m-th moment Λ_m in terms of several spectral parameters. The authors have found a reasonable approximation of Λ_m of the form

$$\Lambda_m = \lambda_0^{\frac{m}{2}}\varphi\left(\alpha_1, \alpha_2, m, \tilde{R}\right), \tag{2.122}$$

where $\tilde{R} = \frac{s_{max}}{S_u} \in [0.15, \ldots, 0.9]$ is a dimensionless parameter related to the maximum stress s_{max} of the process and the ultimate tensile strength of the material S_u. Furthermore, $\varphi(\,\cdot\,)$ is an exponential function defined by

$$\varphi\left(\alpha_1, \alpha_2, m, \tilde{R}\right) = e^{\Psi\left(\alpha_1, \alpha_2, m, \breve{R}\right)}, \tag{2.123}$$

with $\Psi\left(\alpha_1, \alpha_2, m, \breve{R}\right)$ is assumed to take the following polynomial form

$$\begin{aligned}\Psi\left(\alpha_1, \alpha_2, m, \breve{R}\right) &= \left[\frac{2}{9}\left(\Psi_4 - \Psi_3 - \Psi_2 + \Psi_1\right)(m-3) + \frac{4}{3}\left(\Psi_3 - \Psi_1\right)\right]\left(\breve{R} - 0.15\right) \\ &\quad + \frac{1}{6}\left(\Psi_2 - \Psi_1\right)(m-3) + \Psi_1,\end{aligned} \tag{2.124}$$

and the constants $\Psi_i,\ i = 1, \ldots, 4$ are calculated with the help of α_1 and α_2 according to

$$\Psi_1 = -1.994 - 9.381\alpha_2 + 18.349\alpha_1 + 15.261\alpha_1\alpha_2 - 1.483\alpha_2^2 - 15.402\alpha_1^2, \tag{2.125}$$

$$\Psi_2 = 8.229 - 26.510\alpha_2 + 21.522\alpha_1 + 27.748\alpha_1\alpha_2 + 4.338\alpha_2^2 - 20.026\alpha_1^2, \tag{2.126}$$

$$\Psi_3 = -0.946 - 8.025\alpha_2 + 15.692\alpha_1 + 11.867\alpha_1\alpha_2 + 0.382\alpha_2^2 - 13.198\alpha_1^2, \tag{2.127}$$

$$\Psi_4 = 8.780 - 26.058\alpha_2 + 21.628\alpha_1 + 26.487\alpha_1\alpha_2 + 5.379\alpha_2^2 - 19.967\alpha_1^2. \tag{2.128}$$

This simplified model of [Petrucci et al., 2004] requires the knowledge of the material exponent $m \in [3, \ldots, 9]$ and the ultimate tensile strength S_u in addition to the statistical properties of the process in the form of λ_0, α_1 and α_2 in order to compute the rainflow damage intensity given in eq. 2.120.

One of the advantages of this method is the possibility to consider the effect of the stress mean value on the fatigue damage estimation. This could be done by using the zero-mean equivalent stress s_e calculated according to any of the presented correction factors presented in sec. 2.4.2. However, as this method by-pass the estimation of the amplitude probability distribution, it is not possible to get a clear idea which amplitudes have higher damage effect on the structure. Furthermore, this method is still tied with the Gaussian assumption.

2.7.1.10 Bands-Method

Most of the proposed spectral methods assume certain shapes of the PSD function $G(\omega)$, and the methods are tuned to give optimal results for the assumed PSD Shape function. By deviating from the assumed PSD shape function, the accuracy of the calculate damage intensity deteriorates. In order to by-pass the assumption on the shape of the PSD function, [Braccesi et al., 2015a] proposed recently the Bands method (fig. 2.11). The basic idea of the proposed approach is to divide the PSD function $G(\omega)$ into n frequency bands sufficiently narrow so that each band is associated with a Rayleigh distribution. By making use of the proven analytical results, the damage $\mathcal{D}_i$ of each narrow band (see sec. 2.7.1.1) could be calculated and the total damage is then obtained using a particular non-linear combination rule.

Using the spectral decomposition, [Braccesi et al., 2015a] proposed defining a common value of

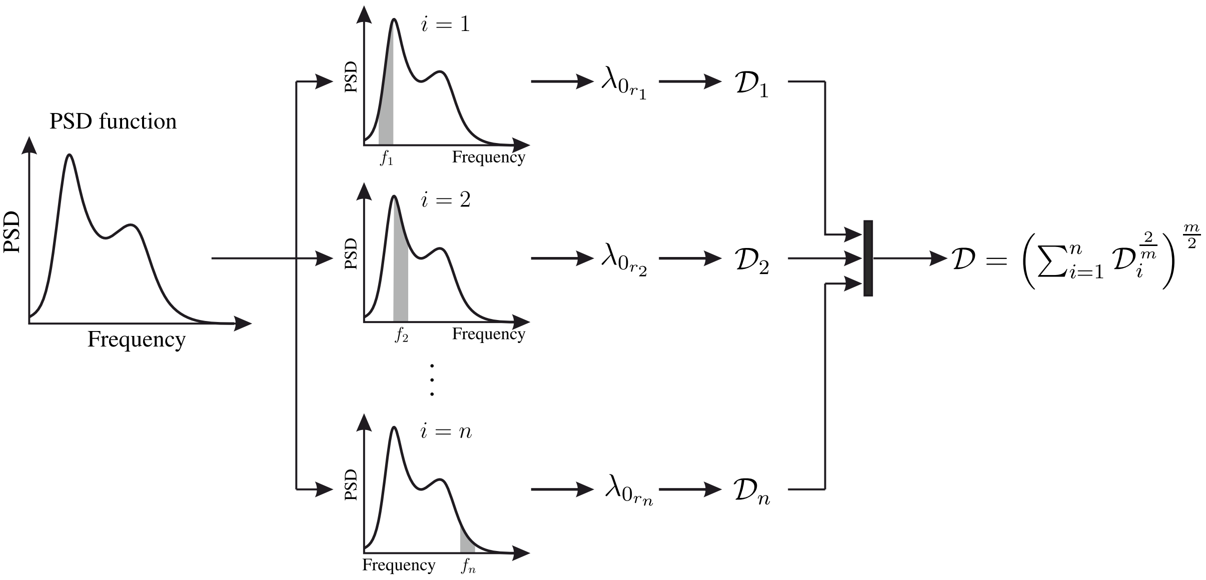

Figure 2.11 Block diagram of fatigue damage estimation using the Bands method.

the up-ward crossing frequency ν_{0_r} (arbitrary chosen) for all the bands, then by imposing an equivalence between the damage of a real i-th condition and the equivalent one, the zero-order reference spectral moment $\lambda_{0_{r_i}}$ of the i-th band is then given as

$$\lambda_{0_{r_i}} = \left(\frac{\nu_{0_i}}{\nu_{0_r}}\right)^{\frac{2}{m}} \lambda_{0_i}, \tag{2.129}$$

where ν_{0_i} and λ_{0_i} are the up-crossing rate and the zero-order spectral moment of the i-th frequency band. Based on this, the damage $\mathcal{D}_i$ of the considered band is given according to eq. 2.87

$$\mathcal{D}_i = T\frac{\nu_{0_r}}{K}\left(\sqrt{2\lambda_{0_{r_i}}}\right)^m \Gamma\left(1+\frac{m}{2}\right). \tag{2.130}$$

By substituting eq. 2.129 into eq. 2.130 it is possible to obtain

$$\mathcal{D}_i = T\frac{\nu_{0_i}}{K}\left(\sqrt{2\lambda_{0_i}}\right)^m \Gamma\left(1+\frac{m}{2}\right) \tag{2.131}$$

which gives the general formula of fatigue damage of the narrow band i. The total damage could be calculated according to the updated formulation of the method presented by [Benasciutti et al., 2016] using the multi-axial 'Projection-by-Projectoin' approach such as

$$\mathcal{D}_{BM} = \left(\sum_{i=1}^{n} \mathcal{D}_i^{\frac{2}{m}}\right)^{\frac{m}{2}}. \tag{2.132}$$

It is clear that the final summation rule is a non-linear summation of the partial damage $\mathcal{D}_i$, and it has similar analogy to the damage estimation in the multi-axial case. The common reference up-ward crossing frequency ν_{0_r} is arbitrary chosen, and the number n of considered spectral bands should be kept within reasonable limits to keep the narrow-band assumption valid.

The main drawback of this approach is the assumption that the considered bands are statistically

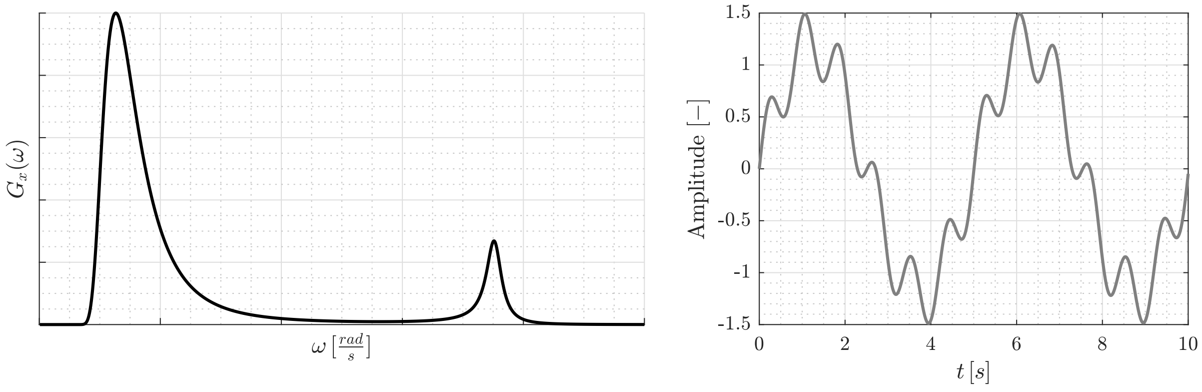

Figure 2.12 Example of bimodal process.

not correlated. If this assumption is violated, this leads to an over estimation of the total fatigue damage as it is clear from the obtained results.

2.7.1.11 Bimodal Methods

A special case of the wide-band stochastic loading is the so-called the bimodal process. This has a spectral density formed by superposition of two well separated narrow-band contributions. The first narrow-band is called the low frequency band (LF), while the second is called the high frequency band (HF) (fig 2.12). The bimodal spectra is a typical loading characteristic of the offshore platforms under wave loading with two well-defined resonant frequencies [Benasciutti et al., 2005a; Benasciutti et al., 2005c].

In the bimodal processes, it is known in advance that two types of cycles are extracted in rainflow count. The first cycle type is the large cycles that are associated to the slowly-varying low-frequency component. The second cycle type is mainly generated by the high-frequency component. Based on this clear separation between the cycle types in the rainflow count, it is possible to conclude that the rainflow damage may conveniently be computed as the sum of two separate contributions. Using this argument, many bimodal spectral methods have been developed for fatigue analysis such as [Cianetti et al., 2005; Fu et al., 2000; Jiao et al., 1990] who proposed correcting the narrow-band estimation using a correction factor that reflects the bimodal characteristics of the loading. [Benasciutti et al., 2005c; Benasciutti et al., 2007] have compared several bimodal methods against their wide-band method explained in sec. 2.7.1.5 and have found that the bimodal method developed by [Jiao et al., 1990] gives good fatigue estimation results. Therefore, this method is considered in this work.

Jiao-Moan Method

The bimodal process $x(t) \in X(t)$ could be written as

$$x(t) = x_1(t) + x_2(t),$$

with $x_1(t)$ corresponds to the low-frequency component and $x_2(t)$ corresponds to the high frequency component. By normalizing this process to have a unit variance, it is possible to obtain the normalised process

$$x^*(t) = x_1^*(t) + x_2^*(t), \tag{2.133}$$

which has $\lambda_0^* = \lambda_{0,1}^* + \lambda_{0,2}^* = 1$, with $\lambda_{0,1}^* = \frac{\lambda_{0,1}}{\lambda_0}$, and $\lambda_{0,2}^* = \frac{\lambda_{0,2}}{\lambda_0}$ are the variances of the normalised components $x_1^*(t)$ and $x_2^*(t)$, respectively; and the higher moments of the normalised components are calculated in similar way. The fatigue damage is given according to this method by

$$\mathcal{D}_{JM} = \chi_{JM} \mathcal{D}_{NB}, \tag{2.134}$$

with the correction factor χ_{JM} is calculated using

$$\chi_{JM} = \frac{\nu_{0,P}}{\nu_0} \left[\left(\lambda_{0,1}^* \right)^{\frac{m}{2}+2} \left(1 - \sqrt{\frac{\lambda_{0,2}^*}{\lambda_{0,1}^*}} \right) + \sqrt{\pi \lambda_{0,1}^* \lambda_{0,2}^*} \frac{m \Gamma\left(\frac{m}{2} + \frac{1}{2}\right)}{\Gamma\left(1 + \frac{m}{2}\right)} \right] + \frac{\nu_{0,2}}{\nu_0} \lambda_{0,2}^*. \tag{2.135}$$

Furthermore, the frequency of large cycles $\nu_{0,P}$ is given by

$$\nu_{0,P} = \lambda_{0,1}^* \nu_{0,1} \sqrt{1 + \frac{\lambda_{0,2}^*}{\lambda_{0,1}^*} \left(\frac{\nu_{0,2}}{\nu_{0,1}} \delta_2 \right)^2}, \tag{2.136}$$

where

$$\nu_{0,1} = \frac{1}{2\pi} \sqrt{\frac{\lambda_{2,1}^*}{\lambda_{0,1}^*}}, \tag{2.137}$$

$$\nu_{0,2} = \frac{1}{2\pi} \sqrt{\frac{\lambda_{2,2}^*}{\lambda_{0,2}^*}}, \tag{2.138}$$

$$\delta_2 = \sqrt{1 - \frac{\lambda_{1,2}^{*2}}{\lambda_{0,2}^* \lambda_{2,2}^*}}. \tag{2.139}$$

The correction coefficient χ_{JM} is equal to unity when $\lambda_{0,1}^* = 1$ or $\lambda_{0,2}^* = 1$, which gives the same fatigue damage of the narrow-band method. For well-separated bimodal process, eq. 2.135 presents good approximation. However, it is possible to get more conservative results than the narrow-band method as $\chi_{JM} > 1$ if the bimodal components are not well-separated. This might happen in case of small values of $\frac{\nu_{0,2}}{\nu_{0,1}}$ combined with large $\lambda_{0,1}^*$ values.

2.7.2 Spectral Fatigue Damage Estimation of Non-Gaussian Loading

The non-Gaussian process deviates from the normal distribution. This deviation could be estimated with the help of two statistical parameters, namely, the skewness γ_{Sk} and the kurtosis γ_{Ku}. If fatigue damage estimation is done on a non-Gaussian loading using Gaussian spectral methods this might lead to an unknown estimation error which is particularly large when $\gamma_{Ku} \gg 3$ [Benasciutti et al., 2017]. This means that the obtained results can not be trusted.

Two different approaches are proposed in literature that enable spectral damage estimation of non-Gaussian loading. The common point between these two approaches is to make use of the well developed spectral damage estimation methods under the Gaussian random loading. These two approaches are referred to as the corrected Gaussian approach and the transformed Gaussian model. Following is a brief description for each approach.

2.7.2.1 Corrected Gaussian Approach

This approach is based on estimating the fatigue damage $\mathcal{D}_G$ under the Gaussian assumption using any of the previously presented Gaussian methods, then the corrected fatigue damage $\mathcal{D}_{nG}$ is calculated using the correction factor χ_{nG} that reflects the non-Gaussianity of the process

$$\mathcal{D}_{nG} = \chi_{nG}\mathcal{D}_G, \tag{2.140}$$

The correction factor χ_{nG} is a function of different parameters of the non-Guassian process and the considered material, i.e.

$$\chi_{nG} = \chi_{nG}\left(\bar{s}, \sigma_s, \gamma_{Sk}, \gamma_{Ku}, m, \dots\right), \tag{2.141}$$

which could be calculated using different approximations such as the one proposed by [Winterstein, 1988], [Wang et al., 2005] and most recently by [Braccesi et al., 2009]. This last approximation is developed using simulation tools and is found to give superior results when compared to the former two proposed correction factors. Therefore, the proposed correction factor of [Braccesi et al., 2009] is considered, thereby, χ_{nG} is given according to the following equation

$$\chi_{nG} = e^{\frac{m^{\frac{3}{2}}}{\pi}\left(\frac{\gamma_{Ku}-3}{5} - \frac{\gamma_{Sk}^2}{4}\right)}. \tag{2.142}$$

This formula has been optimised using numerical simulations for material exponent $m \in [3, 10]$. It shows the existence of a curve, called by the authors as the "*Gaussian damage curve*" formed by kurtosis and skewness couples supplying a corrective coefficient close to unity. However, this method ignores the stress mean value, also it ignores the dependency of the correction factor on the stress RMS value (see eq. 2.141).

Based on this correction factor, it is possible to develop the following steps in estimating the fatigue damage of the non-Gaussian process according to flowchart in fig. 2.19.

The main drawback of this method is that the true distribution of amplitude probability distribution of the non-Gaussian process is still unknown. Therefore, it is not possible to get a clear idea which amplitudes have higher damage effect on the structure.

2.7.2.2 Transformed Gaussian Model Approach

As the Gaussian case is well studied and there are various approximative methods to estimate fatigue damage of Gaussian process, it makes sense to transform the non-Gaussian process into an equivalent Gaussian one. This transformation could be done mathematically with the help of non-linear transformation. It has been used in estimating waves characteristics and later further developed by [Benasciutti et al., 2006] to handle the fatigue estimation of non-Gaussian process problem. The proposed method of [Benasciutti et al., 2006] handles the problem of estimating the joint probability density function of the amplitude and mean of the random non-Gaussian process which could be used to estimate the fatigue damage.

The non-Gaussian time-series $x\left(t\right) \in X\left(t\right)$ of the non-Gaussian process $X\left(t\right)$ could be transformed into an auxiliary Gaussian one $z\left(t\right)$ using a non-linear transformation such as

$$z\left(t\right) = G^{-1}\left(x\left(t\right)\right), \tag{2.143}$$

where $G^{-1}\left(\,\cdot\,\right)$ is continuously differentiable time-independent (memory-less) function with positive derivative (strictly monotonic). This auxiliary loading $z\left(t\right)$ enables estimating the rainflow amplitude cumulative distribution function (CDF) $P_a^G\left(z\right)$ using an appropriate Gaussian method. The amplitude CDF $P_a^G\left(z\right)$ could be then transformed back to consider the non-Gaussian case using

$$P_a^{nG}\left(x\right) = P_a^G\left(G^{-1}\left(x\right)\right) = P_a^G\left(z\right), \tag{2.144}$$

with the amplitude cumulative distribution is simply shifted according to the transformation $G^{-1}\left(\,\cdot\,\right)$. From this last equation, the amplitude PDF $p_a^{nG}\left(x\right)$ of the rainflow cycles could be obtained with simple differentiation and the linear damage rule could be used in the next step to estimate the fatigue damage. The work steps of this approach are illustrated in fig. 2.13.

Different transformation functions $G^{-1}\left(\,\cdot\,\right)$ that transform the non-Gaussian processes into a Gaussian one are proposed in literature such as [Rychlik et al., 1997] transformation which is a non-parametric method based on the crossing intensity ν_0, [Winterstein, 1988; Winterstein et al., 1995] transformation is basically a monotonic cubic Hermite polynomial that uses higher

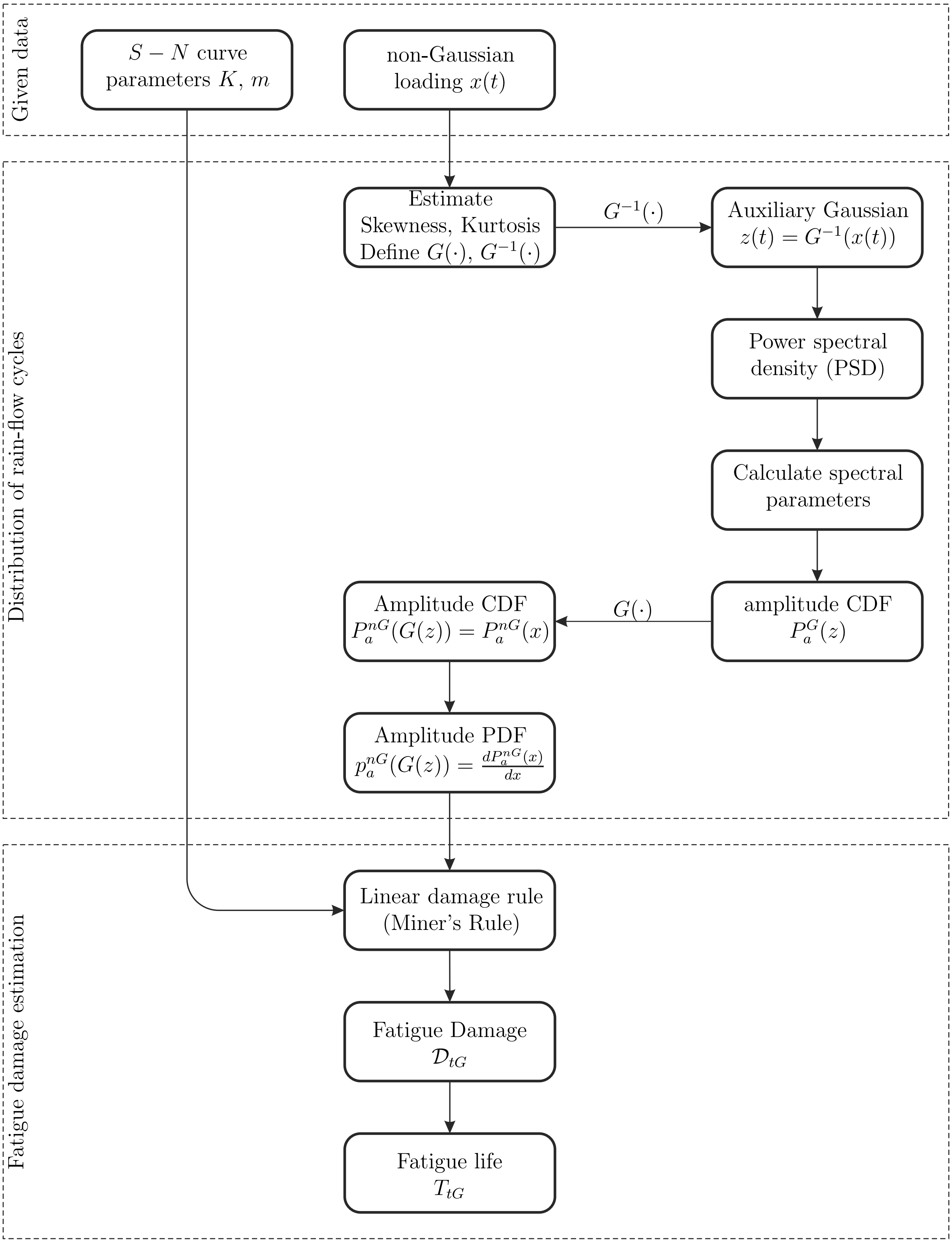

Figure 2.13 Work steps of non-Gaussian fatigue damage estimation using transformed Gaussian model method

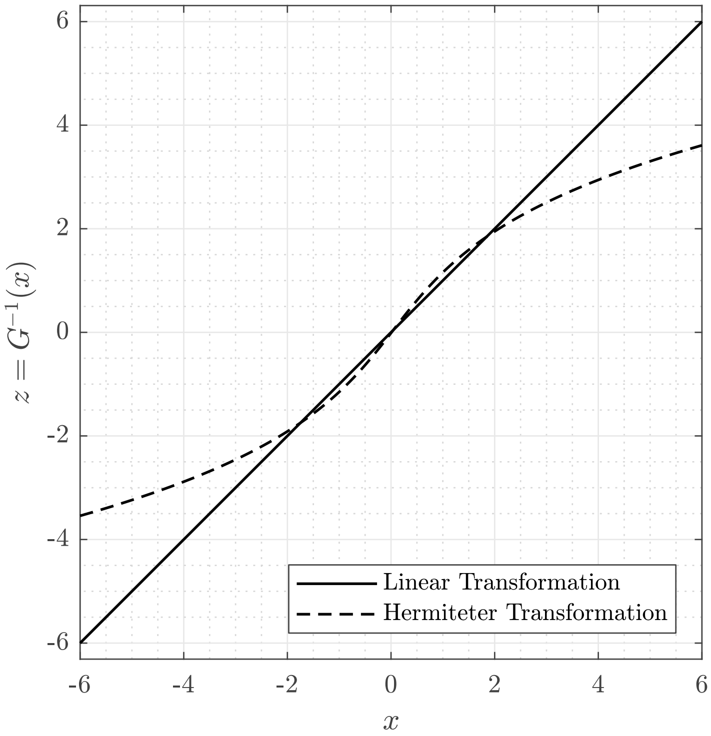

Figure 2.14 Hermiteter and linear transformation functions of the non-Gaussian process.

moments of $x\,(t)$ to compute $G^{-1}\,(\;\cdot\;)$, [Ochi et al., 1994] transformation that employs a monotonic exponential function along with higher moments of $x\,(t)$ to compute $G^{-1}\,(\;\cdot\;)$ and finally the [Sarkani et al., 1994] transformation which uses a monotonic power-law function in addition to higher moments of $x\,(t)$ to compute $G^{-1}\,(\;\cdot\;)$. Fig. 2.14 shows the linear transformation in addition to [Winterstein et al., 1995] transformation for the case of non-Gaussian random loading with skewness $\gamma_{Sk} = -0.1$ and kurtosis $\gamma_{Ku} = 6.28$ as an example. A detailed review of the different Gaussian transformation models is available in [Benasciutti, 2012].

An important advantage of the transformed Gaussian model method over the correction factor one is that the transformed Gaussian model enables the estimation of the rainflow amplitude PDF of the non-Gaussian process. Fig. 2.15 demonstrates how the transformed Gaussian model could be used to transform a non-Gaussian time-series into an equivalent almost Gaussian loading. In this example, the skewness in reduced to zero and the kurtosis is reduced from $\gamma_{Ku} = 6.28$ to a value close to 3, namely, $\gamma_{Ku} = 3.37$. The Hermiteter transformation function $G\,(\;\cdot\;)$ used in this transformation is illustrated in fig. 2.14.

2.8 Non-Stationary Loading

In reality, the wind and wave random loading on wind turbine structures is non-stationary, that means the statistical characteristics are time dependent. For example, the continuous change

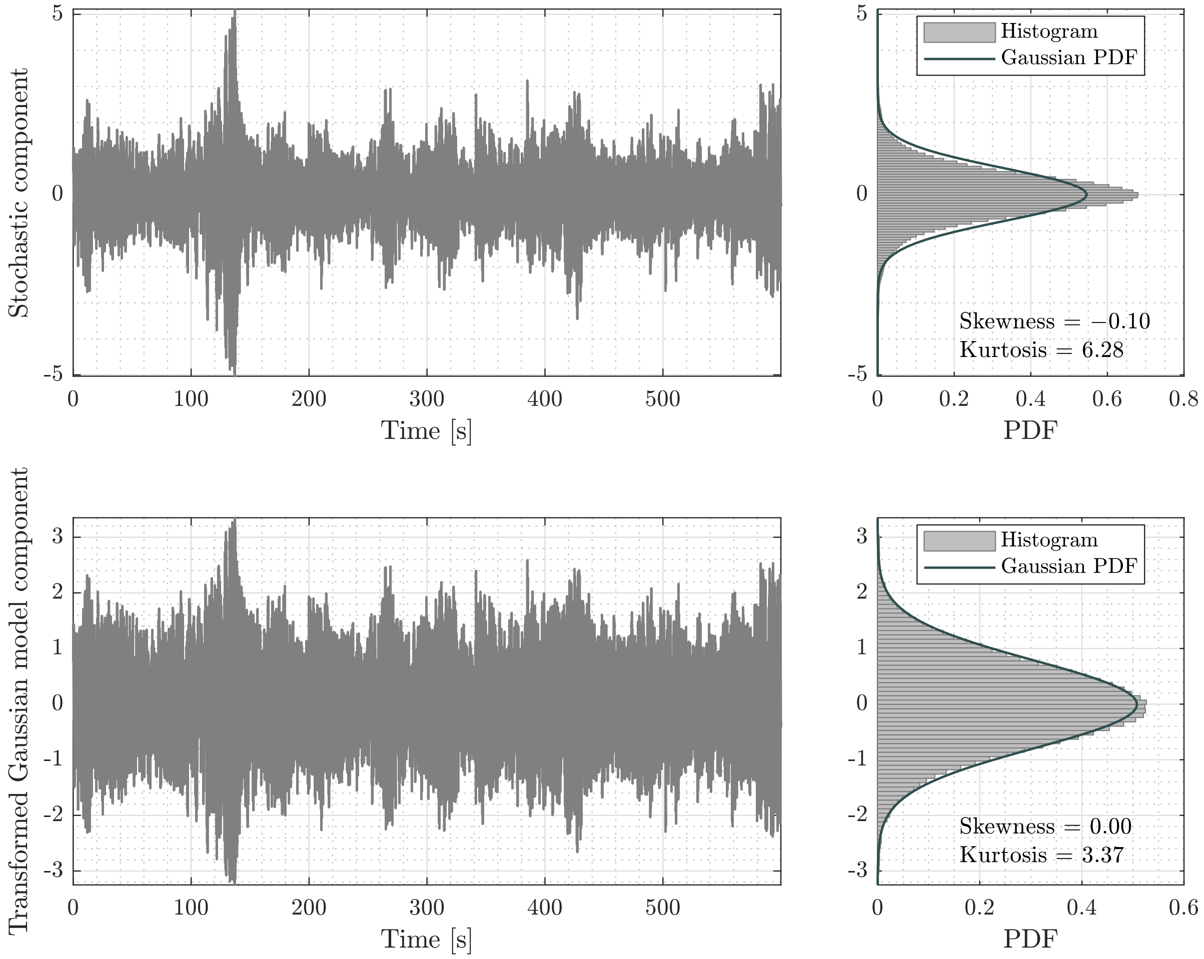

Figure 2.15 Example on using transformed Gaussian Model to transform non-Gaussian time-series to a Gaussian one.

of weather condition, the change of wind direction which will in turn change the rotor and nacelle direction accordingly, leading to the change of the loading mean value at tower base. Furthermore, all spectral methods developed for fatigue analysis assumes zero mean value. That is to say, the loading mean value is not taken into account in fatigue damage estimation in spectral methods.

As the necessary condition required by the spectral methods is hardly to meet in practice, the loading time history should be pre-processed to a suitable form for the spectral methods, then fatigue analysis could be performed as a next step. Several methods could be used to pre-process the loading signals, such as moving average trend estimation, low-pass filtering, parametric trend estimation and the seasonal and trend decomposition using loses (STL) methods [Enders, 2015]. The moving average trend estimation (MATE) is the most common filter in digital signal processing, mainly because it is the easiest digital filter to understand and to use [Smith, 1999]. The results obtained using this simple filter are similar to the results obtained using the other previously mentioned methods which are more complex. Therefore, the pre-processing step is done using the MATE as described in the sec. 2.8.1.

Furthermore, the estimation of the total fatigue damage from the decomposed time-series is not a simple linear summation of the calculated fatigue damage per each time-series component. A possible estimation of the total fatigue damage from the different components could be done using the multi-axial Projection-by-Projection (PbP) method applied to the uni-axial loading combined with PSD spectral decomposition. This approach has been used by [Benasciutti et al., 2013] to prove the well known Single-Moment method. The same approach is used also here to estimate the total fatigue damage from the decomposed time-series using the MATE. Detailed description of this method is given in sec. 2.8.2.

2.8.1 Signal Decomposition Using Moving Average Trend Estimation

In order to obtain a quasi-stationary loading, the measurements should be pre-processed to obtain a signal with quasi-constant statistical properties. For example, the changing mean value could be isolated from the measurements using trend estimation techniques that decompose the time-series $x\left(t\right)$ into two components, the first component is a deterministic trend component $x_d\left(t\right)$ that might take the form of linear or higher order polynomial trend, while the second component is a stochastic irregular one $x_s\left(t\right)$ that is not necessarily a white noise process. The two components could be used to reconstruct the original time-series using

$$x\left(t\right)=x_d\left(t\right)+x_s\left(t\right). \tag{2.145}$$

Different approaches could be used to estimate each component. One of the most common methods is to estimate the deterministic trend $x_d\left(t\right)$ using a moving average filter [Grandell, 2010], and the stochastic component could be then calculated using

$$x_s\left(t\right)=x\left(t\right)-x_d\left(t\right). \tag{2.146}$$

Moving average filter calculates the average of the measured samples over a window of M points, where M is a positive integer. If $x\left[k\right]$ is the original time-series, the deterministic component could be calculated using

$$x_d\left[k\right]=\sum_j w\left[j\right]x\left[k-j+1\right], \tag{2.147}$$

which is the convolution between the time-series and the window w of the moving average filter defined by

$$w=\begin{bmatrix}\frac{1}{2M} & \frac{1}{M} & \cdots & \frac{1}{M} & \frac{1}{2M}\end{bmatrix}^T\in\mathbb{R}^M. \tag{2.148}$$

An example of trend estimation using moving average filter is illustrated in fig. 2.16. The time-series is a $10\,min$ measurement of bending load of a small wind turbine tower (normalised by its standard deviation) where wind speed changes its mean value in addition to the direction. The variation of wind mean value and its direction change the mean tower bending stress value. A moving average filter with window length of $12\,s$ is used to estimate the time dependent trend component; and the stochastic component is then calculated. The original time-series has a constant mean value of $\bar{x} = 0.21$ which is equal to the mean value of the deterministic component $\bar{x}_d$. However, the resulting stochastic component enjoys zero mean value $\bar{x}_s = 0$ and the corresponding histogram is symmetric when compared to that of the original time-series.

By taking a closer look at the corresponding power spectral density of the original time-series, the estimated trend and the stochastic components, it is clear that the PSD of the original loading is decomposed into two spectra, the first component is related to the estimated trend and has high amplitude at very low frequencies; while the second spectrum is related to the stochastic component with zero amplitude zero frequency.

Fig. 2.16 also shows the amplitude-mean histogram obtained from the rainflow counting algorithm for the original loading time-series, the estimated trend and the stochastic components. The amplitude-mean histogram of the original time-series shows many cycles with small amplitude with positive mean. By de-trending the signal, the amplitude-mean histogram is decomposed into two histograms. The first one is related to the estimated trend component and contains mostly cycles with small amplitude in addition to a fewer cycles with large amplitudes; and the second histogram is related to the stochastic component which is symmetric about the zero-mean value and contains most of the cycles of the original time-series.

The window of the moving average filter plays an important rule in the spectral decomposition and in the extraction of the trend and the stochastic components. If the window is too large, the estimated trend tends to be linear, and if the window is too short, the estimated trend tends to follow the original time-series. The optimal MATE window is the one that will isolate the change of mean stress value related to the change of mean wind value and direction.

The process of estimating the trend using the moving average filter then calculating the stochastic component is referred to later in this work as de-trending. Furthermore, the stochastic component is called the de-trended or stochastic time-series.

The resulting stochastic component is not necessarily stationary or even quasi-stationary. This is clear from the illustrated example in fig. 2.16 as the variance of the stochastic component between $100\,s$ and $200\,s$ is about three times higher than that between $200\,s$ and $300\,s$. Such non-stationary loadings can be often modelled as a sequence of stationary load states where the mean value and the variance level changes according to an underlying random process [Benasciutti et al., 2010]. Under the assumption of constant mean for the switching loading, [Benasciutti

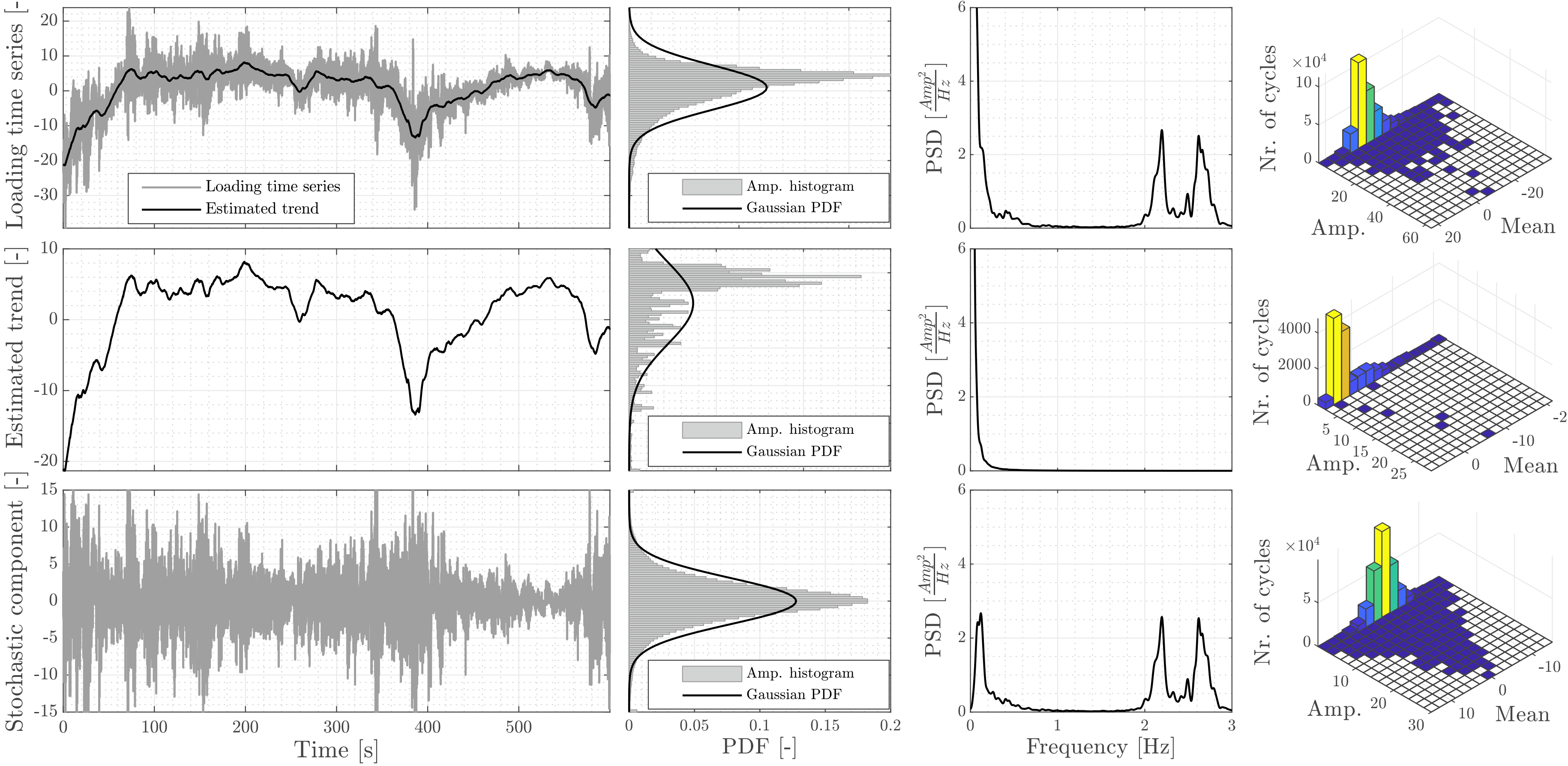

Figure 2.16 Trend and stochastic component estimated using moving average trend estimation filter with window width.

et al., 2010] has showed that a linear combination of single loading spectra would provide a fairly good estimation of the overall loading spectrum of the switching loading.

To obtain the stationary load states from the stochastic component, an automatic data segmentation algorithm based for example on identification techniques could be employed to detect the abrupt changes in the loading. However, it has been found through this work that the spectral fatigue damage results obtained from the segmented stationary load states and that from the stochastic components are similar which does not justify the extra computational effort needed for automatic segmentation. Therefore, the stochastic component resulting from de-trending process is accepted to be roughly stationary and fatigue damage estimation using spectral methods are calculated using it.

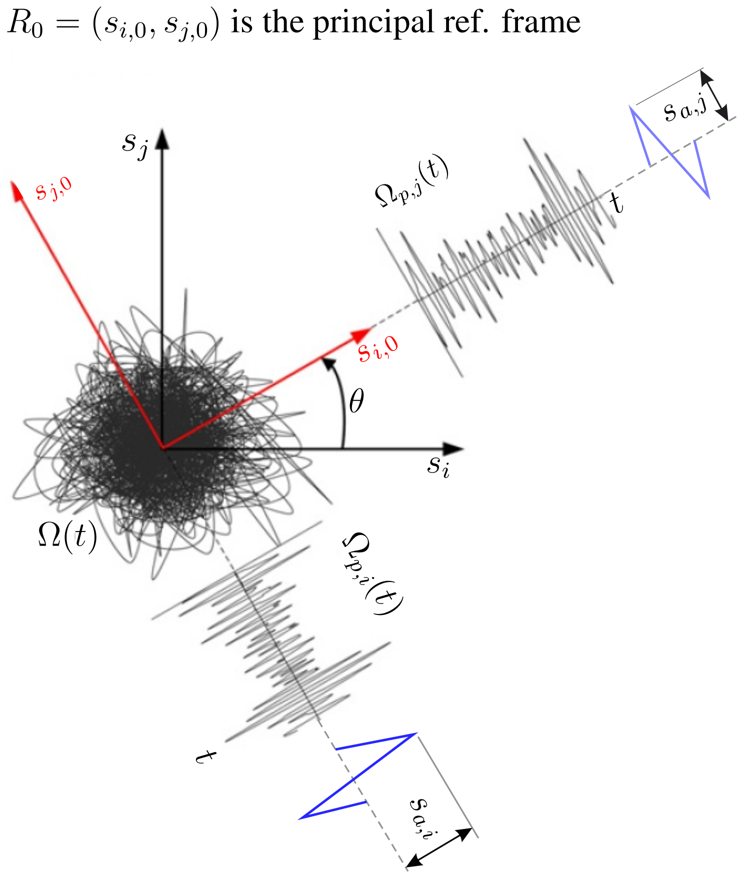

Figure 2.17 Illustration of the Projection-by-Projection method. $\Omega(t)$ is a stochastic loading path in two-dimensional deviatoric space, with uni-axial stochastic projected loadings $\Omega_{p,i}(t)$ and $\Omega_{p,j}(t)$ in the principal reference frame $R_0 = (s_{i,0}, s_{j,0})$ (Source [Benasciutti et al., 2013]).

2.8.2 Projection-by-Projection Criterion

Projection-by-Projection (PbP) method is a multi-axial criterion used for estimating fatigue damage in multi-axial loading. It is based on a non-linear summation of the damage contribution of stress components; defined as projections of the loading path in a deviatoric space along the axes of a suitable principle reference frame [Benasciutti et al., 2013; Benasciutti et al., 2019]. That is to say, if the multi-axial loading is defined by the path $\Omega(t)$ in deviatoric space, the fatigue damage intensity is estimated using

$$\mathcal{D}(\Omega) = \left(\sum_{i} (\mathcal{D}_{p,i})^{\frac{2}{m}}\right)^{\frac{m}{2}}, \tag{2.149}$$

with $\mathcal{D}_{p,i}$ is the fatigue damage calculated from the projected loading i defined by $\Omega_{p,i}(t)$ (see fig. 2.17) and m is the material fatigue exponent (more details are available in [Cristofori et al., 2014; Cristofori et al., 2011]).

The multi-axial PbP criterion has been applied by [Benasciutti et al., 2013] to the uni-axial loading case where the PSD is decomposed into a sum of infinitesimal contributions each with a narrow-band width. Using this PSD decomposition, [Benasciutti et al., 2013] have given the theoretical proof of the well know Single-Moment fatigue damage formula.

Now, considering the uni-axial stochastic loading $x(t)$ with its one sided power spectral density $G_x(\omega)$. De-trending the stochastic loading results into a deterministic component $x_d(t)$ with its PSD $G_{x_d}(\omega)$ and the stochastic component $x_s(t)$ with its PSD $G_{x_s}(\omega)$. By assuming that the deterministic and stochastic components are not correlated, which means that the spectra $G_{x_d}(\omega)$ and $G_{x_s}(\omega)$ are completely non-overlapping, it is possible then to write

$$G(\omega) = G_{x_d}(\omega) + G_{x_s}(\omega) = \operatorname{tr}\left(\begin{bmatrix} G_{x_d}(\omega) & 0 \\ 0 & G_{x_s}(\omega) \end{bmatrix}\right), \tag{2.150}$$

where $\operatorname{tr}(\,\cdot\,)$ indicates the trace operator. Furthermore, it is possible at this point to interpret the two components $x_d(t)$ and $x_s(t)$ as a fictitious multi-axial loading which could be represented using the vector $\underline{x}(t) = \begin{bmatrix} x_d(t) & x_s(t) \end{bmatrix}^T$ that is characterised in frequency domain by the PSD matrix

$$\underline{\underline{G}}_x(\omega) = \begin{bmatrix} G_{x_d}(\omega) & 0 \\ 0 & G_{x_s}(\omega) \end{bmatrix}. \tag{2.151}$$

The matrix $\underline{\underline{G}}_x(\omega)$ is a diagonal one with diagonal elements representing the spectra of the corresponding loading component and the off diagonal terms are the cross-spectra, which are set to zero due to the assumption of uncorrelated loading components.

Based on this new formulation of the problem, the fatigue damage estimation of the uni-axial stochastic process $x(t)$ is similar to the fatigue damage estimation of the multi-axial stochastic process $\underline{x}(t)$. By using the PbP method for multi-axial fatigue damage estimation (eq 2.149), it is possible to conclude that the fatigue damage of the uni-axial stochastic process $x(t)$ defined by $\mathcal{D}$ is a non-linear summation of the fatigue damage of the deterministic component $x_d(t)$ defined as $\mathcal{D}_d$ and the fatigue damage intensity of the stochastic component $x_s(t)$ defined by $\mathcal{D}_s$. This non-linear summation is given as

$$\mathcal{D} = \left[\mathcal{D}_d^{\frac{2}{m}} + \mathcal{D}_s^{\frac{2}{m}}\right]^{\frac{m}{2}} . \tag{2.152}$$

The fatigue damage of each component could be calculated using the appropriate method. While spectral methods could be used for fatigue analysis of the stochastic component, time-domain cycle counting of the deterministic component seems to be the reasonable option.

The main assumption used in developing this last equation is that the deterministic and stochastic components are not correlated. Or in other words, their PSDs are totally not overlapping. This assumption is to some limit true, as the change of wind direction will change the nacelle direction and consequently change the mean value of tower loading regardless of the turbulence intensity of the wind. On the contrary, turbulence intensity depends on the mean wind speed. Therefore, the validity of this assumption should be checked. Another point worth to mention is that the deterministic component is also non-stationary, which limits the use of the spectral methods and the only reasonable estimation is obtained using time-domain estimation of fatigue damage.

2.9 Fatigue Damage Estimation Procedure

Fatigue damage estimation in time domain starts with the extraction of peaks and valleys of the recorded loading history. The second step is to feed these data to the rainflow counting algorithm to extract the number of cycles with similar amplitude and mean value, the result of this step is presented as the mean-range histogram. Miner's rule along with the material fatigue data extracted from the $S-N$ curve are employed to calculate the fatigue damage caused by the loading history. Furthermore, fatigue life could be also estimated from the calculated fatigue damage. These work steps are illustrated in fig. 2.19.

Fatigue damage estimation in frequency domain is not a straightforward process as in time domain. This is related to the stationary and Gaussian assumptions of the loading history used in developing the spectral fatigue damage estimation theory.

The first step in spectral fatigue damage analysis is to check the stationariness of the stochastic process. As the loading time-series is resulting from wind and wave loading on the wind turbine components, it is already proven that this process is not stationary. Therefore, the first step

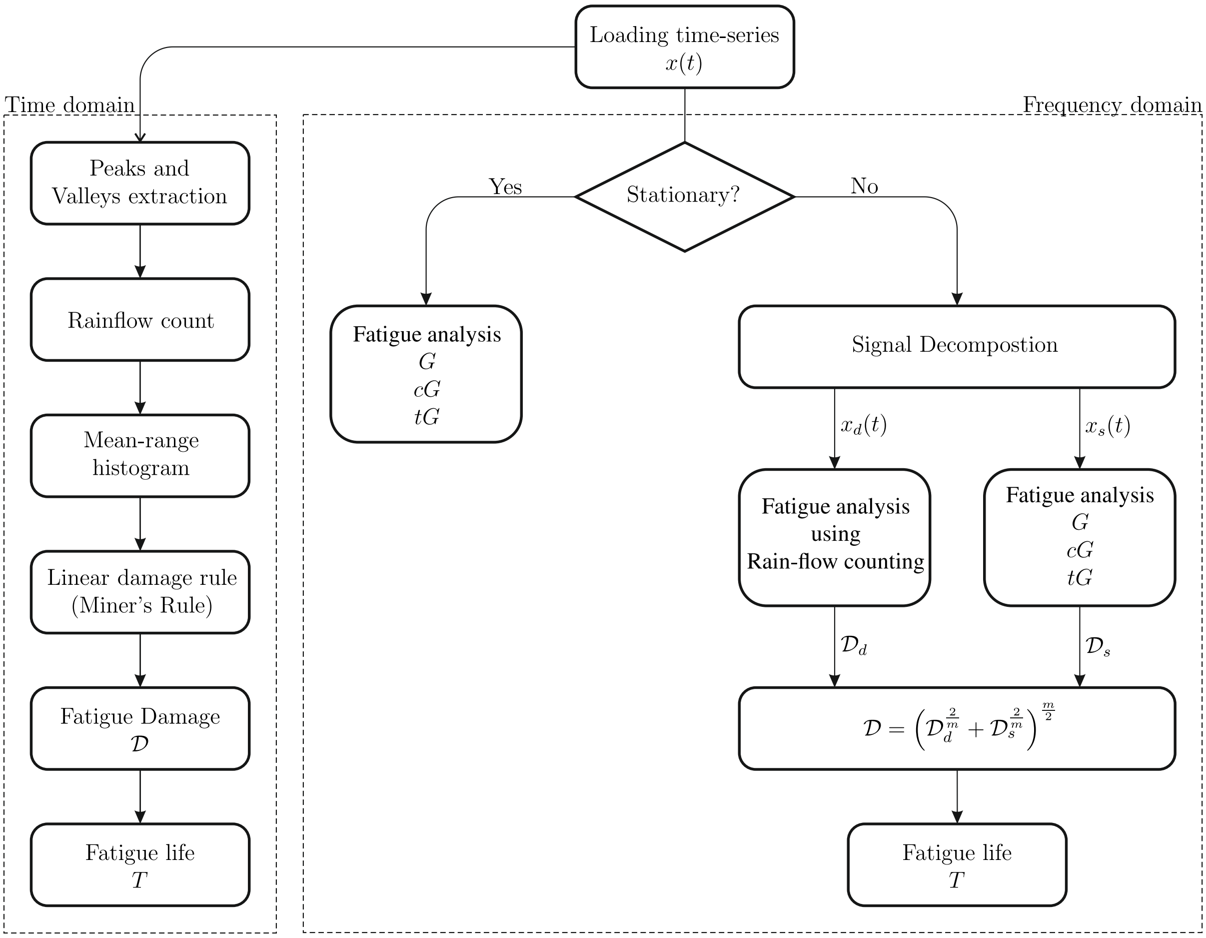

Figure 2.18 General work steps in fatigue damage estimation in time and frequency domains. G, cG and tG are the Gaussian, the corrected Gaussian and the transformed Gaussian fatigue damage estimation procedures, respectively. These procedures are illustrated in fig. 2.19.

is to decompose the process into its deterministic and stochastic components as explained in sec. 2.8.1. Then to run fatigue damage analysis using time domain method for the deterministic component and the frequency domain methods for the stochastic component as illustrated in in fig. 2.19 and explained later in this section. Finally, the total fatigue damage is calculated using the Projection-by-Projection formula as given per eq. 2.152. The proposed approach used to estimate fatigue damage for the non-stationary loading by signal decomposition and later by employing the Projection-by-Projection formula is referred-to later in this thesis as the "De-trending&PbP" approach.

Three different spectral fatigue analysis procedures are developed. The first one is called the Gaussian fatigue damage estimation procedure (index G) and it applies if the loading time-series is of Gaussian or close to Gaussian nature, namely with skewness close to zero ($\gamma_{Sk} = 0$) and kurtosis close to three ($\gamma_{Ku} = 3$). In this procedure, fatigue analysis goes through the following steps: first, the power spectral density is estimated and the various spectral parameters are then calculated and used to estimate the amplitude probability distribution function $p_a(s)$. Following to that, the linear damage accumulation rule in addition to material fatigue properties are employed to calculate the fatigue damage caused by the loading time history, and finally, fatigue life time could be calculated.

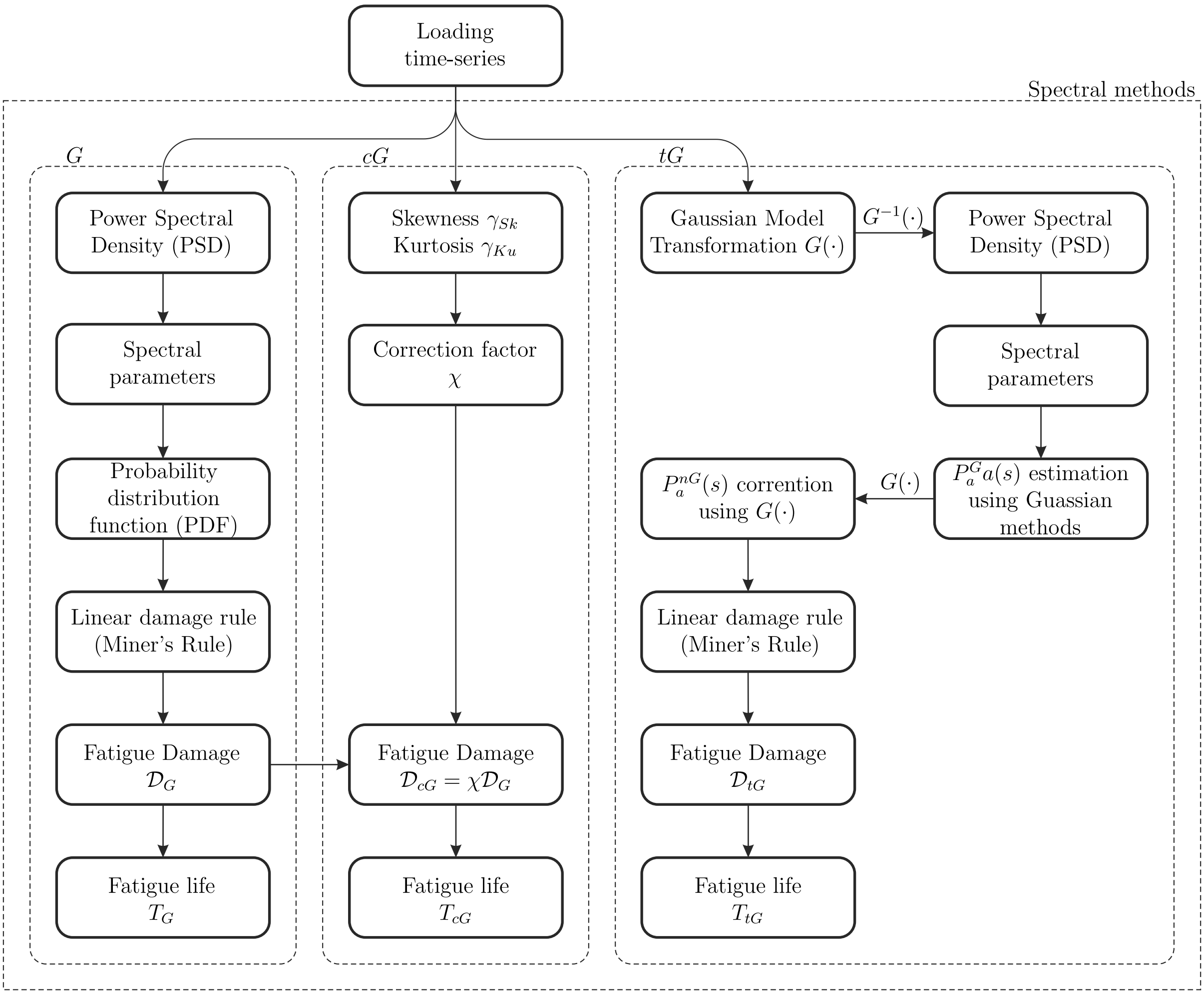

Figure 2.19 General work steps in fatigue damage estimation using spectral methods

The second fatigue analysis procedure takes the non-Gaussianity of the loading time-series into account by correcting the results of the Gaussian procedure. Therefore, this procedure is called the corrected Gaussian fatigue damage analysis procedure (cG). The main point here is in building the correction factor χ based on the skewness and the kurtosis of the time-series, then using it to correct the result obtained by the Gaussian procedure.

The third procedure is called the transformed Gaussian model fatigue damage analysis (tG). The first step in this procedure is the use of the skewness and the kurtosis of the non-Gaussian loading to build the transformation function $G(\,\cdot\,)$ and its inverse $G^{-1}(\,\cdot\,)$ as explained in sec. 2.7.2.2. The transformation function $G^{-1}(\,\cdot\,)$ is then used to transform the stochastic loading into an equivalent time-series that has amplitude distribution much closer to being

Gaussian. After that, the power spectral density of the equivalent time-series is calculated and the spectral parameters are estimated and used to calculate the amplitude cumulative distribution function $P_a^G(s)$ using the Gaussian methods. Next, the transformation function $G(\,\cdot\,)$ is used to transfer back the amplitudes to take the non-Gaussianity into account. This will produce a new amplitude cumulative distribution function $P_a^{nG}(s)$ of the non-Gaussian loading. Numerical derivation of $P_a^{nG}(s)$ is used then to derive the amplitude probability density function $p_a^{nG}(s)$. This in turn along with the material fatigue properties and Miner's rule enable the calculation of the fatigue damage, and consequently, the fatigue life.

It is worth to mention at this point that the main assumption in fatigue analysis of the non-stationary loading is the zero cross correlation between the decomposed stochastic and deterministic components. In addition to that the resulting components are assumed to be stationary if spectral methods are used in post-processing. These conditions should be verified as first step in order to be able to do fatigue analysis of such non-stationary stochastic loading.

The benefits of the proposed fatigue damage analysis strategy could be clarified through the following use-cases. In a wind turbine simulation environment, the design load cases assume constant direction of wind and wave. Furthermore, a pre-defined wind and wave loading with constant mean reference value are considered, thus the deterministic component could be seen as constant mean and an equivalent stress loading in combination with the appropriate $S-N$ curve could be used along with the appropriate spectral method. In this case, fatigue analysis based on the spectral distribution of the wind and/or wave in addition to the frequency response function obtained from a finite element model of the system could be used to estimate the loading spectrum and a good estimation of the fatigue damage could be obtained quickly. Thereby, the proposed strategy helps saving time and computational effort needed for the simulation.

In the case of fatigue analysis of operating wind turbines, the proposed strategy could be used as part of a structural health monitoring system in one of the following scenarios. For online fatigue damage monitoring by observing the fatigue damage rate of the stochastic component against a reference value such as the standard deviation of the measured wind speed (see sec. 4.4). This scenario requires loading measurement at the hot spots of the turbine structure and is based on the assumption that the only reason for the change in the system response to the same wind loading is a structural fatigue damage.

The second scenario focusses on the development of an intelligent fatigue sensor where the data are partially processed online at the sensor level. This scenario aims to reduce the amount of data needed to be collected by the SHM system and the required high sampling rate and storage demand. The idea is based on collecting strain measurement over short periods of time T at sensor level. A signal decomposition could be done online. Due to the slow change characteristics of the deterministic signal it could be down-sampled, thereby, reducing the traffic load at the sensor network. Furthermore, the spectral fatigue analysis of the stochastic signal could be achieved at the sensor level. This requires the calculation of the PSD of the signal over the period T, then calculating the required spectral moments. The estimated fatigue damage is sent at the end over the sensor network for further post-processing by the SHM system. This scenario requires a limited memory and computational capabilities at the sensor level which is possible to have at an acceptable price using a standard digital signal processor (DSP).

2.10 SHM Using Comparative Sensor Data Approach

A new structural health monitoring (SHM) approach is proposed. This novel approach is based on monitoring the linear correlation between the strain or stress sensor measurements. The theoretical concept and an illustrative example are presented in the following sections.

2.10.1 Theoretical Concept

Considering the structure of $n-$degrees of freedoms (DOF) that is subject to the time-dependent external force $F_k(t)$ applied at the $k-$DOF as shown in fig. 2.20. Also considering the strain measurements $\varepsilon_i(t)$, and $\varepsilon_j(t)$ at the $i-$, and $j-$DOFs, respectively. It is possible to derive the linear transfer function between the applied force and the measured strain such as

$$H_{ik}(s) \quad = \quad \frac{\varepsilon_i(s)}{F_k(s)}, \tag{2.153}$$

where $F_k(s)$ and $\varepsilon_i(s)$ are the Laplace transformation of the force $F_k(t)$ and the measured strain $\varepsilon_i(t)$, respectively; while s is the Laplace complex variable. The transfer function $H_{ik}(s)$ can be written in the following from

$$H_{ik}(s) = K_{ik}\tilde{H}_{ik}(s), \tag{2.154}$$

with $K_{ik} \neq 0$ represents the static gain between the two DOFs k and i, while $\tilde{H}_{ik}(s)$ is the normalized transfer function which has unity static gain (i.e. $\tilde{H}_{ik}(s = 0) = 1$). The static gain K_{ik} and the transfer function $\tilde{H}_{ik}(s)$ depend on many factors such as the location of the applied force k and the measured strain i, the geometry of the structure, material properties and not to forget the operational and boundary conditions.

Furthermore, the normalized transfer function $\tilde{H}_{ik}(s)$ can be expressed as

$$\tilde{H}_{ik}(s) = \frac{\prod_{l=1}^{n_{ik,z}} (s - z_{ik,l})}{\prod_{l=1}^{n_{ik,p}} (s - p_{ik,l})}, \tag{2.155}$$

where $z_{ik,l}$, $l \in [1, n_{ik,z}]$ are the zeros with $n_{ik,z} \geq 0$ as the number of zeros of the transfer function $\tilde{H}_{ik}(s)$, and $p_{ik,l}$, $l \in [1, n_{ik,p}]$ are the poles with $n_{ik,p} \geq 0$ as the number of poles of

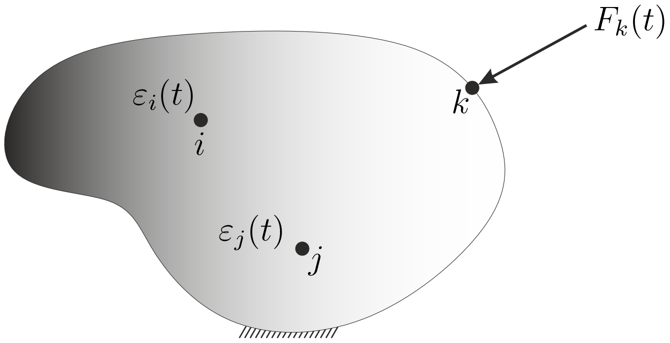

Figure 2.20 Illustration of the theoretical concept

the transfer function $\tilde{H}_{ik}(s)$. Using Eq. 2.154 it is possible to re-write eq. 2.153 such as

$$\varepsilon_i(s) = K_{ik}\tilde{H}_{ik}(s)F_k(s), \tag{2.156}$$

which gives a relation between the input force $F_k(s)$ and the measured strain $\varepsilon_i(s)$. This relation could be further simplified to have only

$$\varepsilon_i(s) \approx K_{ik}F_k(s), \tag{2.157}$$

with this simplification is valid only under the following condition

$$|s| \ll \min\left(|z_{ik,l}|, |p_{ik,m}|\right), \; l \in [1, n_{ikz}], \; m \in [1, n_{ik,p}], \tag{2.158}$$

where $|\cdot|$ is the absolute value or the complex magnitude. The simplified eq. 2.157 can be also written in time domain as

$$\varepsilon_i(t) \approx K_{ik}F_k(t). \tag{2.159}$$

The condition presented in eq. 2.158 implies that the frequency of the applied force is considerably lower than the lowest frequency that correspond to a zero or a pole of the normalized transfer function. If this condition is satisfied, the applied force will be marginally affected by the system dynamics and the measured strain can be derived directly from the applied force using the static gain K_{ik}. This condition is always valid in the case of static loading and can be extended to the case of quasi-static loading when the maximum frequency of the applied force satisfies the condition in eq. 2.158.

The strain at the $j-$DOF can be also derived from the applied force $F_k(s)$ according to

$$\varepsilon_j(s) = K_{jk}\tilde{H}_{jk}(s)F_k(s), \tag{2.160}$$

and $K_{jk} \neq 0$ represents the static gain between the two DOFs k and j, while $\tilde{H}_{jk}(s)$ is the normalized transfer function which has unity static gain (i.e. $\tilde{H}_{jk}(s = 0) = 1$). This last equation can be further simplified to

$$\varepsilon_j(s) \approx K_{jk}F_k(s), \tag{2.161}$$

which is valid if the following condition is satisfied

$$|s| \ll \min\left(|z_{jk,l}|, |p_{jk,m}|\right), \ l \in [1, n_{jk,z}],\ m \in [1, n_{jk,p}], \tag{2.162}$$

and $z_{jk,l}$, $l \in [1, n_{jk,z}]$ are the zeros with $n_{jk,z} \geq 0$ as the number of zeros of the transfer function $\tilde{H}_{jk}(s)$, and $p_{jk,l}$, $l \in [1, n_{jk,p}]$ are the poles with $n_{jk,p} \geq 0$ as the number of poles of the transfer function $\tilde{H}_{jk}(s)$. Finally, Eq. 2.161 can be also written in time-domain as

$$\varepsilon_j(t) \approx K_{jk} F_k(t). \tag{2.163}$$

Furthermore, [Ewins, 2001] defines the transmissibility function $T_{ij,k}(s)$ between the $i-$, and the $j-$DOFs as the ratio between the responses, this gives

$$T_{ij,k}(s) = \frac{\varepsilon_i(s)}{\varepsilon_j(s)} = \frac{K_{ik}}{K_{jk}} \frac{\tilde{H}_{ik}(s)}{\tilde{H}_{jk}(s)}. \tag{2.164}$$

The transmissibility function $T_{ij,k}(s)$ depends on the degrees of freedom i and j, in addition to the excitation location k. The dependency of the transmissibility function on frequency can be removed if the conditions presented in eq. 2.158 and eq. 2.162 are satisfied, this results into

$$T_{ij,k} \approx \frac{K_{ik}}{K_{jk}}, \tag{2.165}$$

which allows to derive the following equation

$$\varepsilon_i(t) \approx T_{ij,k} \varepsilon_j(t) \tag{2.166}$$

that gives a linear relation between the strain at the degrees of freedom i and j.

The linear relation in time domain as presented in eq. 2.159, eq. 2.163 or eq. 2.166 allows to derive the following concept. If the linear relation changes over time, or is lost, this is an indication of either a change in the operating or boundary conditions, a failure in the structure, or finally, a malfunction or a defect sensor. The change of operating conditions can be easily detected using data from other sensors. However, the detection of the change of boundary conditions, structural failure or defect sensor is the first step in structural health monitoring.

Monitoring the linear relation as in eq. 2.159, eq. 2.163 or eq. 2.166 can be done by periodic estimation of the sensors relation status over a pre-defined time duration T. This status could be the slop of the estimated linear regression, or the cross-correlation coefficient of sensors signals. In both methods, the collected sensor measurements per each data-block are compressed into a single scalar where it's stability over time could be simply monitored.

Another possibility is to include the estimated fatigue damage index in the formulation. This could be done in two different forms, the first one is to monitor the linear relation of the estimated fatigue damage index from the DOFs i and j. The second possibility is to monitor the relation between the estimated fatigue damage index at the $i-$th DOF and the standard deviation of the applied force. These last two concepts are illustrated in the following paragraphs.

Monitoring the linear relation between the estimated fatigue damage indices

In order to introduce the fatigue damage index into the formulation, eq. 2.166 is multiplied by the Young's Modulus of the material E to obtain the stress $\sigma_i(t)$ and $\sigma_j(t)$ at the corresponding DOFs, with the relation between the stresses as

$$\sigma_i(t) \approx T_{ij,k}\sigma_j(t). \tag{2.167}$$

The relation between the fatigue damage $\mathcal{D}_i(T)$ and $\mathcal{D}_j(T)$ estimated at the corresponding DOF during the loading time duration T is developed using eq. 2.78 to the form

$$\mathcal{D}_i(T) \approx (T_{ij,k})^m \, \mathcal{D}_j(T), \tag{2.168}$$

with m being the material fatigue exponent. This final equation gives also a direct linear relation between the fatigue damage estimated during the loading time T. Monitoring the stability of this linear relation over time allows, among others, the detection of structural failure.

Monitoring the relation between the fatigue damage index and the standard deviation of the applied force

The fatigue damage index formula of the narrow-band process is given as (See eq. 2.87)

$$\mathcal{D}_{NB} = T\frac{\nu_0}{K}\left(\sqrt{2\lambda_0}\right)^m \Gamma\left(1+\frac{m}{2}\right). \tag{2.169}$$

Knowing that the standard deviation of the stress is given by $\sigma_s = \sqrt{\lambda_0}$, and the zero up-crossing rate is given by $\nu_0 = \frac{1}{2\pi}\frac{\sigma_{\dot{x}}}{\sigma_x} = \frac{1}{2\pi}\sqrt{\frac{\lambda_2}{\lambda_0}}$, by substitution in eq. 2.169, the fatigue damage index could be expressed as

$$\mathcal{D}_{NB} = T\frac{2^{\frac{m}{2}}}{2\pi}\Gamma\left(1+\frac{m}{2}\right)K^{-1}\sqrt{\lambda_2}\sigma_s^{m-1}. \tag{2.170}$$

Furthermore, by using the relation between the standard deviation of the stress and strain in the uni-axial loading case

$$\sigma_s = E\sigma_\varepsilon, \tag{2.171}$$

it is possible to develop eq. 2.159 to get

$$\sigma_{\varepsilon_i} \approx K_{ik}\sigma_{F_k}. \tag{2.172}$$

By substitution of eq. 2.171 and eq. 2.172 in eq. 2.170, it is possible to obtain

$$\mathcal{D}_{NB} = T\frac{2^{\frac{m}{2}}}{2\pi}\Gamma(1+\frac{m}{2})K^{-1}E^{m-1}K_{ik}^{m-1}\sqrt{\lambda_2}\sigma_{F_k}^{m-1}. \tag{2.173}$$

This last formula gives a non-linear relation between the fatigue damage index of the narrow-band loading and the statistical properties of the loading force, namely, the standard deviation of the force and the standard deviation of the stress/force derivative. This non-linear relation could be simplified to a linear form by taking the logarithm of both sides to obtain

$$\log\left(\mathcal{D}_{NB}\right) = \log\left(T\frac{2^{\frac{m}{2}}}{2\pi}\Gamma(1+\frac{m}{2})K^{-1}E^{m-1}K_{ik}^{m-1}\right) + \log\left(\sqrt{\lambda_2}\right) + (m-1)\log\left(\sigma_{F_k}\right). \quad (2.174)$$

The fatigue damage index $\mathcal{D}_{NB}$ depends on two different sets of parameters. The first set of parameters is material/structural specific. This includes the fatigue exponent m, fatigue constant K, Young's modulus E and the static gain K_{ik}. While the second set of parameters is related to the loading/stress nature, namely, the standard deviation of the loading force σ_{F_k} and the standard deviation of the first derivative of the stress $\sigma_{\dot{s}} = \sqrt{\lambda_2}$.

This last formula could be also extended to the estimated fatigue damage index of the wide-band process using any of the methods of the first category (see tab. 2.2). These methods estimate the fatigue damage index of the wide-band process from that of the narrow-band process using a correction factor χ. This allows to derive the following formula

$$\mathcal{D} = \chi T\frac{2^{\frac{m}{2}}}{2\pi}\Gamma(1+\frac{m}{2})K^{-1}E^{m-1}K_{ik}^{m-1}\sqrt{\lambda_2}\sigma_{F_k}^{m-1}. \quad (2.175)$$

Finally, by using the logarithm of both sides, it is possible to obtain

$$\log\left(\mathcal{D}\right) = \log\left(T\frac{2^{\frac{m}{2}}}{2\pi}\Gamma(1+\frac{m}{2})K^{-1}E^{m-1}K_{ik}^{m-1}\right) + \log\left(\chi\sqrt{\lambda_2}\right) + (m-1)\log\left(\sigma_{F_k}\right). \quad (2.176)$$

The only difference between eq. 2.174 and eq. 2.176 is the inclusion of the correction factor χ which depends on the fatigue exponent m and possibly on the $i-$spectral moment. However, the linear relation on the logarithmic scale between the fatigue damage index and the standard deviation of the applied force is still valid.

In this formulation, if the structural/material properties do not change over time, we have a linear relation between the fatigue damage index and the statistical properties of the loading. A change of the structural/material properties will result into shifting this linear relation into a parallel direction. This change of structural/material properties might result for example from a change of boundary condition or a structural failure.

2.10.2 Illustrative Example

Considering the cantilevered beam shown in fig. 2.21. This beam is assumed to have length L, width b and height h. The coordinate system (x, y, z) is attached to the beam as illustrated in the figure. The beam is assumed to be anchored to the $y-z$ plane at $x = 0$. Moreover, the force F is applied against the $y-$direction at $x = L$. The bending moment of the cantilevered beam could be given by

$$M_z(x) = F(L-x), \quad (2.177)$$

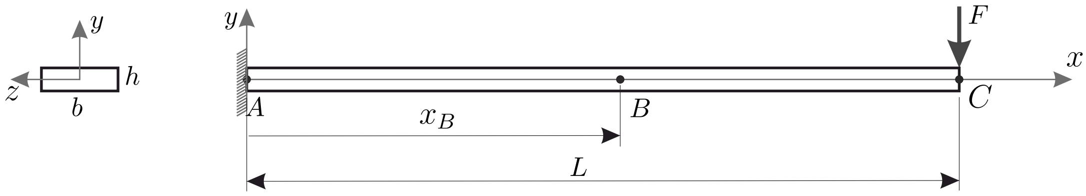

Figure 2.21 Illustrative example using cantilevered beam

and the bending stress s_b at the upper surface of the beam assuming a centroidal distance of $\frac{h}{2}$ is given by

$$s_b(x) = \frac{h}{2I_z} M_z(x), \tag{2.178}$$

with

$$I_z = \frac{h^3 b}{12}. \tag{2.179}$$

By substituting eq. 2.179 and eq. 2.177 into eq. 2.178 it is possible to obtain

$$s_b(x) = \frac{L-x}{6h^2 b} F, \tag{2.180}$$

and this final formula indicates a direct dependency of the stress on the applied force ($s_b \sim F$), with the static gain $K_{static} = \frac{L-x}{6h^2 b}$ as defined in eq. 2.159 and eq. 2.163. This formula also shows an inverse relationship between the bending stress and the beam cross-section dimensions ($s_b \sim \frac{1}{b}$, $s_b \sim \frac{1}{h^2}$). Both relations are valid at any defined location along the beam.

If the applied force $F(t)$ is time dependent, fatigue damage is expected to take place at the location with the highest stress, namely at $x = 0$. And in this beam configuration, fatigue failure is expected to happen along the $z-$direction.

Recalling that fatigue failure goes through three main stages. The first stage is the initiation which is the most complex stage of fatigue failure. The prominent factor about fatigue fracture initiation is the repetitive shear stress that causes the irreversible changes in the metal. Initiation site is very small, never extending for more than two to five grains around the origin. The second stage in fatigue fracture is the propagation. In this stage, the microcrack changes direction and grows perpendicular to the tensile stress. The third stage is the final rupture. In this stage a gradual reduction in the cross-sectional area of the part is caused by the continues propagation of the fatigue crack. This cross-section reduction weakens the part till the final complete fracture occurs. It is possible to distinguish between a ductile or a brittle fracture modes or any combination of them depending upon the metal, stress level, environment, etc.

Starting from the second stage, fatigue cracks will start to affect the effective cross-section dimensions h_{eff} and b_{eff}, where $h_{eff} \leq h$ and $b_{eff} \leq b$. Therefore, for the same loading force F, the reduction in the effective cross-section dimensions will result into an increase in the local bending stress. As long as the change in cross-section dimensions next to the anchor location does not affect the assumed boundary conditions of the cantilevered beam, eq. 2.180 will still be considered as valid. And in the case of time varying loading force $F(t)$ that satisfies the conditions in eq. 2.158 and eq. 2.162, monitoring linear relation between the measured stress at the critical beam location close to the anchor location against the loading force would allow to detect any changes in the structure. These changes might be for example related to change in boundary conditions or (fatigue) damage in the structure.

Moreover, if the bending stress is measured at two different locations. The first one is next to the critical cross-section at $x = 0$ (location A in fig. 2.21) where the stress is given by

$$s_{b,A} = \frac{L}{6h_A^2 b_A} F, \tag{2.181}$$

which is similar to eq. 2.159 with the static gain is given by $K_{AC} = \frac{L}{6h_A^2 b_A}$. The second one is far from the critical cross-section where $x = x_B$ (location B in fig. 2.21) and the stress equation is defined by

$$s_{b,B} = \frac{L - x_B}{6h_B^2 b_B} F, \tag{2.182}$$

and this equation is also equivalent to eq. 2.163 with the static gain given by $K_{BC} = \frac{L-x_B}{6h_B^2 b_B}$. From eq. 2.181 and eq. 2.182 it is possible to obtain the transmissibility $T_{AB,C}$ given in eq. 2.165 such as

$$T_{AB,C} = \frac{L}{L - x_B} \frac{h_B^2 b_B}{h_A^2 b_A}. \tag{2.183}$$

From these last three equations, it is possible to derive the following conclusion. For a given loading force $F(t)$ and assuming no change in boundary conditions, a change in the effective cross-section dimension at the critical location A will affects the the stress at this location. However, the measured stress at the location B will not be affected. If the loading force satisfies the conditions in eq. 2.158 and eq. 2.162, monitoring the linear relation between the fatigue damage estimated from both locations against each other, it is possible to detect the damage in the structure. This procedure is very helpful in case the input loading force $F(t)$ is not measurable such as the aerodynamic loading force over the turbine structure.

The fore-aft tower bending in wind turbines is mainly subject to the aerodynamic thrust force which is not measurable. However, the average thrust force over the rotor disc could be estimated using the following formula

$$F_T = \frac{1}{2} \rho A C_T v^2, \tag{2.184}$$

with ρ as the air density, A as the rotor disk area, C_T as the thrust coefficient and v as the relative wind speed. If the tower is considered as a cantilever beam fixed from the bottom and subject to the thrust force from the top (similar to fig. 2.21), the bending stress is linearly related to the applied force as in eq. 2.180. This allows to derive

$$\sigma_{F_T} = \frac{1}{2}\rho A C_T \sigma_{v^2}. \tag{2.185}$$

In order to use eq. 2.174 or eq. 2.176, the standard deviation of the square of the wind speed σ_{v^2} should be expressed in terms of the standard deviation of the wind speed σ_v. This relation could be developed by starting from eq. 2.7 with the definition of the standard deviation of the random signal x given by

$$\sigma_x = \sqrt{\mathbb{E}\left[(x-\mu)^2\right]}, \tag{2.186}$$

which could be developed to the following form

$$\sigma_x = \sqrt{\mathbb{E}\left[x^2\right] - \left(\mathbb{E}\left[x\right]\right)^2}. \tag{2.187}$$

During the time duration T, the wind speed v could be expressed as

$$v = v_0 + \delta_v, \tag{2.188}$$

with $v_0 = \mathbb{E}[v] \neq 0$ is the mean wind speed over the time duration T, while $\delta_v = v - v_0$, $\mathbb{E}[\delta_v] = 0$ represents the variation of the wind speed about the mean value. The standard deviation σ_{v^2} could be expressed using eq. 2.187 such as

$$\sigma_{v^2} = \sqrt{\mathbb{E}\left[v^4\right] - \left(\mathbb{E}\left[v^2\right]\right)^2}, \tag{2.189}$$

with the terms $\mathbb{E}\left[v^4\right]$ and $\mathbb{E}\left[v^2\right]$ are derived in the following. Starting with the term $\mathbb{E}\left[v^2\right]$ and using eq. 2.188 to get

$$\mathbb{E}\left[v^2\right] = \mathbb{E}\left[(v_0+\delta_v)^2\right], \tag{2.190}$$

which could be simplified into

$$\mathbb{E}\left[v^2\right] = v_0^2 + \mathbb{E}\left[\delta_v^2\right]. \tag{2.191}$$

On the other side, the term $\mathbb{E}\left[v^4\right]$ could be expressed as

$$\mathbb{E}\left[v^4\right] = \mathbb{E}\left[v_0^4 + 4v_0^3\delta_v + 6v_0^2\delta_v^2 + 4v_0\delta_v^3 + \delta_v^4\right], \tag{2.192}$$

and that in its turn could be simplified into

$$\mathbb{E}\left[v^4\right] = v_0^4 + 4v_0^3\,\mathbb{E}[\delta_v] + 6v_0^2\,\mathbb{E}\left[\delta_v^2\right] + 4v_0\,\mathbb{E}\left[\delta_v^3\right] + \mathbb{E}\left[\delta_v^4\right]. \tag{2.193}$$

By substituting eq. 2.193 and eq. 2.191 into eq. 2.189, it is possible to obtain

$$\sigma_{v^2} = 2v_0\sqrt{\mathbb{E}\left[\delta_v^2\right] + \frac{4v_0\,\mathbb{E}\left[\delta_v^3\right] + \mathbb{E}\left[\delta_v^4\right] - \left(\mathbb{E}\left[\delta_v^2\right]\right)^2}{4v_0^2}}, \tag{2.194}$$

which could be approximated to

$$\sigma_{v^2} \approx 2v_0\sqrt{\mathbb{E}\left[\delta_v^2\right]}, \tag{2.195}$$

if the following condition is satisfied

$$\frac{1}{4v_0^2}\left(4v_0\,\mathbb{E}\left[\delta_v^3\right] + \mathbb{E}\left[\delta_v^4\right] - \left(\mathbb{E}\left[\delta_v^2\right]\right)^2\right) \ll \mathbb{E}\left[\delta_v^2\right]. \tag{2.196}$$

Furthermore, by noticing that $\sigma_v = \sqrt{\mathbb{E}\left[\delta_v^2\right]}$, the simplified eq. 2.195 could be written as

$$\sigma_{v^2} \approx 2v_0\sigma_v. \tag{2.197}$$

This final formula allows along with eq. 2.174 or eq. 2.176 the derivation of a linear relation on the logarithmic scale between the estimated fatigue damage index and the standard deviation of the relative wind speed over the rotor disc. For example, using eq. 2.176, it is possible to obtain

$$\begin{aligned}\log\left(\mathcal{D}\right) = \log\left(T\frac{2^{\frac{m}{2}}}{2\pi}\Gamma(1+\frac{m}{2})K^{-1}E^{m-1}K_{ik}^{m-1}\right) + \log\left(\chi\sqrt{\lambda_2}\right) + \\ (m-1)\log\left(\rho A C_T v_0\right) + (m-1)\log\left(\sigma_v\right).\end{aligned} \tag{2.198}$$

The last equation is valid only if the condition presented in eq. 2.196 is satisfied. This condition could be re-written using $\mathrm{Var}\left(\delta_v\right) = \mathbb{E}\left[\delta_v^2\right]$ and $\mathrm{Var}\left(\delta_v^2\right) = \mathbb{E}\left[\delta_v^4\right] - \left(\mathbb{E}\left[\delta_v^2\right]\right)^2$ in the following form

$$\frac{1}{v_0}\mathbb{E}\left[\delta_v^3\right] + \mathrm{Var}\left(\left(\frac{\delta_v}{2v_0}\right)^2\right) \ll \mathrm{Var}\left(\delta_v\right). \tag{2.199}$$

In this condition, the mean value of δ_v is $\mathbb{E}\left[\delta_v\right] = 0$ and the variable δ_v is - to some limit - symmetrically distributed about v_0. This allows to conclude that $\mathbb{E}\left[\delta_v^3\right] \approx 0$. Moreover, considering the fact that the variations of wind speed about the mean value v_0 over the duration T is bounded, that is to say

$$|\delta_v| \le \delta_{max}, \tag{2.200}$$

and if the limit satisfy $\delta_{max} < 2v_0$, the condition

$$\mathrm{Var}\left(\left(\frac{\delta_v}{2v_0}\right)^2\right) \ll \mathrm{Var}\left(\delta_v\right) \tag{2.201}$$

would be satisfied.

Finally, most mechanical components have design features which cause stress concentration such as holes, key-ways, sharp changes of load direction, ...etc. These design features are common locations at which the fatigue process begins due to stress concentration. Therefore, it is important to monitor these locations for fatigue failure. This is done by monitoring the linear relation between the measured structural response next to the critical locations and the measured structural response at another location where structural failure is less likely to happen. Different methods can be employed in monitoring this linear relation such as estimating the linear regression between the responses periodically and monitoring the development of the estimated slope over time. Another possible method is to estimate the cross-correlation coefficient periodically and to monitoring this coefficient over time. Finally, the estimated fatigue damage rate per time duration T can be monitored over time to detect any structural changes.

2.11 Chapter Summary

The main focus of this chapter is the stochastic fatigue analysis. The chapter starts by reviewing the fundamental properties of stationary stochastic process and the random response of linear systems. Then the linear accumulation theory is explained and the required equations for fatigue damage estimation in time and frequency domains are developed. Furthermore, the different methods of fatigue damage estimation of Gaussian processes in frequency domain are presented; in addition to that, two different approaches that enable handling the non-Gaussian processes are also discussed. A new strategy is proposed for fatigue analysis of non-stationary non-Gaussian loading by signal decomposition into quasi stationary stochastic component that could be post-processed using spectral methods and a slowly changing deterministic component that could be analysed using cycle counting in time domain. The overall fatigue damage is then estimated using the projection-by-projection method. Finally, a new SHM approach is proposed in this chapter. This comparative sensor data approach is based on monitoring the linear relation between the measured strain at different pre-defined locations in the structure. As long as the linear relation is maintained, the system is considered as healthy and losing this relation indicates either a change in boundary conditions, a defect sensor, or structural failure.

Chapter 3

Modelling, Simulation and Analysis Tools

In theory, there is no difference between theory and practice. But, in practice, there is.

— Jan L. A. van de Snepscheut

Contents

3.1 Wind Turbine Modelling and Simulation Tools

The general wind turbine structure according to the IEC 64100-3 [IEC, 2009] consists of the rotor-nacelle assembly in addition to the support structure. The support structure of onshore wind turbines consists of the tower, the sub-structure and the foundation, while the support structure of offshore turbines consists of the tower, the platform and the mooring system.

In working with computer simulations, suitable simulation tools and models must be used in order to allow reasonable hi-fidelity simulation results. Many commercial and free tools dedicated to wind turbine simulation are available in the market. These tools vary in their modelling approach, model fidelity, interfacing capabilities with other tools, user customization, etc. The Offshore Code Comparison Collaboration (OC3) project [Passon et al., 2007] compared FAST [Jonkman et al., 2005], Bladed [Bossanyi et al., 2003], ADAMS and HAWC2 [Larsen et al., 2007b] design codes against each other for onshore and offshore turbines. The main conclusion is that the design codes compared well with minor differences related to the used modelling approach of each code.

FAST (Fatigue, Aerodynamics, Structures and Turbulence) is an open source aero-hydro-servo-elastic simulation code that is developed and maintained by the National Renewable Energy Laboratory (NREL) [Jonkman et al., 2005]. This design code is used in this work for two main reasons. The first reason is related to its ability to model onshore and offshore wind turbines, with a utility scale wind turbine model along with many different floating platforms available for research studies. The second reason is related to the possibility of integrating this code in MATLAB®/Simulink® which would allow easy controller design, implementation and post-processing capabilities.

3.2 FAST Design Code

FAST is a moderate complexity open source design code developed and maintained by NREL [Jonkman et al., 2005] and designed to analyse the structural dynamics of horizontal axis wind turbines. Onshore and offshore versions of FAST have been compared against other industry standard wind turbine design tools and have been found to give comparable results [Manjock, 2005; Taubert et al., 2011]. The onshore version of FAST has been certified by Germanischer Lloyed Wind Energy GmbH for the use by the industry for wind turbine certification [Buhl et al., 2006].

The implemented turbine model in FAST assumes the tower, drive-train and blades to be flexible elements [Jonkman et al., 2005; Jonkman et al., 2006]. The bending mode-shapes are used for the analysis where the tower has two fore-aft and two side-side bending modes, while each blade has two flap-wise and one edge-wise bending mode; finally, the drive-train flexibility is modelled through a linear spring and a damper for the low speed shaft. The remaining elements of the wind turbine such as the nacelle, hub, gearbox, high speed shaft and floating platform are modelled as rigid bodies. FAST allows controlling the fidelity of the model by selecting which degrees of freedom to include in the non-linear model.

A linearised representation of the non-linear wind turbine model at specific trim conditions could be also obtained using FAST. The state-space linearised turbine model is of periodic nature with the rotor azimuth angle ψ (i.e. time-varying) is given by

$$
\begin{aligned}
&\dot{\underline{x}} = \underline{\underline{A}}\,(\psi)\,\underline{x} + \underline{\underline{B}}\,(\psi)\,\underline{u} + \underline{\underline{B}}_d\,(\psi)\,\underline{u}_d,\\
&\underline{y} = \underline{\underline{C}}\,(\psi)\,\underline{x} + \underline{\underline{D}}\,(\psi)\,\underline{u} + \underline{\underline{B}}_d\,(\psi)\,\underline{u}_d.
\end{aligned}
$$

This linearised model is helpful in developing the power spectral density at given locations on the tower when the turbine is subject to well known loading spectrum. Using FAST interface to MATLAB®/Simulink®, it is possible to simulate the non-linear turbine model integrated with the turbine controller. Fig. 3.1 illustrates an example of Simulink® model where the base linear control system is implemented to control a utility-scale turbine modelled in FAST.

FAST uses a hydrodynamics module to model the floating platform dynamics. This module uses the linear/Airy wave theory to simplify the hydrodynamics problem into three separate components: hydrostatics, radiation and diffraction. Several assumptions are used to handle the hydrodynamics problem, these assumptions are: A rigid body model of the floating platform with perpendicular tower to the platform (cantilevered). Furthermore, no bending stiffness is assumed for the mooring lines and the inertia (excluding the wind turbine) and the centre of buoyancy lie on the centreline of the undeflected tower. Finally, the platform model has 6 DOFs (translations: surge, sways and heave, rotations: roll, pitch and yaw). The three rotational DOFs are assumed to have small angles and the effects of these assumptions are not considered critical for angles smaller than 20°.

3.3 Reference Wind Turbine Model

The national renewable energy laboratory (NREL) has developed a fictitious $3-$bladed $5MW$ reference wind turbine (RWT) that is suitable for research purposes [Jonkman et al., 2009]. The properties of the RWT are based on a collection of existing wind turbines of similar rating. This turbine is modelled using FAST and could be used in different onshore, offshore and floating configurations according to the implemented substructure (foundation or platform). The main

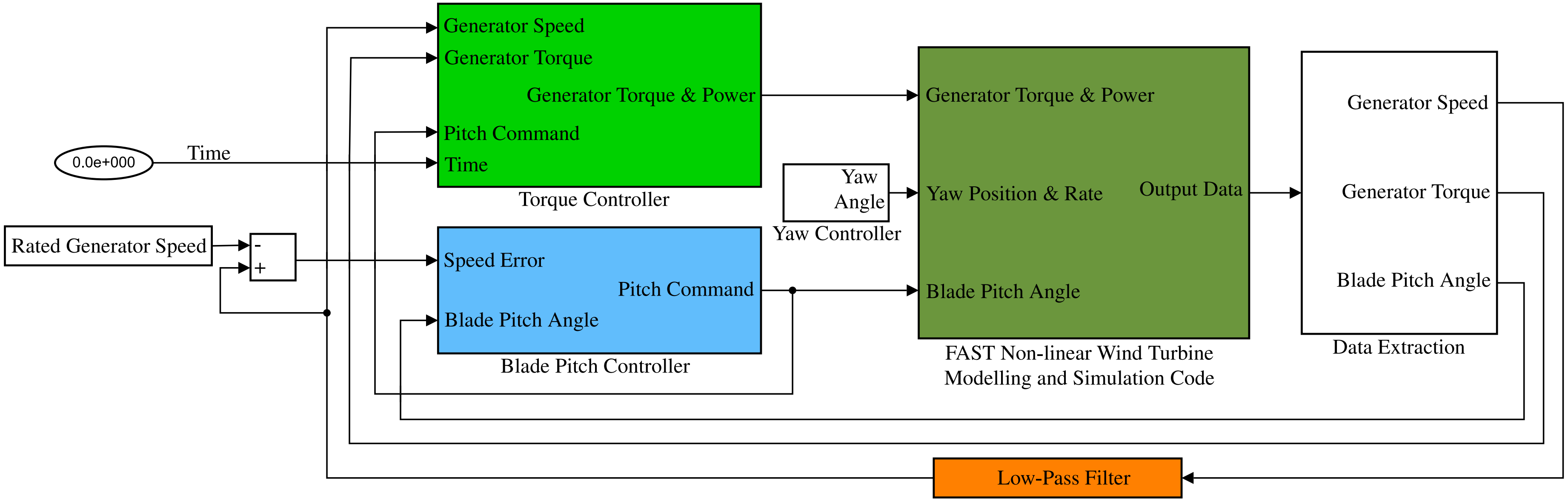

Figure 3.1 Baseline control system of utility scale wind turbine implemented in Simulink®/FAST interface

Table 3.1 NREL $5MW$ reference wind turbine properties [Jonkman et al., 2009]

Rotor orientation, blades	Upwind, 3−blades
Rated generator power	$5,296,610\,watt$
Control	Variable speed, variable pitch
Cut-in, Rated, Cut-out wind speeds	$v_{in} = 3\,\frac{m}{s}$, $v_{rated} = 11.4\,\frac{m}{s}$, $v_{out} = 25\,\frac{m}{s}$
Rotor, Hub diameter	$126\,m$, $3\,m$
Hub height	$90\,m$
Rated rotor speed, Rated generator speed	$12.1\,rpm$, $1173.7\,rpm$
Blade operation	Pitch to feather
Min/Max blade pitch angles	$-1°$, $+90°$
Maximum blade pitch rate	$\pm 8\,\frac{°}{s}$
Maximum blade pitch acceleration	$\pm 150\,\frac{°}{s^2}$
Rated generator torque	$43,093\,Nm$
Maximum generator torque	$47,402\,Nm$
Maximum generator torque rate	$\pm 15000\,\frac{Nm}{s}$

properties of the reference turbine are presented in tab. 3.1.

3.3.1 Regions of Operation

The variable-pitch variable-speed wind turbine operates typically in two different regions, namely, the full load region where wind speed is above its rated value; while the partial load region corresponds to wind speed less than its rated value (fig. 3.2). In the full load region (known also as the above-rated region), the wind has enough energy to run the turbine at its rated rotor speed. The main task of the controller in this region is to adapt the aerodynamic efficiency of the rotor by pitching the blades into or out of the wind in order to keep the rotor speed at its rated value. On the contrary, the maximum aerodynamic efficiency is maintained in the partial load region (known also as the under-rated region) where the wind speed is less than its rated value. The controller task at this region is to follow the maximum power production by changing the rotor speed and consequently the generator torque. The partial load region could also be divided into sub-regions in order to handle the transition at the cut-in wind speed where the rotor should be accelerated till it reaches the power production speed, or the transition at the rated wind speed between the partial and full load regions (fig. 3.2).

Blade pitching is activated only in the full load region, while in the partial load region the blades are kept fixed at an optimal pitch angle in order to maintain the maximum aerodynamic efficiency of the rotor.

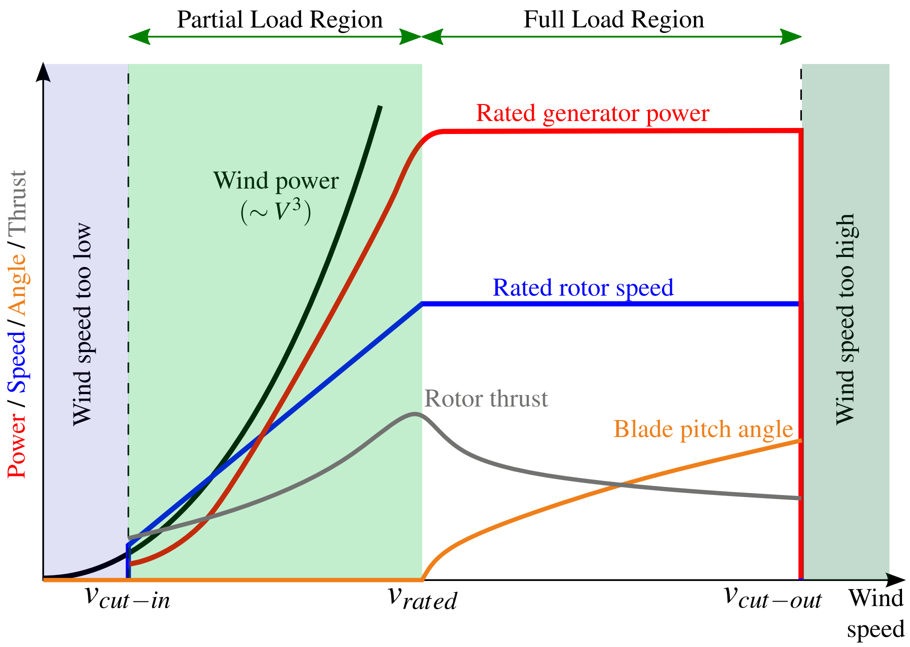

Figure 3.2 Operating regions of the reference wind turbine

3.3.2 Structural Dynamics

A modal analysis of the reference wind turbine gives a wide range of resonance frequencies of the turbine different parts at different directions. The most important frequencies are those related to the tower first and second mode in the fore-aft and side-side directions, the platform rotational degrees of freedom (roll, pitch and yaw) in addition to the drive-train first torsional mode. Rotor modes are the same for all turbine configurations, however, there effect is marginal. Therefore, the rotor is considered as a rigid body. Furthermore, the rotation of the rotor induces non-structural loading on the turbine structure, these loading has main frequencies of $1P$ and $3P$ (related to rotor speed) which corresponds to one per rotation and are three times per rotation, respectively. Tab. 3.2 illustrates the main frequencies of the reference wind turbine for the land-based turbine and the three considered floating platforms.

Due to the rotor rotation, the natural frequencies of the turbine structural changes with the change of wind speed. This is basically related to dynamic stiffness of the blades and the aerodynamic interaction (damping and stiffness) between the rotor and the wind.

3.3.3 Floating Platforms

Floating wind turbines have additional 6 degrees of freedom (DOF) that should be taken into account in wind turbine modelling. These extra DOFs are brought by the lack of rigid foundations and they exhibit larger motion envelope for longer periods. Fig. 3.3 (left) illustrates these extra DOFs.

Table 3.2 Main structural frequencies of the reference wind turbine at wind speed $14\frac{m}{s}$. Results are obtained by analysing the structural response of the reference wind turbine.

			Onshore	Barge	Spar-buoy	TLP
Element	Mode	Abbrev.	Freq. $[Hz]$	Freq. $[Hz]$	Freq. $[Hz]$	Freq. $[Hz]$
Tower	1st tower side-side	f_{T1ss}	0.32	0.35	0.38	0.73
	1st tower fore-aft	f_{T1fa}	0.33	0.54	0.38	0.72
	2nd tower side-side	f_{T2ss}	2.78	2.75	3.5	2.00
	2nd tower fore-aft	f_{T2fa}	2.32	2.43	2.59	2.32
Drive-train	Torsional mode	f_{dt}	2.22	2.22	2.22	2.22
Platform	Roll	f_{PFr}		0.09	0.02	0.22
	Pitch	f_{PFp}		0.08	0.02	0.22
	Yaw	f_{PFy}		0.02	0.12	0.10
Non-structural	$1P$ (at $12.1\,rpm$)	$1P$	0.20	0.20	0.20	0.20
	$3P$ (at $12.1\,rpm$)	$3P$	0.60	0.60	0.60	0.60

Platform motions increase significantly the turbine structural loading. The study of [Jonkman et al., 2007] demonstrates that floating wind turbines have up to six times higher structural loading when compared to land-based turbines. Platform pitch motion can significantly affect turbine loading and power regulation due to the hydro-servo coupling between this motion and the controller efforts to regulate power production. Therefore, regulating these motions is an important part of the design of floating wind turbines. In this regard, several approaches have been followed to reduce platform motion. The first approach is related to the design of the platform itself and the way it interacts with the hydrodynamic loading. This approach has led to various platforms design, three of the basic designs are simulated in this work, namely, Barge platform, Spar-Buoy platform and the TLP platform. The second approach is to modify the turbine design to include passive vibration damping methods such as tuned mass dampers. Finally, the third approach is to use an active control system that can stabilise platform motion using available or extra actuators [Chaaban et al., 2013; Chaaban et al., 2014a; Lackner, 2009].

3.3.3.1 Barge Platform

The barge platform (fig. 3.3) is a simple rectangular platform that utilises buoyancy to maintain stability. This platform does not require minimum water depth due to its shallow draft design. The main aspect considered in its design is being cost effective and easy to install. However, its shallow depth and large water plane make it very sensitive to the incident waves. The main properties of the platform are summarised in tab. 3.3.

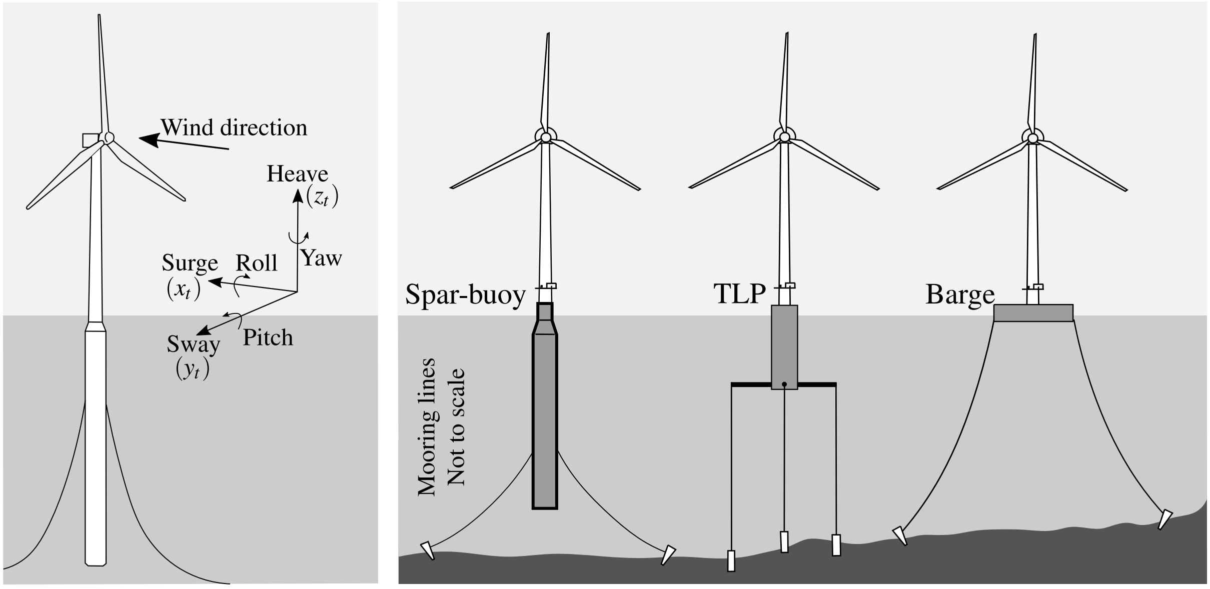

Figure 3.3 Degrees of freedom of floating platform (left) and floating platform concepts (right)

3.3.3.2 Spar-Buoy Platform

The Spar-buoy platform concept achieves hydrostatic stability by means of deep-draft ballast in addition to catenary mooring lines for station-keeping, see fig. 3.3. The interaction with surface waves of the spar-buoy platform concept is minimum as it has its hull underwater. The optimal design of this platform puts the platform's roll and pitch natural frequencies below the wave excitation frequency of most sea states [Jonkman, 2010]. Due to its deep draft, this platform should be deployed in deep water. Tab. 3.3 lists the main properties of the Spar-Buoy platform.

3.3.3.3 Tension Leg Platform

The tension leg platform (TLP) maintains the hydrostatic stability using taut mooring lines. It has a cylindrical hull that is fixed to seabed through four taut mooring lines which are connect to the hull through four spokes and fixed to the seabed using anchors, see fig. 3.3. Most of its hull is underwater in order to minimise the interaction with incident waves, therefore, it is less sensitive to waves when compared to the Barge platform. Furthermore, it has higher stiffness in the roll, pitch and heave motions due to the taut mooring lines. The major drawback of this platform concept is the higher cost related to the need of anchors at seabed and the dependency on the seabed soil ability to support large tensile forces. The main properties of this platform are summarised in tab. 3.3.

Table 3.3 Main properties of the floating platform concepts [Namik, 2012]

Spar-buoy platform		**Tension leg platform (TLP)**		**Barge platform**	
Diameter above taper	$6.5\,m$	Diameter	$18\,m$	Width	$40\,m$
Diameter below taper	$9.4\,m$	Number of spokes	4	Length	$40\,m$
Freeboard	$10\,m$	Spoke length	$18\,m$	Height	$40\,m$
Draft	$120\,m$	Draft	$47.89\,m$	Draft	$4\,m$
Water depth	$320\,m$	Water depth	$200\,m$	Water depth	$150\,m$
Platform mass	$7,466,330\,kg$	Platform mass	$8,600,410\,kg$	Platform mass	$5,452,330\,kg$

3.4 Baseline Control System

The reference wind turbine is equipped with a sophisticated baseline control system (BLCS) [Jonkman et al., 2009]. This control system has two control loops, the collective blade pitch controller which is a gain-scheduled proportional integral (GSPI) controller that employs a gain-scheduling technique to compensate for the non-linearity in the turbine by changing the controller gains according to a scheduling parameter. The second control loop is the generator torque control loop. While the GSPI control loop is active only in the above rated region, the second loop is active in both operating regions however the control objective is changed according to the operating region. The general structure of the BLCS is illustrated in fig. 3.4.

3.4.1 Blade Pitch Actuator Model

The blade pitch actuator system adjusts the angle of the blade by rotating it. In a three bladed wind turbine, three identical pitch systems are used. These systems could be electrical or hydraulic, however, regardless of the system nature they share common components, system response and fault symptoms. The common components include the actuator, the controller and the sensors. The pitch system can be satisfactory modelled as a second order system [Hansen et al., 2007] with a time delay t_d and a reference signal β_{ref} such as

$$\ddot{\beta}\left(t\right) = -2\zeta\omega_n\dot{\beta}\left(t\right) - \omega_n^2\left(\beta\left(t\right) - \beta_{ref}\left(t - t_d\right)\right), \tag{3.1}$$

where the time delay t_d is related to the communication between the turbine controller and the pitch system controller, $\beta\left(t\right)$ is the pitch angle, $\beta_{ref}\left(t\right)$ is the reference pitch angle, ω_n and ζ are the natural frequency and damping ratio of the pitch system model, respectively. The block diagram illustrating the pitch system model along with the constraints on the pitch rate and range are shown in fig. 3.4. The constraints are added to represent the limitations of the actual pitch actuator.

The reference wind turbine modelled in FAST does not have any model for the blade pitch actuator system. Therefore, a model of each blade pitch actuator is added in MATLAB®/Simulink® between the blade pitch controller command and the input to the reference turbine model.

If a hydraulic pitch system is considered, a second order model with natural frequency of $\omega_n = 11.11\,{}^{rad}\!/_{s}$ and damping ratio $\zeta = 0.6$ could be used to model this actuator. The values of the model parameters are used by [Esbensen et al., 2009] to model the hydraulic pitch actuator of a $4.8MW$ fictitious wind turbine. Similarly, [Adegas et al., 2012] used the same parameter values to model the hydraulic pitch actuator of a $2MW$ wind turbine. Therefore, it is accepted in this work that the proposed parameter values of ω_n and ζ give reasonable approximation to the dynamics of the hydraulic blade pitch actuator of the $5MW$ reference wind turbine. Furthermore, the pitch actuator angle is limited between $0°$ and $+90°$, while its velocity is limited to $\pm 8{}^{\circ}\!/_{s}$ [Jonkman et al., 2009].

3.4.2 Gain-Scheduled PI Controller

The gain-scheduled PI controller is a single-input-single-output collective blade pitch controller that is originally developed by [Jonkman et al., 2009] to control the land-based reference $5\,MW$ wind turbine. This controller operates only in the above rated wind speed region to regulate the rotor speed to the rated one. The regulation effect is achieved by collectively pitching the blades to adapt the aerodynamic efficiency according to the wind speed. The GSPI control law takes the following form

$$\beta\left(t\right) = K_P\left(\theta\right) e\left(t\right) + K_I\left(\theta\right) \int\limits_0^t e\left(\tau\right) \mathrm{d}\tau, \tag{3.2}$$

where the error term is the difference between the measured generator speed Ω_g and the rated generator speed $\Omega_{g,rated}$ such as

$$e\left(t\right) = \Omega_g(t) - \Omega_{g,rated}, \tag{3.3}$$

and the proportional $K_P\left(\theta\right)$ and the integral $K_I\left(\theta\right)$ gains change according to the parameter θ that is to be determined online. The chosen scheduling parameter θ is the measured collective blade pitch angle at the previous time step. Assuming a sampling time of Δt, the parameter θ is then given by

$$\theta = \beta\left(t - \Delta t\right). \tag{3.4}$$

Using a simple single degree of freedom model of the wind turbine (the angular rotation of the rotor), in addition to the proposed controller as given in eq. 3.2, [Jonkman et al., 2009] developed the equations required to calculate the proportional and integral gains that allow achieving the prescribed closed loop dynamics defined by the closed loop natural frequency ω_{cn} and damping ration ζ_c. The proportional and integral gains are given as functions of a scheduling parameter θ

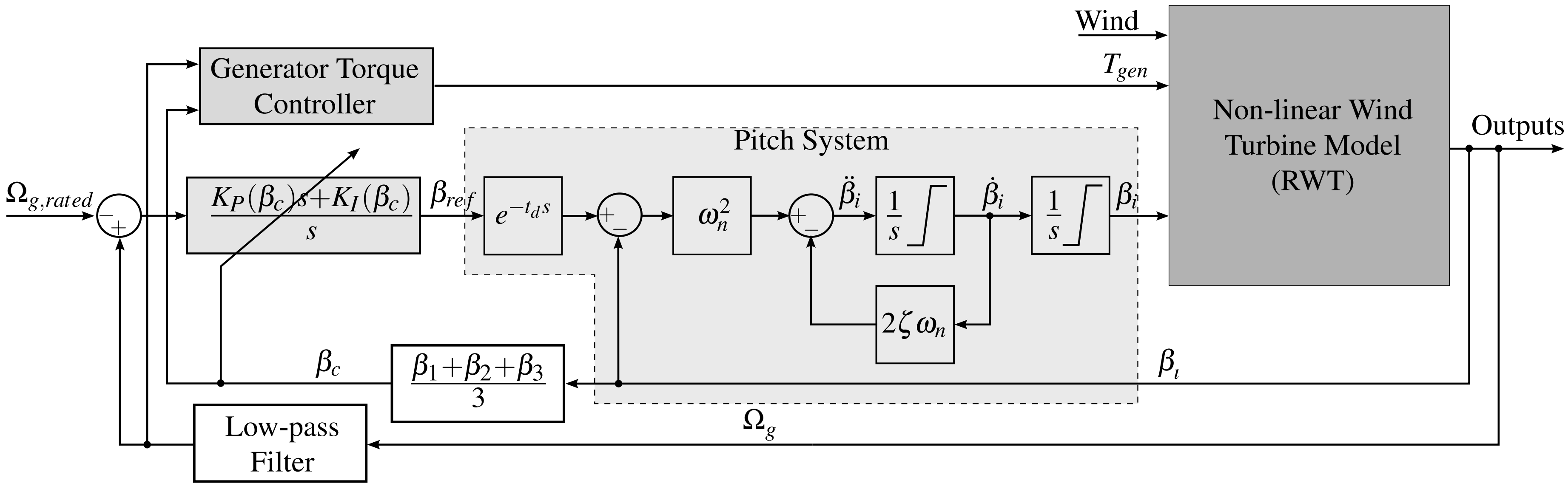

Figure 3.4 Baseline control system of the NREL $5MW$ reference wind turbine. GSPI is the gain scheduled proportional integral controller. $\beta_i = 1, 2, 3$ is the blade pitch angle of each blade.

Table 3.4 Gain-Scheduled proportional controller gains. ω_{cn} is the controller frequency, ζ_c controller damping ratio, $\overline{K}_P$ reference proportional gain, $\overline{K}_I$ reference integral gain and ω_{pp} is the natural frequency of the platform pitching motion.

Installation	$\omega_{cn}\left[\frac{rad}{s}\right]$	$\zeta_c\ [-]$	$\overline{K}_P\ [s]$	$\overline{K}_I\ [-]$	$\omega_{pp}\left[\frac{rad}{s}\right]$
Land-based	0.6	0.7	0.01883	0.00807	
Barge platform	0.4	0.7	0.01255	0.00359	0.54
Spar-buoy	0.1	0.7	0.00314	0.00022	0.12
TLP	0.5	0.7	0.01569	0.00560	0.97

such as

$$K_P(\theta) = \overline{K}_P f(\theta), \tag{3.5}$$

$$K_I(\theta) = \overline{K}_I f(\theta), \tag{3.6}$$

with

$$f(\theta) = \frac{1}{1+\frac{\theta}{\theta_k}}, \tag{3.7}$$

$$\overline{K}_P = \frac{2 I_D \Omega_{r,rated} \zeta_c \omega_{cn}}{N\left(-\left.\frac{\partial P}{\partial \theta}\right|_{\theta=0}\right)}, \tag{3.8}$$

$$\overline{K}_I = \frac{I_D \Omega_{r,rated} \omega_{cn}^2}{N\left(-\left.\frac{\partial P}{\partial \theta}\right|_{\theta=0}\right)}, \tag{3.9}$$

and $\Omega_{r,rated} = 12.1\,rpm$ is the rated rotor speed, $N = \frac{\Omega_g}{\Omega_r} = 97$ is the high-speed to low-speed gearbox ratio, $I_D = 4.3786 \times 10^7\,kg \cdot m^2$ is the drive-train inertia from the low speed shaft end. Furthermore, $\left.\frac{\partial P}{\partial \theta}\right|_{\theta=0} = -25.52 \times 10^6\,\frac{watt}{rad}$ represents the sensitivity of rotor aerodynamic power to the scheduling parameter evaluated at $\theta = 0$. Finally, $f(\theta)$ is a gain correction function that depends on the scheduling parameter θ and the constant $\theta_k = 6.30°$. This correction function is an approximation of the sensitivity of the rotor aerodynamic power to the collective blade pitch angle as derived by [Jonkman et al., 2009]. Finally, the derivation of this controller is developed basically for land-banded turbines by neglecting the negative damping presented by the generator-torque controller.

In order to estimate the initial proportional and integral gains, [Jonkman et al., 2009] set the closed loop natural frequency $\omega_{cn} = 0.6\,\frac{rad}{s}$ and the closed loop damping ration $\zeta_c = 0.7$ to obtained the initial gains $\overline{K}_P = 0.0188$ and $\overline{K}_I = 0.00807$ as per eq. 3.8 and eq. 3.9, respectively. However, when using these values to control floating turbines, the GSPI controller leads to instability in the platform pitching motion due to the servo-induced negative damping of the platform pitching motion [Chaaban et al., 2014b; Chaaban et al., 2014c]. A possible solution to avoid this problem is to reduce the controller frequency below the platform pitch natural frequency and the wave excitation frequency of most sea states as recommended by [Larsen et al., 2007a]. Using this concept, the GSPI is tuned to work with the spar-buoy platform

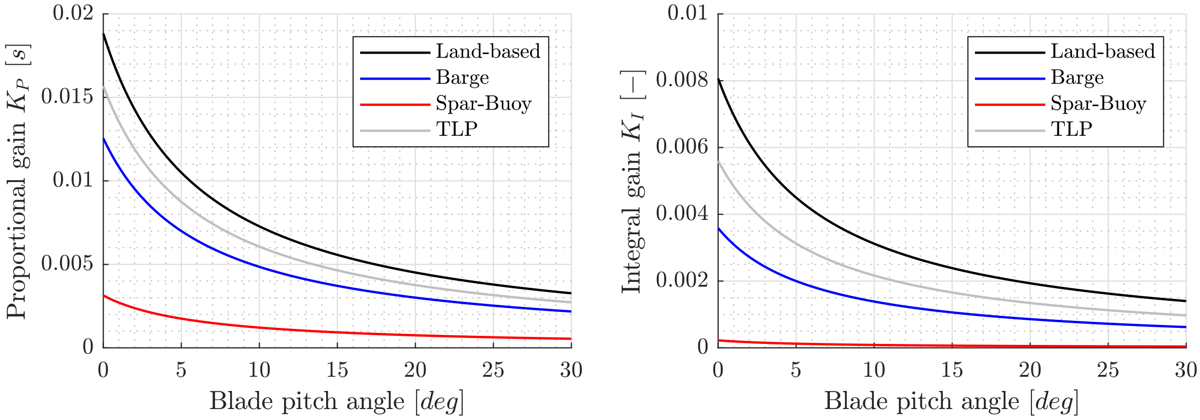

Figure 3.5 GSPI controller gains as function of blade pitch angle.

using a controller frequency of $\omega_{cn} = 0.1 \, \frac{rad}{s}$ as the natural frequency of the Spar-buoy platform pitching motion is $\omega_{PFp} = 0.12 \, \frac{rad}{s}$. Furthermore, the Barge platform has a GSPI frequency of $\omega_{cn} = 0.4 \, \frac{rad}{s}$, hence the platform pitching natural frequency is $\omega_{PFp} = 0.54 \, \frac{rad}{s}$. Finally, the TLP platform pitch natural frequency is higher than that of the Barge platform, therefore, the controller natural frequency is set to $\omega_{cn} = 0.5 \, \frac{rad}{s}$. Tab. 3.4 shows the GSPI controller frequency and gains for land-based and the floating platforms. In addition to that, fig. 3.5 illustrates the dependency of the controller gains on the scheduling parameter, namely, the blade pitch angle.

3.4.3 Generator Torque Control

The generator torque control is mainly used in the under-rated region to follow the maximum power production by changing the rotor speed as function of the mean wind speed. In the above-rated region, two approaches are presently used. The first one uses constant generator torque (rated value) and the generated power ($P_g = \eta_g T_g \Omega_g$, $T_g = const.$, η_g is the generator efficiency) is function of the fluctuations of the rotor speed about its rated value as the wind speed changes. These speed fluctuations should be minimised by the pitch controller. The second approach is to use a constant generator power ($P_g = const.$), which means to adapt the generator torque within certain limits to the changes of the rotor speed in order to produce constant output power. This second approach assumes that the generator torque could be increased above its rated value to some maximum torque (about 10 % of the rated value, see tab. 3.1) and the fluctuations are constrained to a maximum torque rate as given in tab. 3.1.

If the turbine is operating in the partial load region, the pitch controller should set the blade pitch angle to its minimum value (i.e. 0°) and the generator torque is calculated as a function of the rotor speed such as

$$T_g = \frac{\pi \rho R^5 C_{P,max}}{2\lambda^3 N^3} \Omega_g^2, \tag{3.10}$$

where ρ is the air density, R the rotor radius, $C_{P,max}$ the maximum power coefficient and λ the tip speed ratio corresponding to $C_{P,max}$. In the full load region, the controller starts to pitch the blades and the generator torque is given for the constant generator power approach as

$$T_g = \frac{P_{g,rated}}{\eta_g \Omega_g}, \tag{3.11}$$

with $P_{g,rated}$ as the rated output power of the generator. Moreover, if a constant generator torque control approach is considered in the full load region, the generator torque is set to its rated value, namely $T_g = 43,093\, Nm$ as given in tab. 3.1. Finally, The blade pitch angle is used as a reference to switch the generator torque controller between the operating regions.

3.5 Wind and Wave Loading

The stochastic, full-field, turbulent wind speed profiles are generated using TurbSim [Jonkman, 2009]. This tool employs statistical models to numerically simulate time-series of three-component wind speed vector at each point in a two-dimensional vertical grid that is fixed in space. The spectra of the velocity components and the spacial coherence are defined in frequency domain. The inverse Fourier transformation is used to produce the time-series. The underlying theory assumes a stationary process.

Wave loads are generated using the HydroDyn module in FAST. This module assumes irregular waves incident to the offshore substructure defined by JONSWAP/Pierson-Moskowitz spectrum as per [DNV, 2014] and [IEC, 2009] offshore standards. Sea currents are not considered in the simulation study as the study is done according to the design load case 1.2 of the [IEC, 2009] as presented in the following section.

3.6 The IEC 61400 Norm

To ensure that wind turbines are appropriately engineered against damage and hazards within the planned life time, they should be designed and certified according to the IEC 61400 international standard. IEC 61400 is divided into different parts that address different aspects of turbine life from site condition before construction, to turbine components being tested, assembled and operated. The main part that deal with the general design aspects is the IEC 61400-1 which lists the general design requirements [IEC, 2005] and the IEC 61400-3 that specifies additional requirements for offshore wind turbines with fixed foundations [IEC, 2009]. In these

Table 3.5 DLC 1.2 conditions summary [IEC, 2009]

DLC	Wind condition	Waves	Wind and wave Directionality	Sea current
1.2	Normal turbulence model $v_{in} < v_{hub} < v_{out}$	Normal sea state	Co-directional and multi-directional	No currents

v_{in}: cut-in wind speed; v_{hub}: hub-height wind speed; v_{out}: cut-out wind speed

two parts, different design load cases (DLCs) according to the operating conditions and analysis type are defined. Since no standards that cover the design requirements of the floating turbines exist, it is assumed that the IEC 64100-3 extends to cover design requirements of floating wind turbines.

The simulations are carried out in accordance with the DLC 1.2 of the IEC 61400-3 standard. The DLC 1.2 corresponds to fatigue load analysis under power production in normal operational conditions as summarised in Tab. 3.5. The DLC 1.2 requires to run simulations at different hub-height mean wind speed that varies between the cut-in and the cut-out limits. If the turbine is an offshore turbine, a normal sea state with joint probability distribution of significant wave height, wave period and hub-height wind speed should be used. This requires full site specific data which are not available. An acceptable alternative to this is to use the DLC 1.1 condition that requires the use of the expected significant wave height at given wind speed range.

Furthermore, DLC 1.2 requires the wind and waves to be co-directional and multi-directional. This condition could be simplified to consider only one wind and wave direction case due to the axisymmetric properties of the simulated platforms. Wind turbine rotor axis is also assumed to be aligned with the wind direction. The case of misalignment goes under DLC 1.4 which handles the case of ultimate load analysis, and therefore, it is outside the scope of this work.

In the simulated loading data-set used for fatigue analysis, the hub-height wind speed is varied between $v_{in} = 3\,\frac{m}{s}$ and $v_{out} = 25\,\frac{m}{s}$ with $1\,\frac{m}{s}$ speed increment per wind speed bin. Regardless of the wind speed range, the IEC 64100 requires for statistical reasons six $600\,s$ of turbulent wind and irregular waves with different random seeds to be used per each wind speed bin.

Due to the absence of the full site specific data, the wave conditions are based on the same reference site used by [Jonkman, 2007] located north-east of Scotland. In the site data, a single significant wave height exists along with a range of wave periods for a corresponding average wind speed. According to the IEC 64100-3 standard, the necessary condition to apply the linear wave theory in deep water is

$$\frac{H_w}{gT_w^2} \leq 0.002, \tag{3.12}$$

where H_w is the wave-height, T_w is the wave period and g is the gravitational acceleration. As

Table 3.6 Stochastic wind and wave parameters used for the design load cases analysis. Parameters are defined according to the DLC 1.2 of the [IEC, 2009].

Wind Speed $[\frac{m}{s}]$	Wave height $[m]$	Wave period $[s]$	Wind Speed $[\frac{m}{s}]$	Wave height $[m]$	Wave period $[s]$
3	1.0	$8.0 \leq T_w \leq 14.0$	14	3.2	$12.8 \leq T_w \leq 18.8$
4	1.2	$8.4 \leq T_w \leq 14.4$	15	3.4	$13.2 \leq T_w \leq 19.2$
5	1.4	$8.8 \leq T_w \leq 14.8$	16	3.6	$13.6 \leq T_w \leq 19.6$
6	1.6	$9.1 \leq T_w \leq 15.1$	17	3.8	$14.0 \leq T_w \leq 20.0$
7	1.8	$9.6 \leq T_w \leq 15.6$	18	4.0	$14.3 \leq T_w \leq 20.3$
8	2.0	$10.1 \leq T_w \leq 16.1$	19	4.2	$14.7 \leq T_w \leq 20.7$
9	2.2	$11.1 \leq T_w \leq 17.1$	20	4.4	$15.0 \leq T_w \leq 21.0$
10	2.4	$11.6 \leq T_w \leq 17.6$	21	4.6	$15.4 \leq T_w \leq 21.4$
11	2.6	$12.0 \leq T_w \leq 18.0$	22	4.8	$15.7 \leq T_w \leq 21.7$
12	2.8	$12.0 \leq T_w \leq 18.0$	23	5.0	$16.0 \leq T_w \leq 22.0$
13	3.0	$12.4 \leq T_w \leq 18.4$	24	5.2	$16.3 \leq T_w \leq 22.3$

FAST assumes linear wave theory which is a reasonable assumption in deep water, the chosen wave periods should comply with this assumption. Therefore, the wave periods in each wind speed bin are linearly ranged between a minimum and maximum values that satisfy, for a given wave height H_w, the linear wave theory condition presented in eq. 3.12. Tab. 3.6 summaries the wind and wave conditions used in simulation.

3.7 Fatigue Analysis Tools

The implementation of the rainflow counting is based on the developed toolbox by [Nieslony, 2009]. This toolbox starts by converting a given stress time history into a sequence of maxima and minima (peak and valley), i.e. turning points; next, cycle counting (and half-cycles) is performed. The toolbox provides four different outputs which are: the accumulated damage, the amplitude and cycle mean histograms in addition to the so-called rainflow matrix. Using material properties, the stress-range histogram is then calculated and with the help of the corresponding $S-N$ curve and the Palmgren-Miner rule, the fatigue damage is estimated. This process is programmed as MATLAB® function.

Fatigue analysis using spectral-based methods starts by estimating the PSD of the stress either directly from the measured stress time history, or estimated using the PSD of the structural loads (wind or wave) and the transfer function of the structure (see eq. 2.50). The power spectral density itself is calculated using the non-parametric Welch's method [Welch, 1967]. The spectral moments are then estimated from the PSD using eq. 2.22. Finally, the fatigue damage for each spectral method is estimated using the corresponding closed-form formula as presented in chapter 2. These steps are also implemented as MATLAB® functions.

Finally, the implemented transformed Gaussian model in this work is based on the Hermiteter transformation provided by the MATLAB® toolbox for analysis of random waves and loads [WAFO, 2017].

3.8 Performance Metrics of Fatigue Damage Analysis

To quantify the performance of the fatigue damage estimation of different spectral methods against the rainflow counting method, the following performance metrics are used to monitor the process characteristics and the estimated fatigue damage. These performance metrics are calculated for each simulation case, experiment or measured operational time-series. The performance metrics/indices can be grouped into the following main groups

3.8.1 Characteristics of the Loading Time-Series

The purpose of these indices is to get a clear idea about the frequency content of the loading time-series (narrow or wide-band), in addition to check the distribution characteristics and to which limit it is close to the Gaussian distribution.

1. Band-width parameters α_1 and α_2 used to check the band width of the loading history. For narrow-band the values are close to unity, for wide-band the values tend towards 0.
2. Skewness γ_{Sk} monitors the degree of asymmetry of the loading. If the loading is symmetric around its mean $\gamma_{Sk} = 0$.
3. Kurtosis γ_{Ku} measures the contribution of the tails of the load distributions. $\gamma_{Ku} = 3$ for Gaussian process.

3.8.2 Fatigue Damage Analysis in Time-Domain

Fatigue damage analysis in time domain estimates the following indices:

1. Fatigue damage intensity $\dot{\mathcal{D}}_{RFC}$ calculated using rainflow counting method over the time period T.
2. Fatigue damage $\mathcal{D}_{RFC} = T\dot{\mathcal{D}}_{RFC}$.
3. Estimated fatigue life $T_{life,RFC} = \frac{1}{\bar{\dot{\mathcal{D}}}_{RFC}}$ where $\bar{\dot{\mathcal{D}}}_{RFC}$ is the average value of the calculated damage intensity.

3.8.3 Fatigue Damage Analysis in Frequency-Domain

Fatigue damage analysis in frequency domain estimates the following indices:

1. Fatigue damage intensity $\dot{\mathcal{D}}_G$ estimated under the Gaussian assumption over the time period T.
2. Corrected fatigue damage intensity $\dot{\mathcal{D}}_{cG}$ using the correction factor described in sec. 2.7.2.1 for the case of non-Gaussian loading.
3. Corrected fatigue damage intensity $\dot{\mathcal{D}}_{tG}$ calculated using the transformed Gaussian model explained in sec. 2.7.2.2 for the case of non-Gaussian loading.
4. Fatigue damage $\mathcal{D}_i = T\dot{\mathcal{D}}_i$ with $i \in \{G, cG, tG\}$.
5. Estimated fatigue life $T_{life,i} = \frac{1}{\bar{\dot{\mathcal{D}}}_i}$ with $i \in \{G, cG, tG\}$ and $\bar{\dot{\mathcal{D}}}_i$ is the average value of the calculated damage intensity.

3.8.4 Comparison of Fatigue Damage Analysis in Time and Frequency Domains

In order to be able to compare the estimated fatigue damage between the frequency and the time domains, the following dimensionless index is used

$$\eta_i^k = \frac{\mathcal{D}_i^k}{\mathcal{D}^{RFC}}, \tag{3.13}$$

with $\mathcal{D}^{RFC}$ as the fatigue damage estimated using the rainflow counting algorithm, $\mathcal{D}_i^k$ is the spectral fatigue damage estimated using the spectral fatigue damage method k (see tab. 2.2) and the estimation approach $i \in \{G, cG, tG\}$.

This normalization aims to validate the capabilities of the spectral approaches of giving similar fatigue estimation results as the time-domain counting method. Close to unity values $\eta_i^k \approx 1$ means that both methods, spectral and time domain, are giving similar results while larger than unity values $\eta_i^k > 1$ indicates that the corresponding spectral method gives more conservative fatigue damage estimation than the time domain; Conversely, if $\eta_i^k < 1$ then the spectral method will fail to predict the material failure. Another useful aspect of the normalization is in limiting the dependency of the estimation results only to the material exponent m on the $S-N$ curve which is clear from eq. 2.85.

3.8.5 Measured Loading

Most of the spectral fatigue damage methods are tuned for materials with low fatigue damage exponent ($m < 8$). This corresponds only to the turbine components that are made of (welded) construction steel which have fatigue damage exponent $m \approx 3$. This includes basically the tower and the support platform. The other turbine components such as the blades that are made of composite materials ($m \approx 10$), or the gearbox and the high- and low-speed shafts that are made of cast nodular iron ($m \approx 7$), have higher values of the fatigue exponent, therefore, the use of some spectral methods for fatigue damage estimation for these components is not possible.

Based on this, the loading time-series considered in fatigue damage estimation are limited to the measured/simulated tower base bending strains in both directions such as:

1. Tower base fore-aft (FA) bending strain
2. Tower base side-side (SS) bending strain

The bending stress is then calculated using the cross section data. The metrics that characterise the measured loading are calculated per each time-series where they give a clear idea if the loading segment is narrow- or wide-banded and if it is Gaussian or non-Gaussian. Furthermore, the fatigue damage estimation metrics are calculated for each of the spectral methods then normalised by the corresponding metric estimated using the rainflow counting method.

3.9 Weibull Scaling

In order to be able to assess the long term fatigue damage by accounting to the wind speed probability distribution at the installation site, a weighted average is used to obtain the overall averaged performance metrics. The weighted averaged performance metric $\bar{p}$ is obtained from the performance metrics p_i estimated at the wind speed v_i using the following formula

$$\bar{p} = \frac{\sum_{i=1}^{n_b} \xi_i p_i}{\sum_{i=1}^{n_b} \xi_i}, \tag{3.14}$$

where ξ_i is the scaling factor for the i-th wind speed bin and n_b is the number of wind speed bins.

The Weibull distribution given in eq. 3.15 has been found to give a good representation of the variation in hourly mean wind speed over a year [Butron et al., 2001; DNV, 2016]

$$F\left(u\right) = \exp\left(-\left(\frac{u}{c}\right)^k\right), \tag{3.15}$$

with $F\left(u\right)$ as the fraction of time for which the hourly mean wind speed exceeds u. This distribution is characterised by two parameters, the shape parameter k that describes the variability about the mean and the scale parameter c which is related to the annual mean wind speed $\bar{u}$ by

$$\bar{u} = c\Gamma\left(1 + \frac{1}{k}\right), \tag{3.16}$$

with $\Gamma\left(\,\cdot\,\right)$ as the complete gamma function (eq. 2.88). The probability density function could

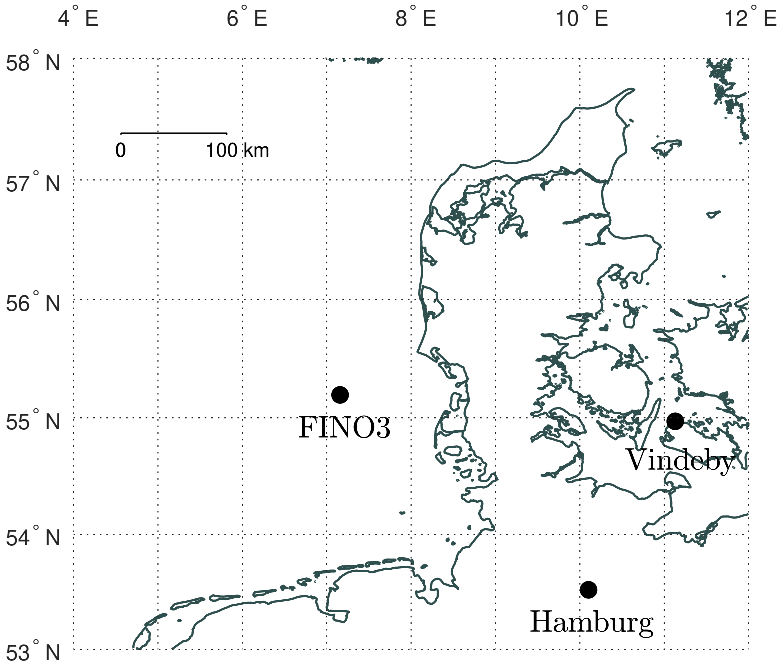

Figure 3.6 Map showing the locations used as reference for building Weibull scaling factors.

be calculated using

$$f\left(u\right) = -\frac{\mathrm{d}F\left(u\right)}{\mathrm{d}u} = k\frac{u^{k-1}}{c}\exp\left(-\left(\frac{u}{c}\right)^{k}\right), \tag{3.17}$$

and the annual mean wind speed $\bar{u}$ is then given by

$$\bar{u} = \int\limits_{0}^{\infty} uf\left(u\right)\mathrm{d}u. \tag{3.18}$$

This last equation allows calculating the annual average wind speed at the measurement reference height h_{ref} which is mostly different from the wind turbine tower top height h_{hub}. If the annual mean wind speed at hub height is not given, a good approximation could be obtained using the vertical shear power low for wind speed calculation according to

$$\bar{u}\left(h\right) = \bar{u}\left(h_{ref}\right)\left(\frac{h}{h_{ref}}\right)^{\gamma}, \tag{3.19}$$

where γ is the vertical shear exponent that takes a nominal value of $\gamma = 0.2$ for onshore locations and $\gamma = 0.14$ for offshore sites.

Weibull scaling factors depend on the turbine location. In order to address this point, two different Weibull parameter sets are considered, the first set represents a suburban location located next to Hamburg (53.5192°N, 10.1029°E), while the second parameter set represents an offshore location in the North Sea at the German research platform FINO3 (55.19501°N, 7.15836°E). The considered turbine locations are shown in fig. 3.6 and the parameter sets are derived from the results obtained by [Gryning et al., 2015] and are presented in tab 3.7. Moreover, fig. 3.7 shows the change of the scaling parameters for both location with the wind speed.

Table 3.7 Selected Weibull Parameters for onshore and offshore sites. Parameter set are derived from the results obtained by [Gryning et al., 2015]

Parameters	Symbol	Unit	Hamburg	Vindeby	FINO3
Shape parameter	k	$[-]$	2.2	2.3	2.45
Scale parameter	c	$[\frac{m}{s}]$	6.2	9.1	11.3
Reference height	h_{ref}	$[m]$	50	48	50
Annual mean wind speed	$\bar{u}$	$[\frac{m}{s}]$	5.5	8.1	10.0
Turbine hub height	h_{hub}	$[m]$	90	90	90
Vertical shear exponent	γ	$[-]$	0.2	0.14	0.14

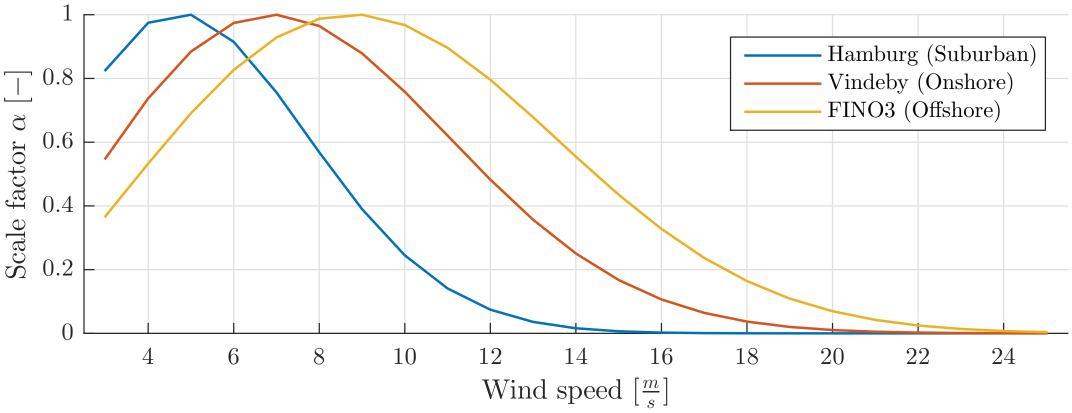

Figure 3.7 Weibull scaling factors for the considered turbine locations. Curves are obtained using parameters listed in tab. 3.7

The work of [Gryning et al., 2015] is based on site measurements using a wind-lidar measurement system. The data from Hamburg location are collected over the period from 15 June 2011 till 23 March 2012, while the data from FINO3 are collected between 29 August 2013 and 26 June 2014. The measurement period in each location is less than one year, however, the measurement results are comparable to the results obtained from Vindeby offshore wind farm (54.97°N, 11.13°E) in Denmark for the period from 1993 to 1997 [Barthelmie et al., 2005] (see tab. 3.7 and fig. 3.7). The main difference in wind characteristics between the three locations is the annual mean wind speed at the reference height that is lower at Hamburg site (suburban) and increases at the Vindeby offshore site (distance from shore about $2\,km$) to the maximum value at the offshore site of FINO3 which is about $80\,km$ away from the nearest shore.

3.10 Chapter Summary

This chapter has introduced the FAST design code used in wind turbine modelling and simulation in addition to the reference wind turbine model and its operating regions. Furthermore, three different floating platforms are reviewed. As the used turbine control system affects the over all loading on the wind turbine, in particular tower loading, a baseline control system is also introduced. Moreover, the wind and wave loading conditions used in simulation are also highlighted. The simulations are done according to the IEC 64100 norm which is a set of design requirements made to ensure that wind turbines are appropriately engineered against damage from hazards within their planned lifetime. The chapter ends by defining the measured signals in addition to a set of performance metrics that are necessary for the overall fatigue damage analysis and evaluation.

Chapter 4

Applications of Fatigue Damage Analysis

If you cannot accurately predict the future then you must flexibly be prepared to deal with various possible futures.

— Edward de Bono

Contents

4.1 Fatigue Analysis Using Simulation Data-Set

The performance of the spectral-based fatigue damage estimation methods is evaluated using as reference the fatigue damage estimations obtained by the industry standard rainflow cycle counting. The previously defined normalised fatigue damage index η (sec. 3.8.4) is used for performance assessment of the spectral methods along with the different approaches. The stress time history data-set used for fatigue analysis is generated from non-linear model of a utility scale wind turbine with land-based and floating offshore with three different platform configurations. The reference wind turbine is subject to turbulent wind and wave loading that cover both operating regions. The simulations are done in accordance with the design load case DLC 1.2 of the IEC 61400 norm. Fatigue analysis of the tower-base bending in fore-aft and

Table 4.1 Structure of the simulation data-set

Turbine configuration	Nr. of wind Speed bins	Nr. of seeds per wind speed bin	Nr. of DLC simulations
Onshore	22 bins	6 different wind profiles	132
Floating - Barge	22 bins	6 different wind and wave profiles	132
Floating - Spar-buoy	22 bins	6 different wind and wave profiles	132
Floating - TLP	22 bins	6 different wind and wave profiles	132
		Total Nr. of DLC Simulations	528

side-to-side directions are carried out first in time domain using the rainflow counting, then in frequency domain using various spectral-based methods combined with presented approaches, the Gaussian, the corrected Gaussian and the transformed Gaussian model. The normalised fatigue damage index η is then estimated for each method/approach and used to evaluate the performance of the frequency domain methods against the industry standard rainflow cycle counting algorithm.

4.1.1 Simulation Data-Set

The reference wind turbine (RWT) equipped with the baseline control system (BLCS) is used to generate the simulation data-set needed for fatigue analysis using time and frequency domain methods. The simulations are done in accordance with the design load case (DLC) 1.2 of the international standard IEC 64100. Four different configurations for the reference turbine substructure are considered. In the first configuration, the turbine is assumed to be installed in land with stiff foundations (called land-based turbine) while the other three configurations are floating turbines with the main three floating platforms, namely, Barge, Spar-buoy and TLP platforms. For each configuration the turbine is subject to turbulent wind speed profiles with mean wind speed that ranges between $v_{in} = 3\,\frac{m}{s}$ and $v_{out} = 24\,\frac{m}{s}$ with a step of $1\,\frac{m}{s}$ per each wind speed bin. At each wind speed bin, the simulation is repeated six times, each time with different wind and wave profiles generated using different seed numbers. Each simulation is run for $700\,s$, however, only the last $600\,s\,(10\,min)$ are saved. Removing the first $100\,s$ is necessary to ensure the stability of the simulation results. Tab. 4.1 summaries the structure of the simulation data-set.

In each simulation, the tower-base bending moments in the fore-aft and side-side directions are recorded. In addition to that, wind speed components in the inertial frame (x_I-axis is down-wind, z_I-axis is against gravity along tower axis) and wave elevation are also recorded in order to assess the characteristics of the stochastic loading. Tab. 4.2 illustrates the measured parameters and their corresponding used units.

Table 4.2 Recorded simulation parameters

Measurement location	Direction	Unit
Tower-base loading moment	Fore-aft (y_t)	$[kN \cdot m]$
Tower-base loading moment	Side-side (x_t)	$[kN \cdot m]$
Wind speed components	x_i, y_i, z_i	$[\frac{m}{s}]$
Wave elevation	z_i	$[m]$

4.1.1.1 Simulation Setup

The wind turbine modelling and simulation tool FAST [Jonkman et al., 2005] along with MATLAB®/Simulink®are used as main simulation platform. The simulation setup structure is illustrated in fig. 3.1, where the generator torque and the GSPI blade pitch controller blocks are included. A low-pass filter is used to filter the high frequency fluctuations in the measured generator speed in order to avoid high frequency commands in the blade pitch angle. Finally, the simulation time step is set to 0.0125 s.

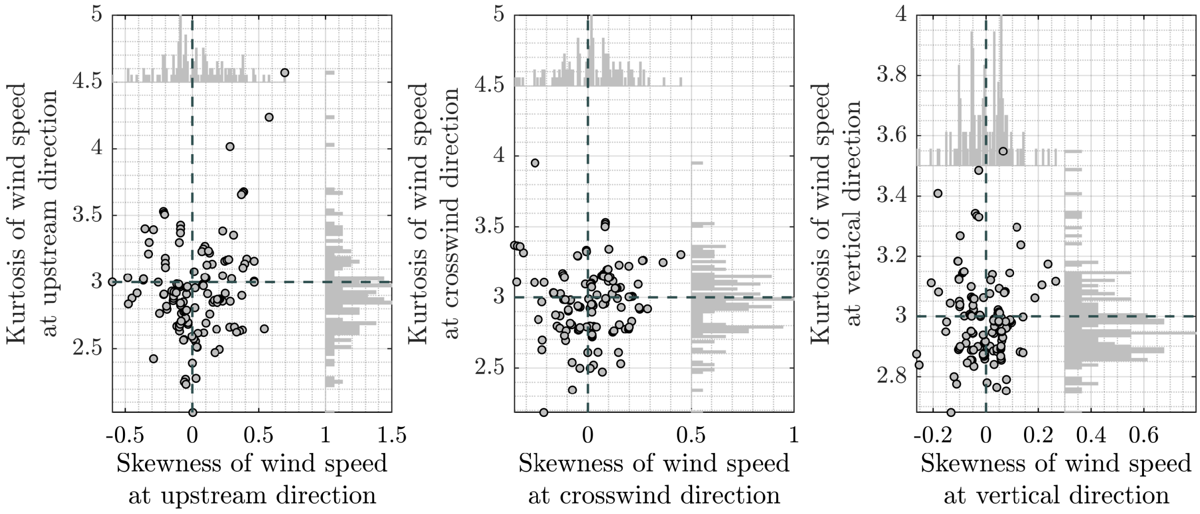

Figure 4.1 Scatter plot of kurtosis vs skewness of measured wind speed at hub height in $x-$, $y-$ and $z-$directions.

4.1.1.2 Stochastic Characteristics of the Simulated Design Load Cases

TurbSim code is used to generate a stationary full field stochastic turbulent wind profile that is based on statistical model [Jonkman, 2009]. The generated wind speed field is defined at the grid points in a two dimensional vertical rectangular gird that is fixed in space. The spectrum of velocity components and spatial coherence are defined in the frequency domain and an inverse Fourier transform produces the wind velocity time-series.

The first step in pre-processing the simulation data-set is to have a closer look at the nature of the stochastic wind loading. The skewness and the kurtosis characteristics of the measured wind speed components in $x-$(normal to rotor), $y-$(horizontal parallel to rotor) and $z-$ (vertical) directions are given in a form of scatter plots as illustrated in fig. 4.1. Furthermore, fig. 4.2 shows an example of the wind speed time history component in down-wind direction ($x-$direction) along with the probability density function (PDF) of the wind speed amplitude compared to a Gaussian distribution. It is clear from these figures that the turbulent wind profiles used in simulation are not of Gaussian nature. In all wind directions, the skewness varies between -0.5 to $+0.5$ and the kurtosis varies between 2 and 4.5. The results scatter more in the $x-$ and $y-$directions while the $z-$direction has less skewness variation.

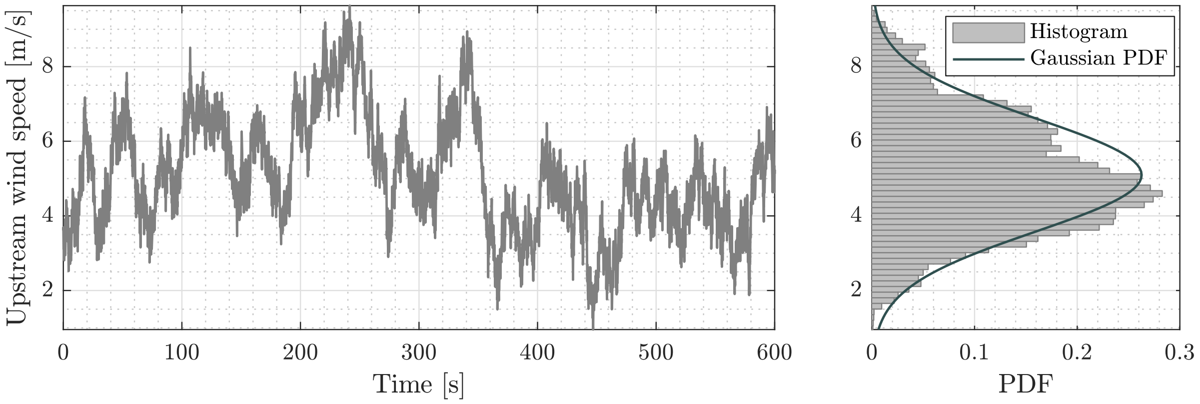

Figure 4.2 Wind speed time history and amplitude probability density function.

As the input wind speed profile is of non-Gaussian characteristics and due to the non-linearity of the wind turbine system, the measured structural loads follow also non-Gaussian distribution. By considering the onshore wind turbine subject to the previously defined DLCs, the scatter plot of the skewness and the kurtosis of the measured tower-base fore-aft and side-side bending moments are shown in fig. 4.7 and fig. 4.8, respectively. From these plots, it is possible to conclude that the skewness and the kurtosis of the tower-base moment in the fore-aft direction scatter more than that of the side-side direction. This is due to the fact that fore-aft loading direction is more affected by wind loading.

4.1.1.3 Fatigue Damage Analysis

Fatigue analysis in the time domain is carried out using the industry standard rainflow counting algorithm, while fatigue analysis in the frequency domain is done using the three different approaches explained in sec. 2.9. These approaches are the Gaussian, the corrected Gaussian and the transformed Gaussian model approaches (see fig. 2.18 and fig. 2.19).

Fatigue analysis in frequency domain starts with the generated simulation data-set. The detrending step in the case of land-based wind turbines could be ignored. This is motivated by the fact that the used wind speed profiles are assumed to be aligned with the nacelle, therefore, there is no yaw motion and the rotor does not change its direction. Furthermore, the generated wind speed profile is assumed to have a constant mean value and the fluctuations about this mean are related to the turbulence nature of the generated wind speed profile. Based on this, there is no justification to de-trend the generated tower base bending strain/stress time-series before using them in fatigue damage estimation in frequency domain.

These arguments are not completely valid for floating wind turbines due to the added extra DOFs of the platform, namely, the platform pitch and yaw motions. While the platform yaw DOF will allow the rotor to turn away from the wind, the platform pitching motion will result in varying velocity of the rotor when it moves with and against the wind. As the aerodynamic loading depends on the relative velocity between the rotor and the up-wind, platform pitching motion will result to a relative wind speed field that has a variable mean value. Based on this, de-trending the simulation data-set in the case of floating turbine is justified. However, this means that the deterministic component should be post-processed using the rainflow counting method in order to get complete fatigue analysis. By doing this, the benefits of using spectral-based methods is then lost in this case, hence, the simulated data-set obtained from the floating wind turbines are post-processed in a similar way to that of the onshore turbines.

The estimated fatigue damage using spectral methods is normalised by the estimated fatigue damage using the rainflow counting method. These normalised results enable good comparison between the time and frequency domain methods; and it allows comparing the effect of skewness and kurtosis of the non-Gaussian process on fatigue damage estimation.

Using spectral methods, fatigue damage is calculated per each design load case (DLC) then averaged over each wind speed bin. A weighed total average over the simulated wind speed range is then calculated with the help of the estimated fatigue damage results per each wind speed bin. The weight per each bin is obtained from the corresponding Weibull scaling curve illustrated in fig. 3.7. The same process is done also for fatigue damage estimation in time-domain.

The obtained weighted averaged fatigue damage of each spectral method $\mathcal{D}^k$ is finally normalised by the corresponding weighted averaged rainflow damage estimation $\mathcal{D}^{RFC}$ such as

$$\eta^k = \frac{\mathcal{D}^k}{\mathcal{D}^{RFC}}, \tag{4.1}$$

with η^k being a dimensionless parameter that represents the normalised fatigue damage index. The dimensionless parameter η^k enables good comparison of the spectral-based fatigue damage estimations against the estimations obtained using the reference rainflow cycle counting algorithm. If $\eta^k > 1$, the spectral method k is said to be conservative (with regard to time domain algorithm), which means that the spectral method is predicting a shorter fatigue life when compared to the fatigue life predicted by the time domain approach. On the contrary, if $\eta^k < 1$ the spectral method is predicting longer fatigue life time when compared to the time domain method. The optimal value of η^k is to be close to unity, namely, $\eta^k \approx 1$. This means that the fatigue damage estimation in frequency domain and time domain are almost similar.

In discussing the obtained results, a distinction is made between good, acceptable and not acceptable fatigue damage estimation of the spectral-based methods against the reference fatigue damage estimation in the time domain. This distinction is based on the acceptable engineering tolerances. If the estimated fatigue damage using spectral methods lies within ±10 % tolerance from the one obtained using time domain method, it is said that the spectral method gives good fatigue damage estimation. This corresponds to $0.9 \leq \eta \leq 1.1$; and if the estimation of the spectral method is outside the ±10 % but within ±20 % tolerance, fatigue damage estimation using spectral methods is said to have an acceptable estimation when compared to the time domain results. This correspond to $0.8 \leq \eta \leq 1.2$. Finally, the estimation of the spectral method is not acceptable if it lies outside the ±20 % tolerance from the time domain estimation results. This corresponds to either $\eta < 0.8$ or $\eta > 1.2$. In this case, there is a hug discrepancy between the fatigue damage estimation results in the frequency and time domains. Tab. 4.3 summaries the classification rules.

Table 4.3 Classification of obtained fatigue damage estimation results

Classification	Tolerance	η range	Meaning
Good	±10 %	$0.9 \leq \eta \leq 1.1$	Spectral fatigue damage estimation gives close (within the given ±10 % tolerance) result to the time domain fatigue damage estimation.
Acceptable	±20 %	$0.8 \leq \eta \leq 1.2$	Spectral fatigue damage estimation gives acceptable (within the given ±20 % tolerance) results comparing to the time domain fatigue damage estimation.
Not acceptable	otherwise	otherwise	Spectral fatigue damage estimation deviates far from the results in the time domain.

Most of the simulated loading signals have band width parameter $\alpha_2 \leq 0.25$ that indicates a wide band loading spectrum. This is clear for example from fig. 4.3 which shows the scatter plot of the band width parameter α_2 of tower bending in the fore-aft and side-side directions of an onshore wind turbine. The same scatter of α_2 values is also observed on the loading of the floating turbines. As the simplified and improved Zaho-Baker methods (ZBs and ZBi) can't be applied for time-series with band width parameter α_2 less than 0.13, namely, $\alpha_2 \leq 0.13$, this would exclude these two methods directly from the fatigue damage estimation. Furthermore, the Petrucci-Zuccarello (PZ) and Ortiz-Chen (OC) methods have shown to give very conservative fatigue damage estimations with $\eta > 2$, therefore, these methods are also excluded from the comparison results presented later.

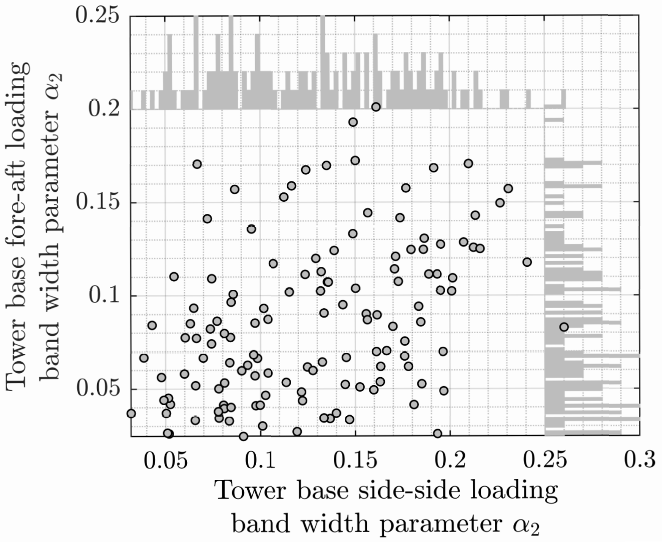

Figure 4.3 Scatter plot of the band width parameter α_2 for onshore turbine tower loading fore-aft and side-side directions.

4.1.2 Onshore Wind Turbine

Wind turbine tower is made of welded structural steel with the main steel grades in use are the $S235$ and $S355$. The fatigue properties of the $S235$ steel material is widely studied and available for example in [Bökamp, 2009]. Moreover, [DNV, 2016] provides the recommended practice for the design of the offshore steal structures. This work adopts the main material design properties of structural steel ($S235$) according to DIN EN 1993-1-1 [DIN, 2014] which are summarized in tab. 4.4.

Table 4.4 Material properties of construction steel $S235$ [DIN, 2014]

Property	Symbol	Value	Unit
Young's Modulus	E	210	$[GPa]$
Poisson's ratio	ν	0.3	$[-]$
Tensile strength	S_u	360	$[MPa]$
Yield strength	S_y	235	$[MPa]$
Fatigue exponent	m	3	$[-]$
Coefficient of linear thermal expansion	α	12×10^{-6}	$[°K^{-1}]$

4.1.2.1 Tower Bending Moment Characteristics

In order to understand the differences in fatigue damage estimation results between the tower fore-aft and side-side directions, the tower bending moment time histories, the amplitude distribution and the corresponding power spectral densities of both directions at mean wind speed of 17 $\frac{m}{s}$ are shown in fig. 4.4. This figure demonstrates the differences in amplitude distribution between the fore-aft and side-side directions. While the side-side direction has a good symmetry (skewness $\gamma_{Sk} = 0.09$, kurtosis $\gamma_{Ku} = 2.8$) with close to Gaussian characteristics, the fore-aft distribution is asymmetric (skewness $\gamma_{Sk} = 0.8$, kurtosis $\gamma_{Ku} = 4.1$) and it drifts far away from the normal distribution characteristics. With the change of wind speed, the bending spectrum shows some changes, such as the $3P$ peak will move to the left at lower rotor speeds. Spectral-based methods under Gaussian assumption can tolerate to some limit the violation of the this assumption, however, if the violation is too strong, the estimation results can't be trusted any more. The sensitivity to the violation of the Gaussian assumption varies between the spectral fatigue damage estimation methods.

The tower bending moment in the fore-aft direction is dominated by the change of mean wind speed over the rotor disk at frequencies lower than $0.1\,Hz$; in addition to that, it is possible to identify higher dynamic response at the tower first fore-aft mode ($f_{T1fa} = 0.33\,Hz$) and with less amplitude at the $3P$ frequency of the rotor ($0.6\,Hz$). On the contrary, the tower side-side bending moment is dominated by the dynamic response at the tower side-side first mode ($f_{T1ss} = 0.32\,Hz$). The variations of wind speed has less effect on the tower bending moment at this direction for frequency less than $0.1\,Hz$.

By performing the rainflow cycle counting on the time-series shown in fig. 4.4, the amplitude-mean histograms shown in fig. 4.5 and fig. 4.6 are obtained. The difference between the histogram in both directions is clear; while the side-side direction has a quasi symmetrical distribution of cycles about a mean value of $5000\,kN \cdot m$ the histogram in the fore-aft direction does not show any symmetry. Furthermore, the tower fore-aft bending moment has few cycles with high amplitudes. These cycles correspond to the change of the mean value of the relative wind speed (between the up-stream wind speed and the rotor linear velocity).

4.1.2.2 Fatigue Analysis of Tower-Base Bending Moment in Fore-Aft Direction

The normalised fatigue damage estimation results of the three spectral approaches over operational wind speed range along with the scatter plot of the skewness and kurtosis of the simulated tower bending moment in the fore-aft direction are presented in fig. 4.7. The skewness-kurtosis scattering shows clear non-Gaussian loading characteristics. However, using the Gaussian approach, the the Empirical $\alpha_{0.75}$ and the Bands methods give good (within $\pm 10\,\%$ tolerance) fatigue damage estimation with the Empirical $\alpha_{0.75}$ being closer to the time domain estimation. An acceptable fatigue damage estimation could be also obtained using the Single-Moment, Dirlik in addition to the second method of Tovo-Benasciutti. The fatigue damage estimations from the other methods are very conservative ($\eta > 1.4$) when compared to the time-domain, therefore, the estimation results using these methods are not acceptable.

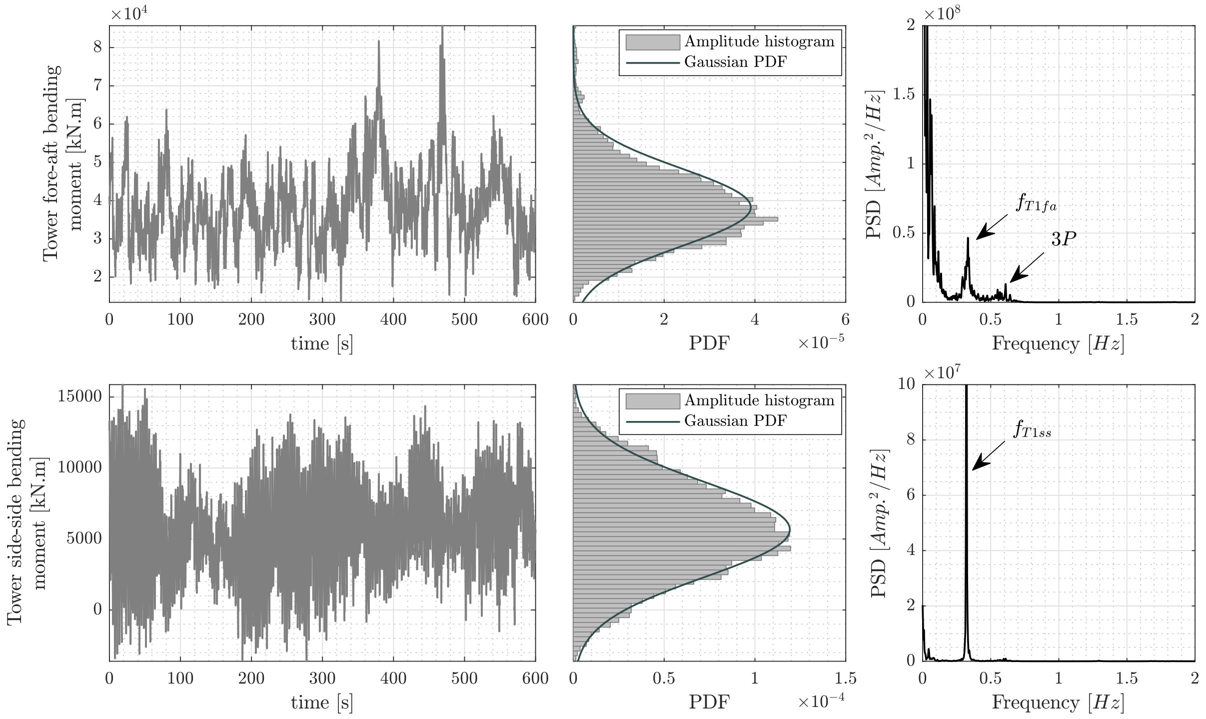

Figure 4.4 Tower bending moment characteristics in fore-aft and side-side directions for wind speed 17 $\frac{m}{s}$.

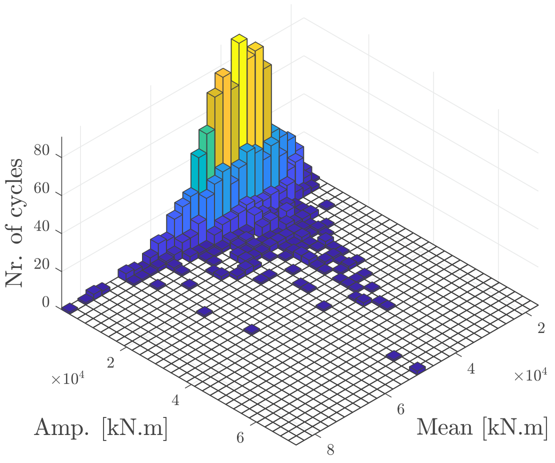

Figure 4.5 Amplitude-mean histogram of tower fore-aft bending moment of land-based reference wind turbine subject to wind speed 17 $\frac{m}{s}$.

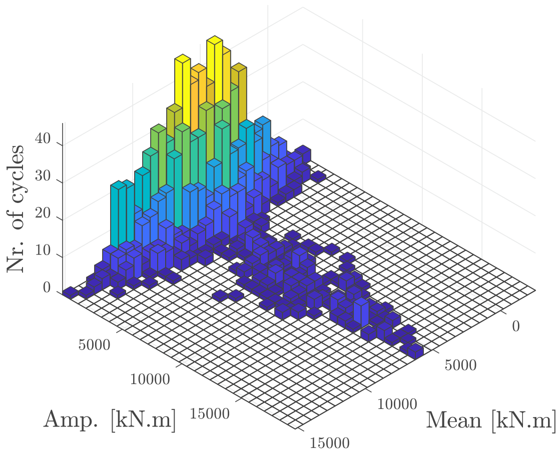

Figure 4.6 Amplitude-mean histogram of tower side-side bending moment of land-based reference wind turbine subject to wind speed 17 $\frac{m}{s}$.

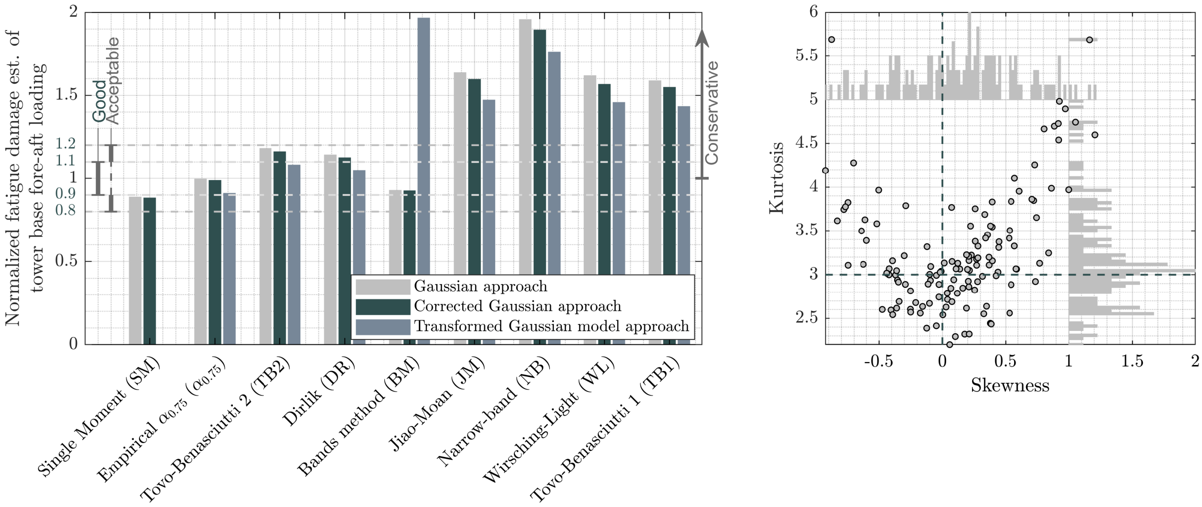

Figure 4.7 Normalised fatigue damage estimation η of tower bending moment in fore-aft direction using three different spectral fatigue damage analysis approaches

Taking into account the non-Gaussianity by either using the corrected Gaussian or the transformed Gaussian model approaches have minor effect on the obtained over all results. The remarkable effect is obtained from transformed Gaussian model approach combined with the Dirlik and Tovo-Benasciutti second method, where good fatigue damage estimation are obtained.

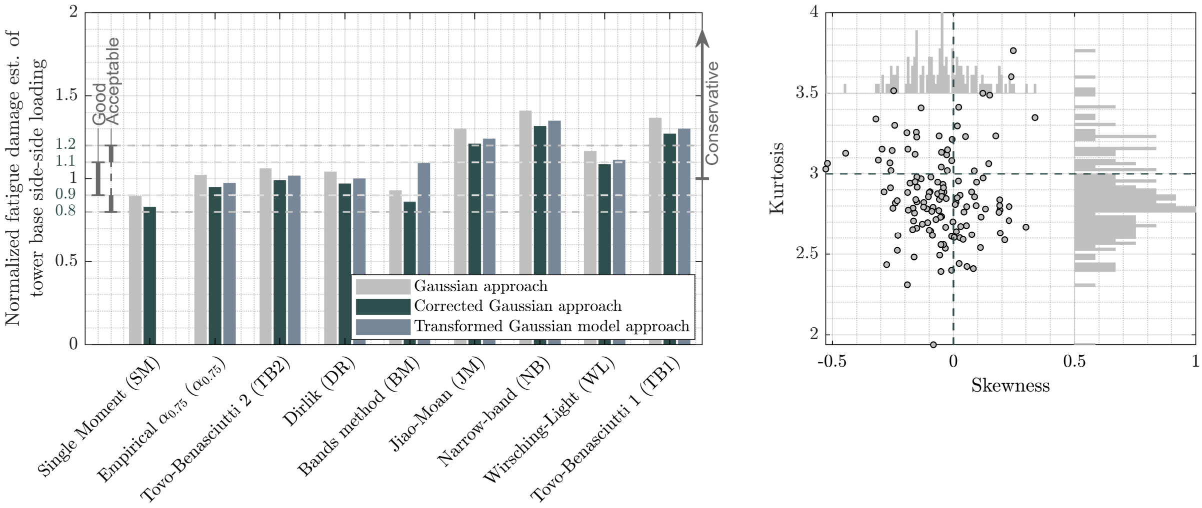

Figure 4.8 Normalised fatigue damage estimation η of tower-base bending moment in the side-side direction.

4.1.2.3 Fatigue Analysis of Tower-Base Bending Moment in Side-Side Direction

The skewness and kurtosis variations of the tower side-side loading are more consistent than that of the fore-aft direction. This is due to the fact that the side-side tower motion is mainly excited by the changes of the generator torque which depends on the rotor speed and consequently on the mean wind speed. This consistency in the skewness and kurtosis is reflected as good fatigue damage estimation of more spectral methods. Using the Gaussian approach, good results are obtained by the Empirical $\alpha_{0.75}$, Tovo-Benasciutti second method, Dirlik and Bands-Methods. These good results are further enhanced by the corrected Gaussian approach, with the exception of the Bands-method where the estimation deteriorates to an acceptable level. The use of the transformed Gaussian model approach has marginal effect when compared to the Gaussian approach; only the Bands-method shows more conservative good estimation with this approach. An interesting result is that the Wirsching-Light method using the corrected Gaussian approach gives good fatigue damage estimation. The normalised fatigue damage estimation results are presented in fig. 4.8.

4.1.2.4 Development of Fatigue Damage Estimation with Wind Speed

By taking a closer look at the development of the normalised fatigue damage estimation with wind speed for the Single-Moment, Empirical $\alpha_{0.75}$, Tovo-Benasciutti second method, Dirlik and Bands methods as illustrated in fig. 4.9 for the fore-aft bending stress and in fig. 4.10 for the side-side bending stress, it is possible to notice that the estimated fatigue damage values change with wind speed and according to the operating regions. The estimation is more consistent in the tower side-side loading direction with the change of wind speed, while in the fore-aft direction the fatigue damage estimation varies between the operating regions with less variations in the full load region. This is related to the activity of the blade pitch control system in the full load region where this controller has the task of keeping constant aerodynamic loading over the rotor disk with the change of mean wind speed. This means that the tower loading has a quasi constant mean value. While in the partial load region, the blade pitching actuator is deactivated and the rotor speed is changed according to the mean wind speed for power optimization purposes. This results into a changing aerodynamic loading over the rotor disk (thrust and toque) with the mean wind speed. The changing aerodynamic loading leads to a continues change in the mean value of the tower loading; and consequently, changes the amplitude distribution with each wind profile.

Figures. 4.9 and 4.10 show also the probability density function (PDF) of the normalised fatigue damage index; from which it is possible to calculate the probability at which a spectral method will give a good and an acceptable estimate of the fatigue damage with regard to the estimation obtained in the time-domain using the the rainflow counting algorithm. The results are presented in fig. 4.11 for both the tower side-side and fore-aft loading. As predicted before, spectral methods have higher probability of good fatigue damage estimation in the side-side loading direction of 98 %, 91 % and 79 % using the Empirical $\alpha_{0.75}$, Dirlik and Tovo-Benasciutti second method, respectively. Moreover, All these methods have more than 97% probability of

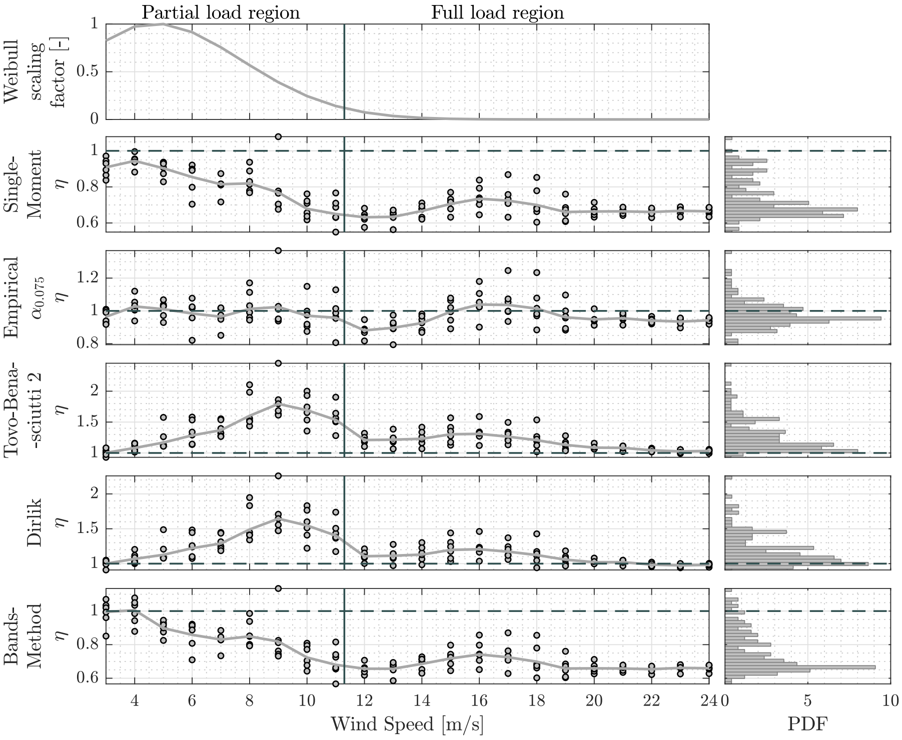

Figure 4.9 Development of normalised fatigue damage estimation η of tower fore-aft bending stress with wind speed. Simulated tower bending stress along with the Gaussian approach are used. The continuous line represents the variations of the mean value of η over the wind speed.

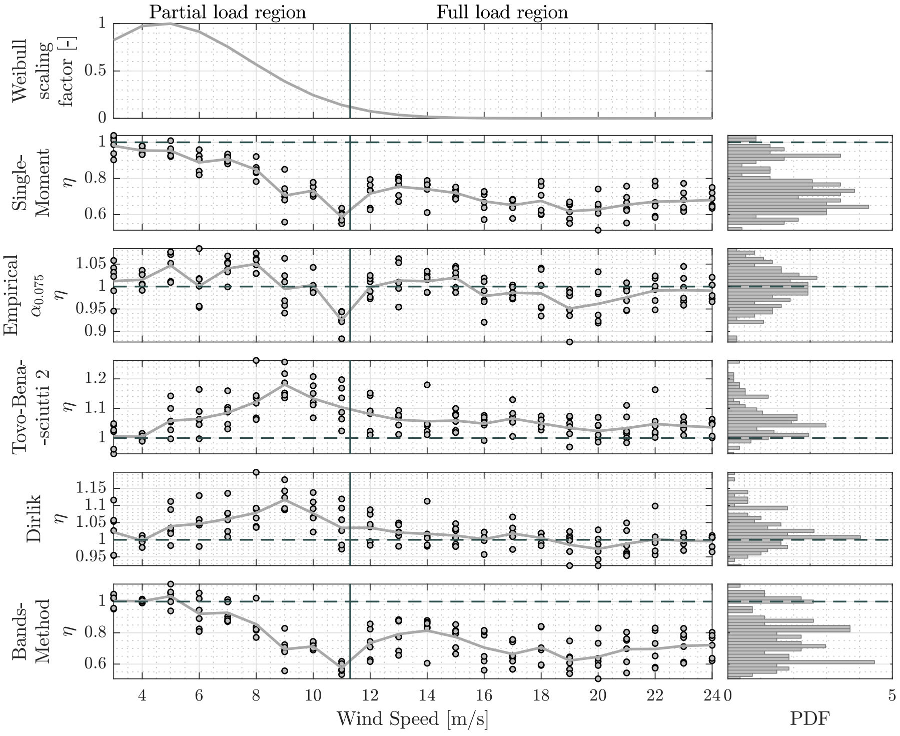

Figure 4.10 Development of normalised fatigue damage estimation η of tower side-side bending stress with wind speed simulated tower bending stress along with the Gaussian approach are used. The continuous line represents the variations of the mean value of η over the wind speed.

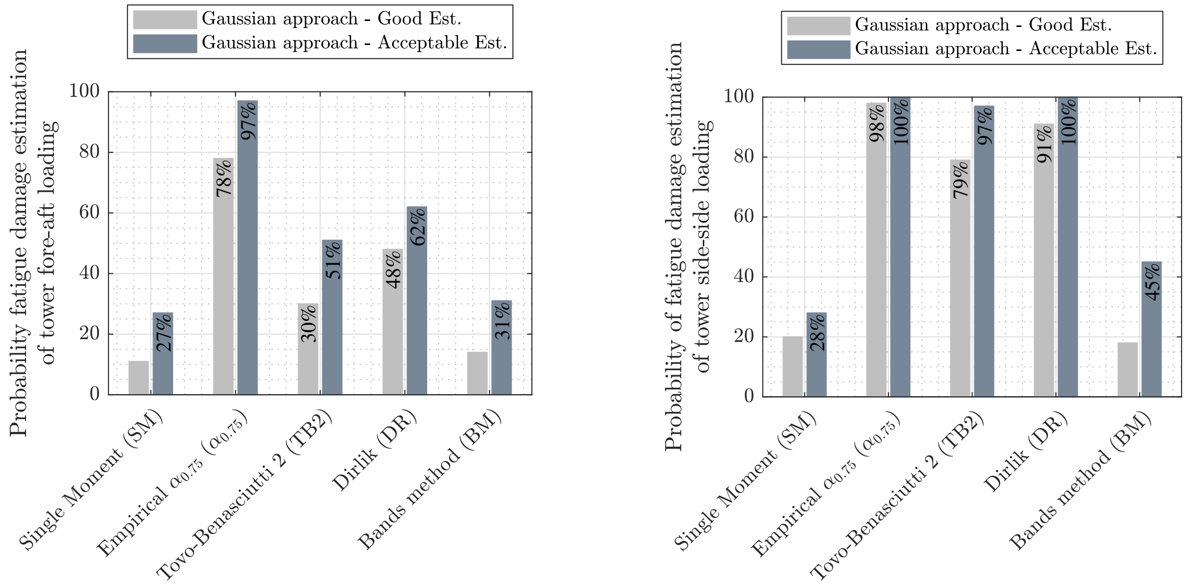

Figure 4.11 Probability of good and acceptable fatigue damage estimation using spectral methods for tower loading in fore-aft and side-side directions of a land-based wind turbine.

giving acceptable fatigue damage estimation.

On the contrary, the maximum probability of good fatigue damage estimation in the fore-aft direction is 78 % using the Empirical $\alpha_{0.75}$ method; and all other methods have less than 50 % chance of giving good estimations. Moreover, there is 97 % probability of obtaining acceptable estimation using the Empirical $\alpha_{0.75}$ method. It is clear from these results that the Empirical $\alpha_{0.75}$ method is the best spectral method for tower estimation of fatigue damage in both directions, however, the estimation accuracy is different according to the loading direction.

4.1.3 Floating Wind Turbines

The results obtained from the land-based wind turbine show that spectral methods are able to deliver good estimation of tower fatigue damage. However, estimation results vary between fore-aft and side-side directions. These results depend also on the spectral method and the operating region.

The load comparison between land-based and offshore turbines with floating platforms show dramatic increase in the loading of the floating structure. This increase is mainly in tower-base fore-aft and side-side bending moments [Jonkman, 2007]. The floating platform type would change the loading spectrum, therefore, the results of the spectral methods are also expected to vary with the platform.

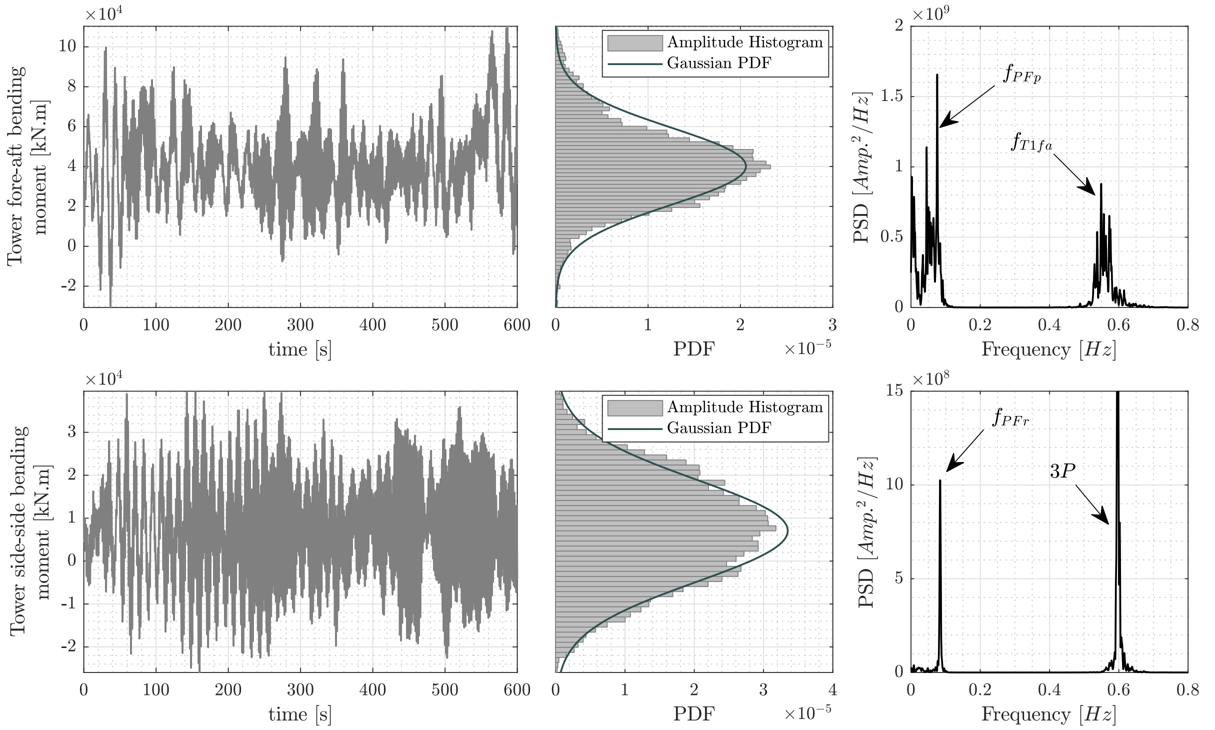

Figure 4.12 Tower bending moment characteristics in fore-aft and side-side directions for wind speed $17\frac{m}{s}$. Reference wind turbine is mounted on Barge platform.

4.1.3.1 Barge Platform

The Barge platform (fig. 3.3) is very sensitive to waves which will result to large platform pitching motion (when compared to the other platforms). The overall increase in structural loading is related to this large pitching motion that induces the oscillatory wind inflow relative to the rotor, therefore, it excites in combination with the spinning rotor inertia the gyroscopic yaw moment which turns the turbine away from the wind.

Tower Bending Moment Characteristics

As the barge platform is very sensitive to the sea waves, the floating turbine structure is subject to different loading spectrum as that of the land-based turbines. Taking for example the recorded tower bending moment at mean wind speed of $17\,\frac{m}{s}$ shown in fig. 4.12, the fore-aft and side-side directions are dominated by the platform pitching and rolling dynamic response at $f_{PLp} = 0.08\,Hz$ and $f_{PFr} = 0.09\,Hz$, respectively. In addition to that, the tower fore-aft loading has high dynamic response at the tower fore-aft frequency of $f_{T1fa} = 0.54\,Hz$, while the tower side-side loading has higher dynamic response at the $3P = 0.6\,Hz$ frequency. Both bending moments show close to Gaussian amplitude distribution with minimal skewness and kurtosis deviations from the ideal values.

The amplitude-mean histogram obtained from the rainflow cycle counting of the bending stress

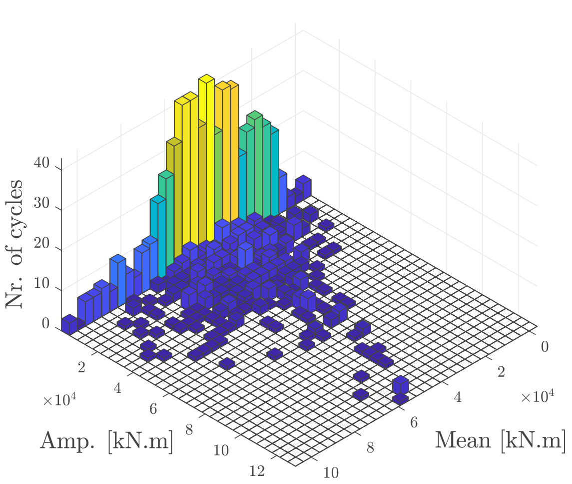

Figure 4.13 Amplitude-mean histogram of tower fore-aft bending moment of offshore reference wind turbine mounted on Barge platform and subject to wind speed 17 $\frac{m}{s}$.

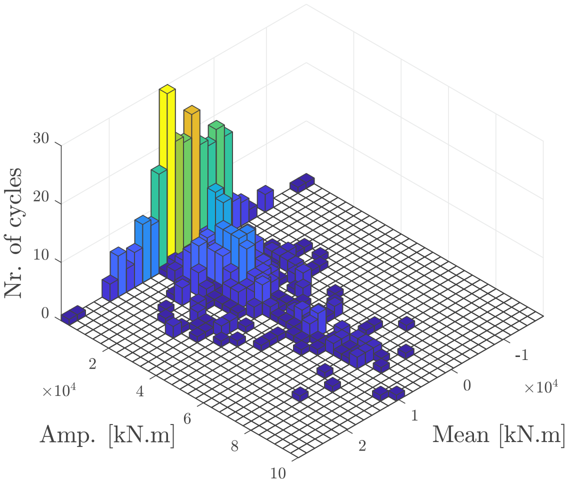

Figure 4.14 Amplitude-mean histogram of tower side-side bending moment of offshore reference wind turbine mounted on Barge platform and subject to wind speed 17 $\frac{m}{s}$.

history shown in fig. 4.12 is presented in fig. 4.13 for the fore-aft loading direction and in fig. 4.14 for the side-side loading direction. In both histograms it is possible to differentiate between the small amplitude cycles with high frequencies which correspond to the aerodynamic loading; and the cycles with larger amplitude and less occurrence, these cycles correspond to the hydrodynamic loading and the interaction between the turbine structure and the wind.

Tower Bending Moment in Fore-Aft Direction

The normalised fatigue damage index of the tower fore-aft bending moment using the simulated time-series is illustrated in fig. 4.15. According to these results, only the Gaussian approach combined with the Empirical $\alpha_{0.75}$ method gives good fatigue damage estimation; while acceptable estimations are obtained using the Single-Moment and Bands-methods. The corrected Gaussian and the transformed Gaussian model approaches do not improve the results.

By having a closer look at the skewness-kurtosis scattering, it is possible to notice positive mean skewness and less scattering of the kurtosis results when compared to the land-based tower fore-aft bending stress (fig. 4.15). The positive skewness could be explained as the mean thrust force over the rotor disc will produce a non-zero mean platform pitching angle. Therefore, the distance between the rotor centre of gravity and the mean tower axis is increased; and tower-base bending moment in the fore-aft direction has a mean value that depends on the mean wind speed.

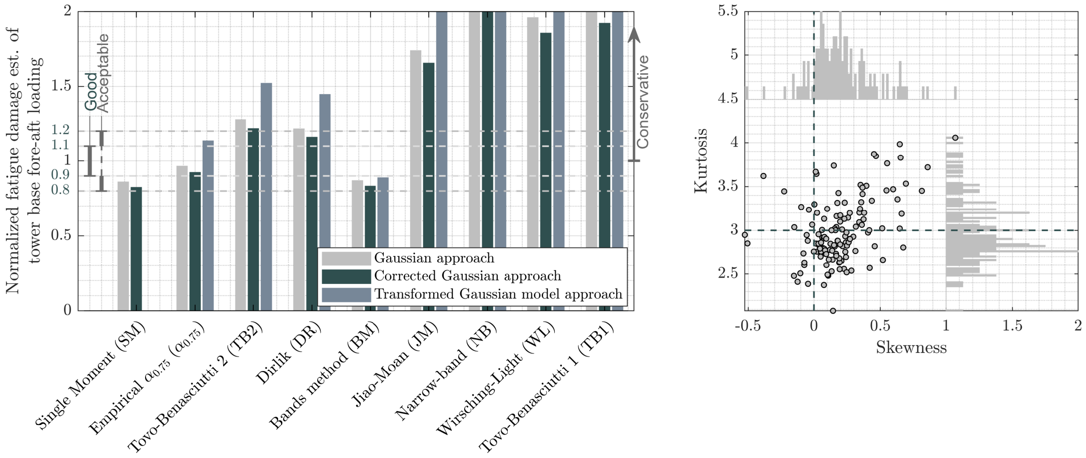

Figure 4.15 Normalised fatigue damage index η of recorded tower fore-aft bending stress using three different spectral fatigue damage analysis approaches. Reference wind turbine is mounted on the floating Barge platform.

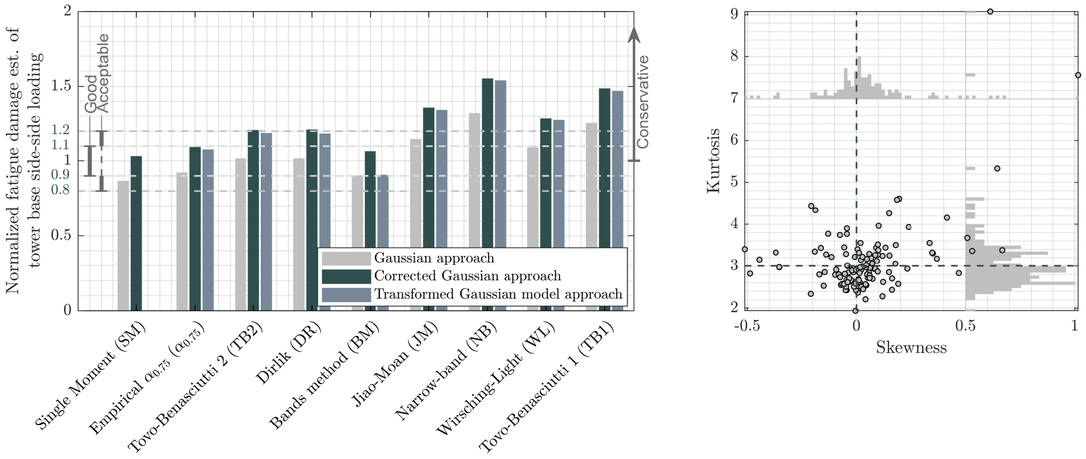

Figure 4.16 Normalised fatigue damage estimation η of recorded tower side-side bending stress using three different spectral fatigue damage analysis approaches. Reference wind turbine is mounted on the floating Barge platform.

Tower Bending Moment in Side-Side Direction

Tower bending moment in this direction enjoys good Gaussian characteristics. This is clear from the skewness-kurtosis scattering illustrated in fig. 4.16 where the skewness ranges between ±0.2 (with some exceptions) and the kurtosis is close to three. Good fatigue damage estimations with regard to the time-domain estimation results are obtained using the Gaussian approach with the Tovo-Benasciutti second method, Dirlik, Wirsching-Light and the Empirical $\alpha_{0.75}$ methods, while acceptable estimations are obtained by the bimodal Jiao-Moan, Band- and the Single-Moment methods. Moreover, the corrected Gaussian and the transformed Gaussian model approaches tend to give more conservative estimations with the exception of the corrected Gaussian model combined with the Single-Moment and Bands methods where good fatigue damage estimation is obtained.

Development of Fatigue Damage Estimation with Wind Speed

By taking a closer look at the development of the normalised fatigue damage index with wind speed as illustrated in fig. 4.17 for the fore-aft bending moment and in fig. 4.18 for the side-side direction. It is possible to notice that the fatigue damage index in the full load region is more consistent and close to unity, while in the partial load region, large deviations from unity are observable. The stability of estimation results in the above rated region is related to the activity of the blade pitching system that keeps minimal change of the aerodynamic forces over the rotor disc which results to more stationary loading.

Furthermore, figures. 4.18, 4.17 show also the probability density function (PDF) of the normalised fatigue damage estimations; from which it is possible to calculate the probability at which a spectral method will give a good and an acceptable estimate the fatigue damage. The results are presented in fig. 4.19 for both the tower fore-aft and side-side bending moment. With regard to the time domain fatigue damage estimations, the best probability of obtaining good fatigue damage estimation is given by the Empirical $\alpha_{0.75}$ method with probability of 86 % and 79 % in the side-side and fore-aft directions, respectively. The probability of good estimation from the other spectral methods do not exceed 60 %. Moreover, it is possible to obtain an acceptable estimation in the side-side direction with probability of 95 %, 91 %, 90 %, 89 % and 82 % using the Empirical $\alpha_{0.75}$, Bands-Method, Single Moment, Dirlik ans Tovo-Benasciutti second method, respectively. In the fore-aft direction the Single-Moment, Empirical $\alpha_{0.75}$ and Bands-Method have similar chances about $88\,\% - 91\,\%$ in giving acceptable estimation.

Tower bending moment in the fore-aft direction is mainly affected by the platform pitching motion that depends on the mean wind speed. This motion exacerbates the tower bending moment due to the rotor and nacelle eccentricity which leads to a changing bending moment mean value. Taking this into account and following the work steps illustrated in fig. 2.18 to run fatigue analysis on non-stationary time-series (de-trending with MATE with $12\,s$ window and using the transformed Gaussian model approach), it is possible to get more good results with 80 % and 74 % probability from Dirlik and Tovo-Benasciutti second method (compared to 23 % and 7 % probability for Dirlik and Tovo-Benasciutti second method, respectively, when using the bending stress history with the Gaussian approach). This could be achieved while maintaining similar good result with 76 % probability from the Empirical $\alpha_{0.75}$ method (79 % using the recorded time-series and the Gaussian approach).

As the spectral methods show more consistent estimations in the above rated region, the probability of obtaining good and acceptable estimations are also illustrated in fig. 4.19. It is worth to mention that more spectral methods are able to give good and acceptable fatigue damage estimates with probability more than 80 % in both fore-aft and side-side loading directions in

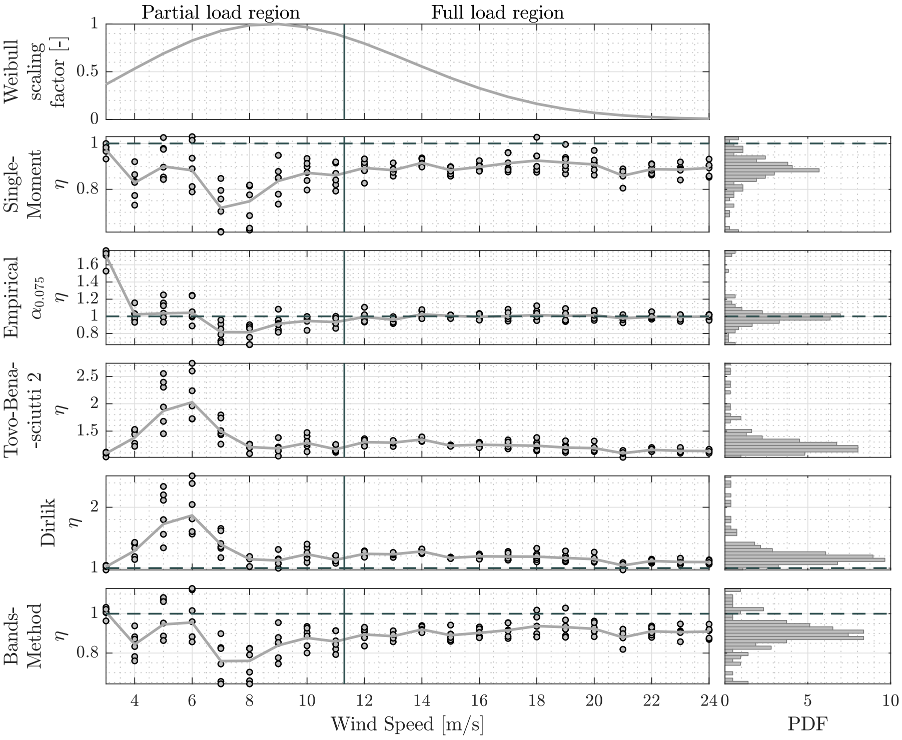

Figure 4.17 Development of normalised fatigue damage index η of tower fore-aft bending moment with wind speed. Estimations are based on recorded tower bending moment on Barge platform along with the Gaussian approach. The continuous line represents the variations of the mean value of η over the wind speed.

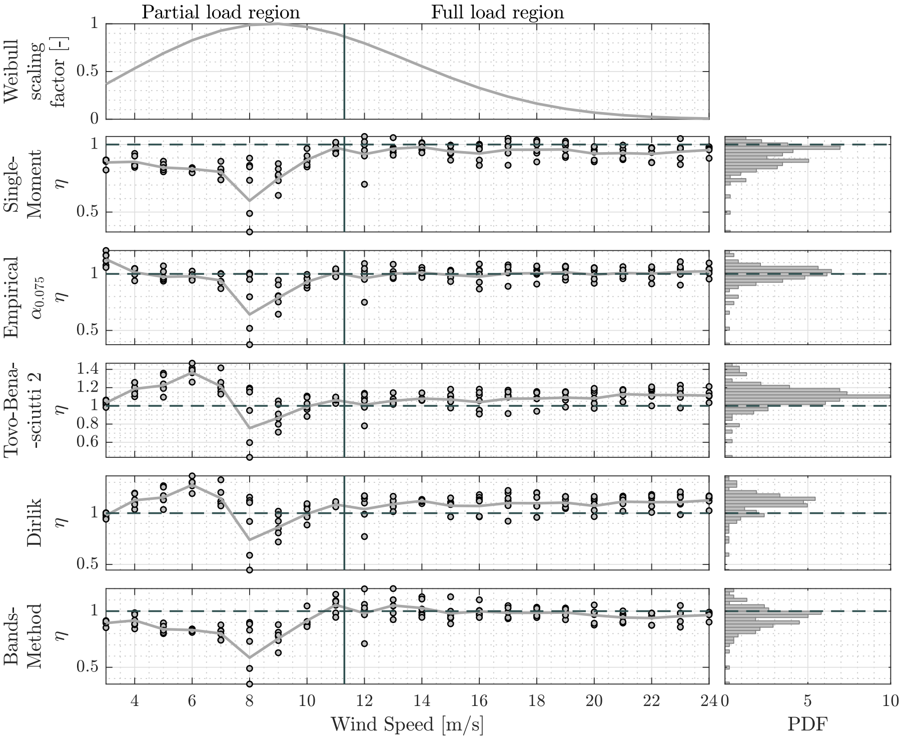

Figure 4.18 Development of normalised fatigue damage index η of tower side-side bending moment with wind speed. Estimations are based on recorded tower bending moment on Barge platform along with the Gaussian approach. The continuous line represents the variations of the mean value of η over the wind speed.

the full load region.

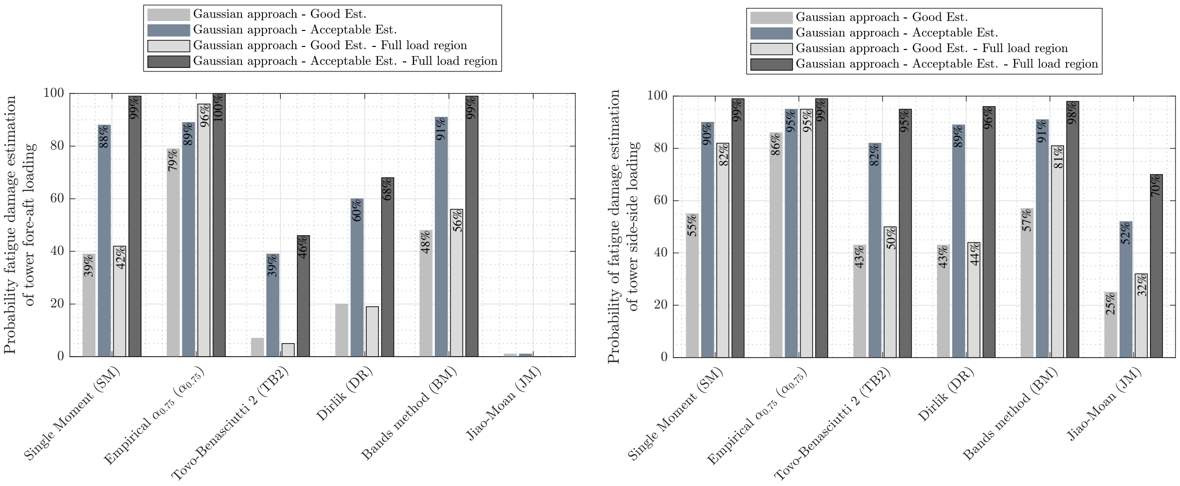

Figure 4.19 Probability of good and acceptable fatigue damage estimation using spectral methods for tower loading for floating wind turbine on Barge platform.

Conclusion

By taking the rainflow counting algorithm as a reference fatigue damage estimation, spectral methods are less accurate in fatigue analysis of tower bending moment of floating wind turbines on Barge platform configuration. Spectral-based fatigue damage estimations are more consistent in the full load region than on the partial load region. The only method that is able to maintain the same level of estimation performance in both loading directions (fore-aft and side-side) in addition to both operating regions is the Empirical $\alpha_{0.75}$. Although the tower bending moment spectrum in both directions looks as a bimodal system, the Jiao-Moan bimodal method fails to give any reasonable estimations.

It is possible to improve the estimation results with regard to the time-domain of the Dirlik method and Tovo-Benasciutti second method by decomposing the stress time-series into a deterministic and stochastic components using a moving average trend estimator filter with window length of $12\,s$. Then using the Transformed Gaussian model approach for fatigue analysis per each signal (deterministic signal is treated as stochastic one at this point and the same spectral method is used for fatigue estimation of both signals). Finally combining the results using the Project-by-Projection concept to obtain the over all fatigue damage value.

4.1.3.2 Spar-Buoy Platform

The Spar-Buoy platform is build to be less sensitive to incident waves. That is achieved by using ballast tanks to attain hydrostatic stability (see fig. 3.3). This design concept led to a low pitching and rolling natural frequencies of $0.02\,Hz$ each (due to symmetry). The main benefit obtained by this design is a reduction in turbine structural loading due to the limited platform motion when compared to that of the Barge platform.

Tower Bending Moment Characteristics

Tower bending moment spectrum on Spar-Buoy platform is different from that on Barge-platform as it is clear by comparing fig. 4.12 and fig. 4.20. The low pitching motion $f_{PFp} = 0.02\,Hz$ of the Spar-Buoy platform could be identified from the tower bending moment in the fore-aft direction. This pitching motion dominates the response in the fore-aft direction while the tower response at its first natural frequency $f_{T1ss} = 0.38\,Hz$ in the side-side direction is more dominant rather than the platform rolling motion $f_{PRr} = 0.02\,Hz$. Both bending moments show close to Gaussian amplitude distribution with minimal skewness and kurtosis deviations from the ideal values. It is also possible to notice that the tower bending moment amplitude in both directions on the Spar-Buoy platform is less than that on the Barge platform.

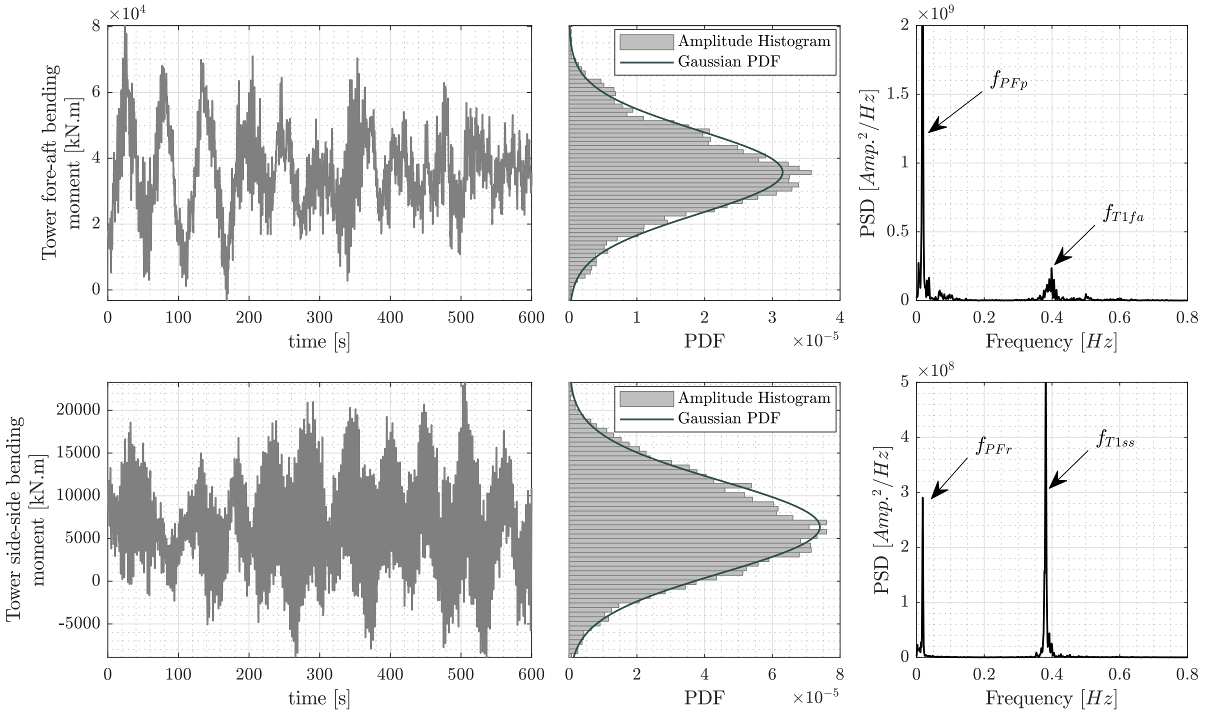

Figure 4.20 Tower bending moment characteristics in fore-aft and side-side directions for wind speed 17 $\frac{m}{s}$. Reference wind turbine is mounted on Spar-Buoy platform.

Tower Bending Moment in Fore-Aft Direction

The normalised fatigue damage index of the tower fore-aft bending stress using the recorded time-series is illustrated in fig. 4.21. It is possible to see that the Empirical $\alpha_{0.75}$ and the Bands methods give good estimation when combined with the Gaussian approach. Acceptable estimations using the same approach are also obtained using the Single-Moment method. The use of the corrected Gaussian and the transformed Gaussian models approaches have marginal effect with the exception of the Bands-Method where the transformed Gaussian approach leads to very conservative estimation.

The skewness-kurtosis scatter plot shows that the tower bending moment in this direction has more skewness than that on Barge platform while the kurtosis stays in similar range.

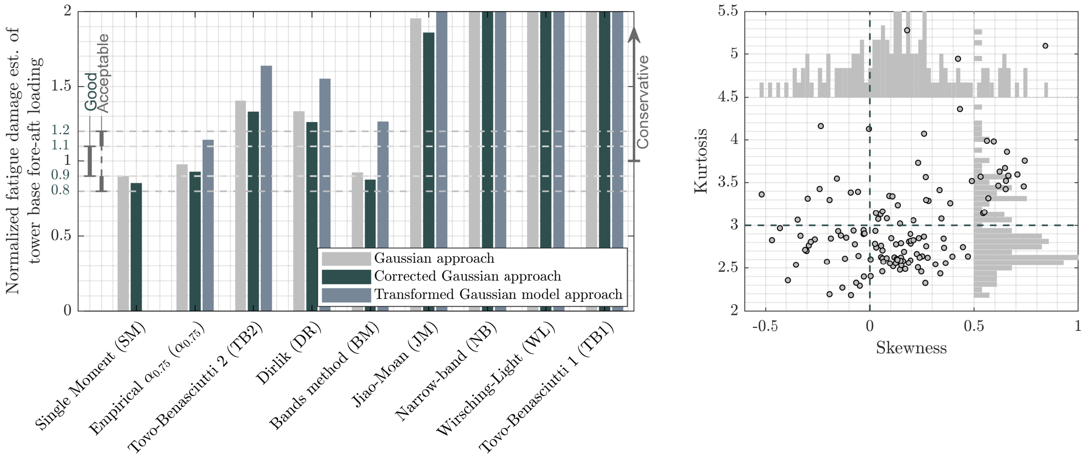

Figure 4.21 Normalised fatigue damage index η of recorded tower fore-aft bending moment using three different spectral fatigue damage analysis approaches. Reference wind turbine is mounted on the floating Spar-Buoy platform.

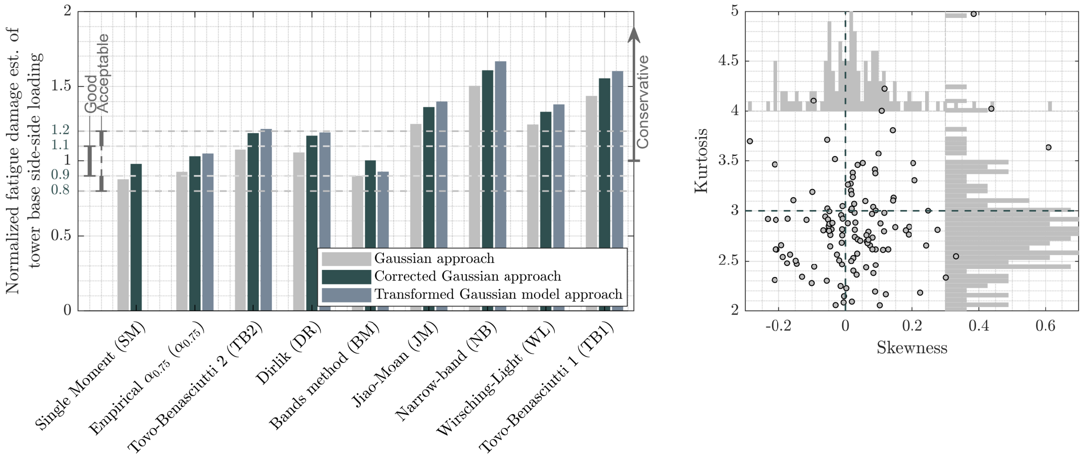

Figure 4.22 Normalised fatigue damage index η of recorded tower side-side bending moment using three different spectral fatigue damage analysis approaches. Reference wind turbine is mounted on the floating Spar-Buoy platform.

Tower Bending Moment in Side-Side Direction

The skewness-kurtosis scatter plot (fig. 4.22) is more scattered than that of Barge platform. The skewness of tower loading in the side-side direction on the Spar-Buoy platform ranges between ±0.5 while the kurtosis goes between 2 and 5. This indicates more deviations from the ideal Gaussian amplitude distribution. Good fatigue damage estimations are obtained using the Empirical $\alpha_{0.75}$, Tovo-Benasciutti second method and Dirlik methods when combined with the Gaussian approach. Taking the non-Gaussianity into account using the corrected Gaussian approach makes the estimation results about 10 % more conservative. This has moved the estimation results of the Single-Moment and Bands methods from being acceptable to be good and on the contrary it moves the good estimation result of Tovo-Benasciutti second method and Dirlik to an acceptable level all with regard to the reference fatigue damage estimation in the time-domain. Finally, the transformed Gaussian model follow the same course of the corrected Gaussian approach.

Development of Fatigue Damage Estimation with Wind Speed

The development of the normalised fatigue damage index with wind speed is illustrated in fig. 4.23 for the fore-aft bending stress and in fig. 4.24 for the side-side direction. Unlike to the obtained results in the case of the Barge platform, fatigue damage estimation is less consistent with the change of wind speed in the side-side tower bending direction. However, in the fore-aft direction, the Empirical $\alpha_{0.75}$ keeps the same level of consistency, while the Dirlik and Tovo-Benasciutti second methods tend to be more conservative with the change of wind speed. As mentioned before, the use of the corrected Gaussian and the transformed Gaussian model approaches do not improve the estimation accuracy with regard to the reference method. The same is observed if the stress time-series are also considered non-stationary.

Furthermore, figures. 4.23 and 4.24 show also the probability density function (PDF) of the normalised fatigue damage index; from which it is possible to calculate the probability at which a spectral method will give a good and an acceptable estimate of the fatigue damage with regard to the reference time domain fatigue damage estimation. The results are presented in fig. 4.25 for both loading directions. The best probability of obtaining good fatigue damage estimation is given by the Empirical $\alpha_{0.75}$ method with probability of 70 % and 71 % in the side-side and fore-aft directions, respectively. The probability of good estimation from the other spectral methods does not exceed 60 %. Moreover, it is possible to obtain an acceptable estimation in the side-side direction with probability of 93 %, 92 % and 89 % using the Bands method, Single-Moment and Empirical $\alpha_{0.75}$, respectively. In the fore-aft direction the Bands-Method, the Empirical $\alpha_{0.75}$ and the Single-Moment methods have a 96 %, 92 % and 91 % probability of giving an acceptable estimation.

Conclusion

With regard to the reference fatigue damage estimation using the rainflow counting algorithm, the Empirical $\alpha_{0.75}$ is again the only method that keeps consistent level of good and acceptable fatigue damage estimation in the case of Spar-buoy platform. However, the performance of the Empirical $\alpha_{0.75}$ combined with the Gaussian approach on Spar-Buoy platform does not match that on Barge platform. Moreover, time-series decomposition doesn't improve the overall results

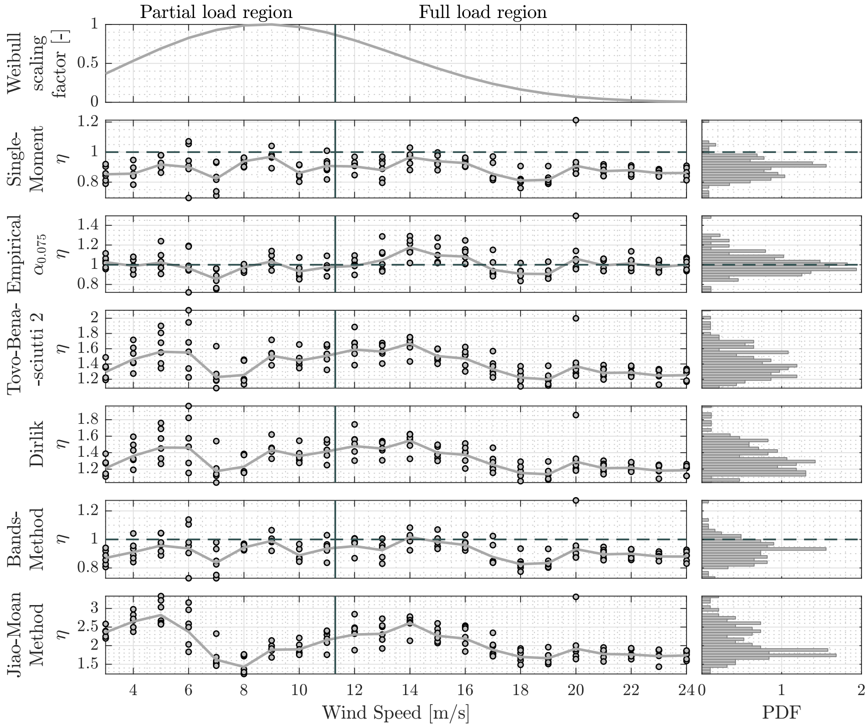

Figure 4.23 Development of normalised fatigue damage index η of tower fore-aft bending stress with wind speed. Estimations are based on recorded tower bending stress on Spar-Buoy platform along with the Gaussian approach. The continuous line represents the variations of the mean value of η over the wind speed.

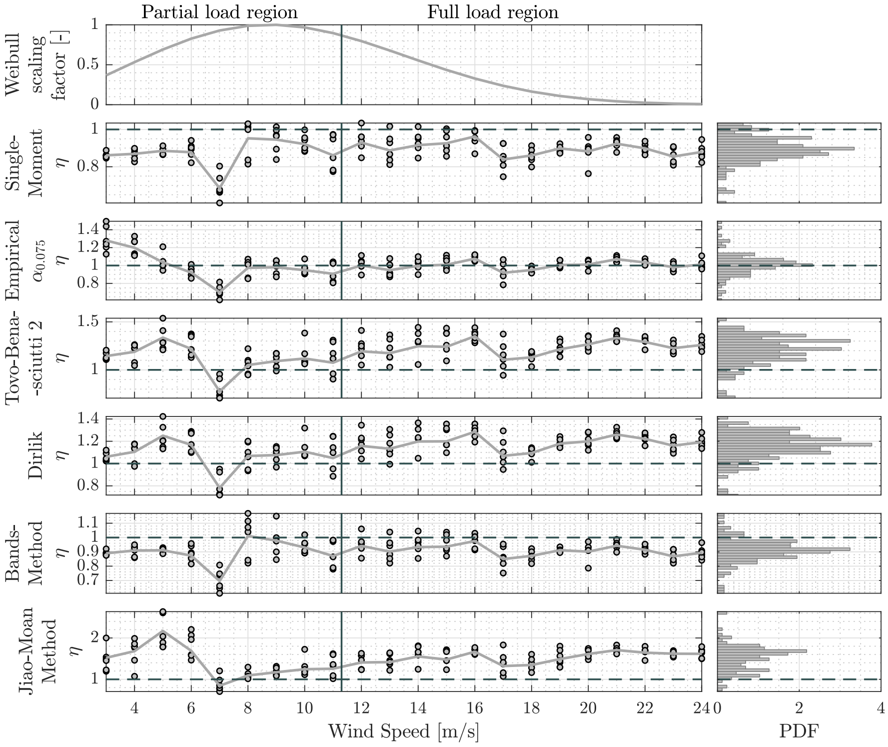

Figure 4.24 Development of normalised fatigue damage index η of tower side-side bending stress with wind speed. Estimations are based on recorded tower bending stress on Spar-Buoy platform along with the Gaussian approach. The continuous line represents the variations of the mean value of η over the wind speed.

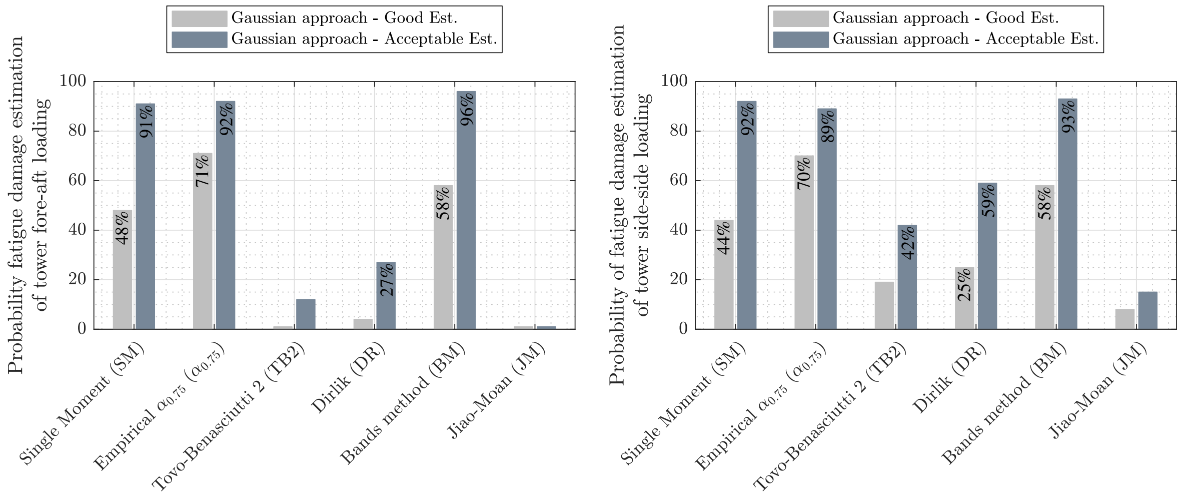

Figure 4.25 Probability of good and acceptable fatigue damage estimation using spectral methods for tower loading for floating wind turbine on Spar-Buoy platform.

(results not shown).

4.1.3.3 Tension Leg Platform

The tension leg platform (TLP) uses taught mooring lines to maintain hydrostatic stability. The platform is a cylindrical hull that is fixed in its location through tensioned mooring lines attached from one side to the hull through four spokes and from the other side to the seabed as shown in fig. 3.3. Most of the platform hull is under the water in order to minimise its interaction with the incident waves thus reducing its sensitivity. Furthermore, the tensioned mooring lines increase the stiffness of the platform roll, pitch and heave motions. This could be clearly seen from the increased natural frequency of the pitch and roll DOF to $0.15\,Hz$ (see tab. 3.2). The main drawback of this deign is its high cost of the anchors and the dependency on seabed soil condition that should support the large tensile forces.

Tower Bending Moment Characteristics

The tower-base bending moment spectrum on TLP is different from that on the previous platforms (fig. 4.26). The increased platform stiffness due to the tensioned mooring lines shifts the tower natural frequencies up. The fore-aft bending moment direction is dominated by the tower fore-aft natural frequency $f_{T1fa} = 0.72\,Hz$ in addition to the wind loading at frequencies below $0.1\,Hz$ and the high dynamic response at the platform pitching frequency $f_{PFp} = 0.22\,Hz$ which is close to $1P = 0.2\,Hz$. On the side-side loading direction, the spectrum shows high dynamic responses at the platform rolling frequency $f_{PFr} = 0.22\,Hz$ and at the tower side-side natural frequency $f_{T1ss} = 0.73\,Hz$. Wind loading in this direction has less effect. Both loading directions have an amplitude distribution that is close to the normal distribution with minimal

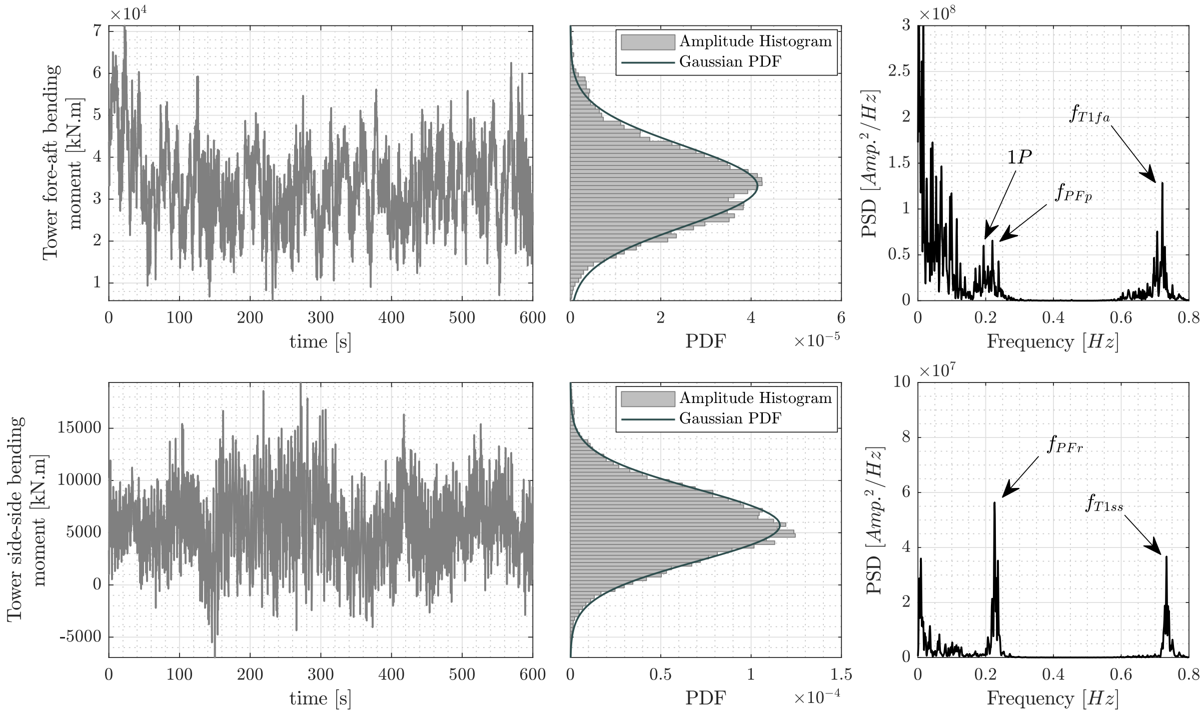

Figure 4.26 Tower bending moment characteristics in fore-aft and side-side directions for wind speed 17 $\frac{m}{s}$. Reference wind turbine is mounted on tension leg platform.

skewness and kurtosis deviations from the ideal values.

Tower Bending Moment in Fore-Aft Direction

Fig. 4.27 shows the changes of the normalised fatigue damage index η of the tower fore-aft bending stress. It is possible to see that the Empirical $\alpha_{0.75}$ gives good estimation with regard to the reference time-domain method when combined with the Gaussian and the corrected Gaussian approaches with minor correction presented by the later. Acceptable estimations using the same approaches are also obtained using the Single-Moment and Bands methods. The use of corrected Gaussian approach has minor effect on the overall averaged estimation. On the contrary, the transformed Gaussian model approach makes the estimations much more conservative. The skewness-kurtosis scatter plot is also shown in the figure.

Tower Bending Moment in Side-Side Direction

Good fatigue damage estimations are obtained using the Empirical $\alpha_{0.75}$, Tovo-Benasciutti second method and Dirlik methods when combined with the Gaussian approach in the tower-based fatigue analysis in the side-side direction (fig. 4.28). Similar to the fore-aft direction, the corrected Gaussian approach has marginal effect and in most cases the transformed Gaussian model approach leads to conservative estimations. Moreover, the skewness-kurtosis scattering has similar pattern to the fore-aft loading direction.

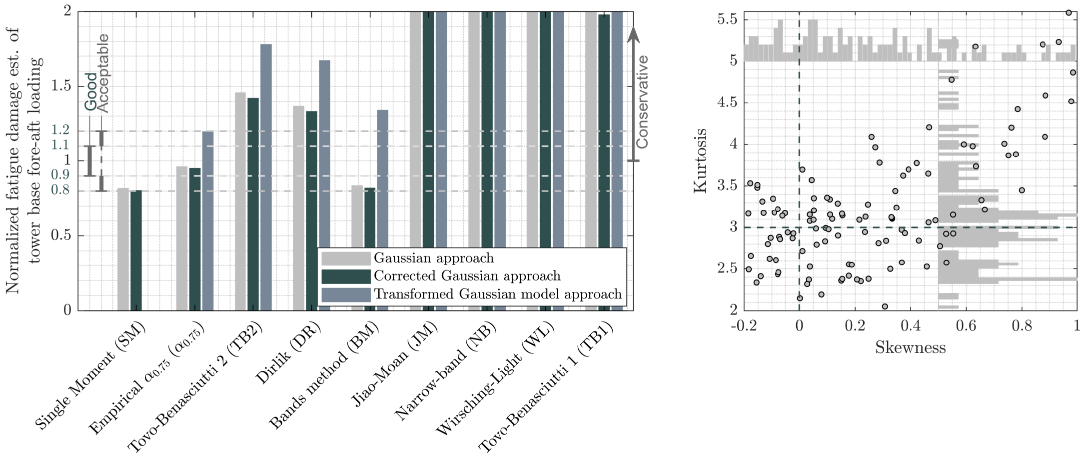

Figure 4.27 Normalised fatigue damage index η of recorded tower fore-aft bending stress using three different spectral fatigue damage analysis approaches. Reference wind turbine is mounted on the floating tension leg platform (TLP).

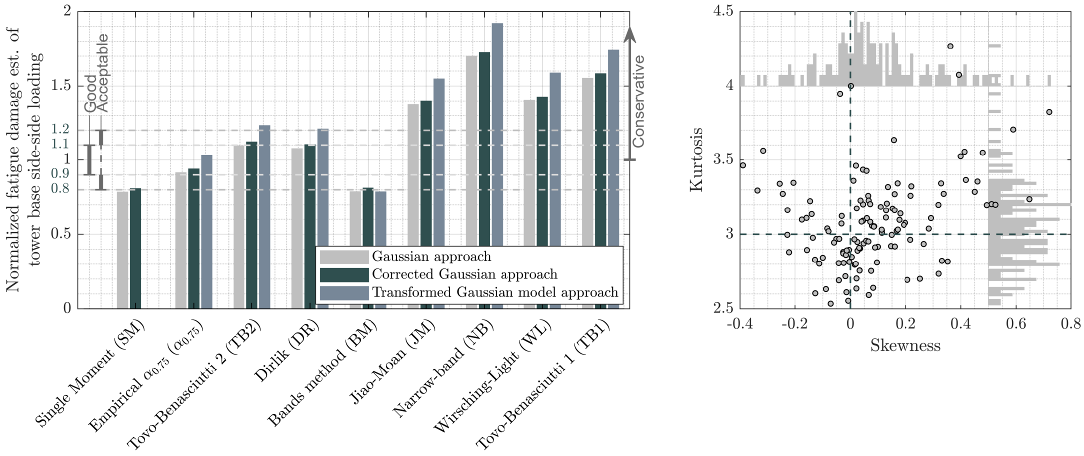

Figure 4.28 Normalised fatigue damage index η of recorded tower side-side bending index using three different spectral fatigue damage analysis approaches. Reference wind turbine is mounted on the floating tension Leg platform (TLP).

Development of Fatigue Damage Estimation with Wind Speed

The development of the normalised fatigue damage index η with wind speed for the side-side and fore-aft tower-base bending stress is shown in fig. 4.29 and fig. 4.30, respectively. The Empirical $\alpha_{0.75}$ method shows consistent estimation with wind speed in the fore-aft direction and to less degree in the side-side direction, while the Tovo-Benasciutti second method and Dirlik methods have more consistent estimations in the full load region while in the partial load regions the estimation varies with the wind speed. The bimodal Jiao-Moan method follow the same pattern with more conservative course. Moreover, the Single-Moment and the Bands methods show the same behaviour in both operating regions with non-conservative estimations.

The probability of obtaining good and acceptable fatigue damage estimation calculated form

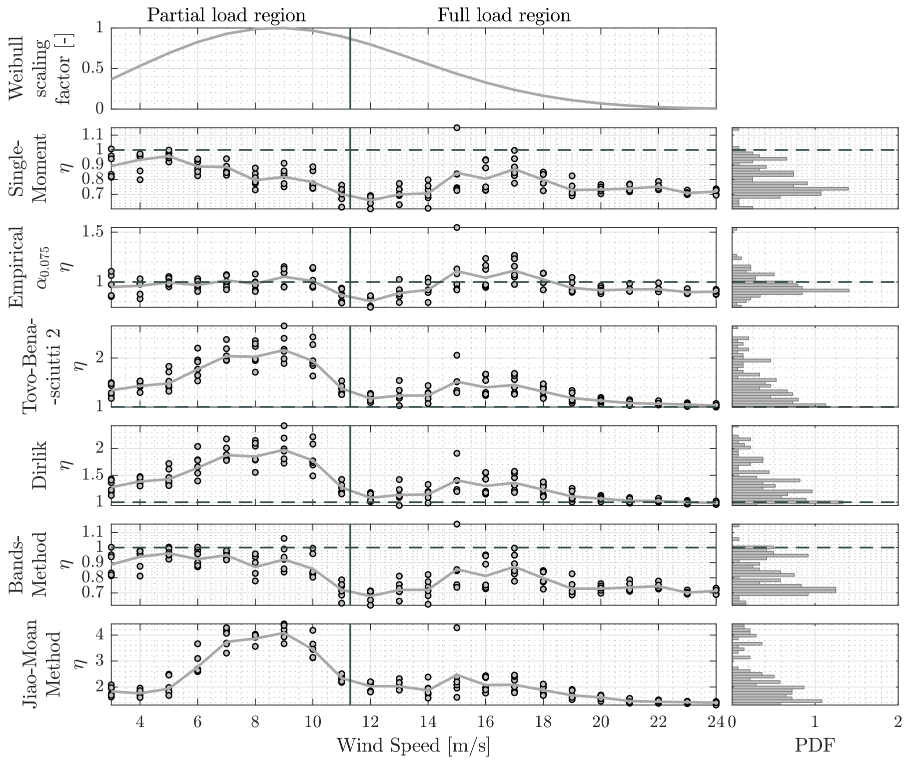

Figure 4.29 Development of normalised fatigue damage index η of tower fore-aft bending stress with wind speed. Estimations are based on recorded tower bending stress on tension leg platform (TLP) along with the Gaussian approach. The continuous line represents the variations of the mean value of η over the wind speed.

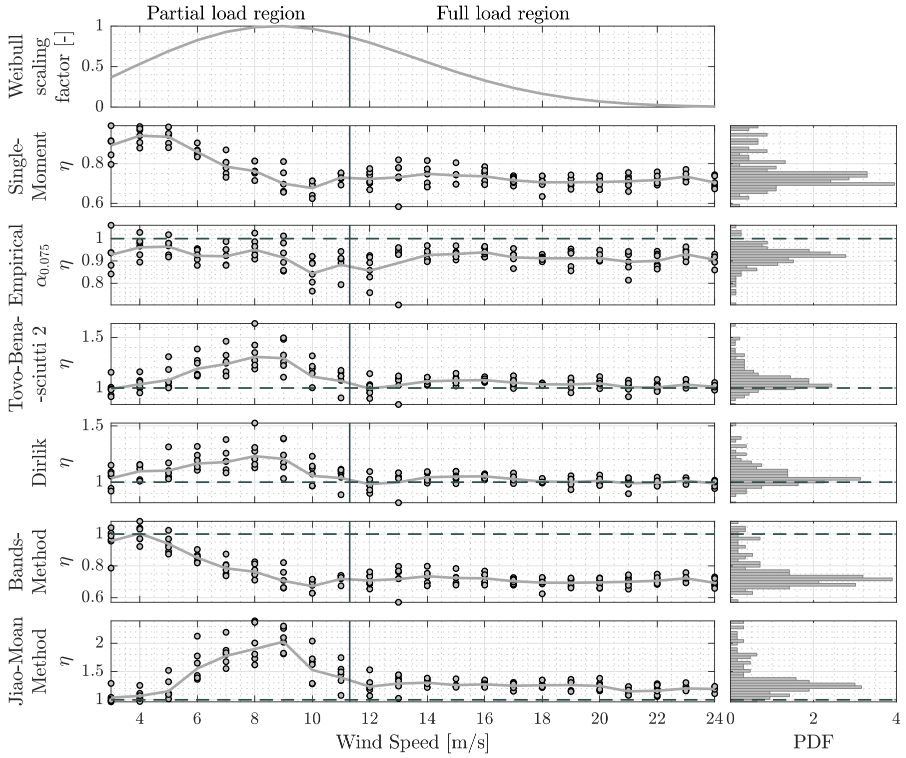

Figure 4.30 Development of normalised fatigue damage index η of tower side-side bending stress with wind speed. Estimations are based on recorded tower bending stress on tension leg platform (TLP) along with the Gaussian approach. The continuous line represents the variations of the mean value of η over the wind speed.

the PDF shown in fig 4.29 and fig. 4.30 is given in fig. 4.31. Once again, the Empirical $\alpha_{0.75}$ has more probability in giving good and acceptable estimations with regard to the reference method in both loading directions with 72 % and 97 % probability of good and acceptable estimation in the side-side direction; and 68 % and 93 % probability of good and acceptable estimate in the fore-aft direction. In addition to the Empirical $\alpha_{0.75}$, Dirlik and Tovo-Benasciutti second method have good chances in giving good and acceptable estimations in the side-side direction while in the fore-aft direction the maximum probability of acceptable estimation is lower than 50 %.

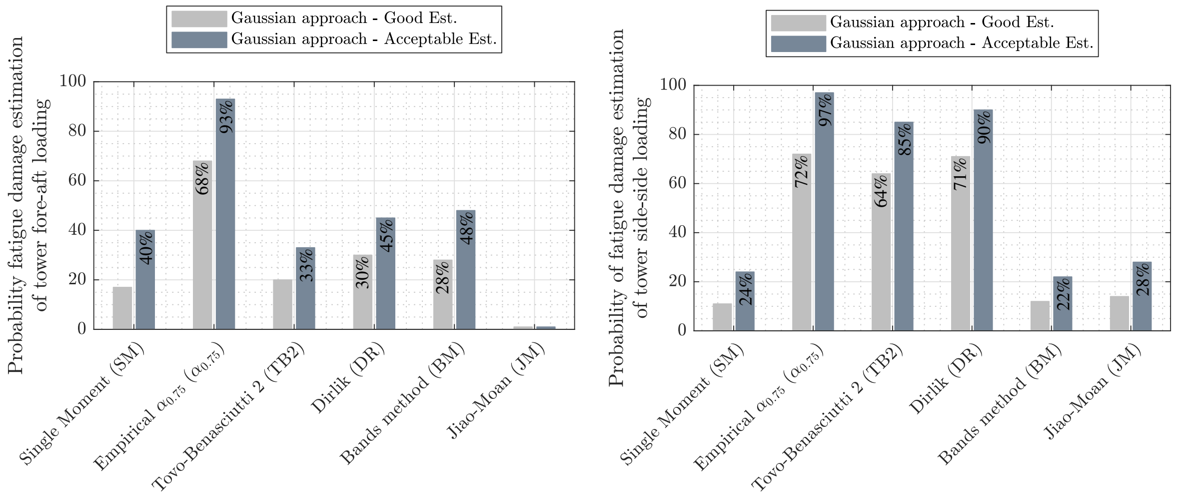

Figure 4.31 Probability of good and acceptable fatigue damage estimation using spectral-based methods for tower bending stress for floating wind turbine on tension leg platform (TLP).

Conclusion

The comparison of the fatigue damage estimation of spectral-based methods against the reference estimation in time-domain using the rainflow cycle counting algorithm shows the Empirical $\alpha_{0.75}$ method being the only spectral method that keeps consistent good and acceptable fatigue damage estimation of tower-base bending stress in both directions and operating regions. Fatigue analysis using this method along with the Gaussian approach has similar probability of good and acceptable estimation to the other floating platforms. Moreover, taking the non-Gaussianity into account by using the corrected Gaussian or the transformed Gaussian model approaches doesn't improve the estimation results. The same applies to decomposing the loading time-series and using the “De-trending&PbP” approach.

4.1.4 Conclusion Obtained from Simulation Data-Set

The dynamic response of the wind turbine due to the stochastic wind and wave loading changes according to the substructure configuration. This change in the dynamic response results into a change in the power spectral density of the monitored loading in addition to the nature of the distributed loading amplitude.

Fatigue analysis of simulated data-set using Gaussian, corrected Gaussian and transformed Gaussian model approaches carried out on tower fore-aft and side-side bending stress at different wind turbine configurations have demonstrated that the spectral-based methods are able to give comparable fatigue damage estimations to the industry standard rainflow cycle counting algorithm. Several spectral methods are able to give good to acceptable fatigue estimations with regard to the reference method, while the rest tend to give conservative estimations when compared to the cycle counting in time domain. That is to say, the use of the spectral method will lead in the worst case scenario to an over estimation of fatigue damage. This might be acceptable in the early design stage.

The overall summary of the obtained results are presented in tab. 4.5. These results show that more spectral-based methods tend to give good to acceptable results in fatigue analysis of the land-based turbine, while conservative fatigue estimation results with regard to the reference estimation are obtained by most spectral methods when used for fatigue analysis of the simulated stress history of the floating turbine configuration. This is related to the added extra degrees of freedom introduced by the floating platform which affect the tower-based stress significantly.

In all studied cases, more spectral-based methods are able to give comparable results to the time-domain fatigue analysis of the tower side-side bending stress. This could be explained that this loading direction is less subject to the change of mean wind and wave loading.

As the tower-based fore-aft bending stress is subject to the change of mean wind speed, spectral fatigue damage analysis of this loading direction should be carefully carried out. With regard to the reference estimation in time domain, only the Empirical $\alpha_{0.75}$ is able to keep the good performance level for all turbine configurations while assuming the Gaussian approach. Moreover, acceptable to good estimation results are also possible to obtain using the Single-Moment and the Bands-methods according to floating turbine configuration.

The transformed Gaussian model approach improves the obtained fatigue results to a good level of the Dirlik and 2$^{\text{nd}}$ Tovo-Benasciutti methods on land-based turbines in both tower loading directions. However, this effect does not extend to the case of floating turbines. On the other side, the corrected Gaussian approach doest not have such effect on the results. Similarly, detrending and PbP approach doesn't also improve the spectral fatigue damage analysis results. This is related to that fact that the deterministic component is still post-processed in this procedure as a stationary Gaussian loading which is far from being realistic. Better result could be obtained by using the rainflow cycle counting to post-process the deterministic component.

This will improve the performance of this procedure, however, the advantage of using spectral fatigue analysis of simulated data is lost in this case as the cycle counting will require actual simulated stress time-series, not only their power spectral density.

Another point should be mentioned is the dependency of the spectral fatigue damage results on the mean wind speed. While good fatigue damage estimations are possible to obtain using for example the Single-Moment, Empirical $\alpha_{0.75}$, 2^{nd} Tovo-Benasciutti and Dirlik methods in the full load region, the estimations scatter at the partial load region. This could be explained by the increase of the aerodynamic loading over the rotor disc with the increase of wind speed in the partial load region due to the power maximization objective of the controller. The increase of the aerodynamic loading results into a change of the mean stress value on the tower fore-aft bending stress which in-turn affects the spectral estimation results. As the reference wind turbine enters the full load region, the blade pitch actuator is activated and the aerodynamic loading over the rotor disk is kept quasi constant due to the control objective of optimal power production. This means keeping constant wind speed mean value over the rotor and, consequently, steady tower fore-aft bending stress mean value. In spite of the higher turbulent intensity at the full load region, many spectral methods are still able to give good fatigue damage estimations with regard to the reference fatigue damage estimation method in time domain.

The obtained results depend on the wind turbine type and its operating regions. The considered reference wind turbine is a variable-speed variable-pitch wind turbine with two main operating regions as illustrated in the turbine power curve. These two regions have different control objectives with different actuators that operate at each region. Other turbine types such as the variable-speed fixed-pitch turbines are stall regulated ones with different power curve. The dynamic response of the stall regulated turbines is different from the reference turbine, therefore, the performance of the spectral-based methods with turbine operating regions will also differ from the presented results. The same applies for other turbine types. Based on this, the presented results are limited to the reference turbine type and extending these results to other wind turbine types is possible if the differences in the dynamics response is taken into account.

Finally, this study shows that spectral methods are a good candidate for fatigue damage analysis of wind turbines. The best performance is obtained using the Empirical $\alpha_{0.75}$ method which is able to give good estimation regardless of the turbine substructure and using only the Gaussian assumption. This means that the Empirical $\alpha_{0.75}$ method can tolerate the violation of the non-stationarity and non-Gaussian assumptions and still gives fatigue damage estimations comparable to the rainflow cycle counting algorithm. Dirlik, the 2^{nd} Tovo-Benasciutti in addition to the Band-methods are able to give good estimation when used for fatigue assessment of the tower side-side loading regardless of the turbine configuration. However, when these methods are used for fatigue damage estimation of the tower fore-aft loading the obtained results deteriorate to an acceptable level and sometimes they tend to give very conservative estimations with regard to the reference fatigue damage estimation in time domain.

In summary, spectral-based fatigue analysis methods are able to give comparable fatigue damage estimations to the rainflow cycle counting algorithm, however, they should be used carefully in fatigue analysis of wind turbines as their performance depend on the monitored stress, turbine configuration, operating region not to forget the spectral method itself.

Table 4.5 Summary of spectral fatigue damage estimation methods using simulation data-set

Land-based	Tower-base - Fore-aft			Tower-base - Side-Side		
Method	G	cG	tG	G	cG	tG
Single-Moment	▓	▓		▓	▓	
Empirical $\alpha_{0.75}$	▒ 78%/97%	▒	▒	▒ 98%/100%	▒	▒
Tovo-Benasciutti 2	▓	▓	▒	▒	▒	▒
Dirlik	▓	▓	▒	▒	▒	▒
Bands Method	▒	▒	░	▒	▓	▒
Bimodal Jiao-Moan	░	░	░	░	░	░

Barge-platform	Tower-base - Fore-aft			Tower-base - Side-Side		
Method	G	cG	tG	G	cG	tG
Single-Moment	▓	▓		▓	▒	
Empirical $\alpha_{0.75}$	▒ 79%/89%	▒	▓	▒ 86%/95%	▒	▒
Tovo-Benasciutti 2	░	░	░	▒	░	▓
Dirlik	░	▓	░	▒	░	▓
Bands Method	▓	▓	▓	▒	▒	▒
Bimodal Jiao-Moan	░	░	░	▓	░	░

Spar-Buoy platform	Tower-base - Fore-aft			Tower-base - Side-Side		
Method	G	cG	tG	G	cG	tG
Single-Moment	▓	▓		▓	▒	
Empirical $\alpha_{0.75}$	▒ 71%/92%	▒	▓	▒ 70%/89%	▒	▒
Tovo-Benasciutti 2	▓	░	░	▒	▓	░
Dirlik	░	░	░	▒	▓	▓
Bands Method	▒ 58%/93%	▓	░	▒	▒	▒
Bimodal Jiao-Moan	░	░	░	░	░	░

TLP platform	Tower-base - Fore-aft			Tower-base - Side-Side		
Method	G	cG	tG	G	cG	tG
Single-Moment	▓	▓		░	▓	
Empirical $\alpha_{0.75}$	▒ 68%/93%	▒	▓	▒ 72%/97%	▒	▒
Tovo-Benasciutti 2	░	░	░	▒	▓	░
Dirlik	░	░	░	▒	▓	░
Bands Method	▓	▓	░	░	▓	░
Bimodal Jiao-Moan	░	░	░	░	░	░

Legend	▒ Good	▓ Acceptable	░ not-acceptable

Probability of Good estimation / Probability of Acceptable estimation

G	Gaussian approach
cG	Corrected Gaussian approach
tG	Transformed Gaussian model approach.

4.2 Fatigue Analysis of Small Wind Turbine

Fatigue analysis in time and frequency domains using operational measurements collected from the tower of a small wind turbine is investigated in this section. The small wind turbine has a rated power of $2.5\,kW$ and is available the University of Siegen. Due to the small dimensions of the wind turbine, it is more sensitive to wind turbulences and to the change of wind direction, which results to considerable changes in tower bending stress mean value that should be taken into account when using spectral fatigue damage estimation methods.

The objective of this study is to investigate the capabilities of the proposed "de-trending&PbP" fatigue damage analysis strategy using operational tower loading. Different spectral methods in combination with the Gaussian, corrected Gaussian and transformed Gaussian approaches are investigated and the performance is evaluated with regard to the reference fatigue damage estimation in time-domain using rainflow cycle counting algorithm.

4.2.1 Small Wind Turbine of University of Siegen

4.2.1.1 Wind Turbine System and Installation Site

The small wind turbine at the University of Siegen (fig. 4.32) is a research turbine with rotor diameter of $3\,m$. Located at the roof of the Paul-Bonatz Campus at university of Siegen. The total hub height of the turbine from ground is $26.3\,m$, while the hub height from the roof is $5\,m$ (see fig. 4.33). The turbine tracks passively the change of wind direction using wind vane. The design wind speed is $6\,\frac{m}{s}$ at a tip speed ratio of 7.5 and the rated power of the generator is $2500\,W$ at wind speed of $11\,\frac{m}{s}$. The main properties of the turbine are given in tab. 4.6. Unlike the reference wind turbine, the used generator has permanent magnets. Furthermore, the blades have fixed pitch angle.

Table 4.6 Main properties of the small wind turbine at university of Siegen

Rotor diameter	$3\,m$
Hub height from roof/ground	$5\,m\,/\,26.3\,m$
Type	Horizontal axis
Installation location	Roof of the Paul-Bonatz Campus, Building A, University of Siegen.
Wind tracking	Passive, wind vane
Design wind speed	$6\,\frac{m}{s}$
Rated tip speed ratio	7.5
Rated wind speed	$11\,\frac{m}{s}$
Rated power	$2500\,W$
Cut-in wind speed	$4\,\frac{m}{s}$
Tower material	Construction steel $S235$

The research turbine is equipped with a wide range of sensors that monitor its operation, structural responses, operating condition and its acoustic emission. A data acquisition system is used to collected all sensor data, convert them to digital form and save the digital signals on a local computer close to the turbine. These data are backed-up daily to a virtual machine at the University of Siegen. Through this virtual machine, the access to the measurements is granted to the researchers. Full turbine system description is available at [Gerhard et al., 2013; Volkmer et al., 2016].

Figure 4.32 The research wind turbine of the University of Siegen.

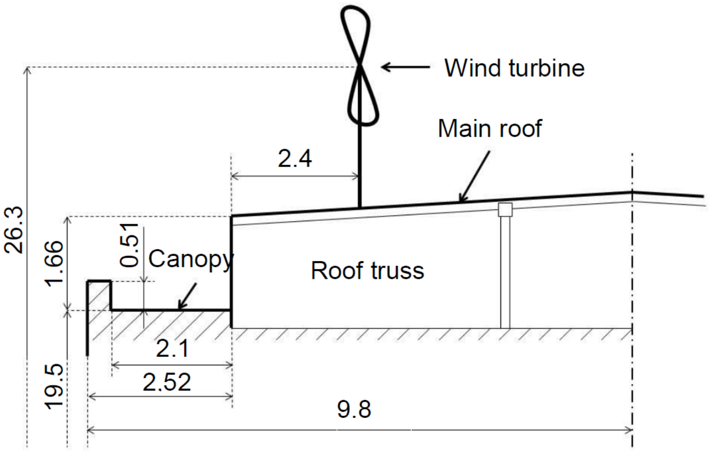

Figure 4.33 Installation location and hub-height of the research wind turbine (Source: [Volkmer et al., 2016]).

4.2.1.2 Structural and Operational Data Acquisition System

Tower-base bending stress in the North-South (NS) and East-West (EW) directions are measured using strain gauge sensors in half-bridge configuration in each direction (see fig. 4.34). The measured analogue strain signals are amplified using an analogue amplifier then collected using the turbine data acquisition system at sampling rate equal to $f_s = 2500\,Hz$ and later in the pre-processing step, the measurements are down-sampled to $250\,Hz$. The use of half-bridge configuration removes the influence of temperature on strain measurement as it is self compensated in this configuration.

The strain measurements are triggered by the rotor speed; that is to say, tower-base strain measurements are recorded as long as the rotor is rotating. This is done under the assumption that if the rotor is not rotating the turbine is not subject to any significant wind loading that might affect its fatigue life. This assumption implies that the wind speed is always below the cut-in wind speed of the turbine. Furthermore, the change of tower loading due to the change

Table 4.7 Measurements and the corresponding sampling rate.

Measurement	Sampling rate
Tower-base bending stress East-West direction	250 Hz
Tower-base bending stress North-South direction	250 Hz
Effective wind speed	10 Hz
Effective wind direction	10 Hz
Rotor speed	10 Hz

of rotor direction without rotating is also neglected.

In addition to the tower structural responses, the turbine operating conditions are also recorded. This includes effective mean wind speed, effective wind speed direction and rotor speed. The operating conditions measurement are collected at a sampling rate of 2500 Hz, then averaged and saved over a window of 250 samples (0.1 s). This means that the actual sampling rate of the operating conditions measurement is 10 Hz.

The measurement campaign started on 17 February 2018 and ended on 23 April 2018. During this period the turbine has recorded more than 300 operating hours ($\sim$ 12.5 days). The collected measurements are divided into data blocks each with 1 h length (in total 302 data blocks). Each data block contains the strain measurements in the North-South and East-West directions in addition to the measured mean wind speed, wind direction and the measured rotor speed.

Figure 4.34 Tower-base bending loading measurement using strain gauge sensors.

The strain sensors are installed on an operating wind turbine, therefore, the calibration was done with the rotor is almost facing north (0°) with very low wind. The visual alignment is used between the direction of sensors installation (NS, EW), the rotor facing north in the

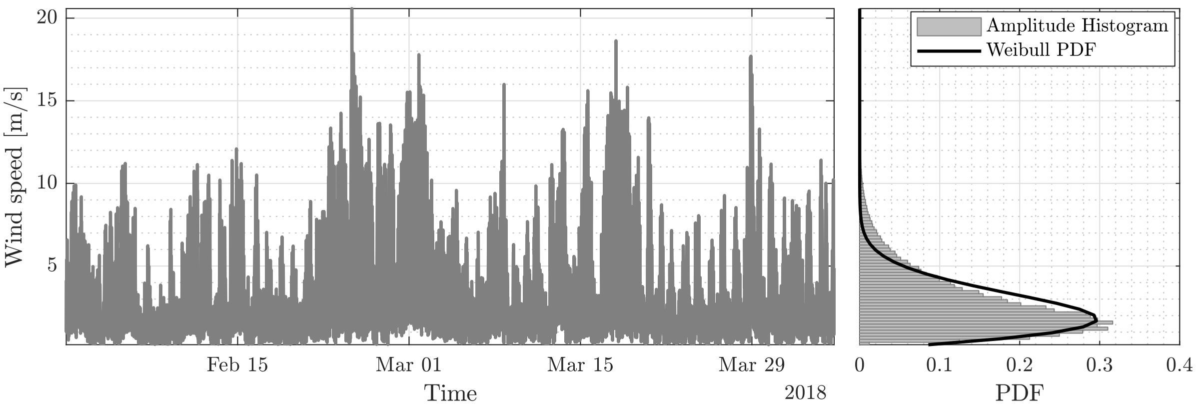

Figure 4.35 Wind speed time history over the measurement campaign period and its amplitude histogram.

calibration phase and the north direction used as reference for wind direction measurement. This means minimal deviations between the reference north directions used for sensor installation, calibration and wind direction measurement are to be expected.

It is important to mention at this point that the installation location and the small dimensions of the research wind turbine make it more responsive to turbulent wind loading when compared to large wind turbines. This implies that the structural responses of the turbine are non-stationary, therefore, the data should be collected at higher sampling rates in order to measure accurately the signal's peaks. Moreover, the non-stationariness should be taken into account when spectral methods are used for fatigue analysis.

4.2.1.3 Wind Characteristics

The amplitude distribution of the wind speed over the campaign period is illustrated in fig. 4.35. Unlike the amplitude distribution of the simulated wind profile which is more likely to be Gaussian, the measured wind speed amplitude is more likely to follow Weibull distribution. Most of the measured wind intensity is located at the wind speeds below $5\,\frac{m}{s}$. Fig. 4.35 shows in addition to the amplitude histogram, the fitted Weibull distribution. Furthermore, the maximum measured wind speed was for short time more than $20\,\frac{m}{s}$ and the turbine kept operating at these conditions.

The wind speed distribution with the direction, or what is known as the wind-rose, is shown in fig. 4.36. It is clear from the wind-rose that most of the significant wind (wind speed higher than the cut-in wind speed of $4\,\frac{m}{s}$) during the measurement campaign are coming from the East-South-East (ESE, 120°) direction and to less degree from the West-South-West (WSW, 270°) direction. The constant change of wind direction leads to a constant change of rotor direction. As the centre of gravity of the rotor is not located at the tower vertical axis, the change of rotor

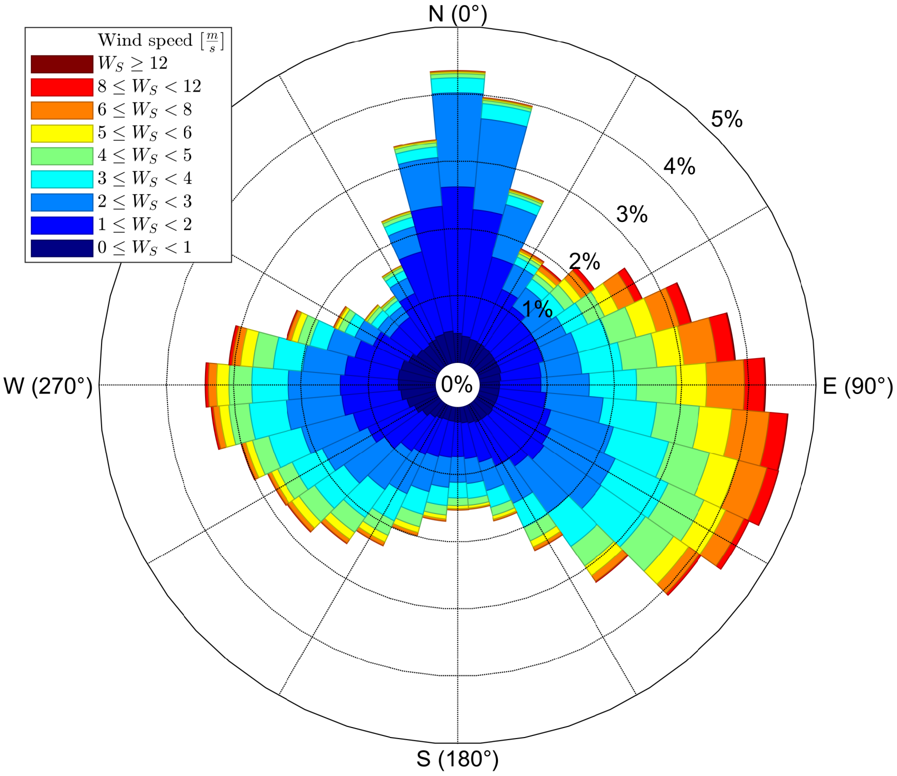

Figure 4.36 Wind speed rose.

direction leads to a change in the mean value of the measured strain at tower-base due to the static loading of the tower. This effect was minimal in the simulation data as the simulations have considered constant wind direction and the rotor direction is kept constant.

4.2.2 Structural Loading Characteristics

Tower-base is the most critical location of the tower as the highest bending stresses are occurring there. An example of the structural response is given in fig. 4.37. Two main natural frequencies of the tower could be easily identified. These two frequencies are related to the tower first mode in East-West $f_{T1ew} = 2.14\,Hz$ and North-South $f_{T1ns} = 2.62\,Hz$ directions. Furthermore, the tower response is mainly dominated by the wind loading in the lower frequency range (less than $0.5\,Hz$); and the amplitude distribution in both measurement directions is far from having Gaussian characteristics.

The maximum measured bending stress is less than $50\,MPa$ which correspond to a wind speed up to $21\,\frac{m}{s}$. This maximum recorded bending stress is considerably smaller than the yield strength and the ultimate tensile strength of the construction steel given by $S_y = 235\,MPa$ and $S_u = 360\,MPa$, respectively. This implies a safety factor of more than four, however, this does not give a clear idea about the tower fatigue life.

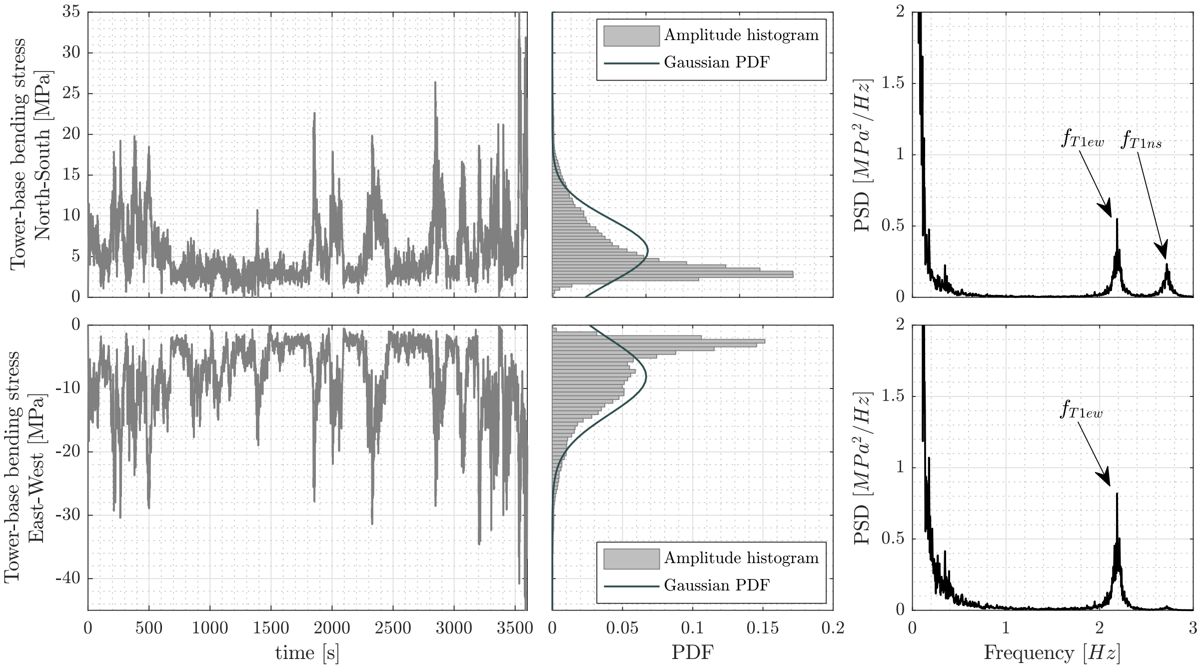

Figure 4.37 Structural loading characteristics.

The loading history illustrated in fig. 4.37 shows a non-stationary loading resulting from the continuous change in the mean value. Furthermore, the amplitude distribution in both directions is far from the normal distribution. By taking a closer look at the skewness-kurtosis scatter plot shown in fig. 4.38 for the North-South direction and in fig. 4.39 for the East-West direction, it is possible to see similar scatter pattern. In this pattern the skewness ranges between ±3 and kurtosis between 2 and 14.

The amplitude-mean cycle count histogram in both directions is also presented in fig. 4.40 for the North-South direction and in fig. 4.41 for the East-West direction. Both histograms show high number of cycles with small amplitudes and a few cycles with large amplitudes.

4.2.3 Fatigue Analysis

Fatigue analysis is curried out on both loading directions (as uni-axial loading case). However, as most of the effective wind speed is in the East-West direction (see fig. 4.36), only the results of the fatigue analysis is this direction are mainly presented in this thesis. The measured loading in the North-South direction shares similar loading characteristics to the East-West direction, however, with less amplitude, therefore, it is regarded as less critical.

The collected measurements are divided into data blocks each of one hour duration. Each data block contains the tower-base measured strain in North-South (NS) and East-West (EW) directions, wind speed, wind direction in addition to rotor speed. Tower-base measurements are

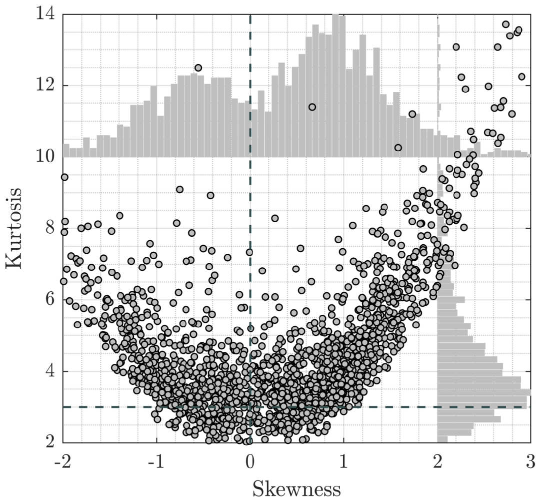

Figure 4.38 Skewness-kurtosis scatter plot of tower-base North-South loading.

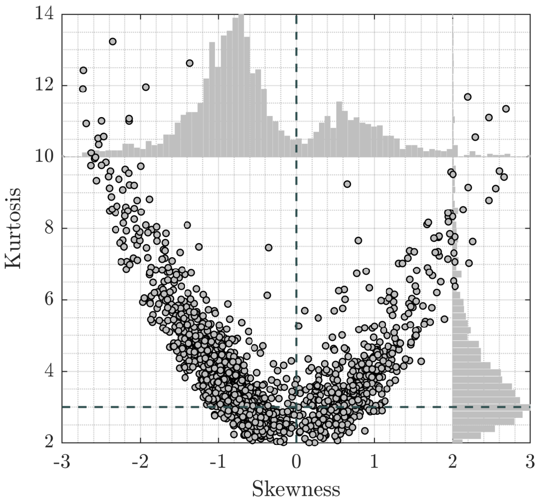

Figure 4.39 Skewness-kurtosis scatter plot of tower-base East-West loading.

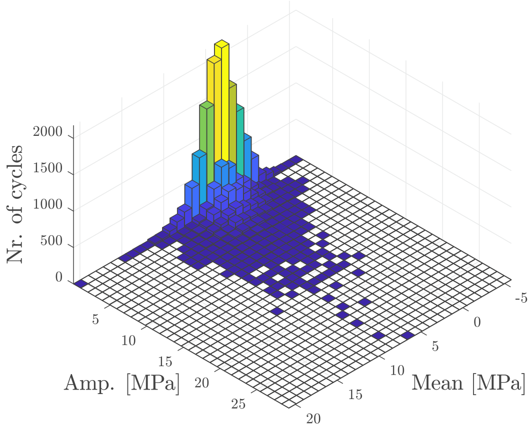

Figure 4.40 Amplitude-mean histogram of tower-base North-South bending stress.

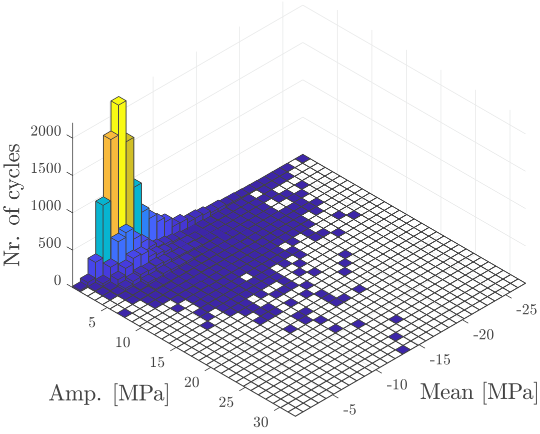

Figure 4.41 Amplitude-mean histogram of tower-base East-West bending stress.

used for fatigue analysis. As the East-West direction is the most loaded one, it is considered as the most critical direction and fatigue analysis is carried out using the uni-axial loading assumption.

Before starting fatigue analysis, the tower-base stress is calculated from the measured strain as explained in sec. 2.3.2, then the calculated stress is filtered using a low-pass filter with cut-off frequency equals to 30 Hz. The filter cut-off frequency is chosen to be 10 times higher than the tower first natural frequency. Therefore, the low-pass filter will not affect the most significant structural response at frequencies below 5 Hz, however, it removes the high-frequency cycles with small amplitude. This will make the rainflow counting algorithm works faster.

The filtered stress signals are then de-trended to extract the deterministic trend in addition to the stochastic component. This step is done with the help of the moving average trend estimator (MATE) explained in sec. 2.8.1. The time window used for MATE is set to $t_{MATE} = 12\,s$. This window is found to give a good compromise between isolating the effect of loading mean value and the stochastic loading. Unlike the stochastic component which could be considered a quasi stationary time-series with symmetric amplitude distribution, the estimated deterministic component is non-stationary and its amplitude distribution has no particular pattern. Fatigue damage estimation is then done according to the "De-trending&PbP" approach explained in sec. 2.9. Furthermore, time domain estimation of fatigue damage using the rainflow cycle counting algorithm is also curried out and used as reference to evaluate the performance of the spectral-based methods.

4.2.3.1 Fatigue Damage Estimation Using Measured Loading

In order to evaluate the performance of the spectral methods, the fact that the measured stress is non-stationary and non-Gaussian is ignored for the moment and various spectral methods combined with the Gaussian approach are used for fatigue analysis. Normalizing the fatigue damage calculated using spectral methods $\mathcal{D}_m^k$ by the fatigue damage calculated using the rainflow counting algorithm $\mathcal{D}_m^{RFC}$, the normalised fatigue damage index is obtained

$$\eta_m^k = \frac{\mathcal{D}_m^k}{\mathcal{D}_m^{RFC}} \tag{4.2}$$

for each data block and each spectral method k. Fig. 4.42 shows the probability density function (PDF) of η_m^k for different spectral methods. From this figure, it is clear that the Empirical $\alpha_{0.75}$ and the Bands methods have similar performance with high probability of delivering similar results to the reference time-domain method. However, their results scatter between 0.5 up till 2 which means for some data blocks the estimation results can't be trusted. Similar behaviour is seen by the Single-Moment method with a PDF peak shifted to 0.8. On the contrary, the Tovo-Benasciutti and the Dirlik methods give a scattering conservative fatigue damage estimations, therefore, their results are not accurate.

The probability of obtaining good fatigue damage estimation from the Empirical $\alpha_{0.75}$ and Bands methods is 74 % and 73 %, respectively; while the probability of obtaining an acceptable damage estimation of these two methods is 88 % each. The tolerances used for good and acceptable classifications are updated for this turbine and are given in tab. 4.8. The reason for this update is explained in the next section.

It is clear at this point that the direct use of the spectral methods for fatigue damage analysis of non-stationary, non-Gaussian loading violates the basic assumptions of the related theory which explains the scattered results. Therefore, fatigue damage analysis of the tower base bending stress is carried out using the "De-trending&PbP" approach.

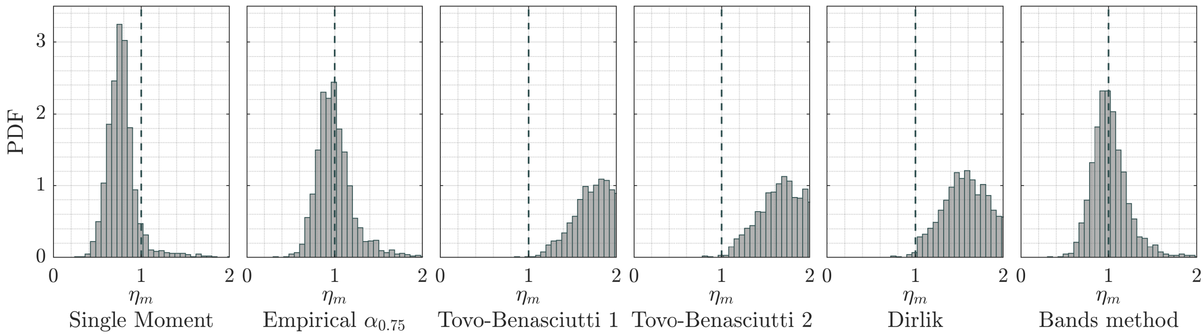

Figure 4.42 Probability density function of the normalised fatigue damage index for fatigue damage estimation from the measured tower base bending stress in the East-West direction using different spectral methods.

4.2.3.2 Deterministic and Stochastic Loading Components

The deterministic component is obtained by filtering the stress measurement using a moving average filter with $12\,s$ window width, while the stochastic one is the difference between the measured loading and the deterministic component. The contribution of each component in the total fatigue damage could be estimated with the help of the time-domain method and using as a reference the fatigue damage estimation of the measured stress $\mathcal{D}_m^{RFC}$. Using the rainflow counting, fatigue damage resulting from the deterministic component $\mathcal{D}_d^{RFC}$ and that from the stochastic component $\mathcal{D}_s^{RFC}$ are calculated. The overall fatigue damage is then estimated with the help of the Projection-by-Projection formula. Using the estimated fatigue damage, the following normalised indices

$$\eta_d^{RFC} = \frac{\mathcal{D}_d^{RFC}}{\mathcal{D}_m^{RFC}} \tag{4.3}$$

$$\eta_s^{RFC} = \frac{\mathcal{D}_s^{RFC}}{\mathcal{D}_m^{RFC}} \tag{4.4}$$

$$\eta_{PbP}^{RFC} = \frac{\mathcal{D}_{PbP}^{RFC}}{\mathcal{D}_m^{RFC}} \tag{4.5}$$

could be obtained for the deterministic, stochastic components and overall fatigue damage, respectively. Theoretically, η_{PbP}^{RFC} should be equal to unity, that is to say, the Projection-by-Projection formula would deliver the same result obtained by the rainflow counting method applied to the measured stress. Furthermore, η_d^{RFC} and η_s^{RFC} values range between zero and unity and they represent the contribution of the corresponding component to the total fatigue damage. By calculating these indices over all data-blocks, fig. 4.43 is obtained. It is clear from this figure that the deterministic component contribution to the total fatigue doesn't exceeds 25 % while the contribution of the stochastic component scatters between 40 % to 80 %. The calculated overall damage using the PbP formula is between 80 % and 110 % which is a good result if the main assumption of the PbP formula of uncorrelated loading components is taken into account.

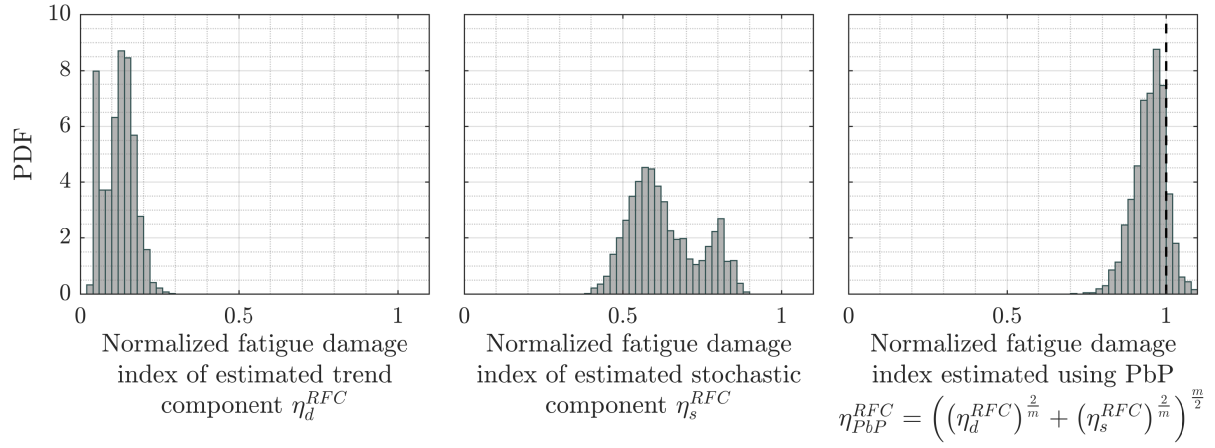

Figure 4.43 The probability density function of normalised fatigue damage of the estimated deterministic (left) and stochastic (middle) components, in addition to the normalised fatigue damage calculated using the Project-by-Projection formula (right).

In order to check the validity of this assumption, the cross-correlation coefficients between the deterministic and stochastic time-series are calculated for all data-blocks. Similarly, the cross-correlation coefficients between the PSD of the deterministic and stochastic components are also calculated for all data-blocks. Fig. 4.44 summaries the obtained results in terms of PDF of the correlation coefficients. It is clear that the determinist and stochastic components are almost not correlated in frequency domain (almost all coefficients are less than 0.1) which satisfies the basic assumption of the Projection-by-Projection formula. However, the cross-correlation coefficients in of time-domain signals indicate week correlation. This is due to the fact that the turbulence intensity of the wind depends on the mean wind speed. This weak correlation introduces an error in the estimated overall fatigue damage calculated using the PbP formula.

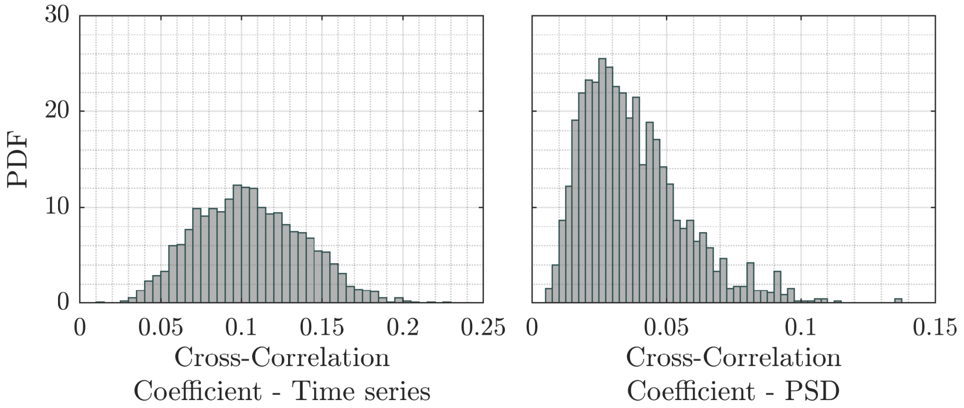

Figure 4.44 The correlation coefficient between the deterministic and stochastic time-series components (left) and the correlation coefficient between the PSD of the deterministic and stochastic components (right).

Based on the performance of the PbP formula, the overall performance of the spectral methods

Table 4.8 Classification of obtained fatigue damage estimation results

Classification	Tolerance	η range	Meaning
Good	±20 %	$0.80 \leq \eta \leq 1.20$	Spectral fatigue damage estimation gives close (within the given ±20 % tolerance) result to the time domain fatigue damage estimation.
Acceptable	±30 %	$0.70 \leq \eta \leq 1.30$	Spectral fatigue damage estimation gives acceptable (within the given ±30 % tolerance) results comparing to the time domain fatigue damage estimation.
Not acceptable	otherwise	otherwise	Spectral fatigue damage estimation deviates far from the results in the time domain.

is classified into good, acceptable and not-acceptable one as explained in tab. 4.8. This classification is similar to that used with simulation data-set, however the tolerance is increased from ±10 % to ±20 % for good estimation, and from ±20 % to ±30 % for acceptable estimation. The reason behind this increased tolerance is to take into account the error presented by the PbP formula as shown in fig. 4.43.

4.2.3.3 Fatigue Damage Caused by Deterministic Component

The characteristics of the deterministic component makes fatigue analysis using rainflow counting the only possible option to estimate the fatigue damage resulting from this component. As shown in fig. 4.43, the fatigue damage contribution of this component is less than 25 %, and is basically resulting from the few cycles with large amplitude generated by the change of mean wind speed and the change of wind direction that leads to changing the nacelle direction.

4.2.3.4 Fatigue Damage Resulting from the Stochastic Component

The stochastic component is quasi-stationary with zero mean value and variance that doesn't change dramatically. The amplitude distribution of this component is symmetric, however, more peaky than Gaussian (*leptokurtic*) as it is clear from fig. 4.45. By using the spectral methods with the presented Gaussian, corrected Gaussian and transformed Gaussian model approaches to estimate the fatigue damage resulting from the stochastic component $\mathcal{D}_s^k$; then normalizing it with that calculated using the rainflow counting algorithm $\mathcal{D}_s^{RFC}$, the normalised fatigue damage index η_s^k is obtained where

$$\eta_s^k = \frac{\mathcal{D}_s^k}{\mathcal{D}_s^{RFC}} \tag{4.6}$$

and k corresponds to the used spectral method. The Gaussian approach is the only approach at this point that gives reasonable fatigue damage estimations as shown in fig. 4.46. The corrected Gaussian approach tends to give very conservative estimations with $\eta_s > 1.5$ (results not shown) and the transformed Gaussian approach has failed to estimate the transformation

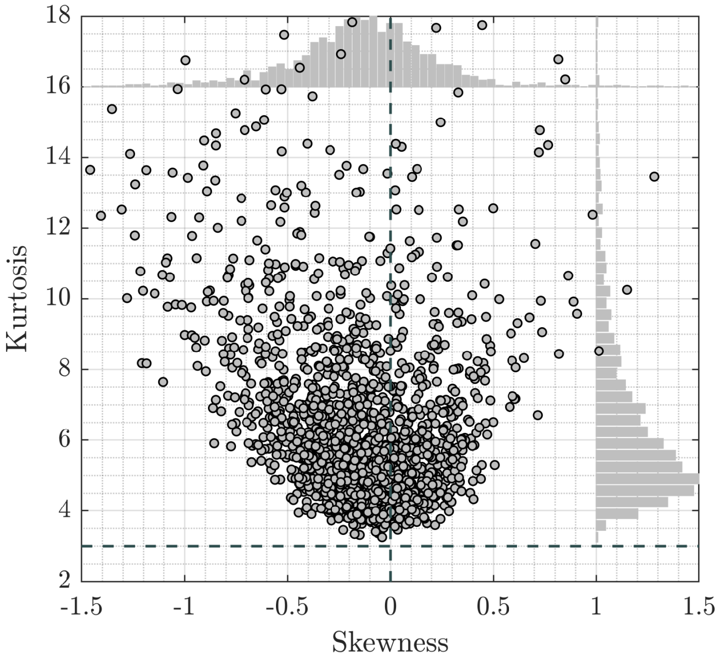

Figure 4.45 Skewness-kurtosis scatter plot of stochastic component.

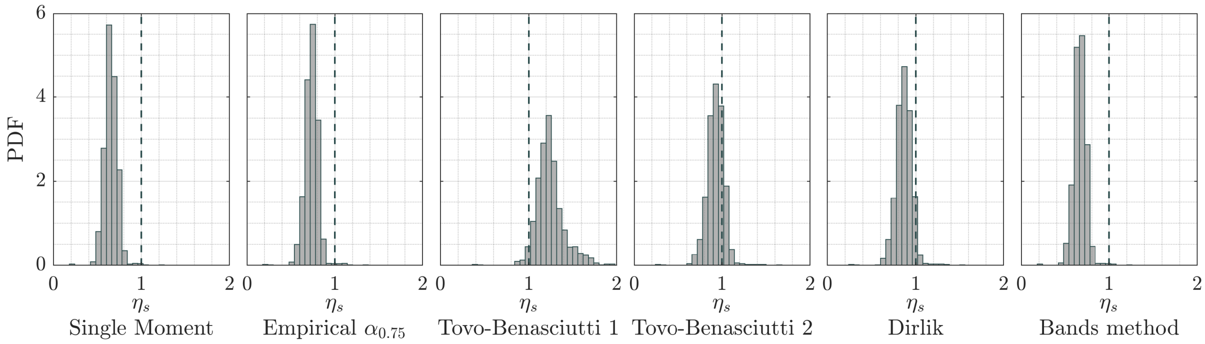

Figure 4.46 Normalised fatigue damage estimation of stochastic component using the Gaussian approach.

function $G(\,\cdot\,)$ and its inverse due to constraints related to the skewness and kurtosis values (fig. 4.45). The obtained results from the Gaussian approach (fig. 4.46) shows that good results could be obtained using Tovo-Benasciutti second method in addition to Dirlik Method. In fact all spectral methods tend to give coherent estimations (within a small range) at certain values of η_s that is different from unity. For example, the Empirical $\eta_s^{\alpha_{0.75}}$ method gives $\eta_s^{\alpha_{0.75}} \in [0.5, 0.9]$ with peak at $\eta_{\alpha_{0.75}} = 0.78$. Similar performance is also obtained by the Single-Moment method and with small shift to the left by the Bands-Method.

4.2.3.5 Fatigue Damage Estimation Using "De-trending&PbP"

Using the "De-trending&PbP" with different spectral methods, it is found that the Gaussian approach is the only approach that is able to deliver acceptable fatigue damage estimation.

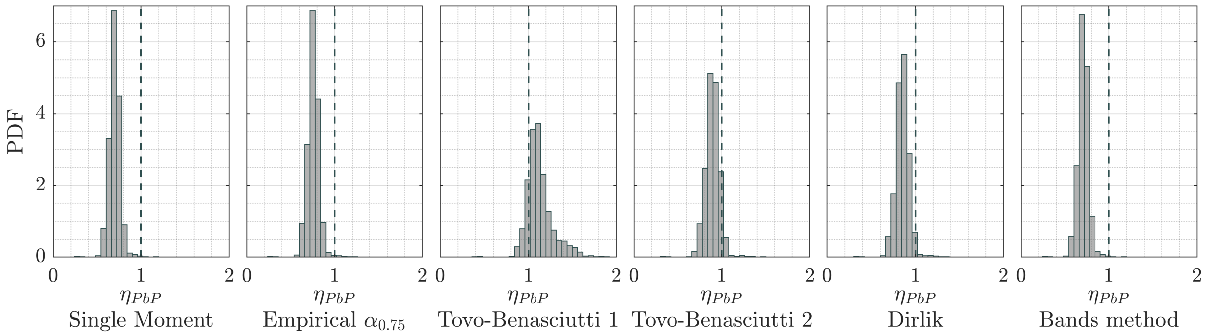

Figure 4.47 Normalised fatigue damage estimation obtained from "De-trending&PbP".

While the corrected Gaussian approach tends to give very conservative estimations and the transformed Gaussian approach failed in many data-sets to estimate the transformation function and its inverse.

Fig. 4.47 illustrates the PDF of the normalised fatigue damage index for different spectral methods used along with the Gaussian approach calculated using

$$\eta^k_{PbP} = \frac{\mathcal{D}^k_{PbP}}{\mathcal{D}^{RFC}_m} \tag{4.7}$$

with k corresponds to the used spectral method, $\mathcal{D}^k_{PbP}$ is the total fatigue damage estimated using the Projection-by-Projection formula and the k spectral method. Finally, $\mathcal{D}^{RFC}_m$ is the reference fatigue damage estimated from the measured loading using the rainflow counting method.

A direct result obtained from the use of the "De-trending&PbP" is the coherent fatigue damage estimations of all spectral methods. This is clear to identify by comparing fig. 4.47 and fig. 4.42. Similar results are obtained from the Single-Moment, the Empirical $\alpha_{0.75}$ and the Bands-Methods with $\eta^k_{PbP} \in [0.5, 1.0]$ and PDF peak at $\eta^k_{PbP} \approx 0.7$. Furthermore, the Tovo-Benasciutti second method and the Dirlik Method have $\eta^k_{PbP} \in [0.7, 1.1]$ with the PDF peak at $\eta^k_{PbP} \approx 0.9$. Finally, the Tovo-Benasciutti first method still gives more scattering estimations with $\eta^{TB1}_{PbP} \in [0.9, 1.6]$ and PDF peak at $\eta^{TB1}_{PbP} \approx 1.1$.

Using the limits illustrated in tab. 4.8, it is possible to estimate the good and acceptable fatigue damage estimations of the measured loading and "De-trending&PbP", each for different spectral methods. Fig. 4.48 shows the obtained results (results are normalised by the fatigue damage estimated using rainflow counting applied to the measured loading). The direct application of spectral methods for fatigue damage estimation (fig. 4.48-left) shows that the Empirical $\alpha_{0.75}$ and the Bands methods have a 74 % and 73 % chance of giving good estimations, respectively. And the probability of giving acceptable estimations goes up to 88 % for both methods. All other spectral methods covered by this work failed to give any reasonable estimations in this

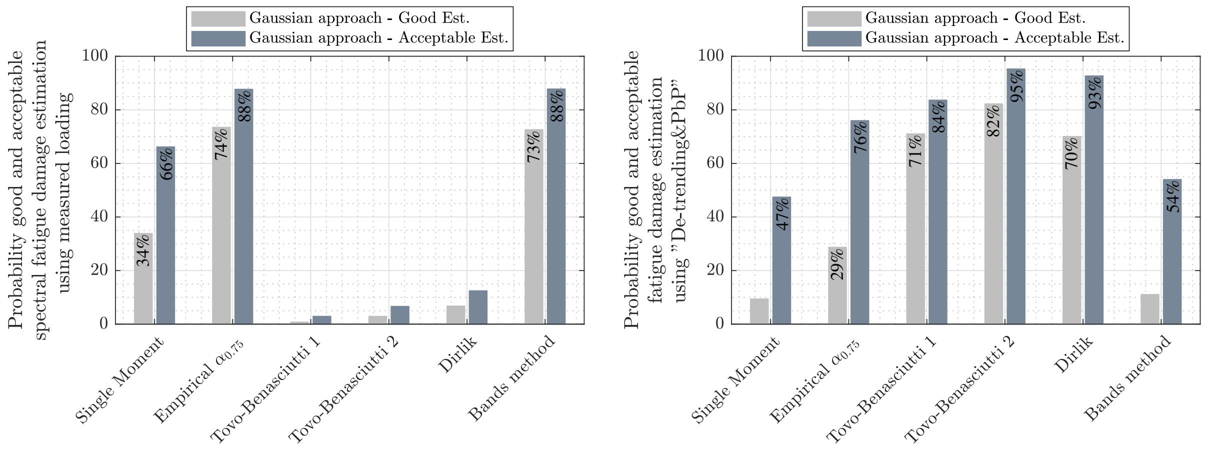

Figure 4.48 Probability of good and acceptable fatigue damage estimation obtained form the direct use of the measured loading and the proposed "De-trending&PbP" strategy using different spectral methods.

case.

On the other hand, the use of the "De-trending&PbP" (fig. 4.48) strategy improves the probability of good and acceptable estimations of the 2nd Tovo-Benasciutti method to 82 % and 95 %, respectively. Similar improved good estimation results are obtained from the 1st Tovo-Benasciutti and the Dirlik methods with probabilities of 71 % and 70 %, respectively; while the acceptable estimations of these two methods go up to 84 % of the first one and up to 93 % of the Dirlik method. Furthermore, the fatigue results obtained using the Empirical $\alpha_{0.75}$ method according to the proposed strategy are far worse from that obtained by direct use of the Gaussian approach.

4.2.3.6 Accumulative Fatigue Damage

Monitoring the development of the fatigue damage over time is an important aspect of fatigue failure prediction. The accumulated fatigue damage is calculated using the estimated fatigue damage per each data-block $\mathcal{D}_i$ as per following

$$\tilde{\mathcal{D}} = \sum_i \mathcal{D}_i. \tag{4.8}$$

Four accumulative fatigue damage estimations are shown in fig. 4.49. The first one is the accumulative fatigue damage estimated by the rainflow counting algorithm applied to the measured loading $\tilde{\mathcal{D}}_m^{RFC}$. The second is the accumulative fatigue damage estimated by the rainflow counting algorithm applied to the deterministic component $\tilde{\mathcal{D}}_d^{RFC}$. The third is the accumulative fatigue damage estimated by either the rainflow counting or a spectral fatigue damage estimation method applied to the stochastic component $\tilde{\mathcal{D}}_s^k$. Finally, the fourth line represents the accumulative fatigue damage estimated using the "De-trending&PbP" approach $\tilde{\mathcal{D}}_{PbP}^k$. Three different

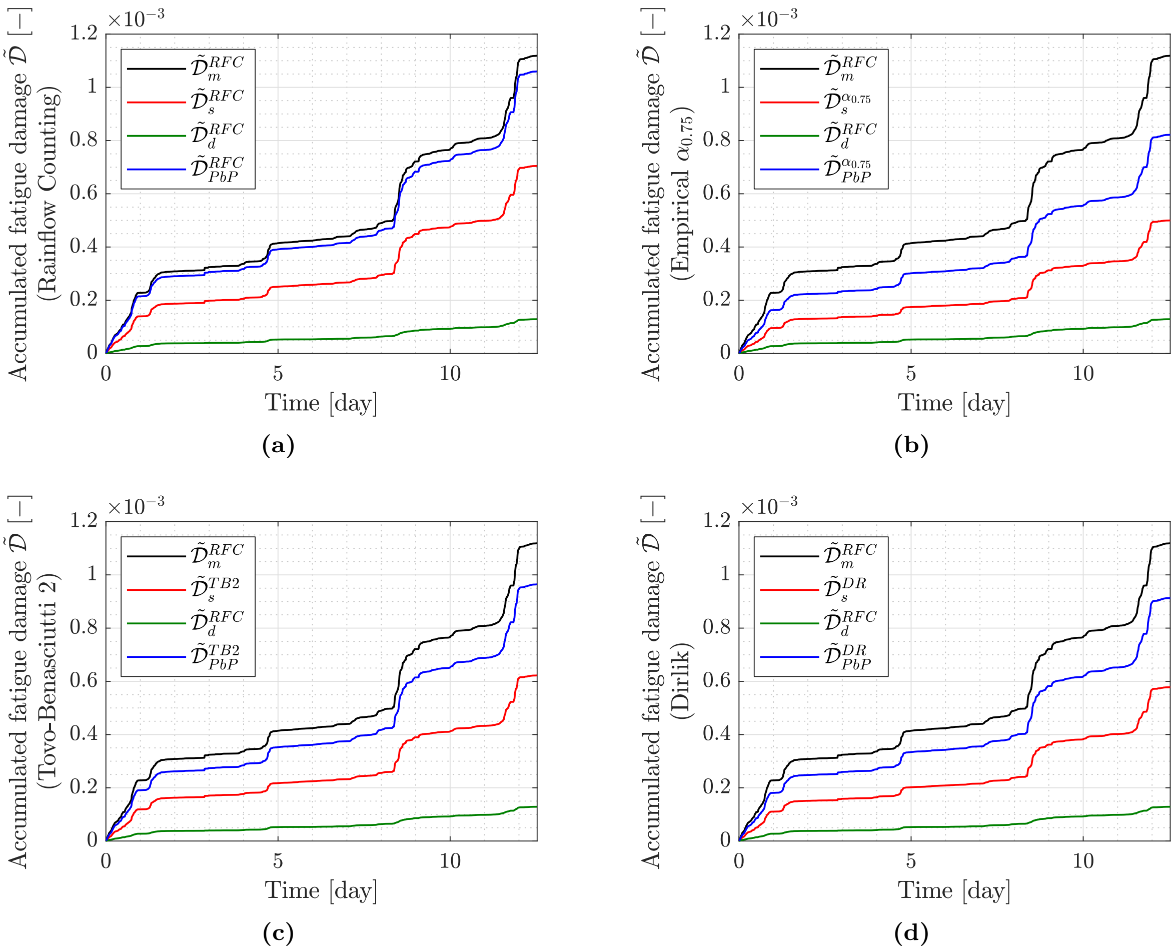

(a) **(b)**

(c) **(d)**

Figure 4.49 Comparison of the accumulative fatigue damage estimated using the rain flow counting algorithm and the De-trending&PbP approach.

spectral methods are considered at this point. This is based on the results obtained from the previous section. The first spectral method is the Empirical $\alpha_{0.75}$ method ($k = \alpha_{0.75}$), which shares the similar behaviour with the Single-Moment and the Bands methods. The second spectral method is the 2nd Tovo-Benasciutti method ($k = TB2$) and finally the last spectral method is the Dirlik method ($k = DR$). In addition to the three spectral methods, the accumulative fatigue damage estimated using the rainflow cycle counting in time domain is also presented ($k = RFC$).

A comparison of the accumulated fatigue damage estimated using the rainflow counting algorithm and the De-trending&PbP approach is illustrated in fig. 4.49a. Four different fatigue damage estimation methods are used along with the De-trending&PbP approach. The first one (fig 4.49a) uses the rainflow counting algorithm for estimating the fatigue damage of the stochastic and deterministic components. The total estimate fatigue damage using the De-trending&PbP approach $\tilde{\mathcal{D}}_{PbP}^{RFC}$ is then compared to the reference estimation $\tilde{\mathcal{D}}_m^{RFC}$ obtained by direct use of the rainflow counting algorithm applied to the measured stress. This figure

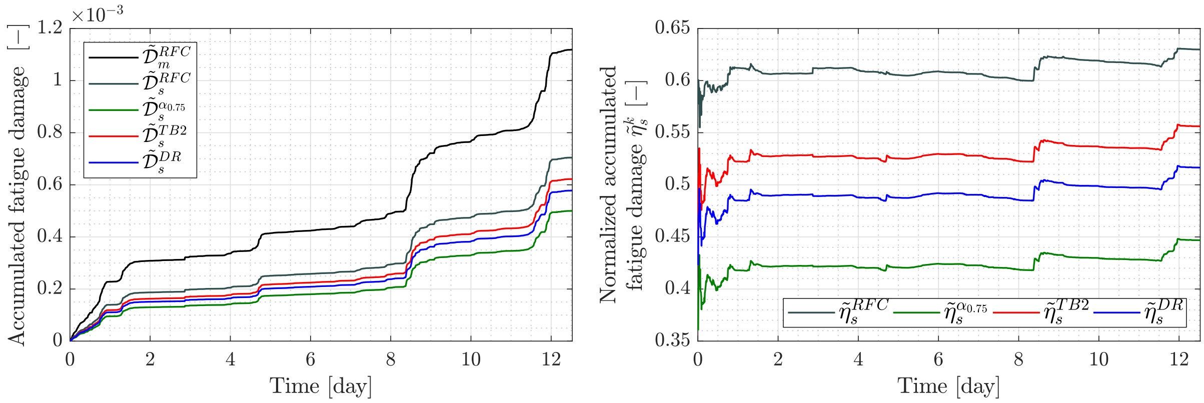

Figure 4.50 Accumulative fatigue damage estimated from the stochastic component using different estimation methods.

shows comparable estimation of the De-trending&PbP approach to the reference estimation over time. On the other hand, the use of the Empirical $\alpha_{0.75}$ (fig. 4.49b), Tovo-Benasciutti second method (fig. 4.49c) and Dirlik method (fig. 4.49d) for fatigue damage estimation of the stochastic component result to an overall accumulated fatigue damage in each case, $\tilde{\mathcal{D}}_{PbP}^{\alpha_{0.75}}$, $\tilde{\mathcal{D}}_{PbP}^{TB2}$ and $\tilde{\mathcal{D}}_{PbP}^{DR}$ that deviates over time from the reference value $\tilde{\mathcal{D}}_m^{RFC}$. This is due to the fatigue damage estimation error presented by the use of the spectral methods.

However, an interesting result could be obtained at this point by comparing the dynamic changes of the accumulated fatigue damage resulted from the stochastic component $\tilde{\mathcal{D}}_s^k$ to each other and to the reference $\tilde{\mathcal{D}}_m^{RFC}$ one. It is clear that the accumulated fatigue damage estimated from the stochastic component $\tilde{\mathcal{D}}_s^k$ follows similar trend regardless of the used method (fig. 4.50 -left). By normalizing the estimated accumulative fatigue damage resulted from the stochastic components to the reference one $\tilde{\mathcal{D}}_m^{RFC}$ (fig. 4.50-right) using

$$\tilde{\eta}_s^k = \frac{\tilde{\mathcal{D}}_s^k}{\tilde{\mathcal{D}}_m^{RFC}},\ k \in \{RFC,\ \alpha_{0.75},\ TB2,\ DR\}, \tag{4.9}$$

it is possible to confirm the previous conclusion. Furthermore, it is possible to conclude that the accumulated fatigue damage obtained from the stochastic component has the same dynamics as the reference one $\tilde{\mathcal{D}}_m^{RFC}$. That is to say, it is possible to use the fatigue damage from the stochastic component for monitoring purposes as the dynamic change of the estimated fatigue damage is mostly captured through the stochastic component. The difference between the lines in (fig. 4.50-right) could be seen as a difference in sensitivity of the used spectral method.

4.2.4 Structural Health Monitoring Using Comparative Sensor Data Approach

The traditional method in fatigue damage detection is to compare the accumulative fatigue damage estimated over time $\tilde{\mathcal{D}}$ with a set critical value $\mathcal{D}_{cr}$ on which the failure is assumed to occur. In this method, the system is considered healthy as long as $\tilde{\mathcal{D}} < \mathcal{D}_{cr}$. The main advantage of this method is its simplicity in addition to its ability to avoid system failure due to fatigue. However, it is not clear how the critical fatigue damage limit $\mathcal{D}_{cr}$ is to be chosen. It has been found by [Sutherland, 1999] of example that failure in wind turbine occurs for values of $\mathcal{D}_{cr} = 0.79, \ldots, 1.53$. This large span of $\mathcal{D}_{cr}$ makes the use of the lower value very conservative and impractical. While the use of higher value of $\mathcal{D}_{cr}$ is possible at the cost of increased risk of turbine failure due to fatigue.

It is possible to overcome the limits of the traditional method by developing a better fatigue damage detection approach based on monitoring the estimated fatigue damage at pre-defined time period against a reference value. This reference value might be for example the standard deviation of the wind speed calculated during the same pre-defined time period. The basic idea behind this monitoring approach is explained in sec. 2.10.

By plotting the logarithm of the fatigue damage per each data-block estimated from the measured stress using rainflow counting, and the fatigue damage estimated from the stochastic component using the rainflow counting and the Tovo-Benasciutti second method, all against the logarithm of the standard deviation of the measured wind speed (see eq. 2.198), fig. 4.51 is obtained. Linear regression is used to estimated the linear relation, which is plotted as a continues black line. Furthermore, if a tolerance δ is defined, this tolerance represents the distance from the estimated linear regression line, two parallel lines are obtained (dashed lines). All points located between these two dashed lines have a distance from the linear regression line less than δ. The direct relation between the logarithm of fatigue damage and the logarithm of the wind speed is clear to identify from Fig. 4.51. The scatter around the linear regression line is related to different factors. One of these factors is that the developed direct relation presented in eq. 2.198 uses the relative wind speed, which is the difference between the wind speed and the rotor disk speed, while fig. 4.51 uses the measured wind speed while the rotor disk speed is ignored.

Similar scatter pattern is observed in fig. 4.51 for the three cases: fatigue damage estimated from the measured loading using the rainflow counting $\mathcal{D}_m^{RFC}$, fatigue damage estimated from the stochastic component using the rainflow counting $\mathcal{D}_s^{RFC}$ and fatigue damage is estimated from the stochastic component using the 2nd Tovo-Benasciutti method $\mathcal{D}_s^{TB2}$. All the three cases have the same linear regression and all the points scatter within the pre-defined distance $\pm\delta$ from the linear regression line. This means that the fatigue failure detection could be done using the stochastic component only and that the spectral methods would give similar results to the time-domain method.

The fatigue damage detection procedure is done in two steps, the first one is to establish a

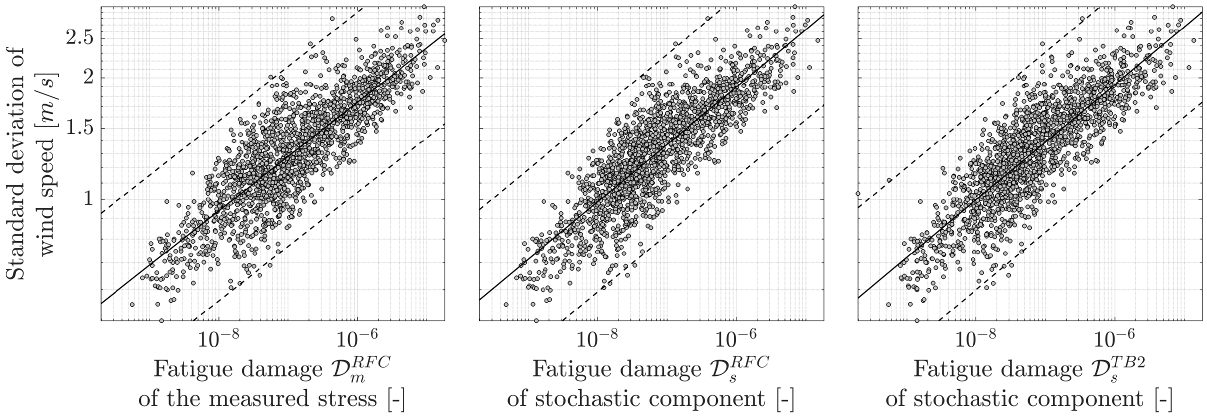

Figure 4.51 Scatter plot of the standard deviation of the wind speed versus the calculated fatigue damage using rainflow counting. Fatigue damage using rainflow counting is calculated for the measured stress in addition to the stochastic component while 2^{nd} method of Tovo-Benasciutti is used to estimate fatigue damage of the stochastic component.

reference scatter, where the system is considered as healthy. In this step, the linear regression line is estimated and the tolerance δ is defined. The second step is to classify the distance of the acquired new point from the linear regression line, either is it located within the set tolerance δ or outside it. In the later case, this means a change in the system that should be further investigated.

4.2.5 Discussion and Conclusion

Fatigue analysis of operational tower loading of a small wind turbine have been addressed in this section. Due to the small dimensions of the turbine and the installation location, the turbine is more subject to turbulent wind loading. This makes the loading far from being stationary.

The direct fatigue analysis of the tower loading using spectral methods demonstrate the limitations of the obtained results due to the violation of the main assumptions of the basic theory. However, fatigue analysis using the proposed “de-trending&PbP” strategy has demonstrated the potentials of the spectral methods. The obtained results using the proposed strategy with different spectral methods are comparable to that obtained using the time-domain cycle counting. The best fatigue damage estimation is obtained by the 2^{nd} Tovo-Benasciutti method and to less accuracy by the 1^{st} Tovo-Benasciutti and Dirlik methods. These results are much better than that obtained by the Empirical $\alpha_{0.75}$ and Bands methods applied directly to the measured loading and combined by the Gaussian approach.

The corrected Gaussian and the transformed Gaussian model approaches failed to improve the fatigue damage estimation results. This is mainly related to the fact that the corrected Gaussian approach depends on a correction factor that is developed only using simulation data-sets, while the transformed Gaussian models has limitations related to the skewness and the kurtosis the prevents building the transformation function. The limitation of both methods in dealing with the non-Gaussian loading case reveals the need for further research on this topic.

Fatigue damage caused by the deterministic component roughly contributes less than 25 % of the total fatigue damage while the rest is caused by the stochastic component. The deterministic component is basically related to the change of relative mean wind speed and its direction. The contribution of this component in the total fatigue damage could be limited using passive or active measures. However, there is an upper limit to the fatigue reduction that could be obtained from these measures. To achieve more reduction in the fatigue loading, the measures should be able to reduce the stochastic loading component.

Estimated fatigue damage from the stochastic component follow the same trend of fatigue estimated using the cycle-counting in time domain. This opens the possibility of using the spectral fatigue damage of the stochastic component for fatigue damage detection purposes. If the estimated fatigue is compared to a reference value that represents the input loading such as the standard deviation of the mean wind speed, it is possible to detect any structural change or damage in the system.

4.3 Fatigue Analysis of Utility Scale Wind Turbine

Utility scale wind turbines have large rotor diameter and high towers with average capacity of $2.5\,MW - 3\,MW$. The large rotor disk and the high tower decreases the turbine sensitivity to turbulent wind, and thereby, the turbine structure would behave as a low-pass filter, unlike the previously studied small wind turbine which is more sensitive to turbulent wind. However, the increased turbine dimensions present another sources of loading such as the turbine sensitivity to the change of wind speed with height (vertical shear).

In this section, a one day tower loading measurements of a research wind turbine with rated power of $500\,kW$ are used for fatigue damage analysis using time and frequency domain methods. The main objective is to estimated the effectivity of the fatigue damage estimation using spectral methods, either by direct use of the measurement, or using the proposed “de-trending&PbP” strategy. Furthermore, to discuss the potentials of using spectral methods in fatigue monitoring.

Figure 4.52 Research wind turbine (Source: [Lachmann, 2014])

Table 4.9 Research wind turbine properties (Source: [Lachmann, 2014])

Rated power	$500\,kW$
Tower type	Enercon $E40$
Tower height	$63\,m$
Hub height	$65\,m$
Number of blades	3
Blade length	$19.13\,m$
Rotor diameter	$40\,m$
Rotor speed	$18 - 36\,rpm$
Cut-in wind speed	$2.5\,\frac{m}{s}$
Rated wind speed	$12\,\frac{m}{s}$
Cut-off wind speed	$25\,\frac{m}{s}$
Tower material	Steel
Construction year	1997

4.3.1 Research Wind Turbine

The research wind turbine is an Enercon $E40 - 500\,kW$ (fig. 4.52) that is located in Dortmund and equipped with a Structural Health Monitoring (SHM) system that is developed by [Lachmann, 2014]. The SHM system consists of a set of nine accelerometers distributed along the tower and the concrete foundation, a set of six displacement sensors mounted on the inner side of the tower and distributed on two levels (three sensors at each level at 120° configuration) in addition to that, temperature sensors are installed next to each displacement sensor to capture any temperature changes that can affect the strain measurement. Other temperature sensors are also installed in both inner-side and outer-side of the tower. Wind speed and wind direc-

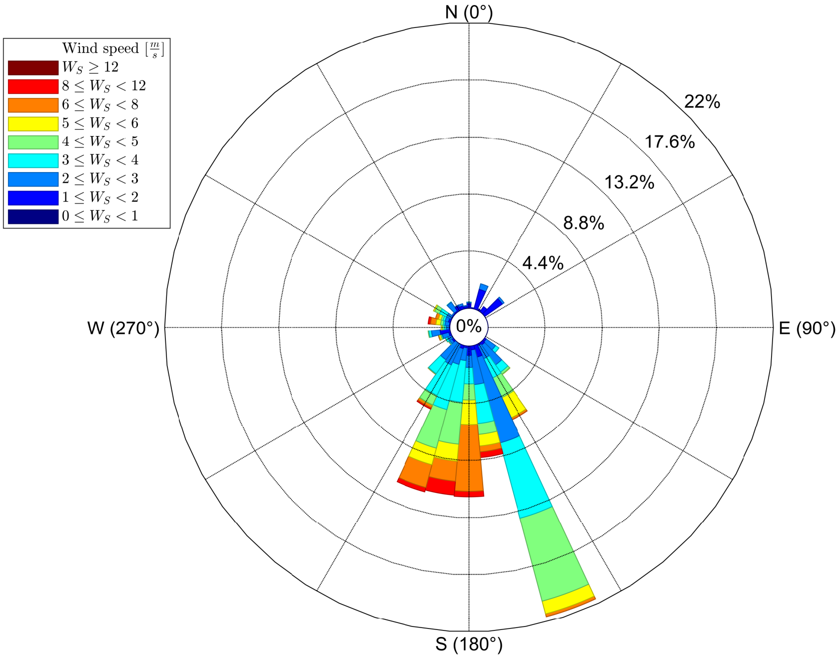

Figure 4.53 Wind Rose

tion are monitored using an ultrasonic anemometer located at $13m$ height nearby the tower, in addition to that the operating conditions of the turbine are also recorded, this includes wind speed measured by the anemometer located at the top of the tower, generator power output, rotor speed, nacelle direction and blade pitch angle.

The used data for fatigue analysis is limited to the recorded measurements on 08.06.2010. The data-set is a 24 hour measurement of the previously mentioned SHM sensors in addition to the operating conditions of the wind turbine. The data are arranged in data-blocks each of one hour duration. This means that the data-set contains 24 data-blocks. The sampling frequency depends on the recorded signal. While the strain sensors in both levels, turbine operating conditions in addition to the ultrasonic wind measurements are recorded at $100\,Hz$ sampling rate, the temperature measurements are recorded at $1\,Hz$ sampling rate.

4.3.2 Wind Characteristics and Operating Conditions

The turbine is subject to south wind in the considered data-set as it is clear from the wind rose shown in fig. 4.53. By taking a closer look at the wind speed development with time as recorded by the anemometer on top of the tower (fig. 4.54), it is possible to see that the turbine is subject to wind speed less than $6\,\frac{m}{s}$. However, higher wind activities up to $12\,\frac{m}{s}$ between 12:00 o'clock and 17:00 o'clock and later before midnight are also available. The lower wind speed below $6\,\frac{m}{s}$ will result to a generated power less than $80\,kW$. At these lower wind speeds, the turbine has been subject to many start-stop cycles, such as the two cycles between 03:00 and 04:00 o'clock and the repeated tries to start the turbine between 16:00 and 19:00 o'clock. These start-stop cycles present high transient loads on the tower.

Fig. 4.54 shows also the tower stress s_5 measured at the lower strain measurement level at about $21\,m$ high in the south direction which corresponds to the main wind speed direction. The effect of the start-stop cycles between 03:00 and 04:00 o'clock are clearly recognised in the stress loading. However, the effect of the start-stop cycles between 16:00 and 19:00 o'clock is not that clear in the stress s_5 loading history due to two main reasons, the first one is that the turbine is shot down for some time and the start-sop cycles are not close to each others, secondly, the nacelle direction (rotor azimuth plot) is changed to follow the change of wind direction at this time period, which will reduce the stress component measured by s_5 but increases it at the other directions.

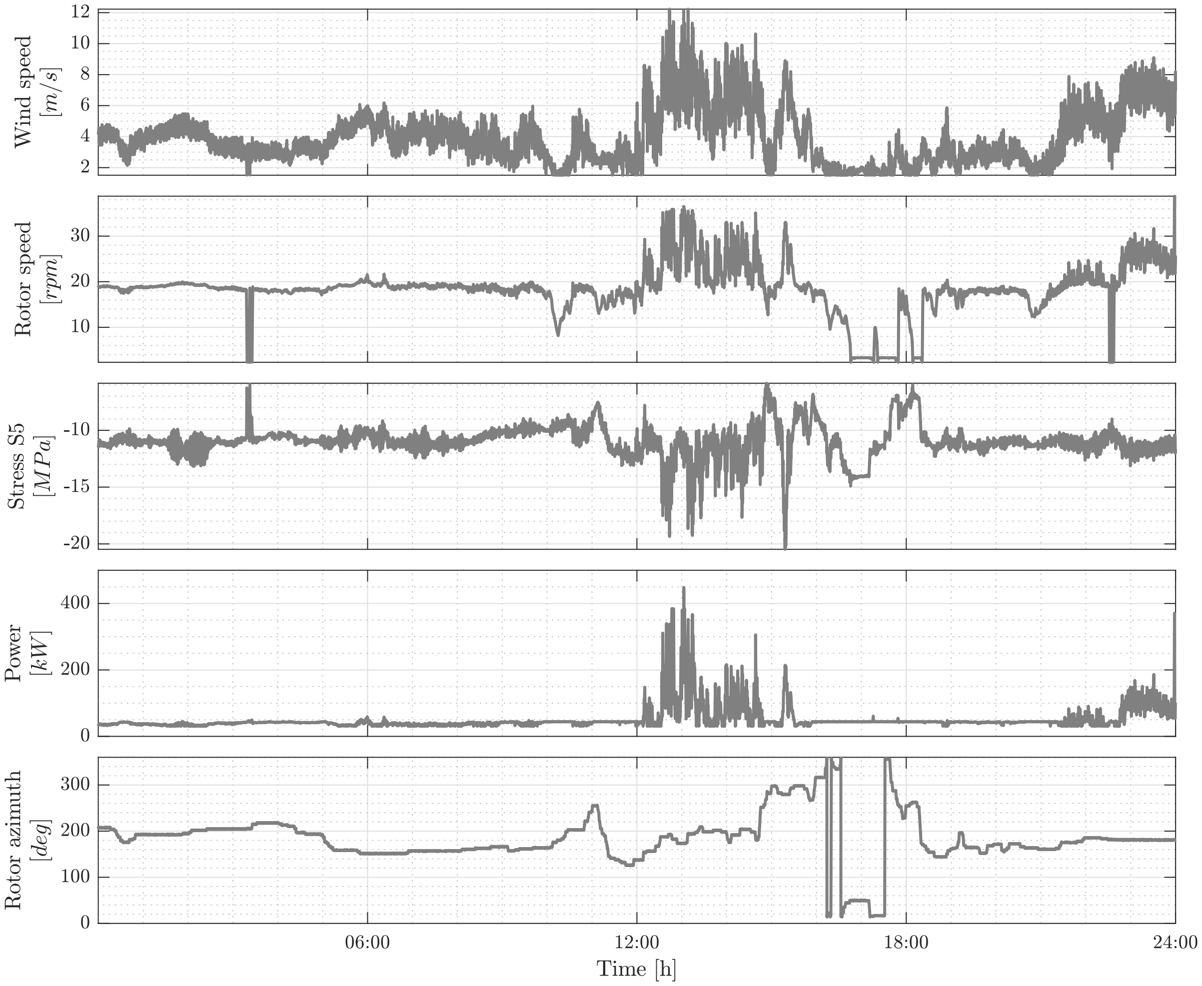

Figure 4.54 Operating conditions of research wind turbine

4.3.3 Tower Loading Measurements

As mentioned before, the tower loading is measured using displacement sensors located at two different levels on the tower, the lower level is located at about $21\,m$ height and the second measurement level is located at about $42\,m$ height. At each level, three displacement sensors with 120° configuration are placed on the inner side of the tower. At the higher level these sensors are called w_1, w_2 and w_3, and the lower level the sensors are called w_4, w_5 and w_6.

Fatigue analysis is limited only to the measurement obtained from sensor w_5 located at the lower level and in the south direction. The main reason that motivates this choice is the high tower loading measured at this level; furthermore, due to the fact that most of the wind are coming from the south direction (see fig. 4.53), the tower will be subject to high bending forces in the south-north direction.

A temperature compensation of the measured displacement is done similar way to [Lachmann, 2014]. Then, the corrected sensor displacement is divided by sensor length to obtain the strain ε_i and the bending stress s_i is obtained using the Young's modulus of the steel $E = 210\,GPa$.

4.3.4 Tower Loading Characteristics

The first tower bending natural frequency of the research wind turbine is about $0.37\,Hz$. If this natural frequency is compared to the natural frequency of the tower of the small wind turbine at the University of Siegen for the same bending mode which is equal to $2.7\,Hz$, it is possible to conclude that the research wind turbine has slower dynamics, therefore, the filtering window should be increased accordingly with similar factor between the natural frequencies. Based on this, the moving average filter window is increased from $T_{MATE} = 12\,s$ for the small wind turbine to $T_{MATE} = 75\,s$ for fatigue analysis of the research wind turbine.

Fig. 4.55 shows the bending stress loading s_5 in addition to the extracted deterministic and stochastic components using a moving average filter with $T_{MATE} = 75\,s$ window length. The tower bending natural frequency could be easily identified from the corresponding power spectral density of the calculated stress s_5. The amplitude distribution of the measured stress doesn't enjoy normal distribution characteristics, however, the stochastic component enjoy a symmetrical amplitude distribution with kurtosis larger than three.

The data-set used in fatigue analysis is built by dividing the stress time history into blocks each of one hour duration. By plotting the skewness-kurtosis scattering, fig. 4.56 is obtained. Comparing this scattering to that obtained from the small wind turbine (fig. 4.38 and fig. 4.39) shows that the research wind turbine has more coherent skewness-kurtosis scatter with skewness

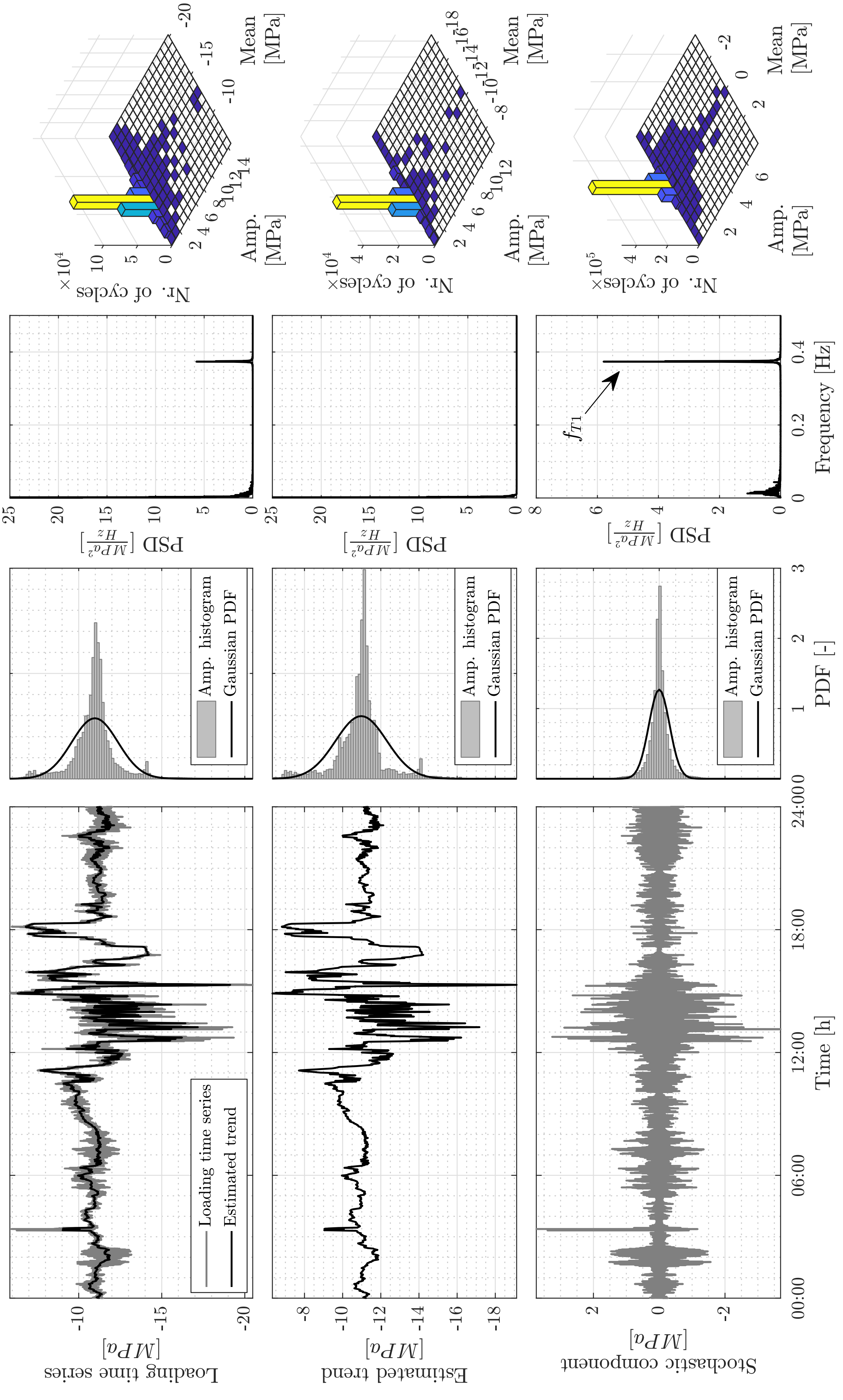

Figure 4.55 Tower loading characteristics (location s_5). Moving average filter window length $T_{MATE} = 75\,s$

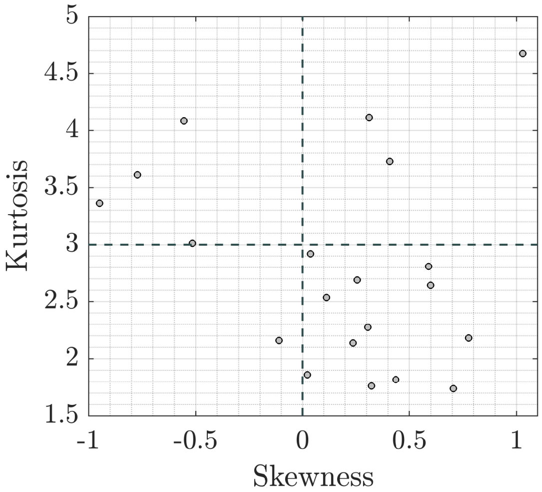

Figure 4.56 Skewness-kurtosis scatter plot of tower stress s_5.

limited to ±1 and kurtosis that ranges between 1.5 and 5. This scatter is even more coherent when compared to that of the stochastic component of tower loading of small wind turbine (fig. 4.45). This means that the loading over the research wind turbine tower is more close to the normal distribution than that of the small wind turbine.

4.3.5 Fatigue Analysis

The first step in fatigue analysis is checking the usability of the Projection-by-Projection formula. By employing the rainflow counting algorithm to estimate fatigue damage of the stochastic component $\mathcal{D}_s^{RFC}$ and the deterministic component $\mathcal{D}_d^{RFC}$, it is possible to calculate the total fatigue damage using the Projection-by-Projection formula $\mathcal{D}_{PbP}^{RFC}$. Normalizing the estimated fatigue damages by the fatigue damage of the loading time history $\mathcal{D}_m^{RFC}$, the following normalised fatigue damage indices η_s^{RFC}, η_d^{RFC} and η_{PbP}^{RFC} are obtained. Fig. 4.57 shows the PDF of the normalised fatigue damage indices for the considered data-set. This figure demonstrates that the contribution of the deterministic component in the total fatigue damage is below 25% with high probability to be close to zero. On the contrary, the stochastic component is more representative to the measured loading in terms of fatigue cycles. The Projection-by-Projection formula gives almost identical results ($\eta_{PbP}^{RFC} \approx 1$) to the obtained fatigue damage by direct use of the rainflow counting algorithm.

Recalling that the main assumption for the use of the Projection-by-Projection formula is a zero cross-correlation between the deterministic and the stochastic components. By calculating this cross-correlation between the two signals using both time-series and both PSDs, the PDFs presented in fig. 4.58 are obtained. These results show clear non-correlation between the two components.

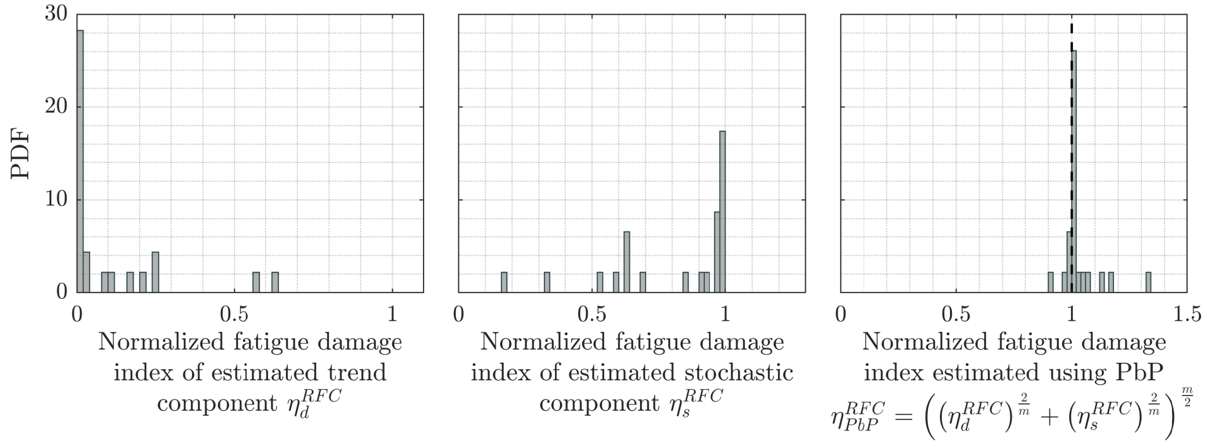

Figure 4.57 Probability density function of normalised fatigue damage of the estimated deterministic (left) and stochastic (middle) components, in addition to the normalised fatigue damage calculated using the Project-by-Projection formula (right).

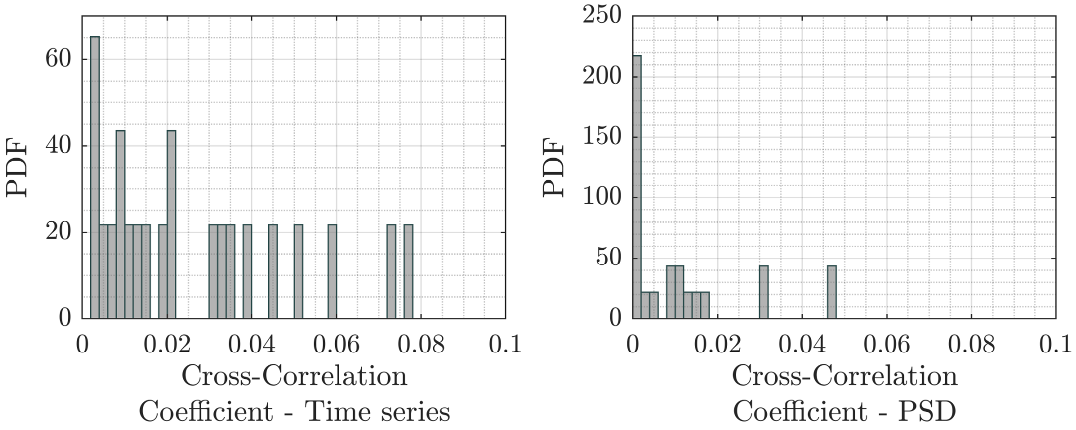

Figure 4.58 Correlation coefficient between the deterministic and stochastic time-series components (left) and the correlation coefficient between the PSD of the deterministic and stochastic components (right).

The second step in fatigue analysis is to evaluate the effectivity of the proposed “de-trending&PbP” method to estimate fatigue damage using the measured loading as reported for example by [Ragan et al., 2007] and [Arany et al., 2014]. Fig. 4.59 shows in the upper row the PDF of the normalised fatigue damage index of fatigue damage estimation using spectral methods applied to the measured loading history η_m^k, $k = \{SM, \alpha_{0.75}, TB2, DR, BM\}$; while the lower row in the figure shows the PDF of the normalised fatigue damage calculated using the “de-trending&PbP” strategy for the same spectral methods η_{PbP}^k. Both cases consider the single-moment (SM), The Empirical $\alpha_{0.75}$, 2nd Tovo-Benasciutti (TB2), Dirlik (DR) and the Bands-methods (BM).

The direct use of the spectral methods give a scattering damage estimations which are in some cases very conservative. This large scattering makes the directed use of spectral methods less useful. On the contrary, fatigue analysis using the proposed strategy (results in the lower

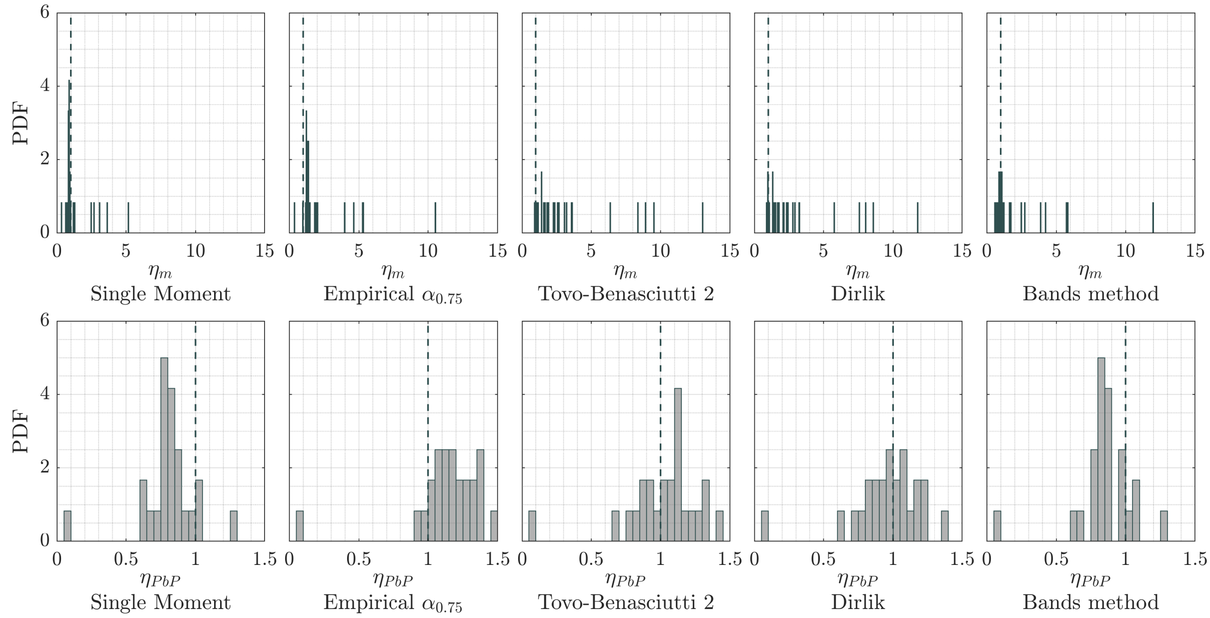

Figure 4.59 Normalised fatigue damage estimation η_m and η_{PbP} for $T_{MATE} = 75\,s$

row in fig. 4.59) gives more coherent results with normalised fatigue damage indices close to unity. While the Single-Moment method tends to be less conservative with normalised damage index $\eta_{PbP}^{SM} \in [0.6,\, 1.1]$, a slightly better result is obtained using the Bands method with similar range of the normalised damage index η_{PbP}^{BM}. The results obtained by the Dirlik method and the Tovo-Benasciutti second method are similar with corresponding normalised damage index ranges between 0.7 and 1.5. Finally, the best result is obtained by the Empirical $\alpha_{0.75}$ method with $\eta_{PbP}^{\alpha_{0.75}} \in [0.9,\, 1.4]$.

In all these methods, two separated data-blocks are clearly to be identified, one data-block with normalised damage index value close to zero and one data-block with normalised damage index far to the right (more than 1.5). By farther inspection of the time history of these data-blocks, it is found that they correspond to a repetitive start-stop cycles at lower wind speeds. For example, the data-block that correspond to the normalised fatigue damage index close to zero represents the measured loading between 03:00 and 04:00 o'clock. The stochastic component of the loading history is illustrated in fig. 4.60-left, where two consecutive start-stop cycles are clearly identified in the stochastic component. The introduced transient structural dynamics due to these start-stop cycles result to non-stationary stochastic component. This means that the spectral methods would give incorrect estimation of fatigue damage in this case. The same could be seen at the measured loading between 17:00 and 18:00 o'clock (fig. 4.60-right) where more than one start-stop cycles are presented in this data-block which will result into over estimating the fatigue damage. The obtained conclusion at this point is that, the estimated fatigue damage depends on the number of start-stop cycles presented in the data-block which will result either in an over or under estimation of the fatigue damage. This means that fatigue damage estimation using spectral methods from data-blocks with start-stop cycles is far from being accurate.

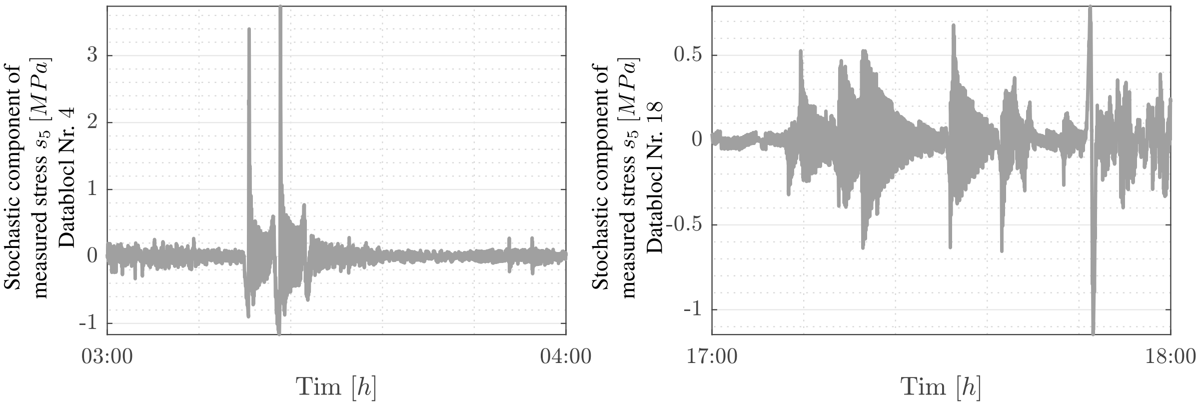

Figure 4.60 Stochastic component of measured loading with start-stop cycles

By considering the same categories for good and acceptable fatigue damage estimation used for the small wind turbine (tab. 4.8), it is possible to calculate the probability of obtaining good and acceptable estimations for both cases. The first case is for direct use of the spectral methods with the measured loading for fatigue damage estimation, while the second case represents fatigue damage estimation using the “de-trending&PbP” strategy. The obtained good and acceptable probabilities of the normalised fatigue damage for both cases are illustrated in fig. 4.61. The maximum probability of obtaining good and acceptable fatigue damage estimation in the first case is 57 % and 74 %, respectively, which is obtained by using the Single-moment method, while the other methods have considerably lower probabilities. These results look much better in the second case, where all methods have 57 % to 74 % probabilities of obtaining good estimations and 70 % to 87 % probabilities of acceptable estimations. Off course, due to the limited sample size, these values should be seen as orientation values that might change if the sample size is increased.

Though the results of the second case still far from being optimal, these results could be improved by adjusting the moving average filtering window. By reducing the window to $T_{MATE} = 10\,s$, this leads to including more cycles into the deterministic component where their fatigue damage effect is accurately estimated using the rainflow counting. At the same time, the stochastic component is having more stable statistical parameters and accordingly becoming more stationary which results in better fatigue damage estimation results from the stochastic methods. At this short moving average filtering window, the probability of obtaining good fatigue damage estimations increases to 79 % for the Single-Moment method (fig. 4.62-left) and to 75 % for the Dirlik and the Bands-Methods. The most notable increase is the acceptable

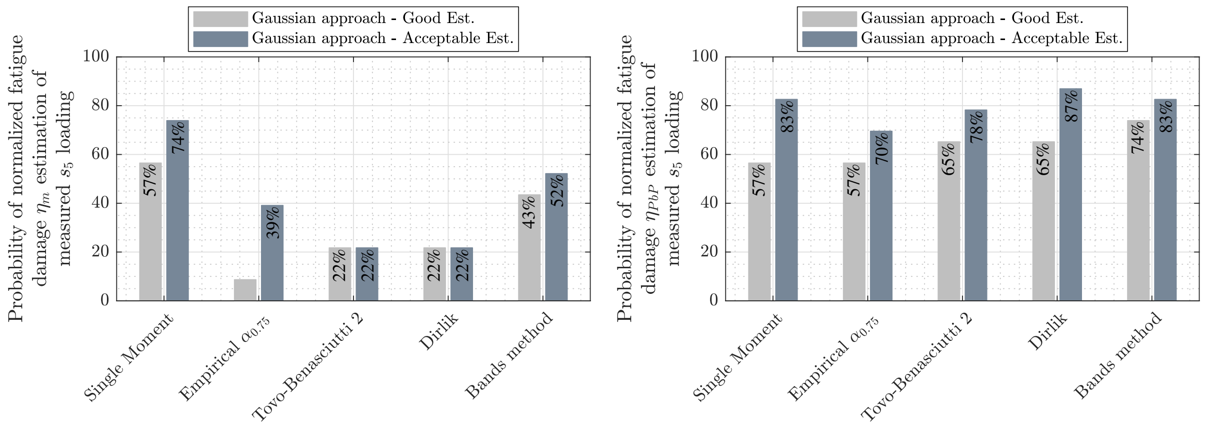

Figure 4.61 Probability of Good and Acceptable fatigue damage estimation using different spectral methods. To the left using measured stress and to the right using Projection-by-Projection formula. $T_{MATE} = 75\,s$

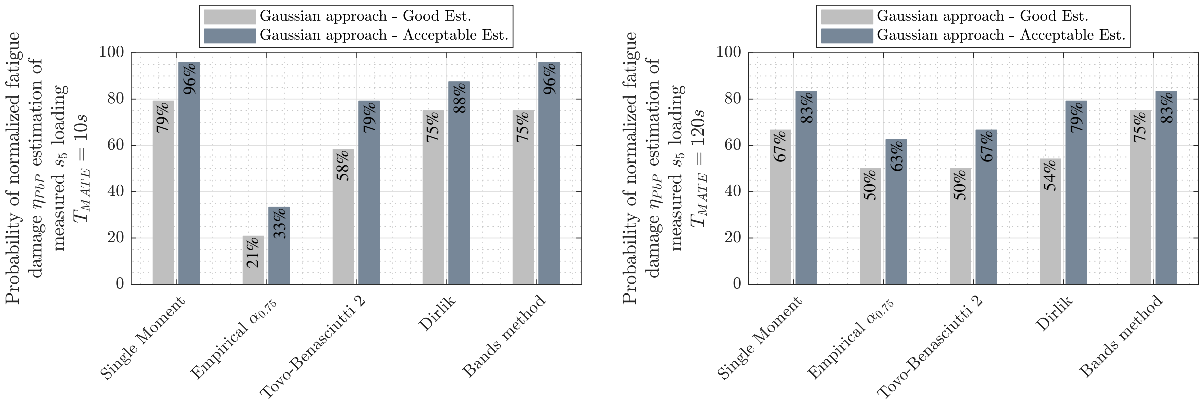

Figure 4.62 Probability of Good and Acceptable fatigue damage estimation using different moving average filtering windows. To the left $T_{MATE} = 10\,s$. To the right $T_{MATE} = 120\,s$.

fatigue damage estimation which goes up to 96 % for the Single-Moment and the Bands-Methods while it keeps its same level for the 2^{nd} Tovo-Benasciutti and Dirlik methods.

On the contrary, if the length of the moving average filtering window is increased to $T_{MATE} = 120\,s$ this will lead to less cycles being included in the deterministic component while the statistical parameters of the stochastic component becomes less stable and this component becomes less stationary. Therefore, the accuracy of fatigue damage estimations of the statistical methods deteriorates and the overall estimation results tend to have less probabilities of having good or acceptable fatigue damage estimations (fig. 4.62-right).

The obtained conclusion at this point is it that, the choice of the length of the moving average filtering window affects the overall fatigue damage estimation results, while short windows are preferred for less computational effort in signal de-trending, they will increase the dependency on fatigue damage estimation from the deterministic component calculated using the rainflow counting which in its turn requires more calculation time and the overall results end to be close to the time-domain fatigue damage estimations. On the contrary, employing longer moving average filtering window increases the computational effort in signal de-trending and resulting into simple deterministic component with less cycles and at the same time drive the stochastic component far from being stationary. This will lead to the deterioration of the overall fatigue damage estimation results using the spectral methods. The optimal filtering window depends on the good understanding of the structural dynamic response.

Fig. 4.63 illustrates the calculated accumulative fatigue damage over all data-blocks using the measured loading and the fatigue damage estimation in time domain $\tilde{\mathcal{D}}_m^{RFC}$, the accumulative fatigue damage estimation using the rainflow counting and the deterministic component $\tilde{\mathcal{D}}_d^{RFC}$, the accumulative fatigue damage calculated using the stochastic component and the different spectral methods $\tilde{\mathcal{D}}_s^k$, $k = \{SM,\, \alpha_{0.75},\, TB2,\, DR,\, BM\}$, the accumulative fatigue damage calculated using the stochastic component and the rainflow counting method $\tilde{\mathcal{D}}_s^{RFC}$ and finally, the overall fatigue damage from the deterministic and stochastic components using the Projection-by-Projection formula $\tilde{\mathcal{D}}_{PbP}^k$, $k = \{SM,\, \alpha_{0.75},\, TB2,\, DR,\, BM\}$.

The first conclusion that could be obtained from fig. 4.63(a) is that the Projection-by-Projection formula gives similar result to the rainflow cycle counting method. Furthermore, the fatigue damage estimated using the rainflow counting and the stochastic component follow the same trend of the overall fatigue damage. This means that the stochastic component could be used for monitoring purposes and in combination with the deterministic component the total fatigue damage could be calculated. The same conclusion could be extended to the use of the spectral methods for fatigue damage estimation from the stochastic component and the overall fatigue damage obtained using the Projection-by-Projection formula. However, the results depend on the used spectral method; while the Empirical $\alpha_{0.75}$ method tends to be conservative $\left(\mathcal{D}_{PbP}^{\alpha_{0.75}} \geq \mathcal{D}_m^{RFC}\right)$, the other methods tend to be less conservative $\left(\mathcal{D}_{PbP}^k < \mathcal{D}_m^{RFC},\right.$ $\left.k = \{SM,\, DR,\, BM\}\right)$. The only exception is presented by the 2$^{\text{nd}}$ Tovo-Benasciutti method which seems to be the only method to capture through the stochastic component the increased fatigue damage due to the high wind activity between 12:00 and 16:00 o'clock.

The second conclusion obtained from observing the accumulative fatigue damage is that the deterministic component captures fatigue damage related to the change of the mean wind speed, or in other words, the fatigue damage related to the change of loading mean value. This is clear for example in the region between 00:00 and 12:00 o'clock where the turbine is subject to low wind speeds with slowly changing mean value (see fig. 4.54 and 4.55), the same operating condition is observed between 16:00 and 24:00 o'clock. In both regions the accumulated fatigue

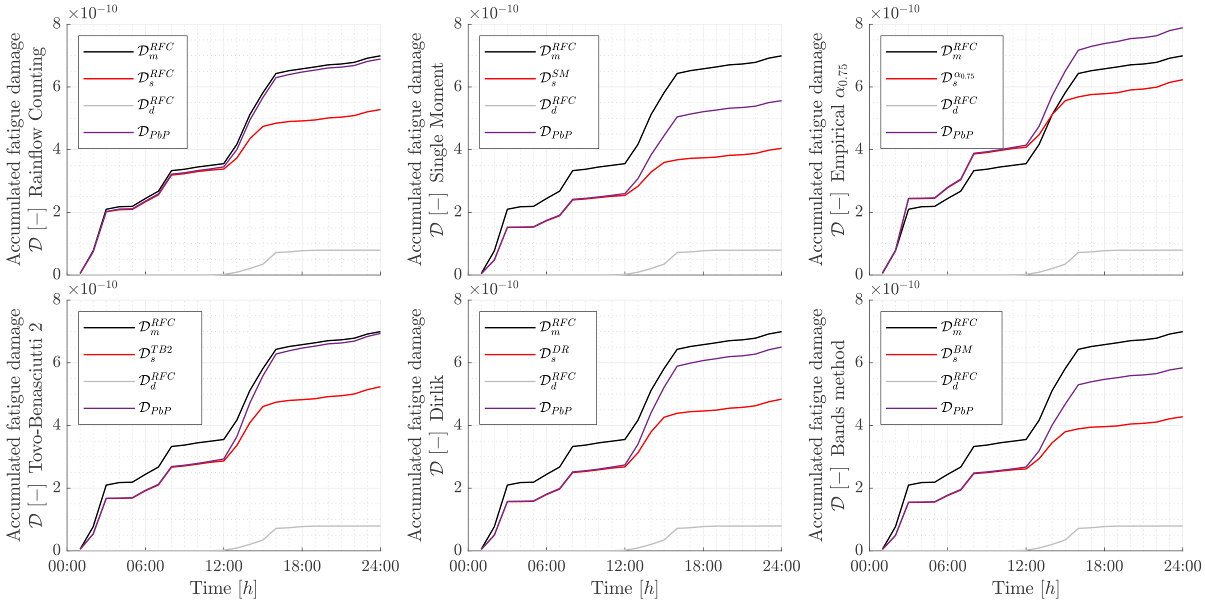

Figure 4.63 Accumulative fatigue damage using different estimation methods. $T_{MATE} = 75\,s$

damage estimated from the deterministic component is almost constant. The only change is seen between 12:00 and 16:00 o'clock where the turbine was subject to highly turbulent wind with wind speed reaching $12\frac{m}{s}$. The fatigue damage related to the change of mean value of the turbulent wind is captured by the deterministic component, while the fatigue damage related to the fluctuation of the wind loading about this mean value is captured effectively by the stochastic component as it is clear from the figure.

4.3.6 A New Approach for Structural Health Monitoring

By using the illustrated SHM approach in sec. 2.10, it is possible to plot the scatter of the estimated fatigue damage against the standard deviation of the measured wind speed as shown in Fig. 4.64. This figure also illustrates the linear regression estimated from the data-set in addition to a selected tolerance region. Due to the limited number of data blocks only 24 points are presented in this scatter. This limited number of data blocks prevents deriving a conclusive conclusion. However, it is possible to derive the following statements.

The first statement is derived from the positive inclination of the linear regression. This indicates a direct relation between the standard deviation of the wind speed and the corresponding fatigue damage. An increased deviation of the wind speed results into an increased fatigue damage.

The second statement is obtained from comparing closely the three scatter plots available in Fig. 4.64. The one to the left represents the scatter of the fatigue damage directly estimated from the measured loading using the rainflow counting. The middle plot represents the scatter

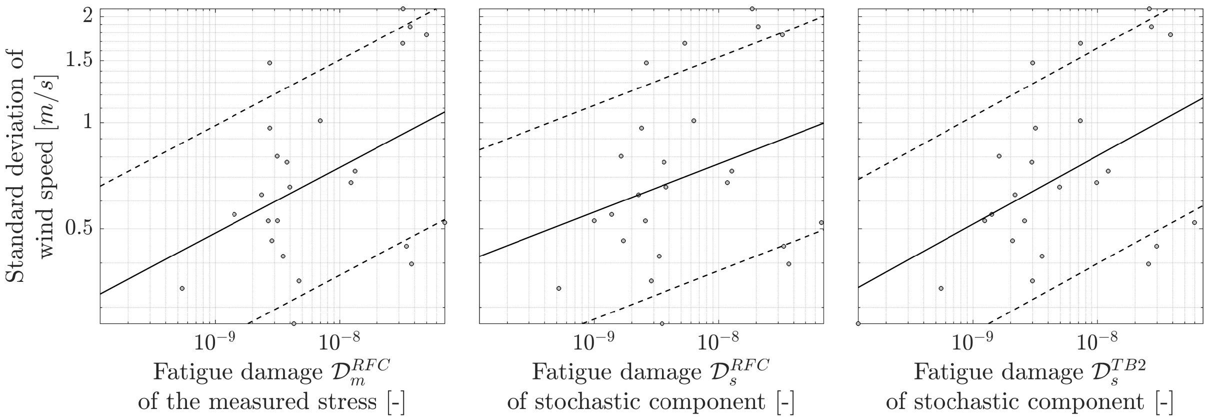

Figure 4.64 Scatter plot of the calculated fatigue damage using rainflow counting versus the standard deviation of the wind speed. Fatigue damage using rainflow counting is calculated for the measured stress in addition to the stochastic component while 2nd method of Tovo-Benasciutti is used to estimate fatigue damage of the stochastic component.

of the fatigue damage estimated from the stochastic component using also the rainflow cycle counting. Finally to the right, the plot represents the scatter of the fatigue damage estimated from the stochastic component using the 2nd Tovo-Benasciutti method. Similar scatter to this final plot could be obtained using other spectral methods. All plots against the standard deviation of the wind speed. A close comparison shows similar scatter pattern. This means that the obtained scatter pattern using spectral methods from only the stochastic component represents completely that obtained from the measured loading using the standard time-domain approach.

The final statement is related to the scatter pattern itself. By observing it using the 2nd Tovo-Benasciutti method. It is clear that most of the points are located within the chosen tolerance region. Only three points are located out-side of this region. These points correspond to low wind speed standard deviation with high estimated fatigue damage. The same three points could be noticed in the other scatter plots. The inspection of the related time-series of these points show that they correspond to the start-stop cycles of the turbine. These cycles result into high fatigue damage estimations at lower wind speeds. These three points are clearly separated from the other points in the scatter plot which make them easy to identify.

Plotting the scatter of the estimated fatigue damage per each data-block against the standard deviation of the wind speed could be used for fatigue damage detection. A proper definition of the tolerance region make the detection of any abnormality in the system/structure easy to detect.

4.3.7 Discussion and Conclusion

This section has discussed the use of the new “de-trending&PbP” strategy along with different spectral methods in fatigue analysis of operating utility-scale wind turbine. Due to the nature of the wind loading, only tower base bending measurement that corresponds to the main wind direction is used for fatigue analysis. The window of the moving average filter has been adjusted according to the dynamic response of the turbine.

Decomposing the measurement into a deterministic and stochastic components have been done as first step. Then with the help of the rainflow cycle counting followed by the projection-by-projection formula fatigue damage has been estimated. This primary fatigue analysis shows that the estimated fatigue damage using the PbP formula is very close to that obtained by direct cycle counting in time domain.

The second step has compared fatigue damage estimations obtained by the direct use of the spectral methods using the Gaussian approach to that obtained using the “de-trending&PbP” strategy. This comparison demonstrates that the proposed method has improved dramatically spectral fatigue damage estimations in comparison to the time domain cycle counting.

This comparison has also shown a few data blocks that scatter too far from the distribution centre. By taking a closer look at these data blocks, it is found that they correspond to measurements with high transient dynamic response due to successive start-stop cycles of the turbine. These transient dynamic responses have been included in the stochastic component which make the corresponding stochastic data-block far from being stationary. These resulted into a violation of the basic assumption of the theory of the stochastic methods, thus the faulty estimation of the fatigue damage from these data-blocks. Such transient dynamic response put hard constraints on the use of the proposed “de-trending&PbP” strategy. A simple solution is to classify such data-blocks in a separate group, which is easy to achieve using the standard turbine operational measurements. Fatigue analysis of this separate group is to be achieved using the standard rainflow cycle counting as it is the only available method that can handle such transient loading effectively.

The estimated stochastic components have a symmetric amplitude distribution with high kurtosis (too peaky distribution). Therefore, it is far from being Gaussian. The use of the corrected Gaussian does not improve the results (results not shown); and the transformed Gaussian model failed in most cases in estimating the transform function. However, in case it is possible to estimate it, the estimation results are close to that obtained from the Gaussian approach (results not shown). This allows to conclude that the used methods aimed to handle the non-Gaussianity of the loading failed to achieve that. This is due two main reasons. The first reason is related to the development of the corrected Gaussian method which is based only on simulated data and it has never been tested with real measurements. The second reason is related to the transformed Gaussian model which is basically developed to deal with loading from the waves which have different characteristics when compared to wind loading. Basically, this difference could be seen as the wind loading is more turbulent, thus the loading has higher kurtosis values which prevented the calculation of the transfer function. This conclusion leaves the door open to develop other methods that could take the non-Gaussianity of the loading into account during fatigue damage analysis.

Using the “de-trending&PbP” strategy along with the Gaussian approach for fatigue damage analysis shows that good estimations are obtained by the Single-Moment, Empirical $\alpha_{0.75}$, Tovo-Benasciutti second method, Dirlik and Bands methods. with probability ranging between 57 % and 74 % where the best performance is obtained using the Bands-method. These results depend on the used window length of the moving average filter as this window controls the cycle contents of the deterministic and stochastic components. To maintain the benefits of the spectral fatigue analysis, the cycle contents of the deterministic component should be kept as low as possible. This means increasing the window length of the moving average filter. However, this increase is limited by two factors. The first one is the computational effort needed for signal decomposition in case of long window of the filter while the second factor is related to the characteristics of the stochastic component. Therefore, The optimal window length should be carefully chosen.

Comparing the accumulated fatigue damage estimated from different methods demonstrate the good performance of the proposed “de-trending&PbP” strategy. Furthermore, spectral fatigue damage estimated from the stochastic component follows the same trend as that of the rainflow cycle counting. This clearly shows the potentials of using spectral methods for fatigue monitoring.

This last conclusion has been confirmed by plotting the scatter of the estimated fatigue damage from different methods against the standard deviation of the wind speed. The positive trend confirm the direct relation between the estimated fatigue damage per each data-block and the standard deviation of the wind speed for the same period. Furthermore, the blocks with high dynamic response due to the start-stop cycles are also clear to identify as they form a clearly separated group from the rest of the scatter. This indicates that any change in turbine structure will be reflected as a change in the scatter pattern.

4.4 Proof of Concept of Using Comparative Sensor Data Approach for SHM

The previous sections compared fatigue damage estimation results obtained from time and frequency domains using simulation and operational measurements. The main obtained conclusion is that some spectral methods with the "de-trending&PbP" approach are capable of giving comparable fatigue damage estimations to the time domain. Furthermore, the previous sections demonstrated the potentials of using spectral methods in fatigue damage detection.

The used standard technique for fatigue damage detection is to compare the accumulated fatigue damage to a critical value; when the accumulated fatigue damage reaches this critical value, fracture of the component due to fatigue damage is assumed to happen. This section presents an alternative approach for structural health monitoring (see sec. 2.10). This approach is based on monitoring the change of the calculated fatigue damage per a pre-defined time duration T against a reference value such as the fatigue damage estimated from a reference location or the standard deviation of the loading applied to the structure (see fig. 4.51 and fig. 4.64).

This section focus on fatigue damage detection, therefore, only fatigue damage estimations in time domain are used. The previous sections have demonstrated the ability of the spectral methods to obtain similar results to the time domain, hence, the results of fatigue analysis using the spectral methods are not presented in this section.

4.4.1 Experimental Design

The aim of the experimental part is to monitor the fatigue life of a specimen subject to stochastic loading. This is done by monitoring the accumulated fatigue damage over time from one side, and from the other side, by monitoring linear relation between the fatigue damage at the monitored location and a reference value. The reference value could be the standard deviation of the input loading, or the fatigue damage estimated from a loading on the specimen measured at a non-critical location.

Property	Symbol	Unit	AlMgSi0,5	S235
Young's Modulus	E	GPa	70	210
Yield strength	S_y	MPa	160	235
Ultimate strength	S_u	MPa	215	360
Fatigue exponent	m	–	11.8	3

Table 4.10 Main properties of specimen materials.

Two different specimen sets are used in this experiment. The first set uses specimens made of aluminium (AlMgSi0,5) and the second set uses specimens made of construction steel (S235). The main properties of these materials are illustrated in tab. 4.10. Both specimen sets share the same design with different dimensions that takes into account the material properties and the limitations of the used shaker.

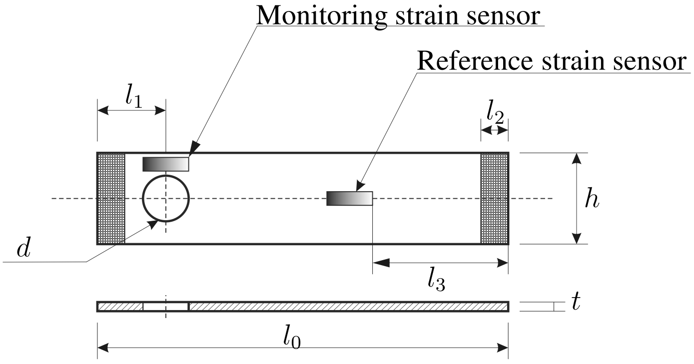

Figure 4.65 Specimen dimensions.

Table 4.11 Specimen dimensions

	Material	
Dimension	AlMgSi0,5	S235
l_0	$100\,mm$	$140\,mm$
l_1	$20\,mm$	$30\,mm$
l_2	$10\,mm$	$10\,mm$
l_3	$40\,mm$	–
h	$20\,mm$	$20\,mm$
t	$2\,mm$	$3\,mm$
d	$8\,mm$	$8\,mm$

The experimental setup is shown in fig. 4.67. Each specimen is clamped from its lower side to a base plate and from its upper side to the shaker rod. The dark areas in fig. 4.65 illustrate the clamping regions. Furthermore, close to the base of the specimen, a through hole is present in order to introduce stress concentration on the hole lateral sides which would initiate fatigue cracks. This design ensure that the fatigue failure will start from the hole lateral sides towards the outer sides of the specimen. By installing strain sensors next to the hole as shown in fig. 4.65, it is possible to monitor the fatigue life time of the specimen during the experiment. Finite element analysis (fig. 4.67) gives a stress concentration factor of $k_{sc} = 1.4$ between the mean stress at the sensor location and the lateral sides of the hole. Moreover, the last specimen is equipped with a reference strain sensor that is installed in the upper part of the specimen as shown in fig. 4.65. Finally, the modal analysis of the clamped specimens show that the first natural frequency of the aluminium specimens is $f_{Alu,1} = 142\,Hz$ while the first natural frequency of the construction steel specimen is $f_{S235,1} = 118\,Hz$.

In this experimental setup, a shaker is used to apply the bending force to the specimen. The applied force is monitored using a load cell located between the shaker and the specimen. The shaker is driven by an analogue amplifier that is driven by the analogue output of the DS1104 R&D controller board from dSpace® which is integrated with a desktop computer (PC). The measured strain and force are amplified and the resulting analogue signals are fed to the analogue to digital inputs of the DS1104 R&D controller board where they are converted into digital form and saved to the PC hard disk. The applied force by the shaker is calibrated in such way that the maximum bending stress value would be less than 75 % of the yield strength of the specimen material.

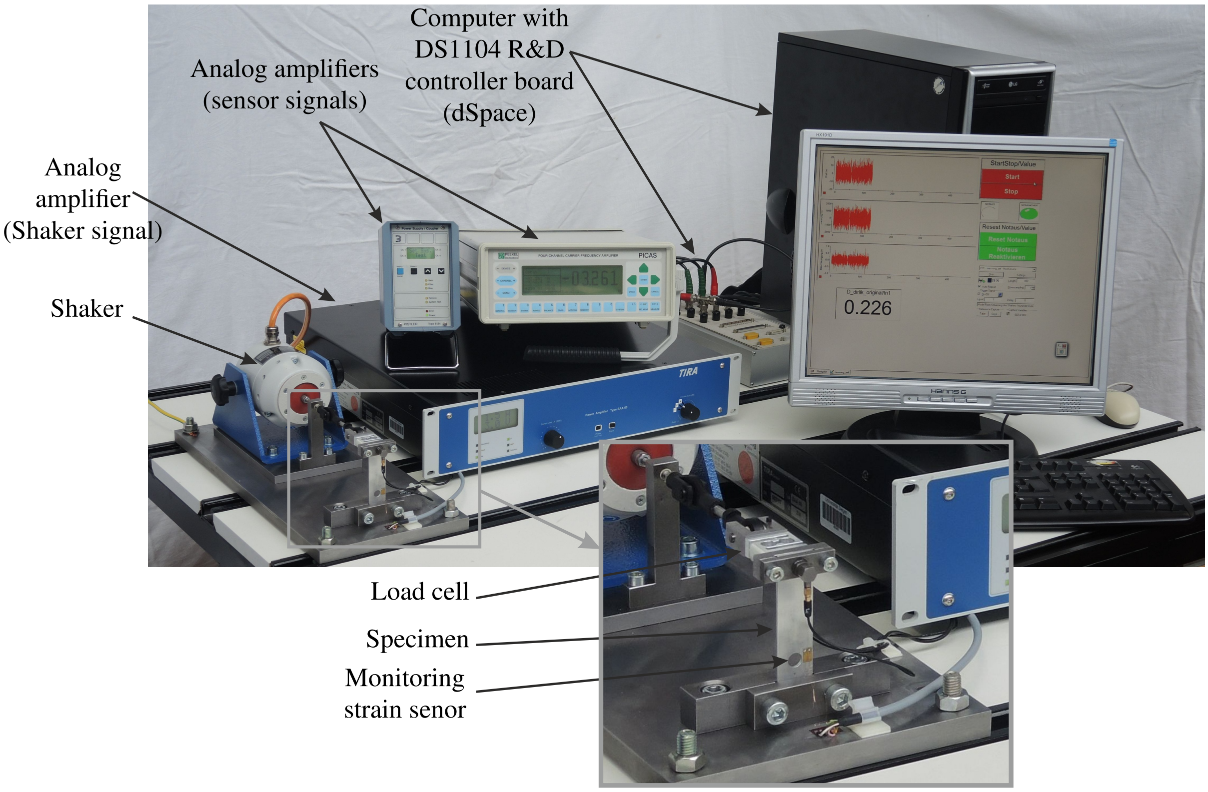

Figure 4.66 Experimental setup

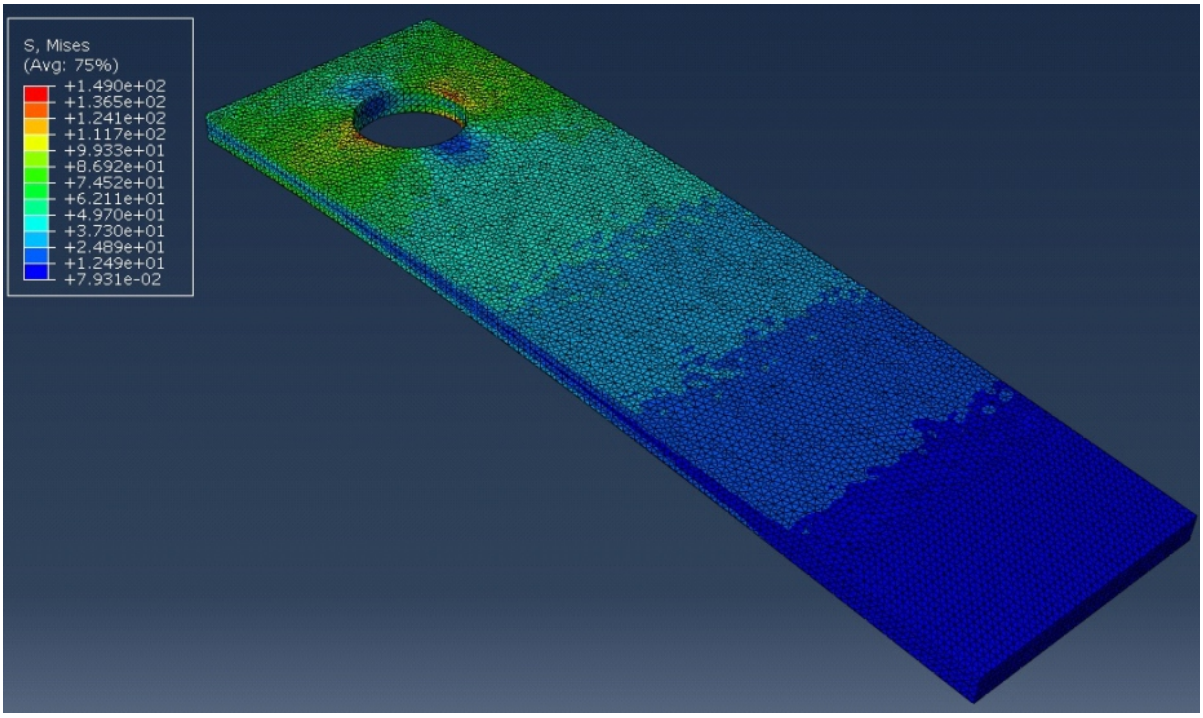

Figure 4.67 Finite element analysis of the Aluminium specimen

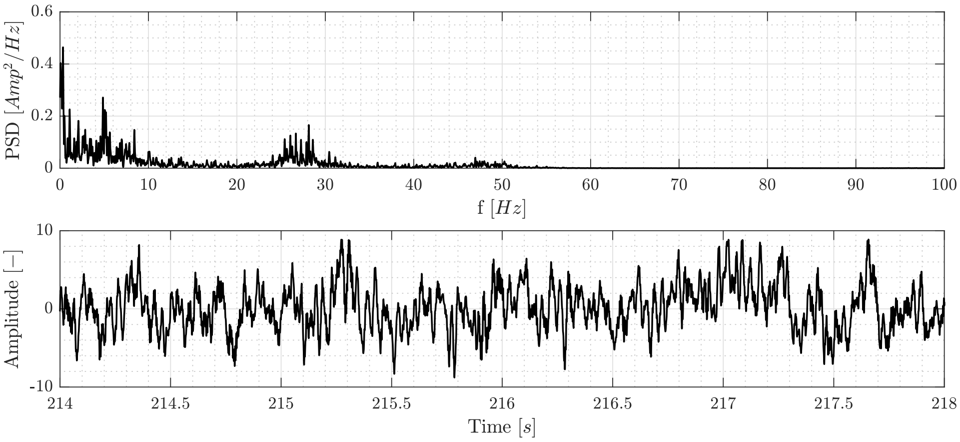

Figure 4.68 Applied experimental loading spectrum and a generated time-series.

The specimen is subject to a loading spectrum similar to the one observed by the reference wind turbine tower-base in the fore-aft direction. The loading spectrum is taken from the wind turbine simulation tool FAST, where the reference wind turbine is operated in the full load region and is subject to turbulent wind profile. In order to reduce the time needed for the experiment, the loading spectrum is shifted to higher frequencies by a factor of 15, which means that the natural frequency of the turbine tower is shifted from $0.33\,Hz$ to $5.2\,Hz$. This means that the necessary condition presented in eq. 2.158 is valid in this experiment as the maximum frequency of the loading is considerably lower than the lowest frequency of the system dynamics. The loading spectrum is used to generate the loading time series that are used to drive the shaker. Due to the limited memory if the dSpace® board, the generated time series are limited to 20 minutes. Fig. 4.68 illustrates the loading spectrum and an example of the generated time series.

Bending strain is captured using strain sensors mounted next to the hole (see fig. 4.65) on both sides of the specimen in half-bridge configuration. This strain sensor is called the monitoring sensor. The experiment was designed first to use only the monitoring strain sensor, in addition to the load cell to measure the loading force, later a second strain sensor in half-bridge configuration is used (see fig. 4.65). This sensor is called the reference sensor. The idea of using the monitoring and the reference sensors is to compare the fatigue damage rate obtained from both sensors against each other instead of comparing the monitoring strain sensor data against the loading force.

The data collected by the dSpace® control board are sampled at $1000\,Hz$. These data are grouped in data-blocks each of $480s$ duration, then saved directly to the hard-disk. The choice of the data-block duration is related to the maximal available memory in the dSpace® control board. In total nine aluminium and three construction steel specimens are tested. However, due to defect strain sensors (in three aluminium specimens) during the experiment, the corre-

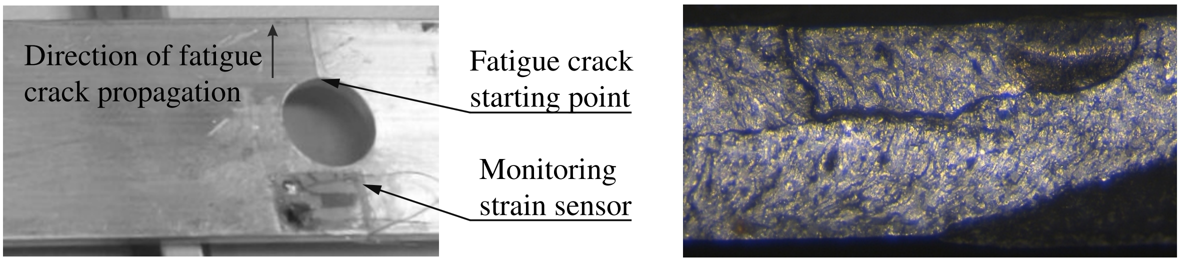

(a) Fatigue crack starting point and propagation direction. **(b)** Microscopic photo of fatigue crack surface.

Figure 4.69 Fatigue failure of aluminium specimen.

sponding specimens are excluded. Tab. 4.12 gives an overview of the specimens and the used sensors.

Table 4.12 Overview of specimens and used sensors.

Material	Specimen Nr.	Sensor		Comments
		Monitoring	Reference	
Alu	P1	●		
	P2	●		
	P3	●		Defect strain sensor during the experiment
	P4	●		
	P5	●		
	P6	●		Defect strain sensor during the experiment
	P7	●		
	2DMS-P1	●	●	Defect strain sensor during the experiment
	2DMS-P2	●	●	
S235	P0	●		
	P1	●		
	P2	●		

During the experiment, the measured strain next to the hole is monitored and the experiment is automatically stopped if the root mean square (RMS) value of the monitored strain reaches a pre-define threshold. At this threshold the fatigue failure is considered to happen. All specimens had fatigue cracks in the opposite side to the monitoring strain sensors locations. These cracks started from the inner side of the hole and propagates towards the outer side of the specimen. Fig. 4.69 shows an example of the fatigue failure in aluminium specimen.

The stress loading is calculated from the measured strain then fatigue damage rate per each data-block is estimated using the rainflow counting. The results are discussed considering two aspects: the accumulated fatigue damage over time and the fatigue damage rate per each data block compared to a reference value such as the standard deviation of the input loading or the estimated fatigue damage rate of the measured reference loading. The main objective is to detect fatigue failure as early as possible.

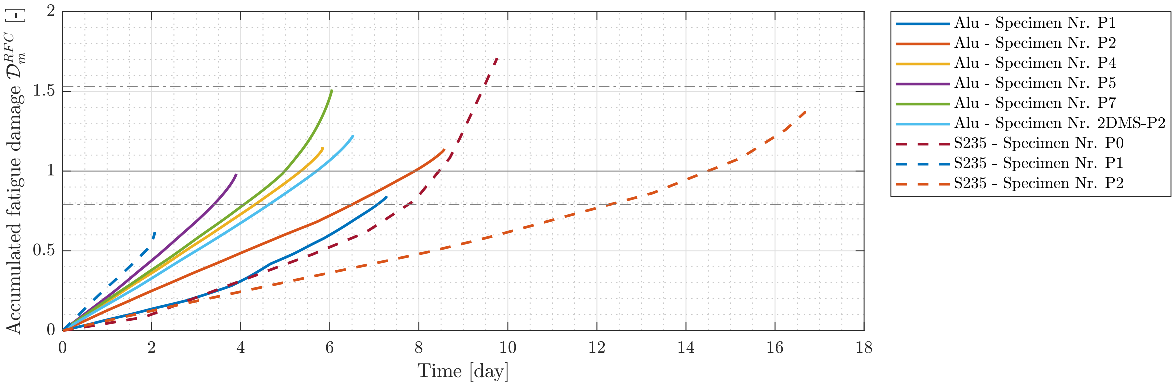

Figure 4.70 Accumulated fatigue damage over time. Aluminium specimens in continuous line style, construction steel in dashed line style.

4.4.2 Accumulated Fatigue Damage

The accumulated fatigue damage over time for the aluminium and the construction steel specimens are illustrated in fig. 4.70. While the results obtained from the aluminium specimens are presented in continuous line style, dashed line style is used to represent the results of the construction steel specimens. The fatigue failure (corresponds to the last point in the presented accumulated fatigue damage progress) is considered to occur when the accumulated fatigue damage shows an abrupt change, as at this point, fatigue crack becomes visible at the hole side and the time it needs to propagate till it reaches the outer side of the specimen is a few hours (depends on material and loading amplitude) for both materials. Before this abrupt change in the fatigue damage, there has been no visual signs of fatigue failure.

The slope of the accumulated fatigue damage depends on the loading amplitude which has been manually adjusted a few times during the experiment. This explains the slight change of the accumulated fatigue damage rate of some curves. The time needed by the aluminium specimens to have fatigue failure range between four and nine days while the construction steel specimen P1 failed after almost 2 days and the P0 and P2 specimens failed after about 10 and 17 days, respectively. The accumulated fatigue damage at failure is roughly within the range $\tilde{\mathcal{D}} \in [0.6, \ldots, 1.7]$. The dispersion of the accumulated fatigue damage at failure makes the use of this measure to avoid fatigue failure unreasonable as choosing the lower value as the critical fatigue damage, namely $\mathcal{D}_{cr} = 0.6$, might be very conservative, while choosing any higher value would increase the risk of undetected fatigue failure.

4.4.3 Comparative Sensor Data Approach as SHM System

The previous sub-section has demonstrated that the use of the absolute accumulated fatigue damage index is not practical for fatigue failure detection due to its stochastic nature. This section, discusses the proposed fatigue failure detection approach based on the estimated fatigue damage index.

In this experimental part two different sets of specimens are tested, the first set of specimens use two different strain measurement sensors, the first one is the monitoring sensor located at the critical location, the second strain sensor is the reference one, that is used to measure the loading where it is less likely to have fatigue failure. The second set is equipped with only the monitoring strain measurement sensor located next to the hole at the most critical location where fatigue failure is expected to occur. In addition to the monitored loading measurement, the input loading force is also measured and used as reference. In the following the obtained results are presented.

4.4.3.1 Fatigue Damage Detection Using Monitoring and Reference Strain Measurements

The results obtained from an aluminium specimens equipped with a monitoring and reference strain sensors (specimen Nr. 2DMS_P2) are examined in this section. Fig. 4.71 shows the obtained fatigue damage detection results. In this experiment, fatigue failure has occurred after about 6.5 days, however, the reference strain sensor failed after 4.9 days. Using the rainflow counting algorithm to estimate fatigue damage caused by the monitoring and the reference loading per each data-block (each of $480\,s$ duration); and plotting the reference fatigue damage $\mathcal{D}^{RFC}_{m,reference}$ against the monitored fatigue damage $\mathcal{D}^{RFC}_{m,monitored}$, the scatter plot shown in fig. 4.71 is obtained. Furthermore, fig. 4.71 shows also the progress of the standard deviation per each data-block during the experiment of the monitored and the reference responses.

The scatter plot shows for the first part (first 2 days) a linear relation between the monitored and reference fatigue damage rate values. Using the data collected for the first two days (almost one third of the time till failure of the specimen) to estimate the linear regression between the monitored and fatigue damage rate, the continuous line shown in fig. 4.71 is obtained.

Let δ be a scalar that represents the distance between the linear regression line and a parallel one, it is possible to obtain two parallel lines to the linear regression, each at distance δ. The parallel lines are shown on the figure as dashed ones. By setting the appropriate distance δ, it is possible to define a tolerance region where all points gathered in the first two days of the experiment that feature a linear relation (blue colour) are located within it (between the two dashed lines). After three days, some points start to shift out-side the tolerance region (red colour). The number of points located out-side this region increase with time till 4.4 days where all points are completely out-side the tolerance region and basically located at one side. With time progress the points deviates far from the linear regression. The deviation of the calculated

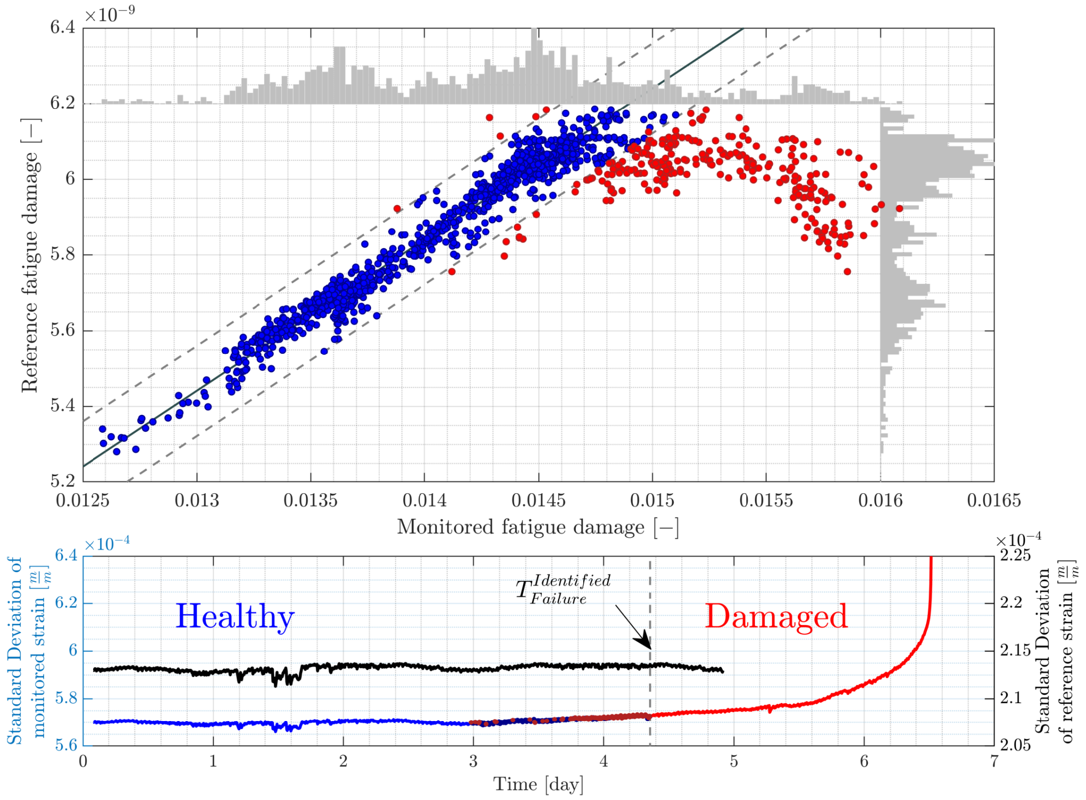

Figure 4.71 Fatigue damage detection of Aluminium specimen Nr. 2DMS-P2 using strain measurement as reference

fatigue damage from the monitoring sensor to the right indicates an increase in the estimated fatigue damage value, while at the same time, the estimated damage from the reference sensor keeps the same level.

By taking a closer look at the standard deviation of the monitored and reference strains, it is possible to notice that for the first three days, both plots share similar trend, after that, the standard deviation of the monitored strain starts to slightly increase while the reference one keeps the same level. The increase of the standard deviation of the monitored strain exacerbates over time till complete damage failure occurs after six and half days. Through the regular visual inspection of the specimen during the experiment duration till a few hours before failure, no signs of failure could be identified on the outer surface. In the last few hours, the crack becomes visible on the hole side (at stress concentration point) and starts to propagate towards the outer-side of the specimen.

By making use of the linear regression and the pre-defined tolerance region, it is possible to distinguish three main stages of the specimen during the experiment. In the first stage, the monitored and the reference fatigue damage rate feature a linear correlation. In this stage the specimen is considered as healthy. The second stage starts when the points begin to scatter between in-side and out-side of the tolerance region. In the second stage, fatigue failure starts (or already started, but its effect is clear now) and the material at the monitored location starts to weaken. With time progress, stage three is reached where all scatter points are located outside the tolerance region and the material in this stage could be considered as damaged due to fatigue.

The main feature that could be obtained from this strategy is the detection of fatigue failure in the early stages using a simple fatigue index. The tolerance region plays a key-role in the identification of the three stages. This tolerance region could be defined at the first period when the component is subject to the operational loading and is updated regularly. The second stage gives the early warning of fatigue failure, the duration of this stage depends on the fatigue fracture characteristic (ductile of brittle) and the loading spectrum. Finally, in the last stage fatigue failure happens and the component could be classified in this stage as damaged.

4.4.3.2 Fatigue Damage Detection Using Monitoring Strain Measurement and Input Loading as Reference

This approach uses the standard deviation of the input loading as reference to be compared on a logarithmic scale with the progress of the monitored fatigue damage. In total, seven aluminium and three construction steel specimens are monitored using this approach. Similar steps to that illustrated in sec. 4.4.3.1 are followed and the same three stages could be also identified.

Aluminium Specimens

Fig. 4.72 shows fatigue monitoring results of the specimen Nr. 2DMS-P2. This figure follows the same structure as fig. 4.71, however the reference is changed from the fatigue damage obtained from the reference loading to the standard deviation of the measured loading force. The scatter in the first one and half day (red points to the left) is coherent and shows a linear relation between the monitored and reference values. At the end of the second day the scatter is shifted to the right and with time progress, the linear relation between the reference and monitored values is clear to identify (blue points in the scatter plot). After about four and half days, the scatter starts again to shift to the right till the points are located outside the tolerance region and the specimen could be classified as damaged. The reason for the scatter shift at the end of the second day is not clear, however, a possible reason could be a change of the boundary conditions such as fixing screws not being tightened properly. Due to this scatter shift a linear regression using the data collected for the first two days will be useless for fatigue failure detection purpose, however it gives an indication of a behavioural change that requires system inspection.

By using the data collected during the third day, the linear regression presented in the fig. 4.72

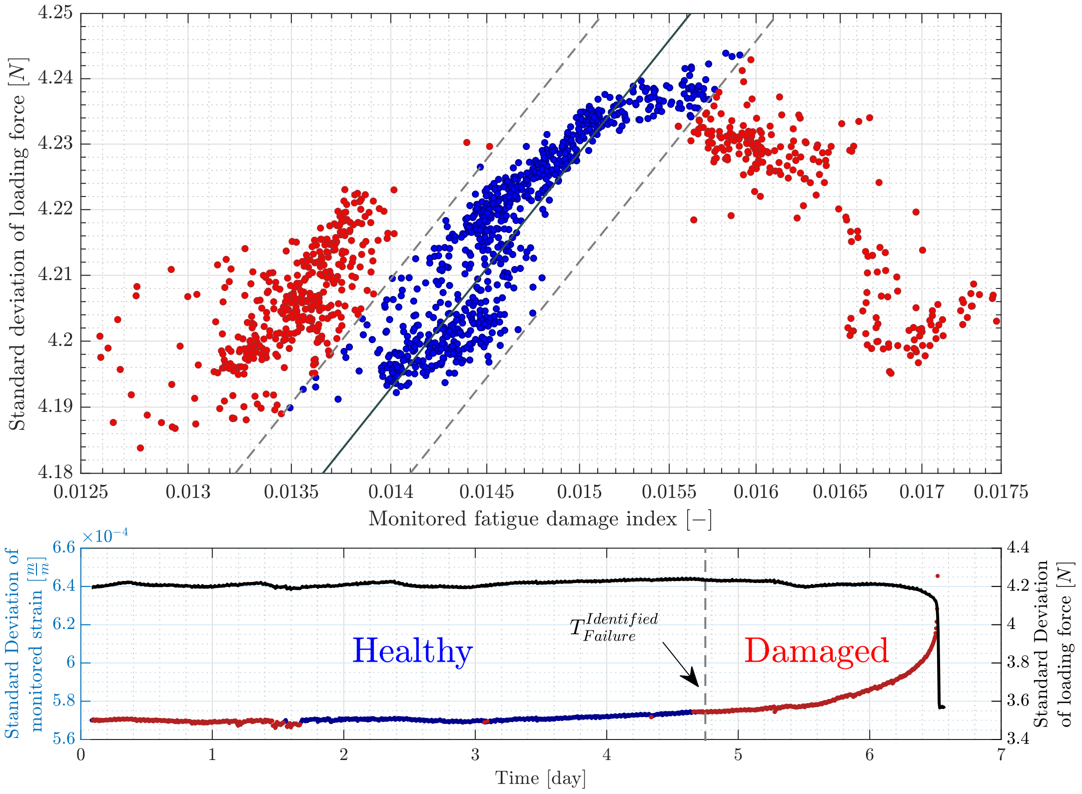

Figure 4.72 Fatigue damage detection of Aluminium specimen Nr. 2DMS-P2 using standard deviation of loading measurement as reference.

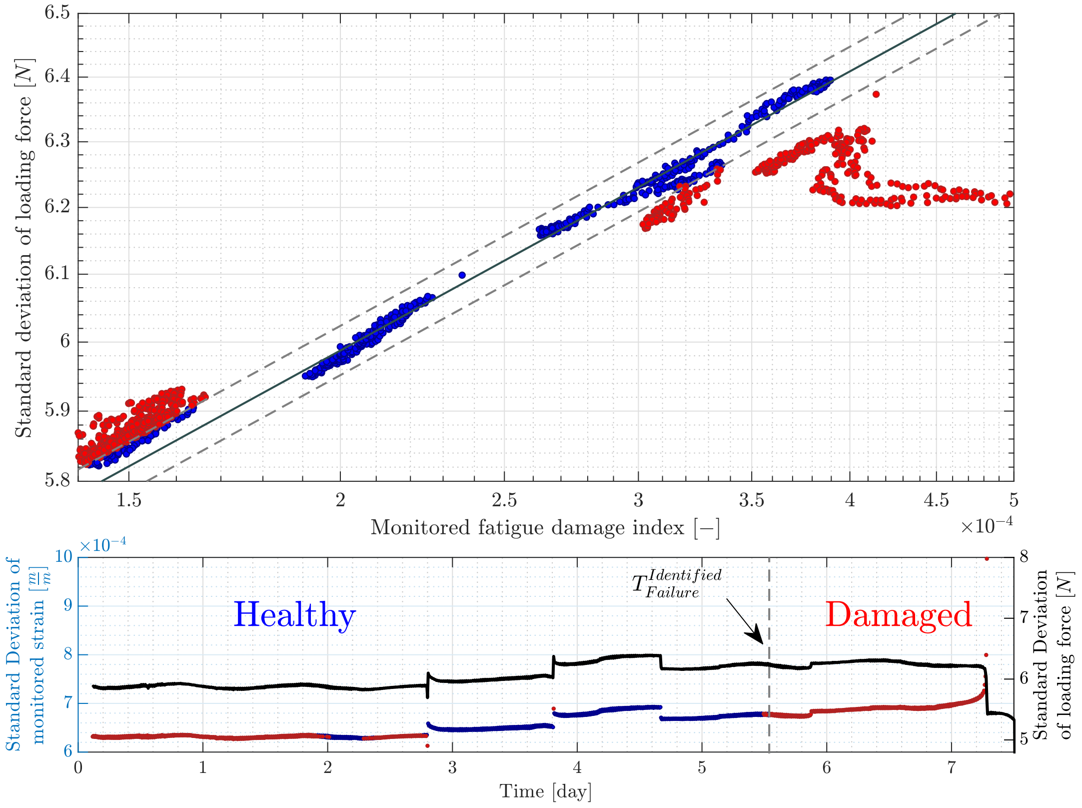

Figure 4.73 Fatigue damage detection of Aluminium specimen Nr. P1.

is obtained. Defining a tolerance region to include all the points of the third day will result into having two sets of points outside the defined tolerance region. The red points to the left correspond to the data collected during the first two days. This sub-dataset indicates a change in the system that requires system inspection and if the system has been found healthy, they could be disregarded from the monitoring process. The second set of red points to the right of the tolerance region shows clearly how the fatigue damage increases for the same loading level. This scatter indicates that fatigue damage could be detected after 4.8 days, which is a little bit late when compared to the previous monitoring approach (fig. 4.71) that is able to detect fatigue damage about half day earlier.

Furthermore, fatigue monitoring results are also illustrated in fig. 4.73 (specimen Nr. P1), fig. 4.74 (specimen Nr. P2), fig. 4.75 (specimen Nr. P4), fig. 4.76 (specimen Nr. P5) and fig. 4.77 (specimen Nr. P7). These figures follow the same structure presented before in subsec. 4.4.3.1. In these figures, it is possible to distinguish three stages. In the first stage the specimen is considered as healthy and blue colour is used in it. The second stage gives the early indications of fatigue failure and it ends when a clear indication of failure is available. This stage is referred to as the warning stage and both blue and red colours are used inside it. In the third stage the specimen is considered as damaged and the red colour is used for it.

The monitored fatigue damage rate in addition to the standard deviation of the loading force per each data-block collected in the first two days are used to build the linear regression. The tolerance region is defined to include all the points obtained in this period. Before the scatter starts to deviate outside the tolerance region the specimen could be considered as healthy. The end of the warning stage in this thesis is defined by the last point located inside the tolerance region. This is possible as the data are post-processed offline. This might not be possible in case of online monitoring. However, the presented results show that even if high threshold is used to define the end of the warning stage, it is still possible to detect fatigue damage before the complete structural failure.

The duration of the warning phase differ largely between the specimens. While the short duration of about five hours is observed in specimen Nr. P4, it may take as long as three days as in specimen Nr. P1. The duration of this phase has direct relation to the standard deviation of the loading force. That is to say, the higher is the loading force amplitude, the shorter is the warning region.

In all these results the same scatter patter is observed. While linear relation dominates in the first phase, the scatter in the second and third phase starts to extend to the right, that indicates an increase in the estimated fatigue damage rate at the same loading level and the linear relation clearly identified in the first phase is absent in the second phase and it takes different direction

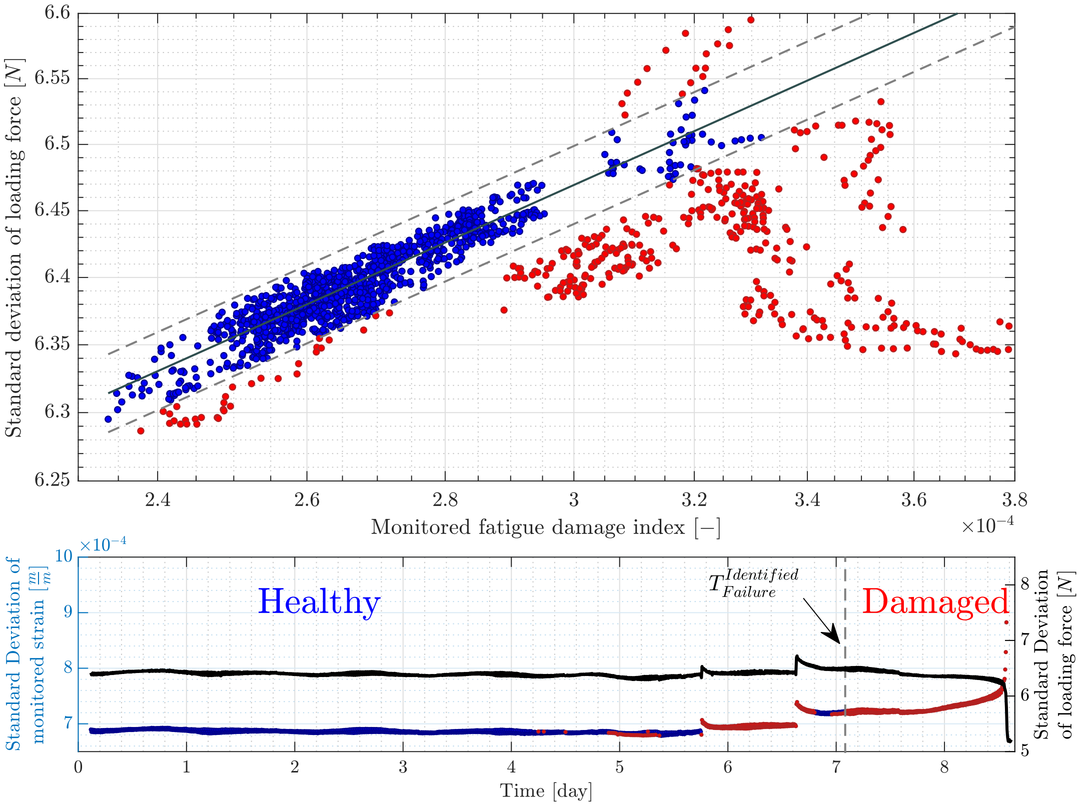

Figure 4.74 Fatigue damage detection of Aluminium specimen Nr. P2.

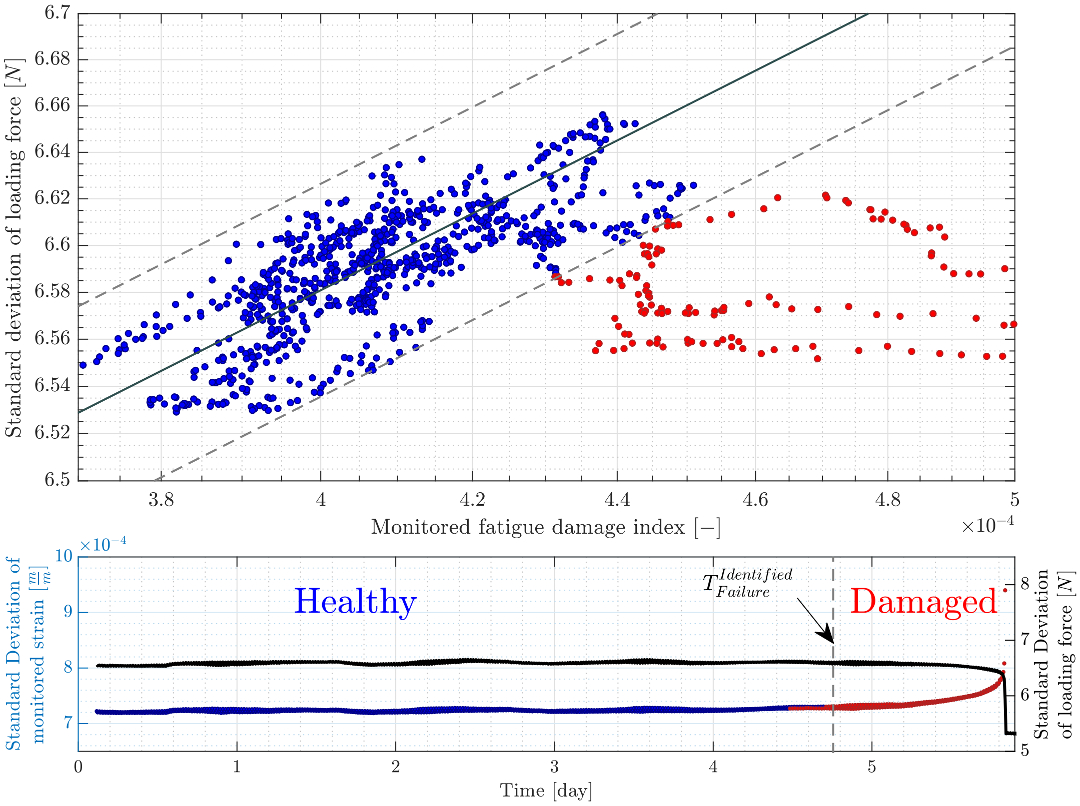

Figure 4.75 Fatigue damage detection of Aluminium specimen Nr. P4.

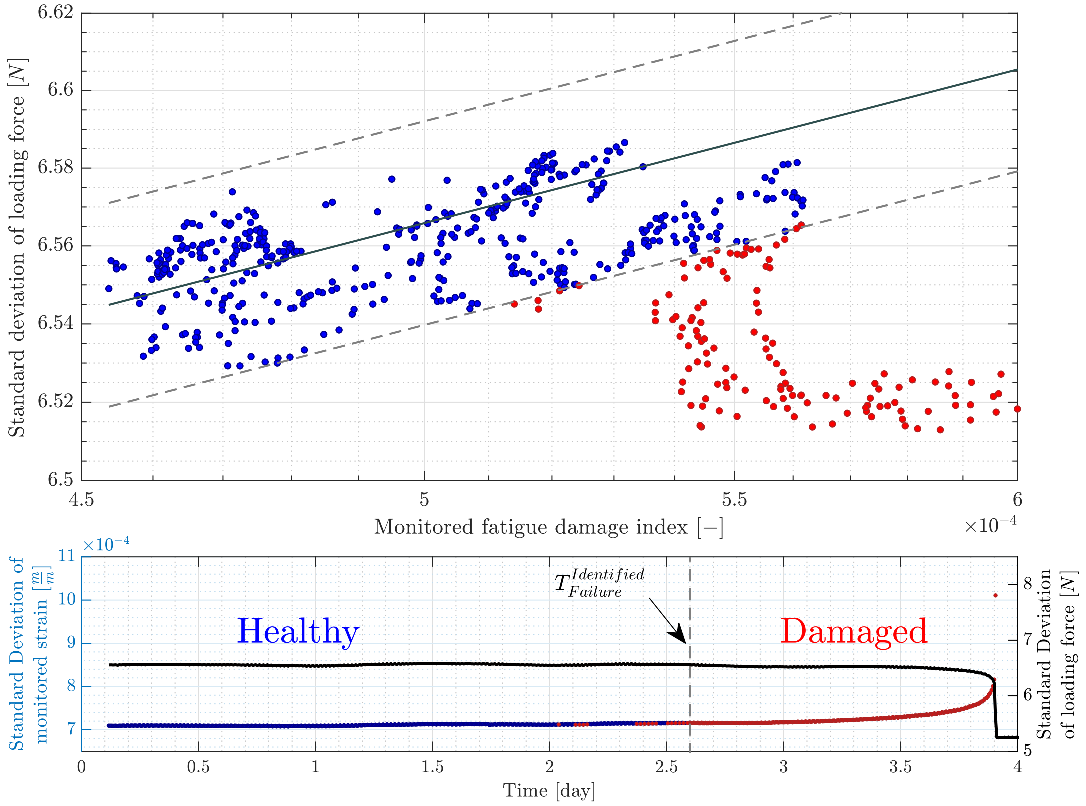

Figure 4.76 Fatigue damage detection of Aluminium specimen Nr. P5.

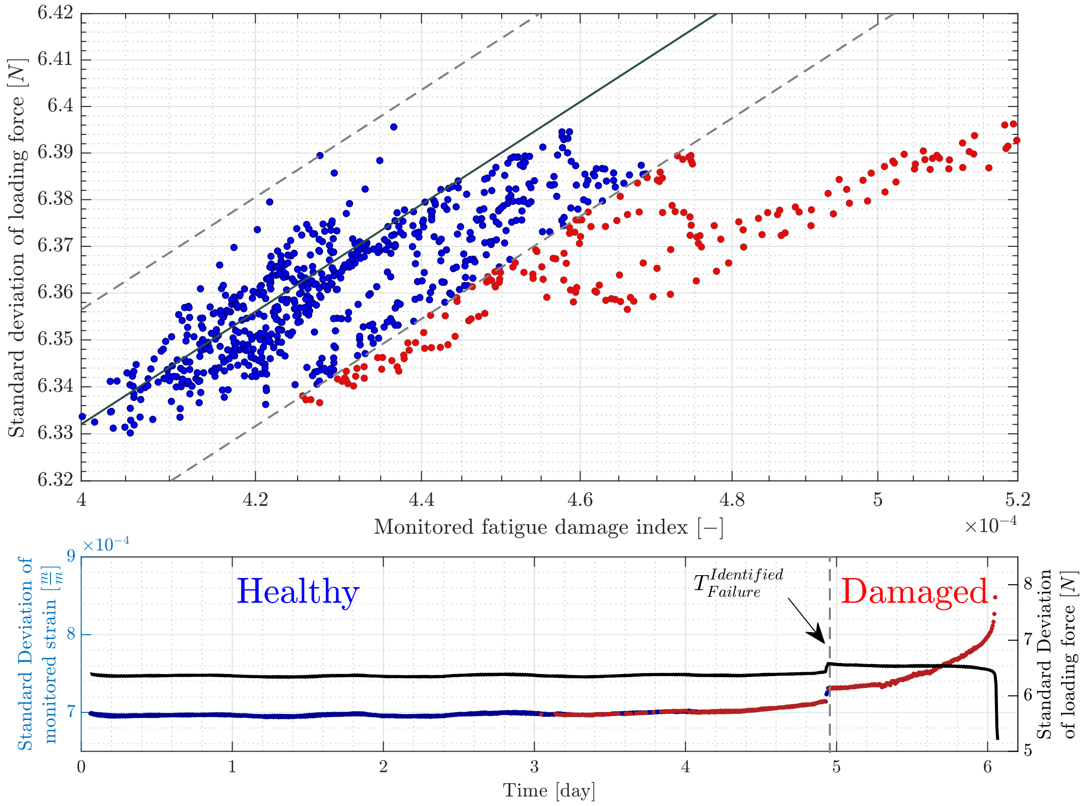

Figure 4.77 Fatigue damage detection of Aluminium specimen Nr. P7.

in the third one.

Finally, tab. 4.13 presents a summary of the accumulative fatigue damage in addition to the identified time of failure $T_{Failure}^{Identified}$ using the proposed monitoring approach. $T_{Failure}^{Identified}$ corresponds to the last point of the second stage and as of this time point the specimen is considered as damaged. Comparing these values to the time of failure $T_{Failure}^{\mathcal{D}_{cr}}$ identified using the accumulative fatigue damage presented in fig. 4.70, it is possible to observe that $T_{Failure}^{Identified}$ corresponds to 67 % – 83 % of $T_{Failure}^{\mathcal{D}_{cr}}$. In both cases, fatigue damage is detected early enough before the catastrophic failure.

Construction Steel Specimens

The results obtained from construction steel specimens are not as clear as that obtained from the aluminium specimens. This is due to ductile fatigue fracture of the aluminium and the brittle one of the construction steel. However, it is still possible to identify fatigue failure with considerable time before the complete failure of the material. An example of fatigue failure detection of construction steel specimens is presented in fig. 4.78 (specimen Nr. P1). In order to build the linear regression and the corresponding tolerance region, the data collected during the first day are considered. The tolerance region is defined such as all scatter points for this early periods are located inside it. Moreover, the same three phases as before are used, however, the second phase (warning phase) is hard to identify due to the brittle fatigue facture of construction steel. Based on this, it is reasonable to consider the first deviation of the scatter outside the tolerance region to be considered as a true indication of damaged specimen.

Experiment Summary

Tab. 4.13 presents a summary of the accumulative fatigue damage in addition to the identified time of failure $T_{Failure}^{Identified}$ using the proposed monitoring approach. Comparing the identified failure time to $T_{Failure}^{\mathcal{D}_{cr}}$ demonstrates the possibility to detect fatigue failure as early as 62 % of $T_{Failure}^{\mathcal{D}_{cr}}$ (specimen Nr. P1, construction steel) and as late as 97 % of $T_{Failure}^{\mathcal{D}_{cr}}$ (specimen Nr. P0, construction steel). In both cases fatigue failure is detected early enough before the complete failure of the specimen.

4.4.4 Summary of Results

Tab. 4.13 summaries at which values of $\mathcal{D}_{m}^{RFC}$ the complete fatigue failure occurs and the time needed $T_{Failure}^{\mathcal{D}_{cr}}$; in addition to that, the time at which the material could be completely classified as damaged $T_{Failure}^{Identified}$, both obtained from the proposed fatigue failure detection

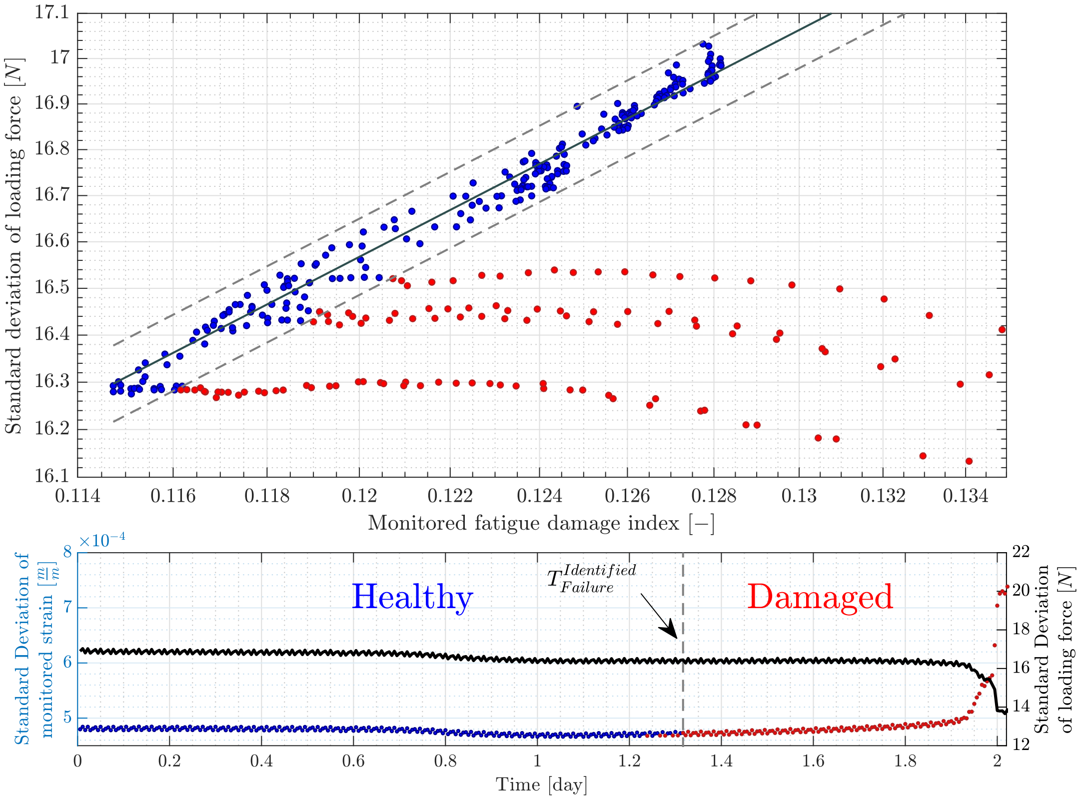

Figure 4.78 Fatigue damage detection of construction steel specimen Nr. P1.

approach. Using this approach it is possible to detect fatigue damage as early as when the material is about 62 % (construction steel specimen Nr. P1) of its fatigue life $T^{\mathcal{D}_{cr}}_{Failure}$; and as late as 97 % (construction steel specimen Nr. P0) of the material fatigue life $T^{\mathcal{D}_{cr}}_{Failure}$. These results depend on the pre-defined tolerance region that is set shortly after the material is put into service and updated gradually with time.

4.4.5 Conclusion

The main advantage of the proposed approach over the accumulative fatigue damage monitoring method is the absence of the dependency on the critical accumulated fatigue damage value at which the failure occur. On the contrary, the proposed approach is an adaptive one as it compares the fatigue damage calculated over a pre-defined time period, against a reference value such as the standard deviation of the input loading or the reference fatigue damage, both estimated for the same time period.

The experimental results demonstrate the ability of the proposed approach in the early detection of the fatigue failure in both specimen materials, aluminium and construction steel. However, due to the ductile fatigue fracture, the second phase is clearly to be identified in the aluminium specimen results, while the brittle fatigue fractures makes the existence of such phase very short.

Table 4.13 Summary of experimental fatigue failure detection results. The identified time of failure $T_{Failure}^{Identified}$ obtained using the fatigue failure detection approach are referenced to the time of failure at the critical accumulated fatigue damage index $T_{Failure}^{\mathcal{D}_{cr}}$ in order to obtain the listed percent (%) results.

Specimen		Accumulated fatigue damage		Fatigue failure detection
Material	Nr.	$\mathcal{D}_m^{RFC-Failure}$ $[-]$	$T_{Failure}^{\mathcal{D}_{cr}}$ $[day]$	$T_{Failure}^{Identified}$ $[day\,(\%)]$
Alu	P1	0.843	7.3	5.5 (75 %)
	P2	1.140	8.6	7.1 (83 %)
	P4	1.147	5.8	4.7 (81 %)
	P5	0.983	3.9	2.6 (67 %)
	P7	1.511	6.1	5.0 (82 %)
	2DMS-P2	1.226	6.5	4.7 (72 %)
S235	P0	1.709	9.8	9.5 (97 %)
	P1	0.618	2.1	1.3 (62 %)
	P2	1.369	16.7	15.2 (91 %)

The rainflow cycle counting is mainly used in fatigue damage estimation as the focus of this section the early fatigue detection. Spectral methods have also been tested and comparable results are also obtained. Due to the similarity of the results, only that obtained from rainflow cycle counting are presented.

Both ways of building the scatter plot either using a reference fatigue damage or using a statistical measure of the loading have demonstrated the ability of early fatigue damage detection. However, it is worth to mention at this point that the experimental result obtained using reference fatigue damage estimated from a second bending strain measurement (sub-sec. 4.4.3.1) is not conclusive due to the failure (due to strain gauge de-bonding) of the reference strain sensor shortly after the specimen is classified as damaged. Therefore, repeating this experiment to confirm the obtained results is recommended.

The proposed approach requires very good knowledge of the loading pattern on the component and the most critical locations at which the fatigue is highly to occur. This is related to the necessity to install a monitoring sensor next to the critical location to monitor it. Furthermore, it would be better to use a loading measurement sensor close to the monitoring one as a reference value rather than using the loading input which might be difficult to measure.

4.5 Chapter Summary

The main focus of this chapter is to demonstrate the potentials of the proposed new strategies and techniques in fatigue failure detection. This is done using four different cases: using hi-fidelity simulation environment, operational tower loading measurement of a small wind turbine, operational tower loading measurement of a utility-scale wind turbine and finally using an experimental setup.

The potentials of using spectral methods for fatigue damage analysis in the early design stages have been demonstrated using hi-fidelity simulation environment. The simulations are based on the design load case (DLC) 1.2 of the international standard IEC 64100-3. In addition to that, realistic wind and wave loading from different onshore and offshore locations are used in the simulation. The performance of the spectral fatigue analysis depends on the wind turbine configuration, the operating region, the loading used for fatigue analysis and finally the used spectral method.

Wind turbine configuration varies with the considered sub-structure that changes the turbine dynamic response. While land-based turbines have rigid foundations and are subject to only wind loading, floating wind turbines are subject to wind and wave loadings. In addition to that, the floating platform adds six degrees of freedom that affects significantly the dynamics and the loading of the turbine structure. Spectral methods used for fatigue analysis of land-based turbine gives in general better results which are comparable to the standard cycle-counting method. This is clear from the spectral fatigue analysis results, using the tower fore-aft loading, shown in tab. 4.5.

The performance of the spectral methods depend on the operating region. The best performance is obtained at the full load region where fatigue damage estimations are more consistent. In the partial load region, the change of the mean aerodynamic loading over the rotor disk due to the controller objective of power optimization affects the results of the spectral methods, so they change with the mean wind speed.

Spectral methods give better estimation results for the tower side-side loading. This is due to that fact that this loading direction is less sensitive to the change of the mean wind speed. The better performance is the same for all turbine configurations. Tower fore-aft loading is more subject to the change of the mean aerodynamic loading in addition to the effect resulting from the platform pitching motion. This mainly introduce a varying mean value into the loading in addition to deviating the loading amplitude distribution from being Gaussian. Both factors affect the results of the spectral fatigue analysis of this loading direction.

Moreover, the estimation results depend highly on the used spectral method. Using the simulation data-set, the Empirical $\alpha_{0.75}$ demonstrated its ability to give consistent good estimations for all turbine configurations and in both loading directions using only the Gaussian approach. The second method that shows also consistent results is the Bands method which is able to give acceptable estimations for all turbine configurations for the tower fore-aft loading and good estimations for the side-side loading. The performance of the other methods depend on the loading direction and the turbine configuration as illustrated in tab. 4.5.

Fatigue analysis of operational tower loading for a small and utility-scale wind turbines show the capabilities of the proposed "de-trending&PbP" strategy. Using this strategy it is possible to obtain comparable fatigue damage estimation to the time domain. In the case of small wind turbine loading, the best spectral method to give good estimations is the Tovo-Benasciutti second method. While in the case of utility-scale wind turbine, almost similar performance is obtained using the Single-Moment, Empirical $\alpha_{0.75}$, Tovo-Benasciutti second method, Dirlik and Bands-method with slightly better performance by the last method.

Furthermore, fatigue analysis of the operational tower loading of the small and utility-scale wind turbine shows that the estimated fatigue damage from the stochastic component using any of the spectral methods follow the same trend as that obtained using the cycle-counting in the time domain. This open the possibility to using the spectral fatigue damage estimation from the stochastic component for fatigue monitoring. This is further demonstrated by the scatter of the estimate spectral fatigue damage against the standard deviation of the measured mean wind speed.

This chapter ends with an experimental demonstration of the use of the estimated fatigue damage index as part of a structural health monitoring system. The experimental setup demonstrates using many specimens made of aluminium and construction steel the possibility of early detection of structural failure. The proposed approach for SHM is an adaptive online approach that monitors the estimated fatigue damage per a pre-defined time period against a reference value. This could be either fatigue damage estimated from a reference measurement, or against a statistical measure such as the standard deviation of the loading.

Chapter 5

Conclusions and Recommendations

> *When one has finished building one's house, one suddenly realises that in the process one has learned something that one really needed to know in the worst way - before one began.*
>
> — Friedrich Nietzsche

Contents

5.1 Conclusions

Wind turbines are complex systems operating in harsh environment. The dynamic response of the turbine due to wind and wave loading depends on the characteristics of the loading and the turbine configuration. Land-based wind turbines have rigid foundations and are subject to only wind loading while floating offshore turbines experience additional degrees of freedom that, especially the platform pitch motion, affect significantly the turbine structural loading. Furthermore, interaction with the waves add another source of loading on the wind turbine.

The integrated design approach of wind turbines aims to optimise turbine structure in terms of cost, fatigue damage and service life time. This motivates the development of new approaches capable of saving time, computational effort, resources in addition to reducing the cost of energy. Wind turbines are required to be operational for at least 20 years, therefore, fatigue damage analysis is the key driver in the integrated design process and in the development of turbine structural health monitoring systems.

Fatigue analysis using frequency-domain methods have been an active topic of research in the past few years and it has found its way to many applications. Wind turbines are subject to random loading which makes it logical to use the random vibration fatigue theory. However, frequency-domain fatigue analysis is developed under certain assumptions that are hard to meet in the case of wind turbine loading. This includes for example the stationarity of the loading and the assumption of Gaussian amplitude distribution under which most of the spectral methods are developed. Finally, most frequency-domain methods assume zero-mean of the stochastic loading.

The main objective of this research is to address systematically the assumptions related to the frequency domain fatigue analysis methods and to develop new strategy that enable using spectral methods for wind turbine fatigue analysis. Furthermore, the objective is to quantify the performance of the proposed strategy against the standard time domain cycle counting estimation for different wind turbine configurations (rigid-foundations, different floating platforms) and operating conditions. The performance assessment is carried out using hi-fidelity simulation environment as long as using operational tower loading of a small and utility-scale wind turbines. The simulation data-set aims to replicate to some limit the integrated design process at the early design stages where limited information are available and fatigue assessment in short time is required. On the other side, the operational data-set demonstrates the potentials of using the spectral methods of fatigue analysis.

To help categorise the main conclusions of this thesis, this chapter review the set research objectives introduced in Chapter 1, the obtained results and the derived conclusions.

Objective 1: This research aims firstly to review the theoretical basis of the spectral fatigue analysis; secondly, to address the limitations of the frequency-domain methods and to develop a new strategy that enables using spectral methods for wind turbine fatigue analysis.

Stationarity of the random loading is the main required assumption in the theory of random vibration fatigue analysis. Under this assumption, many spectral methods are developed to deal with a class of random loading that enjoys Gaussian amplitude distribution while the non-Gaussian loading class is dealt with by making use of the methods developed for the first class. In both cases, spectral methods assumed zero-mean random loading.

A new strategy is proposed in this thesis to deal with the non-stationary, non-Gaussian wind turbine tower loading. This strategy is based on the decomposition of the loading time-series into a signal (referred to as deterministic signal) that represents the mean change of the loading resulting for example from the change of mean wind speed or wind direction; and a second signal (referred to as stochastic signal) that represents the stochastic changes about this mean value.

The decomposition could be done using different methods, however, the most computationally effective one is the moving average filter.

The deterministic signal still non-stationary and contains a few cycles with relatively large amplitudes with no sharp peaks and has basically very low frequency content (less than $0.1\,Hz$). The characteristic of this signal allows to down-sample it, thus, reducing the required transmission band-width, sampling rate of the data-acquisition system and the needed storage space. However, the only possibility to estimate fatigue damage resulting from this signal is the standard rainflow cycle counting.

The stochastic signal is quasi-stationary with zero mean value and symmetrical amplitude distribution with skewness higher than 3 (more peaky than Gaussian distribution). The standard deviation of this signal depends on the wind turbulence intensity. Segmentation techniques and classifiers could be used to divide this signal into stationary segments then to classify them according to their standard deviation values. This would allow post-processing each segment as a stationary one. However, the obtained operational results does-not justify the added computational complexity due to segmentation and classification, thus, the stochastic signal in its quasi-stationary form is considered to satisfy the stationarity assumption required for spectral fatigue analysis.

Three different approaches are proposed to estimate fatigue damage of this stochastic component. The first approach (called the Gaussian approach) ignores the fact that the amplitude distribution is non-Gaussian, thus, the Gaussian spectral methods are directly applied to estimation fatigue damage resulting from this signal. The second approach is referred to as the corrected Gaussian which tries to correct the estimation obtain with the Gaussian approach using a correction factor based on the skewness and kurtosis of the loading. The third approach is the transformed Gaussian model. This approach employs a transformation function (and its inverse) based on the skewness and kurtosis of the loading to estimate the cycle distribution using Gaussian methods, then using the inverse transformation and the linear fatigue accumulation, fatigue damage is estimated.

The multi-axial “Projection-by-Projection” fatigue criterion is used to estimated the total fatigue damage from the deterministic and stochastic components. The procedure of decomposing the loading, and using the appropriate method to estimate fatigue damage resulting from each component then to combine the estimations by employing the non-linear summation rule PbP is called the “de-trending&PbP” strategy.

The proposed strategy enables using spectral methods for fatigue analysis of wind turbines. This strategy by-pass the stationarity assumption be decomposing the non-stationary loading into a non-stationary loading (deterministic) and a quasi-stationary one (stochastic). The effort needed to analyse the non-stationary part could be drastically reduced due to the nature of this loading component, however, still should be done in time-domain. While the stochastic signal could be analysed using the appropriate spectral method. The only assumption required for this strategy is the non-correlation between the stochastic and deterministic components. This assumption could be removed by extending the PbP method to handle the correlation between the signal. However, due to the nature of both signals and in order to keep the proposed strategy as simple as possible, this assumption is regarded as reasonable.

The proposed strategy helps making use of the potentials of the frequency domain fatigue analysis, such as reducing the computational effort, the required high band-width and sampling rate of the data acquisition system in addition to the needed storage space, at the same time maintaining accurate fatigue damage estimations.

Objective 2: To evaluate the performance of the frequency-domain methods against the standard time-domain cycle counting. This comparison is done using the above mentioned data-sets: simulation and operational. The simulation data-set aims to replicate the integrated design process at early stages. While the operational data-set from small and utility scale wind turbine aims to evaluate the performance of the spectral-based methods against the industry standard rainflow cycle counting algorithm using operational stress measurement.

Performance assessment of the proposed strategy is done using three different loading data-sets. The first loading data-set is obtained using a hi-fidelity simulation environment and is based on the design load case (DLC) 1.2 of the international standard IEC 61400-3 for offshore wind turbines. Spectral fatigue analysis using the simulation data-set aims to replicate the integrated design process of the wind turbine. This design process requires intensive simulation and computational effort.

In the simulation data-set, the wind and wave loading are assumed stationary with constant mean value and are aligned with the turbine down-wind direction. Therefore, in such controlled environment, it is justified to assume that the loading is quasi-stationary and has a constant mean value. These assumptions are valid in the case of land-based turbines with rigid foundation. However, in the case of floating wind turbines, the added DOFs of the platform introduce a varying mean value to the tower loading, thus, the loading deviates from being stationary, therefore, it is more logical to use the proposed "de-trending&PbP" strategy. Hence this strategy requires the use of the time-domain cycle counting for the deterministic component, this will negates the potential benefits of the spectral methods as this will require again the intensive simulation. Therefore, the floating platform tower loading is "roughly" regarded as quasi-stationary and spectral fatigue analysis of the simulation data-set is carried out using the Gaussian, the corrected Gaussian and the transformed Gaussian model approaches. The results are presented in relative sense to the fatigue damage estimations obtained using the standard time-domain cycle counting.

The main conclusion derived from fatigue damage analysis of this data-set is that the performance of the spectral methods depend on the wind turbine configuration, the operating region, the loading used for fatigue damage analysis and finally the used spectral method. The performance of the spectral methods is more consistent in the above rated region, while in the partial load region the performance changes with the mean wind speed. This is due to the controller effect of power optimization that results into a varying aerodynamic loading over the rotor disk. Furthermore, the spectral methods have better performance in analysing fatigue damage of land-based turbines with rigid foundations, while the performance of most spectral methods deteriorate for the floating platforms. The performance also varies according the dynamics of the platform itself. Moreover, tower side-side loading is less sensitive to the change of mean wind speed and the changing dynamics of the floating platform, therefore, the performance of the spectral methods is better on this loading direction as on the tower fore-aft loading. Finally, the performance depends also on the spectral method itself. The Empirical $\alpha_{0.75}$ has proven to be the most robust method with consistent good estimation using the Gaussian approach in all turbine configurations and tower loading direction. In summary, spectral methods have good potentials in fatigue analysis of wind turbines at the early design stages, however, they should be used carefully as their performance vary according to the above mentioned factors. The results of spectral fatigue analysis of the simulation data-set are summarised in tab. 4.5.

Fatigue analysis of the operational tower loading from the small wind turbine using the proposed “de-trending&PbP” strategy demonstrates the potentials of the spectral methods. The obtained results using the proposed strategy with different spectral methods are comparable to that obtained using the time-domain cycle counting. Using the Gaussian approach, the Tovo-Benasciutti second method has the best performance followed by the 1^{st} Tovo-Benasciutti and Dirlik methods.

Many spectral methods with the Gaussian assumption demonstrate good performance when used within the “de-trending&PbP” strategy for fatigue analysis of the tower loading of the utility-scale wind turbine. However, the performance is sensitive to the high dynamic response initiated by the start-stop cycles of the turbine at lower wind speeds. If the data-blocks corresponding to these cycles are classified and post-processed using the time-domain cycle counting, while the rest are analysed using the spectral methods, good performance using Single-Moment, Empirical $\alpha_{0.75}$, Tovo-Benasciutti 2^{nd}, Dirlik and Bands methods is possible. The classification of the data-blocks is possible based on standard turbine measurements. The accumulated fatigue damage in this case could be estimated using the Projection-by-Projection criterion. This technique can guarantee the accuracy of the fatigue analysis results while at the same time, the benefits of the spectral methods could be still used.

Objective 3: To explore the potentials of using the online estimated fatigue damage for early detection of fatigue failure. This point is very important for implementing an online fatigue detection as part of a structural health monitoring system.

An online approach is proposed in this thesis for structural health monitoring. This approach is based on monitoring the linear relation between the estimated fatigue damage per a pre-defined time period against a reference value. This could be either fatigue damage estimated from a reference measurement, or against a statistical measure such as the standard deviation of the loading. An experimental demonstration of the use of the estimated fatigue damage index as part of a structural health monitoring system is presented in this thesis. The experimental setup demonstrates the possibility of the early structural damage detection before the occurrence of the final fatigue failure. This early detection is possible using specimens made of aluminium as long as using specimens made of construction steel. Tab. 4.13 summaries the obtained results of early structural damage detection.

The main advantage of the proposed online structural monitoring approach over the traditional accumulative fatigue damage monitoring method is the absence of the dependency on the critical accumulated fatigue damage value at which the failure occur. Furthermore, fatigue monitoring in this approach is possible using either the estimated fatigue damage from the time-domain or the one estimated using the “de-trending&PbP” method or even the estimated spectral fatigue damage from the stochastic component which have been demonstrated using the operational estimations from small and utility-scale wind turbine to follow the same trend as that of the time-domain.

5.2 Recommendations

Below is a list of topics that are yet to be explored. These topics have the potentials to improve the performance of the proposed fatigue damage strategy and the damage monitoring method. These topics are listed in the following paragraphs.

Taking the non-Gaussianity of the loading time-series into account have been tested using two different approaches, the corrected Gaussian and the transformed Gaussian model. These approaches have been used for fatigue damage analysis of the simulated data-set in addition to the operational tower loading of the small and utility-scale wind turbine. The obtained results demonstrate that both methods have failed to give better estimation. This is mainly related to the fact that the corrected Gaussian approach is based on a correction factor that is developed only using simulation data-sets, while the transformed Gaussian models has limitations related to the skewness and the kurtosis that prevent building the transformation function. The limitation of both methods in dealing with the non-Gaussian loading case reveals the need for further research on this topic.

The proposed method of fatigue damage monitoring has demonstrated its potentials using the experimental setup. Early fatigue detection is possible by comparing the monitored fatigue damage to a reference one estimated from another sensor, or by comparing it to the standard deviation of the loading. For the first case, Two specimens have been planned, but due to the reference sensor failure in the first specimen at the early stages of the experiment, only the results of the second specimen are presented. At this point it is worth to mention that the reference sensor in the second specimen has also failed after about 5 days. During this period early fatigue detection was possible, but the conclusion can not be considered as conclusive as it is not clear if the sensor had sudden failure or due to gradual strain gauge de-bonding. Therefore, further similar experiments are recommended before drawing a conclusive conclusion.

On the other side the early fatigue detection based on comparing the monitored fatigue damage against the standard deviation of the input loading has given consistent results for all eight specimens (five from aluminium and three from construction steel) and the drawn conclusion at this point is conclusive.

Before being able to apply this method on a real system, the following points should be taken into account. The proposed monitoring method assumes very good knowledge of the structure and the critical location of the system (hot spots), therefore, sensors should be located exactly at these locations in order to be able to capture any change in the local responses. Moreover, the boundary conditions are assumed to be constant and does not change during the monitoring period, otherwise, any change in these boundary conditions might be interpreted as structural damage. The same applies on the structure itself. Any change in the structure, for example ice on the turbine blades, might be interpreted as damage in the structure. Finally, the experiment has assumed only one damage in the specimen, the case of complex structure this assumption might be hard to meet. These challenges should be addressed properly before putting the proposed method into practice.

Bibliography

Arany, L., Bhattacharya, S., Macdonald, J., & Hogan, S. (2014). Accuracy of frequency domain fatigue damage estimation methods for offshore wind turbine support structures. *Second International Conference on Vulnerability and Risk Analysis and Management (ICVRAM) and the Sixth International Symposium on Uncertainty, Modeling, and Analysis (ISUMA)*, 1293–1302. https://doi.org/10.1061/9780784413609.130

Adegas, F. D., Sloth, C., & Stoustrup, J. (2012). *Structured linear parameter varying control of wind turbines*. In J. Mohammadpour (Ed.). C. W. Scherer (Ed.), *Control of linear parameter varying systems with applications*. Springer. https://doi.org/10.1007/978-1-4614-1833-7

Barthelmie, R., Hansen, O. F., Enevoldsen, K., Højstrup, J., Frandsen, S., Pryor, S., Larsen, S., Motta, M., & Sanderhoff, P. (2005). Ten years of meteorological measurements for offshore wind farms. *Journal of Solar Energy Engineering*, *127*(2), 170–176. https://doi.org/10.1115/1.1850489

Benasciutti, D., Cristofori, A., & Tovo, R. (2013). Analogies between spectral methods and multiaxial criteria in fatigue damage evaluation. *Probabilistic Engineering Mechanics*, *31*, 39–45. https://doi.org/10.1016/j.probengmech.2012.12.002

Braccesi, C., Cianetti, F., & Tomassini, L. (2015a). Random fatigue. A new frequency domain criterion for the damage evaluation of mechanical components. *International Journal of Fatigue*, *70*, 417–427. https://doi.org/10.1016/j.ijfatigue.2014.07.005

Benasciutti, D., Braccesi, C., Cianetti, F., Cristofori, A., & Tovo, R. (2016). Fatigue damage assessment in wide-band uniaxial random loadings by PSD decomposition: Outcomes from recent research. *International Journal of Fatigue*, *91*, 248–250. https://doi.org/10.1016/j.ijfatigue.2016.06.011

Benasciutti, D. (2012). *Fatigue analysis of random loadings - A frequency-domain approach* (Doctoral dissertation). University of Ferrara, Italy.

Bendat, J. S. (1964). *Probability functions for random responses: Prediction for peaks, fatigue damage, and catastrophic failures*. National Aeronautics and Space Administration.

Bossanyi, E., Fleming, P. A., & Wright, A. D. (2012). Field test results with individual pitch control on the NREL CART3 wind turbine. *50th AIAA Aerospace Sciences Meeting including the New Horizons Forum and Aerospace Exposition*, (AIAA 2012-1019).

Buhl, M., & Manjock, A. (2006). A comparison of wind turbine aeroelastic codes used for certification. *44th AIAA Aerospace Sciences Meeting and Exhibit*. https://doi.org/10.2514/6.2006-786

Bökamp, H. (2009). Schneider: Bautabellen für Ingenieure - mit Berechnungshinweisen und Beispielen, herausgegeben von Prof.-Dr.-Ing. Alfons Goris. *Beton- und Stahlbetonbau*, *104*(7). https://doi.org/10.1002/best.200990071

Bossanyi, E. (2009). *Controller for 5MW reference turbine* (tech. rep. 11593/BR/04). European Upwind Project report.

Bossanyi, E. A., & Quartan, D. C. (2003). *GH bladed theory manual* (tech. rep. 282/BR/009). Garrad Hassam and Partners Ltd.

Braccesi, C., Cianetti, F., Lori, G., & Pioli, D. (2005). Fatigue behaviour analysis of mechanical components subject to random bi-modal stress process: Frequency domain approach. *International Journal of Fatigue*, *27*(4), 335–345. https://doi.org/10.1016/j.ijfatigue.2004.09.004

Braccesi, C., Cianetti, F., Lori, G., & Pioli, D. (2009). The frequency domain approach in virtual fatigue estimation of non-linear systems: The problem of non-gaussian states of stress. *International Journal of Fatigue*, *31*(4), 766–775.

Braccesi, C., Cianetti, F., Lori, G., & Pioli, D. (2015b). Random multiaxial fatigue: A comparative analysis among selected frequency and time domain fatigue evaluation methods. *International Journal of Fatigue*, *74*, 107–118. https://doi.org/10.1016/j.ijfatigue.2015.01.003

Brandt, A. (2011). *Noise and vibration analysis: Signal analysis and experimental procedures*. John Wiley & Sons, Ltd. https://doi.org/10.1002/9780470978160

Benasciutti, D., & Tovo, R. (2004). *Rainflow cycle distribution and fatigue damage in Gaussian random loadings* (tech. rep. No. 129). Dipartimento di Ingegneria, Università degli Studi di Ferrara.

Benasciutti, D., & Tovo, R. (2005a). *On fatigue damage computation in random loadings with threshold level and mean value influence* (tech. rep. No. 139). Dipartimento di Ingegneria, Università degli Studi di Ferrara.

Benasciutti, D., & Tovo, R. (2005b). Spectral methods for lifetime prediction under wide-band stationary random processes. *International Journal of Fatigue*, *27*(8), 867–877. https://doi.org/10.1016/j.ijfatigue.2004.10.007

Benasciutti, D., & Tovo, R. (2005c). Comparison of spectral methods for fatigue damage assessment in bi-modal random processes. *9th International Conference on Structural Safety & Reliability (ICOSSAR)*.

Benasciutti, D., & Tovo, R. (2006). Fatigue life assessment in non-Gaussian random loadings. *International Journal of Fatigue*, *28*(7), 733–746. https://doi.org/10.1016/j.ijfatigue.2005.09.006

Benasciutti, D., & Tovo, R. (2007). On fatigue damage assessment in bi-modal random processes. *International Journal of Fatigue*, *29*(2), 232–244. https://doi.org/10.1016/j.ijfatigue.2006.03.013

Benasciutti, D., & Tovo, R. (2010). On fatigue cycle distribution in non-stationary switching loadings with Markov chain structure. *Probabilistic Engineering Mechanics*, *25*(4), 406–418. https://doi.org/10.1016/j.probengmech.2010.05.002

Benasciutti, D., & Tovo, R. (2017). Fatigue life assessment models under random loadings: State-of-the-art and future perspectives. *5th Symposium on Structural Durability in Darmstadt (SoSDiD 2017).*

Butron, T., Sharpe, D., Jenkins, N., & Bossanyi, E. (2001). *Wind energy handbook*. John Wiley & Sons Ltd.

Berglind, J. J. B., & Wisniewski, R. (2014). Fatigue estimation methods comparison for wind turbine control. *arXiv: Optimization and Control*. https://arxiv.org/abs/1411.3925

Barradas Berglind, J. d. J., Wisniewski, R., & Soltani, M. (2015). Fatigue load modeling and control for wind turbines based on hysteresis operators. *IEEE Press. American Control Conference*, 3721–3727. https://doi.org/10.1109/ACC.2015.7171908

Benasciutti, D., Zanellati, D., & Cristofori, A. (2019). The "Projection-by-Projection" (PbP) criterion for multiaxial random fatigue loadings. *Frattura ed Integrità Strutturale*, *47*(47), 348–366. https://doi.org/10.3221/IGF-ESIS.47.26

Camblong, H., Nourdine, S., Vechiu, I., & Tapia, G. (2011). Comparison of an island wind turbine collective and individual pitch LQG controllers designed to alleviate fatigue loads. *IET Renewable Power Generation*, *6*(4), 267. https://doi.org/10.1049/iet-rpg.2011.0072

Cristofori, A., & Benasciutti, D. (2014). *"Projection-by-Projection" approach: A spectral method for multiaxial random fatigue* (tech. rep. No. 2014-01-0924). SAE Technical Papers. https://doi.org/10.4271/2014-01-0924

Cristofori, A., Benasciutti, D., & Tovo, R. (2011). A stress invariant based spectral method to estimate fatigue life under multiaxial random loading. *International Journal of Fatigue*, *33*(7), 887–899. https://doi.org/10.1016/j.ijfatigue.2011.01.013

Chaaban, R., & Fritzen, C.-P. (2013). Model predictive and individual blade pitch control for stabilizing platform pitching motion of floating offshore wind turbines. *European Wind Energy Association (EWEA) Offshore Event 2013.*

Chaaban, R., & Fritzen, C.-P. (2014a). Reducing blade fatigue and damping platform motions of floating wind turbines using model predictive control. *Proceedings of the 9th International Conference on Structural Dynamics, EURODYN 2014.*

Chaaban, R., & Fritzen, C.-P. (2014b). Structural load analysis of floating wind turbines under blade pitch system faults. In N. Luo (Ed.). Y. Vidal (Ed.). L. Acho (Ed.), *Wind Turbine Control and Monitoring* (pp. 301–334). Springer.

Chaaban, R., & Fritzen, C.-P. (2014c). Structural load analysis of tension leg floating wind turbine under blade pitch system faults. *Proceedings of the 6th World Conference of Structural Control and Monitoring.*

Cianetti, F., Braccesi, C., Lori, G., & Pioli, D. (2005). A frequency method for fatigue life estimation of mechanical components under bi-modal random stress process. *SDHM Structural Durability and Health Monitoring*, *1*(4), 277–290.

Cosack, N. (2010). *Fatigue load monitoring with standard wind turbine signals* (Doctoral dissertation). Universität Stuttgart.

Carpinteri, A., Spagnoli, A., & Vantadori, S. (2017). A review of multiaxial fatigue criteria for random variable amplitude loads. *Fatigue & Fracture of Engineering Materials & Structures*, *40*(7), 1007–1036. https://doi.org/10.1111/ffe.12619

DIN. (2014). *Eurocode 3: Design of steel structures - Part 1-1: General rules and rules for buildings.* German version EN 1993-1-1:2005/A1:2014. https://doi.org/10.31030/2151589

Dirlik, T. (1985). *Application of computer in fatigue analysis* (Doctoral dissertation). University of Warwick.

DNV. (2014). *Offshore standard - Design of offshore wind turbine structures* (tech. rep. DNV-OS-J101). DNV.

DNV. (2016). *Recommended practice - Fatigue design of offshore steel structures* (tech. rep. DNVGL-RP-C203). DNV.

Downing, S. D., & Socie, D. F. (1982). Simple rainflow counting algorithms. *International Journal of Fatigue*, *4*(1), 31–40. https://doi.org/10.1016/0142-1123(82)90018-4

Eiken, O. (2017). *Fatigue damage in an offshore wind turbine using probability density evolution* (Master's thesis). Norwegian University of Science and Technology, Department of Structural Engineering. http://hdl.handle.net/11250/2455580

Enders, W. (2015). *Applied econometric time series.* Wiley.

Esbensen, T., & Sloth, C. (2009). *Fault diagnosis and fault-tolerant control of wind turbines* (Master's thesis). Aalborg University.

Ewins, D. J. (2001). *Modal testing: Theory and practice.* John Wiley & Sons Inc.

Fu, T.-T., & Cebon, D. (2000). Predicting fatigue lives for bi-modal stress spectral densities. *International Journal of Fatigue*, *22*(1), 11–21. https://doi.org/10.1016/S0142-1123(99)00113-9

Gao, Z., & Moan, T. (2007). Fatigue damage induced by non-Gaussian bi-modal wave loading in mooring lines. *Applied Ocean Research*, *29*(1–2), 45–54. https://doi.org/10.1016/j.apor.2007.06.001

Gao, Z., & Moan, T. (2008). Frequency-domain fatigue analysis of wide-band stationary gaussian processes using a tri-modal spectral formulation. *International Journal of Fatigue*, *30*(10), 1944–1955. https://doi.org/10.1016/j.ijfatigue.2008.01.008

Grandell, J. (2010). *Time series analysis*. Department of Mathematics, KTH.

Gryning, S. E., Floors, R., Pena, A., Batchvarova, E., & Brmmer, B. (2015). Weibull wind-speed distribution parameters derived from a combination of wind-lidar and tall-mast measurements over land, coastal and marine sites. *Boundary-Layer Meteorology*, *159*(2), 329–348. https://doi.org/10.1007/s10546-015-0113-x

Gerhard, T., Sturm, M., & Carolus, T. H. (2013). Small horizontal axis wind turbine: Analytical blade design and comparison with RANS-prediction and first experimental data. *ASME Turbo Expo 2013: Turbine Technical Conference and Exposition*. https://doi.org/10.1115/GT2013-94158

Hammerum, K., Brath, P., & Poulsen, N. K. (2007). A fatigue approach to wind turbine control. *Journal of Physics: Conference Series*, *75*. https://doi.org/10.1088/1742-6596/75/1/012081

Hansen, M. H., & Kallesøe, B. S. (2007). Servo-elastic dynamics of a hydraulic actuator pitching a blade with large deflections. *Journal of Physics: Conference Series*, *75*. https://doi.org/10.1088/1742-6596/75/1/012077

IEC. (2005). *International standard IEC 61400-1 - third edition* (tech. rep. IEC 61400-1:2005(E)). International Electrotechnical Commission.

IEC. (2009). *Wind turbines: Part 3: Design requirements for offshore wind turbines* (tech. rep. IEC 61400-3). International Electrotechnical Commission.

Jonkman, J. M., & Buhl Jr., M. L. (2005). *FAST user's guide* (tech. rep. NREL/EL-500-38230). National Renewable Energy Laboratory (NERL).

Jonkman, J. M., & Buhl, M. L. (2007). Loads analysis of a floating offshore wind turbine using fully coupled simulation. *WindPower 2007 Conference & Exhibition*, (NREL/CP-500-41714).

Jiao, G., & Moan, T. (1990). Probabilistic analysis of fatigue due to Gaussian load processes. *Probabilistic Engineering Mechanics*, *5*(2), 76–83. https://doi.org/10.1016/0266-8920(90)90010-H

Jonkman, J., Butterfield, S., Musial, W., & Scott, G. (2009). *Definition of a 5-MW reference wind turbine for offshore system development* (tech. rep. NREL/TP-500-38060). National Renewable Energy Laboratory (NREL).

Jonkman, J. M. (2007). *Dynamics modelling and loads analysis of an offshore floating wind turbine* (Doctoral dissertation). National Renewable Energy Laboratory (NERL).

Jonkman, B. J. (2009). *TurbSim user's guide (version 1.5)* (tech. rep. NREL/TP-500-46198). National Renewable Energy Laboratory (NREL).

Jonkman, J. M. (2010). *Definition of the floating system for phase IV of OC3* (tech. rep. NREL/TP-500-47535). National Renewable Energy Laboratory (NREL).

Jonkman, J. M., & Sclavounos, P. D. (2006). Development of fully coupled aeroelastic and hydrodynamic models for offshore wind turbines [NREL/CP-500-39066]. *ASME Wind Energy Symposium*.

Körber, A. (2014). *Extreme and fatigue load reducing control for wind turbines: A model predictive control approach using robust state constraints* (Doctoral dissertation). Technischen Universität Berlin.

Kihl, D. P., & Sarkani, S. (1999). Mean stress effects in fatigue of welded steel joints. *Probabilistic Engineering Mechanics*, *14*(1), 97–104. https://doi.org/10.1016/S0266-8920(98)00019-8

Kumar, A. A. (2011). *Multivariable control of wind turbines for fatigue load reduction in the presence of nonlinearities* (Doctoral dissertation). The University of Auckland.

Lackner, M. A. (2009). Controlling platform motions and reducing blade loads for floating wind turbines. *Wind Engineering*, *33*(6), 541–554. https://doi.org/10.1260/0309-524X.33.6.541

Lachmann, S. (2014). *Kontinuierliches Monitoring zur Schädigungsverfolgung an Tragstrukturen von Windenergieanlagen* (Doctoral dissertation). Fakultät für Bau- und Umweltingenieurwissenschaften der Ruhr-Universität Bochum.

Larsen, T. J., & Hanson, T. D. (2007a). A method to avoid negative damped low frequent tower vibrations for a floating, pitch controlled wind turbine. *Journal of Physics: Conference Series*, *75*, 1–11. https://doi.org/10.1088/1742-6596/75/1/012073

Larsen, T. J., & Hansen, A. M. (2007b). *How 2 HAWC2, the user's manual* (tech. rep. Risø-R-1597(ver. 3-1)(EN)). Risø National Laboratory.

Larsen, C. E., & Irvine, T. (2015). A review of spectral methods for variable amplitude fatigue prediction and new results. *Procedia Engineering*, *101*, 243–250. https://doi.org/10.1016/j.proeng.2015.02.034

Larsen, C., & Lutes, L. (1991). Predicting the fatigue life of offshore structures by the single-moment spectral method. *Probabilistic Engineering Mechanics*, *6*(2), 96–108. https://doi.org/10.1016/0266-8920(91)90023-W

Lescher, F., Zhao, J. Y., & Martinez, A. (2006). Multiobjective $H_2 = H_\infty$ control of a pitch regulated wind turbine for mechanical load reduction. *In Proc. European Wind Energy Conf.*

Maes, K., Iliopoulos, A., Weijtjens, W., Devriendt, C., & Lombaert, G. (2016). Dynamic strain estimation for fatigue assessment of an offshore monopile wind turbine using filtering and modal expansion algorithms. *Mechanical Systems and Signal Processing*, *76-77*, 592–611. https://doi.org/10.1016/j.ymssp.2016.01.004

Manjock, A. (2005). *Evaluation report: Design codes FAST and ADAMS for load calculation of onshore wind turbines* (tech. rep. No. 72042). Germanischer Llyod WindEnergy GmbH.

Màrquez, F. P. G., Tobias, A. M., Pèrez, J. M. P., & Papaelias, M. (2012). Condition monitoring of wind turbines: Techniques and methods. *Renewable Energy*, *46*, 169–178. https://doi.org/10.1016/j.renene.2012.03.003

Miles, J. W. (1954). On structural fatigue under random loading. *Journal of the Aeronautical Sciences*, *21*(11), 753–762. https://doi.org/10.2514/8.3199

Miner, M. A. (1645). Cumulative damage in fatigue. *Journal of Applied Mechanics*, *12*(3), 159–164.

Mršnik, M., Slavič, J., & Boltežar, M. (2013). Frequency-domain methods for a vibration-fatigue-life estimation – Application to real data. *International Journal of Fatigue*, *47*, 8–17. https://doi.org/10.1016/j.ijfatigue.2012.07.005

Murakami, Y. (1992). *The rainflow method in fatigue: The Tatsuo Endo memorial volume.* Butterworth-Heinemann Ltd. https://doi.org/10.1016/C2013-0-04533-1

Namik, H. (2012). *Individual blade pitch and disturbance accommodating control of floating offshore wind turbines* (Doctoral dissertation). The University of Auckland.

Nieslony, A., & Böhm, M. (2012). Mean stress value in spectral method for the determination of fatigue life. *Acta Mechanica et Automatica*, *6*(2), 71–74.

Niesłony, A., & Böhm, M. (2015). Mean stress effect correction in frequency-domain methods for fatigue life assessment. *Procedia Engineering*, *101*, 347–354. https://doi.org/10.1016/j.proeng.2015.02.042

Newland, D. E. (1993). *An introduction to random vibrations, spectral and wavelet analysis.* Prentice Hall.

Nieslony, A. (2009). Determination of fragments of multiaxial service loading strongly influencing the fatigue of machine components. *Mechanical Systems and Signal Processing*, *23*(8), 2712–2721. https://doi.org/10.1016/j.ymssp.2009.05.010

Nieslony, A. (2010). Comparison of some selected multiaxial fatigue criteria dedicated for spectral method. *Journal of Theoretical and Applied Mechanics*, *48*(1), 233–254.

Nourdine, S., Camblong, H., Vechiu, I., & Tapia, G. (2010). Comparison of wind turbine LQG controllers using individual pitch control to alleviate fatigue loads. *18th Mediterranean Conference on Control and Automation, MED'10*. https://doi.org/10.1109/med.2010.5547822

Njiri, J. G., & Söffker, D. (2016). State-of-the-art in wind turbine control: Trends and challenges. *Renewable and Sustainable Energy Reviews*, *60*, 377–393. https://doi.org/10.1016/j.rser.2016.01.110

Ochi, M. K., & Ahn, K. (1994). Probability distribution applicable to non-Gaussian random processes. *Probabilistic Engineering Mechanics*, *9*(4), 255–264. https://doi.org/10.1016/0266-8920(94)90017-5

Ortiz, K., & Chen, N. K. (1987). Fatigue damage prediction for stationary wideband processes. *Procceedings of the Fifth International Conference on Applications of Statistics and Probability in Soil and Structure Engineering.*

Olagnon, M. (1994). Practical computation of statistical properties of rainflow counts. *International Journal of Fatigue*, *16*(5), 306–314. https://doi.org/10.1016/0142-1123(94)90267-4

Papadimitriou, C., Fritzen, C.-P., Kraemer, P., & Ntotsios, E. (2011). Fatigue predictions in entire body of metallic structures from a limited number of vibration sensors using kalman filtering. *Structural Control and Health Monitoring*, *18*(5), 554–573. https://doi.org/10.1002/stc.395

Passon, P., Kühn, M., Butterfield, S., Jonkman, J., Camp, T., & Larsen, T. J. (2007). OC3 – benchmark exercise of aero-elastic offshore wind turbine codes. *Journal of Physics: Conference Series*, *75*. https://doi.org/10.1088/1742-6596/75/1/012071

Petrucci, G., & Zuccarello, B. (2004). Fatigue life prediction under wide band random loading. *Fatigue & Fracture of Engineering Materials & Structures*, *27*(12), 1183–1195. https://doi.org/10.1111/j.1460-2695.2004.00847.x

Rice, S. O. (1944). Mathematical analysis of random noise. *The Bell System Technical Journal*, *23*(3), 282–332. https://doi.org/10.1002/j.1538-7305.1944.tb00874.x

Rychlik, I., Johannesson, P., & Leadbetter, M. R. (1997). Modelling and statistical analysis of ocean-wave data using transformed gaussian processes. *Marine Structures*, *10*(1), 13–47. https://doi.org/10.1016/S0951-8339(96)00017-2

Ragan, P., & Manuel, L. (2007). Comparing estimates of wind turbine fatigue loads using time-domain and spectral methods. *Wind Engineering*, *31*(2), 83–99. https://doi.org/10.1260/030952407781494494

Rychlik, I. (1987). A new definition of the rainflow cycle counting method. *International Journal of Fatigue*, *9*, 119–121. https://doi.org/10.1016/0142-1123(87)90054-5

Rychlik, I. (1993). On the ‘narrow-band’ approximation for expected fatigue damage. *Probabilistic Engineering Mechanics*, *8*(1), 1–4. https://doi.org/10.1016/0266-8920(93)90024-P

Sherratt, F., Bishop, N., & Dirlik, T. (2005). Predicting fatigue life from frequency domain data. *Engineering Interity*, *18*, 12–26.

Schäfer, A. (2016). Structural health monitoring of wind turbines: Monitoring systems for rotor blades, towers and foundations. *Offshore Days 2016.*

Sarkani, S., Kihl, D., & Beach, J. (1994). Fatigue of welded joints under narrowband non-Gaussian loadings. *Probabilistic Engineering Mechanics*, *9*(3), 179–190. https://doi.org/10.1016/0266-8920(94)90003-5

Smith, S. W. (1999). *The scientist and engineers guide to digital signal processing* (Second Edition). California Technical Publishing.

Sonsino, C. M. (2007). Course of SN–curves especially in the high-cycle fatigue regime with regard to component design and safety. *International Journal of Fatigue*, *29*(12), 2246–2258. https://doi.org/10.1016/j.ijfatigue.2006.11.015

Sutherland, H. J. (1999). *On the fatigue analysis of wind turbines* (tech. rep. SAND99-0089). Sandia National Laboratories.

Taubert, M., Clauß, S., Freudenberg, H., Keil, A., & März, M. (2011). *Wind turbine design codes: Eine validierung von alaska/Wind mit BLADED, FAST und FLEX5* (tech. rep.). Institut für Mechatronik, Chemnitz.

Tchakoua, P., Wamkeue, R., Ouhrouche, M., Slaoui-Hasnaoui, F., Tameghe, T. A., & Ekemb, G. (2014). Wind turbine condition monitoring: State-of-the-art review, new trends, and future challenges. *Energies*, *7*(4), 2595–2630. https://doi.org/10.3390/en7042595

Thöns, S. (2012). *Monitoring based condition assessment of offshore wind turbine support structures* (Doctoral dissertation). Institut für Baustatik unk Konstruktion, ETH. Zurich. https://doi.org/10.3929/ethz-a-009753058

Tovo, R. (2002). Cycle distribution and fatigue damage under broad-band random loading. *International Journal of Fatigue*, *24*(11), 1137–1147. https://doi.org/10.1016/S0142-1123(02)00032-4

Volkmer, K., & Adam, T. (2016). *The wind turbine of the University of Siegen* (tech. rep. B-83-001-A). Institut für Fluid- und Thermodynamik, Universität Siegen.

van Kuik, G. A. M., Peinke, J., Nijssen, R., Lekou, D., Mann, J., Sørensen, J. N., Ferreira, C., van Wingerden, J. W., Schlipf, D., Gebraad, P., Polinder, H., Abrahamsen, A., van Bussel, G. J. W., Sørensen, J. D., Tavner, P., Bottasso, C. L., Muskulus, M., Matha, D., Lindeboom, H. J., . . . Skytte, K. (2016). Long-term research challenges in wind energy - a research agenda by the european academy of wind energy. *Wind Energy Science*, *1*, 1–39. https://doi.org/10.5194/wes-1-1-2016

WAFO. (2017). *A Matlab toolbox for analysis of random waves and loads - Tutorial for WAFO version 2017* (tech. rep.). Lund University.

Wedman, S. (2010). *Lebensdauerüberwachung in mechatronischen Systemen* (Doctoral dissertation). Universität Paderborn.

Welch, P. D. (1967). The use of fast fourier transform for the estimation of power spectra: A method based on time averaging over short, modified periodograms. *IEEE Transactions on Audio and Electroacoustics*, *15*(2), 70–73. https://doi.org/10.1109/TAU.1967.1161901

Winterstein, S. R. (1988). Nonlinear vibration models for extremes and fatigue. *Journal of Engineering Mechanics*, *114*(10), 1772–1790. https://doi.org/10.1061/(ASCE)0733-9399(1988)114:10(1772)

Winterstein, S., & Jha, A. (1995). Random models of second order waves and local wave statistics. *Proceedings, 10'th ASCE Engineering Mechcanical Speciality Conference*, *2*, 1171–1175.

Wirsching, P. H., & Light, M. C. (1980). Fatigue under wide band random stresses. *Journal of the Structural Division*, *106*(7), 1593–1607.

Wang, X., & Sun, J. Q. (2005). Effect of skewness on fatigue life with mean stress correction. *Journal of Sound and Vibration*, *282*(3), 1231–1237. https://doi.org/10.1016/j.jsv.2004.05.007

Wirsching, P., & Shehata, A. M. (1977). Fatigue under wide band random stress using the rainflow method. *Journal of Engineering Materials and Technology*, *99*(3), 205–211. https://doi.org/10.1115/1.3443520

Zhao, W., & Baker, M. J. (1992). On the probability density function of rainflow stress range for stationary gaussian processes. *International Journal of Fatigue*, *14*(2), 121–135. https://doi.org/10.1016/0142-1123(92)90088-T